

# Optomechanics with Superfluid Helium-4

Thesis by

Laura De Lorenzo

In Partial Fulfillment of the Requirements  
for the Degree of  
Doctor of Philosophy

The Caltech logo, consisting of the word "Caltech" in a bold, orange, sans-serif font.

California Institute of Technology  
Pasadena, California

2016

(Defended May 20, 2016)

© 2016

Laura De Lorenzo

All Rights Reserved

To John

"Deep into that darkness peering, long I stood there wondering, fearing,  
Doubting, dreaming dreams no mortal ever dared to dream before"

# Acknowledgements

There are many people to whom I owe my gratitude for their guidance and support along this journey. Firstly I would like to thank my adviser, Professor Keith Schwab, for teaching me how to approach a new and challenging experiment and for mentorship and counsel throughout my PhD. I would like to acknowledge the other members of my thesis and candidacy committees: Professor Rana Adhikari, Professor Yanbei Chen, Professor Andrei Faraon and Professor Kerry Vahala. Thank you for lending your time and expertise.

It is my pleasure to recognize all my fellow graduate students and the post docs whose time in the Schwab lab overlapped with mine: Ari Weinstein, Chan U Lei, Emma Wollman, Junho Suh, KC Fong, Matt Shaw, Harish Ravi, Harpreet Arora, and Aaron Pearlman. Thank you for your advice and support. I wouldn't have made it through without you. I would also like to thank our theory collaborators, Swati Singh and Igor Pikovski, for patiently teaching me about gravitational wave detectors. I would be remiss if I did not also recognize the members of the Eisenstein lab, specifically Debaleena Nandi, Chandni U., Erik Henriksen, and Johannes Pollanen. Thank you for countless discussions and encouragement and for the use of your vacuum furnace. I must also thank Tim Blasius and Louise Reina for being supportive and understanding friends. Thank you to the many other graduate students and post docs who encouraged me along the way: Alex Krause, Richard Norte, Simon Gröblacher, Carly Donahue, Justin Cohen, Seán Meenehan, Jeff Hill, Amir Safavi-Naeini, and Tao Paraiso.

I would like to recognize support from Mark and Bo in the PMA machine shop. Thank you for teaching me how to use the lathe and the mill and for hours of machining advice and instruction.

It is my pleasure to recognize my friends Eisha, Christy, and Jim for being my workout buddies and for bringing some outside perspective to my life. Most importantly, I would like to express my gratitude to my family: my parents, my brother Donald, sister-in-law Jen, and my sister Julie. Certainly I would not be here today without you. Finally, I am indebted to John, for having the patience to tolerate all six years.

# Abstract

We demonstrate the utility of superfluid helium-4 as an extremely low loss optomechanical element. We form an optomechanical system with a cylindrical niobium superconducting  $TE_{011}$  resonator whose  $40\text{ cm}^3$  inner cylindrical cavity is filled with  ${}^4\text{He}$ . [1] Coupling is realized via the variations in permittivity resulting from the density profile of the acoustic modes. Acoustic losses in helium-4 below 500 mK are governed by the intrinsic nonlinearity of sound, leading to an attenuation which drops as  $T^4$ , indicating the possibility of quality factors (Q) over  $10^{10}$  at 10 mK. In our lowest loss mode, we demonstrate this  $T^4$  law down to 50 mK, realizing an acoustic Q of  $1.35 \cdot 10^8$  at 8.1 kHz. When coupled with a low phase noise microwave source, we expect this system to be utilized as a probe of macroscopic quantized motion, for precision measurements to search for fundamental physical length scales, and as a continuous gravitational wave detector. Our estimates suggest that a resonant superfluid acoustic system could exceed the sensitivity of current broad-band detectors for narrow-band sources such as pulsars [2].

# Contents

<b>Acknowledgements</b>	<b>iv</b>
<b>Abstract</b>	<b>vi</b>
<b>1 Helium-4</b>	<b>1</b>
1.1 Historic Background . . . . .	1
1.2 Basic Properties . . . . .	4
1.3 Two Fluid Model . . . . .	5
1.4 Equations of Motion . . . . .	7
1.5 Thermomechanical Effect . . . . .	8
1.6 Elementary Excitations . . . . .	9
1.7 Second Sound . . . . .	11
1.8 Vortices . . . . .	12
<b>2 Optomechanics</b>	<b>14</b>
2.1 Introduction . . . . .	14
2.2 Our System . . . . .	17
2.3 Microwave Modes . . . . .	20
2.3.1 TE Modes of a Cylinder . . . . .	20
2.3.2 TM Modes of a Cylinder . . . . .	22
2.3.3 Quality Factor of Cylindrical Microwave Resonators . . . . .	23
2.3.4 Brief Introduction to Superconductivity . . . . .	24
2.3.5 Microwave Quality Factor of Niobium . . . . .	28

2.3.6	Microwave Modes in Sapphire . . . . .	29
2.4	Acoustic Modes . . . . .	30
2.4.1	Acoustic to Microwave Coupling Strength . . . . .	33
2.5	Cavity Heating . . . . .	36
2.5.1	Thermal Model . . . . .	36
2.5.2	Dielectric Heating . . . . .	40
2.6	Notes about Temperature Stability . . . . .	42
<b>3</b>	<b>Circuit Equations</b>	<b>44</b>
3.1	Inductively Coupled RLC Circuit . . . . .	44
3.2	Equivalent Parallel Circuit Model . . . . .	47
3.3	Circulating Cavity Voltage . . . . .	54
3.4	Sideband Voltages . . . . .	59
3.4.1	Upconverted Signal Power . . . . .	64
3.5	Sideband Cooling . . . . .	68
3.6	Detection Temperature . . . . .	69
<b>4</b>	<b>Acoustic Loss Mechanisms</b>	<b>71</b>
4.1	Attenuation in Pure $^4\text{He}$ . . . . .	71
4.2	Attenuation from Impurities . . . . .	75
4.2.1	Lowering Impurity Concentration . . . . .	79
4.2.2	Isotopic Purification . . . . .	80
4.3	Other Acoustic Dissipation Mechanisms in $^4\text{He}$ . . . . .	81
4.4	Container Loss . . . . .	82
<b>5</b>	<b>Experimental Details and Results</b>	<b>89</b>
5.1	Niobium Cavity Description . . . . .	89
5.1.1	Niobium Cavity Results . . . . .	92
5.2	Description of Experimental Setup . . . . .	96
5.3	Experimental Run Procedure . . . . .	103

5.4	Measurement Procedure	113
5.5	Notes on Each Run	115
5.5.1	General Notes	115
5.5.2	Run 1	118
5.5.3	Run 2	119
5.5.4	Run 3	120
5.5.5	Run 4	125
5.5.6	Run 5	132
5.5.7	Planned Runs	139
5.6	Future Improvements	140
5.6.1	Superfluid Valve	140
5.6.2	Decreasing Suspension Loss	144
5.6.3	Decreased Dielectric Heating	145
5.7	Sapphire	145
<b>6</b>	<b>Outlook</b>	<b>149</b>
6.1	Ground State Cooling	149
6.1.1	Low Phase Noise Microwave Source	152
6.2	Gravitational Wave Detector	155
6.3	Testing Minimum Length Scales	160
<b>A</b>	<b>Table of Variables</b>	<b>165</b>
<b>B</b>	<b>Bessel Functions</b>	<b>168</b>
B.1	Zeroes of Bessel Functions of the First Kind	168
B.2	Extrema of Bessel Functions of the First Kind	169
B.3	Extrema of Bessel Functions of the First Kind, Acoustic	170
<b>C</b>	<b>Niobium Cylinder Drawings</b>	<b>171</b>
<b>D</b>	<b>Valve Drawings</b>	<b>174</b>

<b>E Sinter Drawings</b>	<b>180</b>
<b>F Suspension Drawings</b>	<b>184</b>
<b>G Sapphire Drawings</b>	<b>187</b>
<b>Bibliography</b>	<b>190</b>

# List of Figures

1.1	The heat capacity of helium versus temperature. The transition point at 2.17 K is known as $T_\lambda$ because of the shape of the heat capacity through transition.	6
1.2	a) The dispersion curve of helium II showing the linear phonon contribution (blue) and the roton minimum (red). b) The superfluid (red) and normal fluid (blue) fractions of helium below $T_\lambda$ . . . . .	10
2.1	a) An SEM of a nanomechanical resonator used in our lab, showing a capacitor with the top plate suspended surrounded by a spiral inductor (courtesy Chan U Lei). b) The canonical example of a microwave optomechanical system: an RLC circuit with a capacitor plate that is free to vibrate. . . . .	15
2.2	Diagrams of our superfluid optomechanical systems: a) the cylindrical niobium cell with an inner diameter of 3.56 cm and height of 3.95 cm. Two hermetically sealed dielectric probes are used to couple microwaves into and out of the cavity. A capillary allows the cell to be filled at low temperatures. b) A vertical slice through the center of the sapphire cavity setup, showing the ring of ${}^4\text{He}$ and the fill line. The top cylinder, which supports the whispering gallery modes, is 5 cm in diameter and 3.1 cm in height. The helium annulus has an inner diameter of 2.2 cm, an outer diameter of 4 cm, and a height of 0.64 cm. The sapphire and the microwave couplers are mounted to an aluminum cavity which reduces the microwave loss from the evanescent fields. . . . .	17
2.3	Cylinder of height $L$ and radius $a$ in cylindrical coordinates. . . . .	20

2.4	The profiles of every superfluid acoustic mode for the niobium cavity design up to a frequency of 12 kHz. Below each mode is its frequency and mode number $(l, m, n)$ , where $l$ , $m$ , and $n$ indicate the number of nodes in the longitudinal, azimuthal, and radial directions. The white areas of the profiles indicate node locations. . . . .	32
2.5	A simplified representation of the thermal conduction from the superfluid helium to the mixing chamber. The helium is treated as a capacitance $C_{He}$ connected to the cell $C_{Nb}$ through the Kapitza boundary resistance $R_K$ , and the cell is connected to the mixing chamber through the resistance of the suspension system $R_{Susp}$ . Arrows represent heating due to dielectric loss in both the niobium ( $\dot{Q}_{Nb}$ ) and the helium ( $\dot{Q}_{He}$ ) and the cooling power of the dilution refrigerator ( $\dot{Q}_{MC}$ ). . . . .	40
2.6	The maximum temperature increase (red) and decrease (blue) over which a source originally centered in the superfluid acoustic resonator will remain within the bandwidth of the resonator, assuming that at all temperatures the $Q$ is limited by the three phonon process. . . . .	43
3.1	The equivalent circuit model for the inductively coupled niobium cavity ( $R_C, L_C, C_C$ ) parametrically coupled to the superfluid acoustic mode ( $C_M$ ). . . . .	45
3.2	a) The input circuit inductively coupled to the microwave cavity and b) its T circuit equivalent. . . . .	47
3.3	The Thevenin (series) and Norton (parallel) equivalent circuits. The impedance $Z_{th} = Z_N$ . . . . .	48
3.4	Solving for the thevenin impedance ( $Z_{th}$ ) of Fig. (3.2b). The intermediate impedances $Z1$ and $Z2$ are referenced in the text. . . . .	49
3.5	The parallel equivalent to Fig. (3.1). On the right the simplified version where the resistors $R_{ext}$ and $R_C$ are combined into $R_T$ and the capacitors $C_C$ and $C_M$ are combined into $C_T$ . . . . .	54

3.6	The scattering picture for a cavity drive tone ( $\omega_p$ ) applied on either the red or blue sideband. On the red or Anti-Stokes sideband, the pump frequency is $\omega_p = \omega_C - \omega_M$ and the upper sideband is incident with $\omega_C$ ; in this case the mechanics is preferentially damped. For a drive on the blue or Stokes sideband the pump frequency is $\omega_p = \omega_C + \omega_M$ , the lower sideband is incident with $\omega_C$ , and the mechanics is driven to higher occupations. . . . .	65
3.7	The phonon occupation of the mechanical mode is determined by its coupling both to the thermal bath through its intrinsic dissipation $\gamma_M$ and to the optical bath through the optomechanical coupling rate $\Gamma_{opt}$ . . . . .	68
4.1	Possible a)four phonon and b)three phonon scattering processes. . . . .	72
4.2	shows the expected absorption coefficient for an 8.1 kHz mode from the 3PP (green) and the $^3\text{He}$ impurity for concentrations $x =:$ $10^{-7}$ (red), $10^{-9}$ (blue), $10^{-10}$ (black), and $10^{-12}$ (grey), assuming the mean free path of $^3\text{He}$ atoms becomes limited by the cell diameter of 3.6 cm. . . . .	75
4.3	shows the expected quality factor versus temperature for an 8.1 kHz mode including effects of both the 3PP and the $^3\text{He}$ impurity for concentrations $x =:$ $10^{-7}$ (red), $10^{-9}$ (blue), $10^{-10}$ (black), and $10^{-12}$ (grey), assuming the mean free path of $^3\text{He}$ atoms becomes limited by the cell diameter of 3.6 cm. . . . .	78
4.4	A simplified diagram of how helium-4 can be isotopically purified via heat flush. The helium-3 atoms move with the normal fluid component. In the counterflow that is set up when helium II is heated, the normal fluid flows away from the heat source while the superfluid flows toward it. The superleak serves to define the direction with which the normal fluid moves away from the resistor. . . . .	81
4.5	COMSOL simulation showing distortions of the niobium cell due to the $l = 1$ , $m = 0$ , $n = 0$ superfluid acoustic mode with a frequency of 5984 Hz. . . . .	86
5.1	Pictures of the niobium microwave cavity after etching, showing a mirror finish: (a) the cell body and (b) the cell lid. . . . .	90

5.2	Transmission spectrum of the niobium cavity at 300K for stub couplers (blue) and loop couplers (red). In both the loop and stub coupled cavities, the couplers are located on the lid at a radius $r = 0.64a$ ( $a$ is the cavity radius), where the $TE_{011}$ magnetic mode is maximum. Modes are labeled by TE or TM and the mode number (n,m,l). There are three sets of degenerate modes: $TE_{010}/TM_{110}$ , $TE_{011}/TM_{111}$ and $TE_{012}/TM_{112}$ . . . . .	94
5.3	(a) S21 measurement of the $TE_{011}$ mode at 1.6 K, demonstrating a microwave $Q$ of $3.60 \cdot 10^8$ or a cavity linewidth of 30 Hz. (b) $Q$ of the $TE_{011}$ mode versus temperature. Data is represented by blue circles and the connecting line is a guide to the eye only. The red line is the expected quality factor from the BCS losses of Eqn. (2.20). The purple line is the expected quality factor including both the BCS loss and the residual resistance $R_0$ , where $R_0$ is calculated from the highest Q data point and found to be $2 \mu\Omega$ . . . . .	96
5.4	The plumping panel used to fill the niobium cavity with helium. . . . .	97
5.5	The helium fill line from the 1 K plate to the niobium cell. The line is thermally anchored at each stage with sintered-silver heat exchangers. . . . .	99
5.6	The plumbing panel used to actuate the cryogenic valve. . . . .	102
5.7	From Run 4, January 2015: a) With the cell on the fridge and initially under vacuum, frequency shifts of the $TE_{011}$ mode while filling the cell with $^4\text{He}$ gas. The cell is filled by applying $\approx 1.2$ bar of pressure from the helium cylinder attached to the plumbing panel. Notice the impedance of the fill line is such that filling requires $\approx 30$ minutes. b) With the cell on the fridge and initially filled with about one bar of $^4\text{He}$ gas, frequency shifts of the cell while evacuating to vacuum. After 90 minutes of pumping, the cell's frequency has returned approximately to the starting vacuum frequency from a). An additional 30 minutes or even 130 minutes of pumping do not appear to shift the frequency any further. . . . .	105

5.8	From Run 4, January 2015: The $TE_{011}$ and $TM_{111}$ modes at 77 K. Notice that the $TE_{011}$ appears as a dip rather than a peak. Checking the frequency shifts is easier using the $TM_{111}$ mode in this case. . . . .	107
5.9	From Run 4, January 2015: a) Frequency shifts of the $TM_{111}$ mode as the cell is filled with $^4\text{He}$ gas, starting with the cell in vacuum and thermalized to $\approx 77$ K. Notice that the total frequency shift is greater than at 300 K because helium is denser at lower temperatures. Also note that the frequency shifts more quickly because the conductance of capillaries improves at lower temperatures as the background pressure drops. b) Pumping on the cell at 77K with the cryogenic valve closed. The $TM_{111}$ mode frequency remains constant as expected if no helium is exiting the cell. c) Pumping on the cell at 77K with the cryogenic valve open. The frequency shifts back to the vacuum value within about an hour. . . . .	109
5.10	a) The vapor pressure of helium versus temperature and b) the density of helium versus temperature. . . . .	111
5.11	Pictures of the cell for each run of the fridge with complete descriptions given in the text: a) Run 1, b) Run 2, c) Run 3, d) Run 4, and e) Run 5. . . . .	112
5.12	A schematic of the microwave measurement circuit. OS2 is a microwave signal generator used to pump the niobium cavity on the red sideband ( $\omega_p = \omega_C - \omega_M$ ). OS1 is an audio frequency generator used to drive the piezoelectric actuator (PZT) which excites the acoustic mode. The upconverted signal from the superfluid acoustic mode is mixed down to an audio signal and measured on a lock-in amplifier. . . . .	113
5.13	Superfluid acoustic $Q$ versus mixing chamber temperature for the first run (circles) and second run (triangles) of the experiment. Each color denotes a different mode, as shown in the legend. The red line shows the expected loss from the 3PP (Eqn. (4.2)) and the blue line shows the expected loss from the helium-3 impurity (Eqn. (4.5)), assuming $\omega_M/2\pi = 8115$ Hz. . . . .	119

5.14	The frequency of the $TE_{011}$ mode at 550 mK before and after the $3 V_{pp}$ piezo drive for the 10 kHz mode is turned on. Notice that, before the drive, the frequency is stable (the 10 and 20 minute plots are on top of each other), but after the drive is turned on, the mode shifts up in frequency until it reaches a new stable value (the 50 and 60 min plots are on top of each other). The new value is about 1 kHz above the original frequency, or $\approx 3$ cavity linewidths. . .	123
5.15	Superfluid acoustic $Q$ versus mixing chamber temperature for the third run (circles) and fourth run (triangles) of the experiment. Each color denotes a different mode, as shown in the legend. The red line shows the expected loss from the 3PP (Eqn. (4.2)), while the navy blue and light blue lines show the dissipation expected from $^3\text{He}$ impurities at concentrations of $10^{-6}$ (Eqn. (4.5)) and $2 \cdot 10^{-10}$ (Eqn. (4.6)), respectively, assuming in all cases a mode frequency of 8115 Hz. . . . .	125
5.16	The frequency of the $TE_{011}$ mode with the cell full of helium, cryogenic valve closed, and fridge at its base temperature while the fill line from the cryogenic valve to room temperature was evacuated with a rough pump. Notice that the cell frequency continued to shift upward indicating that the cell was slowly emptying and the cryogenic valve was not leak tight to superfluid $^4\text{He}$ . . . . .	127
5.17	The continuous heat exchanger of our Kelvinox 400H dilution refrigerator with Teflon shims inserted between each coil at 90 degree increments. . . . .	128
5.18	A ring down of the 8115 Hz mode, showing the highest quality factor we have measured: $1.35 \cdot 10^8$ . The mixing chamber temperature was 30 mK, but if the $Q$ is limited by the 3PP as given in Eqn. (4.2), the helium temperature is 44 mK. . . . .	129

5.19	Thermalization curves for the superfluid helium, extracted from the quality factor of the 8115 Hz mode by assuming $Q$ is limited by the 3PP, upon heating the fridge to a) 50 mK, b) 60 mK, c) 80 mK, and d) 200 mK. Data points are shown as red circles; the black line is an exponential fit to the data. The final fridge temperature and the time constant of the exponential fit are shown on each figure. Notice that the final temperature of the helium in some cases differs from the mixing chamber temperature. . . . .	130
5.20	The thermal time constants calculated from the exponential fits in Fig. (5.19) plotted versus the final fridge temperature for each data set. The connecting line serves as a guide to the eye only. Notice that the time constants at low temperatures are extremely long. . . . .	131
5.21	Superfluid acoustic $Q$ versus mixing chamber temperature. Data from Run 5 are shown as diamonds at 20 mK. For comparison the data from Runs 3 and 4 are shown as faded circles and triangles, respectively. Each color denotes a different mode, as shown in the legend. The red line shows the expected loss from the 3PP (Eqn. (4.2)), while the navy blue and light blue lines show the dissipation expected from $^3\text{He}$ impurities at concentrations of $10^{-6}$ (Eqn. (4.5)) and $2 \cdot 10^{-10}$ (Eqn. (4.6)), respectively, assuming in all cases a mode frequency of 8115 Hz. . . . .	134
5.22	Helium temperature inferred from the measured superfluid acoustic quality factor versus power incident on the cavity. The blue and red lines indicate that the cell is attached to the mixing chamber with a copper wire (Run 4) or a silver rod (Run 5), respectively. Note that while the heating is reduced with the silver rod, the difference between the two setups is not substantial. . . .	136

5.23	a) the Pound Drever Hall frequency stabilization circuit. AM modulation is used to add sidebands to the source before it is incident on the cavity. The signal from the cavity is split in two: one branch is measured on a spectrum analyzer (SA) and the second is mixed down to the sideband frequency and measured on a lock-in. One quadrature of the signal from the transmitted sidebands is used as an error signal, which is first fed into a PID controller and then input to the FM modulation on the source. The red circuit is at acoustic frequencies and the blue circuit is the error signal. b) the PDH error signal from the lock-in. . . . .	138
5.24	Pictures of the cell planned for future runs: a) is similar to the copper wire setup used in Runs 3 and 4, but with an annealed 5N silver wire with a diameter of 0.10 cm. The copper tubes to which the wire is soldered are machined with a smaller diameter section at the top (0.635 cm) so that the wire exits closer to the cell's center keeping the cell level. b) shows a different approach to attaching the wire to the the cell and fridge. One copper piece is bolted to cell (or fridge), and a second copper piece is used to clamp onto the 0.23 cm diameter silver wire. . . . .	139
5.25	Damage to the niobium lid preventing leak tight operation of the cell . . . . .	140
5.26	Pictures of machined valve pieces for design 2. The housing is brass, the guide, plunger, and seal are stainless steel, the needle is Torlon, and the bellows are nickel. Here the bellows have already been soldered to the plunger and guide. . . . .	144
5.27	The sapphire pieces after machining: a) the bottom piece of the cavity design, showing the annular cavity that will be filled with helium, b) the top piece of the cavity design, c) the test piece of equal size to the final bonded piece, before polishing. . . . .	146

5.28	The bonded and polished sapphire cavity: a) side view. Note the discontinuity in the outer edge at the location of the bond line, b) top view, c) view from the top edge with the cavity sitting in the base of the aluminum shielding cavity. Notice the fill line connecting the annular cavity to the base of the sapphire mushroom. . . . .	147
5.29	a) Transmission measurements of the highest $Q$ mode of the test resonator (no annular cavity) at both 300K (red, $f_0 = 10.97$ GHz) and 77K (blue, $f_0 = 11.06$ GHz). At 300 K, the $Q$ is $66 \cdot 10^3$ , and at 77 K the $Q$ s of the left and right peaks are $2.4 \cdot 10^6$ and $2.8 \cdot 10^6$ , respectively. b) The highest quality factor "mode" that could be found at 77K in the spectrum of the bonded resonator, $f_0 = 11.05$ GHz. . . . .	148
6.1	The phonon occupation of the superfluid acoustic mode versus the number of pump photons ( $n_P$ ) in the sideband cooling tone, ignoring the effects of dielectric heating, for three starting temperatures: 40 (blue), 20 (green) and 10 mK (red), assuming that $Q$ is limited by temperature. In each case, the curve that continues to drop with increasing photon number ignores the effect of source phase noise, while the curve that reaches a local minimum includes the effect. The black curves denote sources of various phase noise ( $-140, -160, -180, -200$ dBc/Hz), as labeled on the figure. . . . .	150
6.2	The phonon occupation of the superfluid acoustic mode versus the number of pump photons ( $n_P$ ) in the sideband cooling tone, including the effects of dielectric heating, for three starting temperatures: 40 (blue), 20 (green) and 10 mK (red), assuming that $Q$ is limited by temperature. In each case, the curve that continues to drop with increasing photon number ignores the effects of heating and source phase noise, while the curve that reaches a local minimum includes both effects. The black curves denote sources of various phase noise ( $-140, -160, -180, -200$ dBc/Hz), as labeled on the figure. . . . .	152

6.3	A schematic of our low phase noise microwave source as described in the text. The left circuit is the self resonant loop of a sapphire whispering gallery mode resonator, with control loops for both phase (red) and amplitude (blue). The right circuit consists of a microwave source and a divider and provides tunability to the source. . . . .	153
6.4	The minimum detectable strain $h_{min}$ versus integration time $\tau_{int}$ for our superfluid acoustic detectors [2], G1 (blue) and G2 (red) assuming mechanical Q of $10^{10}$ (dotted) and $10^{11}$ (solid). Also shown is the achieved strain sensitivity of LIGO-S6 (solid, black) and the design sensitivity of advanced LIGO (dotted black). The stars indicate the limit set by LIGO and the limit expected from advanced LIGO. The spin down limit of the pulsar J1301+0833 is also shown as the dotted horizontal line. . . . .	159
6.5	The experimental scheme proposed by Pikovski et al. [3] to measure the commutator's deformation. An input signal is incident on a polarizing beam splitter, then an electro optic modulator and a second beam splitter. The field reflects from the optical cavity and enters the delay line. The length of the delay line is such that the mechanical oscillator evolves by one quarter of a mechanical period between each interaction. After all four interactions, the signal is measured interferometrically with the reference. . . . .	162
6.6	The minimum required pump power to achieve $n_M \ll \lambda N_P$ . The red line shows $n_M/\lambda$ resulting from the sideband cooling tone with pump photons $n_P$ . $n_P$ from the sideband cooling tone is shown with the green line. The blue line shows the total of $n_P$ from the sideband cooling tone plus $N_P = n_m/\lambda \cdot 10$ (fulfilling $N_P \gg n_m/\lambda$ ) for the phase space manipulations of Pikovski et al.'s [3] scheme. 164	
C.1	Drawing of the cylinder body, machined from RRR grade niobium. . . . .	171

C.2	Drawing of the cylinder top, machined from niobium with a minimum purity of 99.8%. Shown here is the final design with the fill line and microwave ports located at the position of the radial node in helium modes with only one radial node. . . . .	172
C.3	Drawings of the cap for the microwave ports of niobium cavity. Shown is the final design with cutouts to allow all the pieces to fit on the niobium cavity lid. . . . .	173
D.1	Drawing of the valve assembly. . . . .	174
D.2	Drawing of the guide, which is made from stainless steel. . . . .	175
D.3	Drawing of the housing, which is made from brass. . . . .	176
D.4	Drawing of the seal, which is made from stainless steel. . . . .	177
D.5	Drawing of the plunger, which is made from stainless steel. . . . .	178
D.6	Drawing of the needle, which is made from Torlon, a stiff plastic that does not easily deform at low temperatures. . . . .	179
E.1	Drawing of the top for the sintered-silver heat exchangers. . . . .	180
E.2	Drawing of the bottom for the sintered-silver heat exchangers. . . . .	181
E.3	Drawing of the sintered-silver heat exchangers assembly. . . . .	182
E.4	Drawing of the pressing piece for the sintered-silver heat exchangers. . . . .	183
F.1	Drawing of the copper L brackets used to mount the cell to the mixing chamber in Run 1. . . . .	184
F.2	Drawing of the square copper bracket used to mount the cell to the mixing chamber in Run 2. . . . .	185
F.3	Drawing of the silver rod used to mount the cell to the mixing chamber in Run 5.186	
G.1	Drawing of the sapphire test resonator. . . . .	187
G.2	Drawing of the bottom sapphire piece for the two piece helium filled sapphire cavity. . . . .	188
G.3	Drawing of the top sapphire piece for the two piece helium filled sapphire cavity.189	

# List of Tables

4.1	The highest measured mechanical quality factors of several high $Q$ materials. Also shown are the frequency of the measure mode and the temperature at which the measurement was taken. . . . .	85
5.1	The TE and TM mode frequencies up to 13.5 GHz for the niobium cavity. The expected frequencies are calculated from Eqns. (5.1) and (5.2) for a cavity with a diameter of 3.556 cm and length of 3.955 cm. The frequencies were measured with a vector network analyzer at 300 K and the spectrum is given by the red line shown in Fig. (5.2). The final column shows the difference between expected and measured frequencies: $(f_{exp} - f_{meas}) / f_{exp} \cdot 100$ . The only experimentally missing modes are the $TE_{110}$ , $TE_{210}$ , and $TE_{310}$ . . . . .	95
5.2	A table of the superfluid acoustic modes up to and including the highest frequency mode found experimentally. The first column gives the mode numbers, the second the expected frequency from Eqn. (2.24). The third column indicates whether or not the mode is degenerate. The fourth column is the experimentally measured frequency of the mode from Run 4 at the base temperature of fridge; for most of the degenerate modes, only one peak could be found, and many modes were altogether not detectable. The fifth column is the highest $Q$ measured in any run for the given mode. . . . .	114

5.3	Table describing the approximate diameter (d) in $\mu\text{m}$ and length (L) in m of the fill line between the 1 K plate, still, cold plate (CP), mixing chamber (MC), and cell for each run of the experiment. Not shown is the capillary connecting the room temperature valve at the top of the fridge to the 1 K stage, which is 300 $\mu\text{m}$ in diameter and $\approx 1.3$ m in length; this line was provided by Oxford and has remained unaltered. Over time, the capillaries below 1 K have been increased in length and decreased in diameter in order to limit thermal conduction and acoustic losses. . . . .	117
5.4	Table summarizing the changes in the experimental setup for all fridge runs, including the choice of cavity suspension, the final coaxial cabling to the cell, and other important notes. . . . .	117
A.1	Table of variables . . . . .	167
B.1	Bessel function zeros. . . . .	168
B.2	Bessel function extrema, microwave modes. . . . .	169
B.3	Bessel function extrema, acoustic modes. . . . .	170

# Chapter 1

## Helium-4

### 1.1 Historic Background

Helium is an element of superlatives: along with neon, it is the only element for which no known compounds exist; additionally, it is the lone element which does not freeze without pressurization. After hydrogen, helium is both the second lightest and second most abundant element, comprising 24% of the universe's elemental mass [4]. Because of its unique properties, helium played a central role in refrigeration techniques and in low temperature physics, enabling such monumental discoveries as superconductivity and superfluidity [5]. Today liquid  $^4\text{He}$  has widespread use as a coolant for superconducting magnets with applications from MRI machines to the Large Hadron Collider. Further, the invention of the dilution refrigerator, a continuously running cryostat which relies on the dilution of the lighter isotope  $^3\text{He}$  with the significantly more common  $^4\text{He}$ , eventually led to a commercial product which reliably reaches temperatures in the tens of millikelvin range. The dilution refrigerator has become an indispensable tool in physics, in fields as varied as quantum information and fundamental studies of condensed matter. Since the existence of helium was confirmed in 1895, few elements have had the same tremendous impact on physics.

The first hints of helium's discovery came in August of 1868, when French astronomer Pierre-Jules-César Janssen observed a new spectral line in the sun's prominence during a solar eclipse in India [6]. Because of its proximity to the sodium doublet, this line was dubbed  $\text{D}_3$ . Unbeknownst to Janssen, British astronomer Joseph Norman Lockyer found

the same 587.49 nm yellow line in October of 1868, while observing the prominence in London [4]. At the time, neither man accorded D<sub>3</sub> much significance, other than to report its existence. Both Janssen and Lockyer were recognized instead for independently arriving at a new spectroscopic method, which allowed viewing of the prominence of the sun in the absence of an eclipse [6].

Lockyer did however continue to study the sun, teaming with noted British chemist Edward Frankland to outline the composition of the prominences by reproducing spectral observations with known gases in a laboratory setting. While it was only a small piece of their work, Lockyer and Frankland tried recreating D<sub>3</sub> with hydrogen at various temperatures and pressures [6]. After failing to do so, they began informally referring to the line as "helium," without any public claim of discovery. The name derives from the Greek word "helios," for sun, and the ending "ium" reflected their belief that a metallic element was responsible for D<sub>3</sub> [4]. The word "helium" does not appear in literature until 1871, when president of the British Association for the Advancement of Science, William Thomson, noted that Frankland and Lockyer proposed that an as yet unknown substance produced the D<sub>3</sub> spectral line [6]. The claim was met critically by the scientific community at the time, as a mere spectral observation failed to meet the standard of elemental discovery. Notably, Mendeleev, who was responsible for creating the periodic table of the elements, publicly noted that such an assumption was unjustified in 1889 [6].

While there was no consensus of "helium's" existence, it was known widely in literature, though often referred to simply as the "D<sub>3</sub> spectral line." It was at first thought to occur only in the sun but was later found in many other stars throughout the universe. In fact, helium is one of the most common elements in stars, where it is formed from nuclear fusion of hydrogen atoms [4]. In 1882, Italian geologist Luigi Palmieri claimed to find the D<sub>3</sub> line in gases escaping from a volcanic eruption at Mt. Vesuvius [6]. However he failed to collect any of the gas and his claim remained unsubstantiated. Helium was also mentioned by many scientists who thought it was a constituent form of matter. For example, British chemist William Crookes theorized that due to its light weight, as evidenced by its presence in the sun's corona, helium was a unit composing all other forms of matter [6].

In 1889 American geochemist William Francis Hillebrand was studying samples of the mineral uraninite ( $\text{UO}_2$ ) when he noted bubbling from the material after exposure to sulphuric acid. He collected and analyzed the gas, determining it to be nitrogen [6]. On a hunch informed by Hillebrand's work, in 1895 William Ramsay obtained a sample of clevite (uraninite with about 10% other rare minerals), to look for compounds of the newly discovered gas argon. He quickly realized he had discovered a new gas that was neither nitrogen nor argon, and upon observation of the telltale  $\text{D}_3$  spectral line, he concluded that this at last was the elusive helium [6]. Working independently, Per Theodor Cleve and his student Nils Abraham Langlet also discovered helium in samples of clevite in Uppsala, Sweden. Langlet was further able to measure helium's density to be twice that of hydrogen [6].

Interestingly, in April of 1895, Ramsay wrote to Lockyer suggesting a name change to "helion" in keeping with the other noble gases, but nothing came of his request [4].

Even after helium's discovery in uranium minerals, it was thought to be extraordinarily rare on Earth. Because of the helium atom's small mass, it moves with velocities fast enough to escape the Earth's gravitational pull. While helium would have been a dominant component of Earth's early atmosphere, today it comprises only 0.00052%. Though helium was discovered in uranium minerals, it exists there only in trace amounts.

The assumption of helium's scarcity changed in 1903, when a company drilling for natural gas near Dexter, Kansas struck a geyser of gas, escaping at a rate of 9 million cubic feet per day [7]. To celebrate their find and the expectant economic boom for the town, the people of Dexter planned to light the gas on fire using a burning bale of hay. After a day of jubilation, the hay bale failed to light the geyser. In fact, the flame was extinguished on repeated trials [7]. Intrigued, geologist Erasmus Howard collected samples of the gas and analyzed them at the University of Kansas. With the help of colleagues Hamily Cady and David McFarland, the mysterious gas was determined to be only 15 % methane and 72% nitrogen. Most interestingly, after using charcoal immersed in liquid air to remove the other components, they found the signature  $\text{D}_3$  spectral line and determined the gas was almost 2% helium [7]. To this day, natural gas fields, where it is a product of radioactive alpha decay, are the largest suppliers of helium worldwide.

Soon after helium's discovery on Earth, there was a race to liquefy the newfound element. Heike Kamerlingh Onnes of Leiden became the first to do so in 1908, using Joules Thompson cooling. He found that helium-4 liquified at 4.2 Kelvin. Onnes' work opened up new frontiers in cryogenic physics, paving the way for important discoveries. Most notably, superconductivity was discovered only three years later, in 1911; today Onnes is known as "the father of low-temperature physics [5]."

## 1.2 Basic Properties

The most common isotope of helium is helium-4, which is composed of two protons and two neutrons. Having no nuclear spin,  ${}^4\text{He}$  behaves as a boson. The only other stable isotope is helium-3, which has a fractional abundance of about 1 part in  $10^6$  [8]. With only one neutron,  ${}^3\text{He}$  is a fermion and thus behaves very differently from helium-4. Though neither are stable, two other helium isotopes have been observed: helium-6, which has a half life  $\tau_{1/2} = 0.82$  s and helium-8, with a half life of  $\tau_{1/2} = 0.12$  s [4].

With two electrons, helium has a filled s shell, resulting in a highly symmetric structure. The sole permanent dipole exists in the isotope  ${}^3\text{He}$ , which has a small nuclear magnetic moment. For helium-4, the only interatomic binding force is the attractive interaction between momentarily induced dipoles known as the van der Waals force. Further, the van der Waals force between helium atoms is the weakest of any substance. The weak interatomic forces coupled with the small atomic masses lead to low boiling temperatures of 4.21 K (helium-4) and 3.19 K (helium-3); these are the lowest boiling points of all known substances.

As mentioned above, solidifying helium cannot be done with temperature alone; it requires 25 bar of pressure. Imagine that each atom occupies a volume of space, roughly a sphere of radius  $R = V_A^{1/3}$  where  $V_A$  is the atomic volume. From quantum mechanics we expect an uncertainty in momentum  $\delta p \approx h/R$ , where  $h$  is the Planck constant. Therefore

each atom has an energy of localization given by [9]:

$$E_0 \approx (\delta p)^2 / 2m_4 = \frac{\hbar^2}{2m_4 V_A^{2/3}}, \quad (1.1)$$

where  $m_4$  is the mass of a helium-4 atom. Because of helium's small mass, the zero point energy is comparable in magnitude to the potential energy of the liquid state. Therefore the total energy of the liquid state reaches a minimum at a high atomic volume. While at low enough temperatures ( $T < 4.2$  K), the interatomic potentials become strong enough to form a liquid, the liquid state remains low density, and the solid state does not form with temperature alone.

### 1.3 Two Fluid Model

As liquid helium is cooled beyond 4.2 K it undergoes a second order phase transition at a critical temperature  $T_\lambda = 2.17$  K. This temperature is known as the lambda point because of the shape of the specific heat versus temperature through transition (see Fig. (1.1)). Below  $T_\lambda$  we refer to the fluid as HeII.

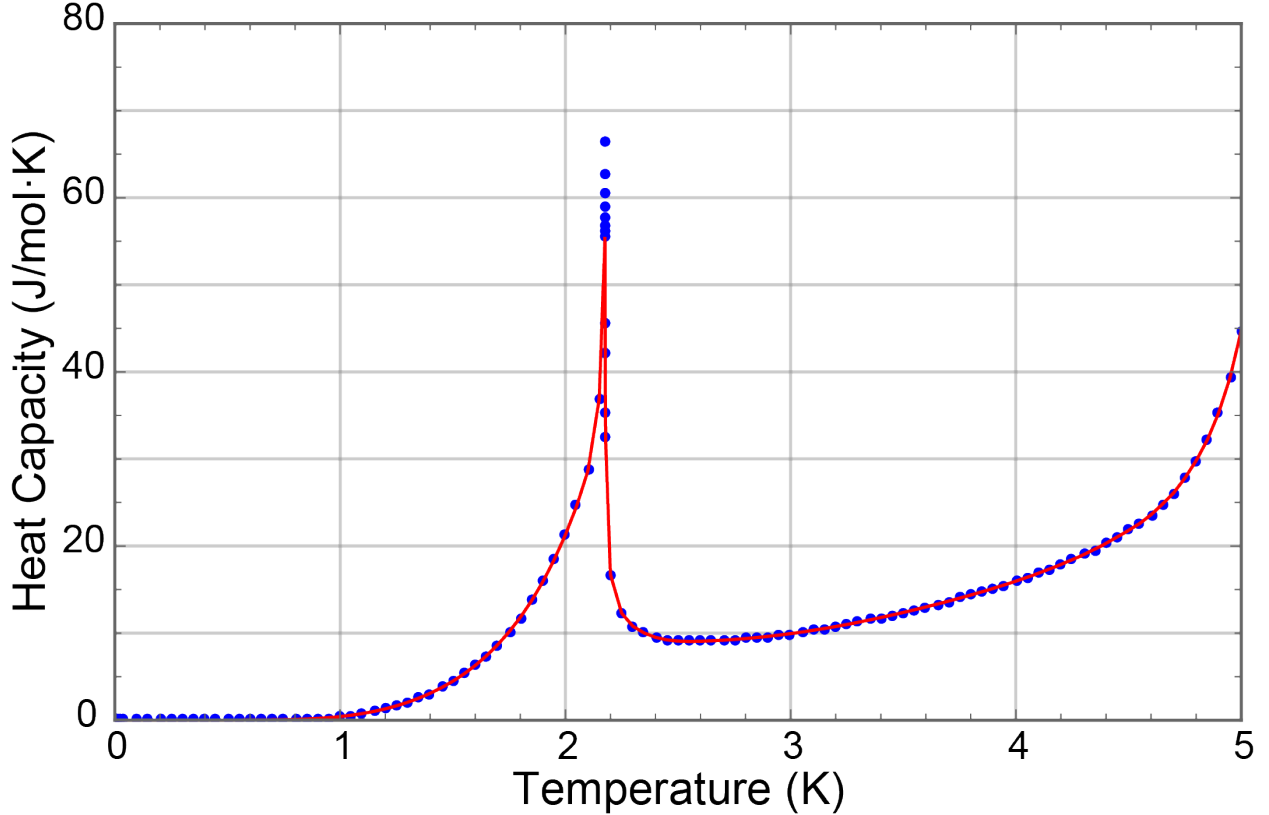


Figure 1.1: The heat capacity of helium versus temperature. The transition point at 2.17 K is known as  $T_\lambda$  because of the shape of the heat capacity through transition.

One of the interesting and initially unexplained results from early experiments on HeII was the measurement dependent viscosity of the fluid. Measurements of rotating viscometers showed a resistance not much different from that of  ${}^4\text{He}$  gas. Meanwhile, measurements of viscosity based on flow rates through small capillaries demonstrated flow rates nearly independent of the pressure differential, indicating virtually zero resistance to flow.

Tisza [10] was able to reconcile these results with the two fluid model of helium-4: below  $T_\lambda$ , helium behaves as if it were composed of two non interacting fluids, which are called the superfluid and the normal fluid. The total density of helium ( $\rho$ ) can be written as the combination [11]:

$$\rho = \rho_N + \rho_S, \quad (1.2)$$

where  $\rho_N$  and  $\rho_S$  are the densities of the normal fluid and superfluid, respectively. The

relative values of the densities depend on temperature; At absolute zero,  $\rho_N = 0$  and  $\rho_S = \rho$  while at  $T_\lambda$ ,  $\rho_N = \rho$  and  $\rho_S = 0$ .

The superfluid component moves without viscosity and carries no entropy. It is the superfluid component which can flow without friction through a small capillary. The normal fluid component behaves like an ordinary viscous liquid and carries the total entropy of the fluid. Andronikashvili's experiment, where he measured the fluid's viscosity with a rotating wire viscometer, famously produced a curve of normal fluid density versus temperature [12]; see Fig. (1.2b).

While the two fluid model has been very successful in explaining the experimental behavior of helium-4, it is important to remember that all helium atoms are identical. It is not possible to pick an individual atom and claim that it is part of the superfluid or the normal fluid component.

## 1.4 Equations of Motion

We will now enumerate the equations of motion for HeII. Each fluid moves with its own local velocity so the total momentum per unit volume can be written as [11]:

$$\mathbf{j} = \rho_N \mathbf{v}_N + \rho_S \mathbf{v}_S, \quad (1.3)$$

where  $v_N$  and  $v_S$  denote the velocities of the normal fluid and superfluid components. The momentum is related to the density ( $\rho$ ) through the equation of continuity:

$$\nabla \cdot \mathbf{j} = -\frac{\partial \rho}{\partial t}. \quad (1.4)$$

Euler's equation of motion in the absence of viscosity and for small velocities, where quadratic terms in the velocity can be discarded, gives [11]:

$$\frac{\partial \mathbf{j}}{\partial t} = -\nabla P, \quad (1.5)$$

where  $P$  is the pressure. When viscosity can be ignored, the fluid motions are reversible and entropy is conserved. In this limit [11]:

$$\frac{\partial(\rho S)}{\partial t} = -\nabla \cdot (\rho S v_N), \quad (1.6)$$

where  $S$  is the entropy per gram of helium-4. The change in internal energy  $U$  of a fluid is given by [11]:

$$dU = TdS - PdV + GdM, \quad (1.7)$$

where  $G$  is the Gibbs free energy.  $T$  is temperature, and  $dM$  is a change in the mass. If the mass of the fluid is increased by adding particles to the superfluid, while maintaining a constant volume, then  $dV = dS = 0$  such that  $dU = GdM$ . Therefore the work ( $W$ ) of moving a mass  $\Delta M$  of superfluid from point A to point B ( $dx$ ) is given by:

$$\Delta W = \nabla G \cdot dx \cdot \Delta M. \quad (1.8)$$

From this we can write an equation for the motion of the superfluid [11]:

$$\frac{dv_S}{dt} = S \nabla T - \frac{1}{\rho} \nabla P. \quad (1.9)$$

## 1.5 Thermomechanical Effect

A classic superfluid helium experiment is the illustration of the fountain effect [13]. A superleak, formed by packing a tube with emery powder, connects a bath of He II to a small capillary which emerges from the helium bath. When the capillary side of the superleak is heated, superfluid flows quickly into the tube and shoots out the end of the capillary like a fountain.

This simple experiment illustrates the inseparability of mass flow and heat flow in He II. When the capillary is heated, both its temperature and normal fluid fraction increase in comparison to the bath. Only the normal fluid component can carry heat, but it cannot

travel away from the heat source through the superleak; instead, when the capillary is heated,  $\rho_S$  rushes through the superleak to diminish the superfluid gradient. The superfluid from the bath flows toward the heat source with enough velocity to form a fountain.

The fountain effect is also known as the thermomechanical effect and we can estimate its size from the equations of motion. In equilibrium the fluid is not accelerated:  $dv_S/dt = 0$ . From Eqn. (1.9) it follows that:

$$\frac{\Delta P}{\Delta T} = \rho S. \quad (1.10)$$

When helium II is heated, normal fluid flows away from the source of heat, and in order to retain equal density everywhere, the superfluid flows in the opposite direction; this is known as counterflow. An important implication of this effect is that the fluid emerging from the capillary is expected to be colder than the bath because its superfluid fraction is greater. Because  $^3\text{He}$  moves with the normal fluid component, this connection between heat flow and mass flow can be exploited to isotopically purify  $^4\text{He}$  as will be discussed in Section 4.2.2.

## 1.6 Elementary Excitations

Below  $T_\lambda$ , the thermal de Broglie wavelength of the helium atoms becomes comparable to their interatomic spacing. As noted by Landau [14], at this point the behavior of superfluid helium must be described in terms of elementary excitations. These excitations have energy  $\epsilon = c_4 q$ , given by the dispersion curve. Here  $q$  is momentum and  $c_4$  is the speed of sound. Impressively, Landau deduced a form of the dispersion curve in 1941, which was not confirmed experimentally until the late 1950s with neutron scattering experiments [11]. It is important to note that in his treatment of helium II, Landau ignored the interactions between excitations. This is a good approximation at low temperatures where the density of excitations is small ( $T < 1.5$  K), but as the temperature approaches  $T_\lambda$  this assumption breaks down and the dispersion curve and helium II properties will be different.

The shape of the helium II dispersion curve is shown in Fig. (1.2a); exact numeric values along the curve depend on the helium temperature. At low momenta, close to the origin,

the dispersion curve is linear:  $\epsilon = c_4 q$ . This region describes the low energy phonons which move with the sound velocity  $c_4$ . At higher momenta, the curve reaches a local minimum; the region around the minimum is specified by:

$$\epsilon = \Delta + \frac{(q - q_0)^2}{2\mu}. \quad (1.11)$$

From neutron scattering experiments at 1.1 K, these constants are found to be [15]:

$$\begin{aligned} \Delta/k_B &= 8.65 + / - 0.04 \text{ K}, \\ q_0/\hbar &= 1.91 + / - 0.01 \text{ \AA}^{-1}, \\ \mu &= 0.16 \cdot m_4, \end{aligned}$$

where  $m_4$  is the mass of a helium atom,  $k_B = 1.38 \cdot 10^{-23}$  J/K is the Boltzmann constant, and  $\hbar = h/2\pi = 1.05 \cdot 10^{-34}$  J·s is the reduced Planck constant. The excitations described by this high energy minimum are known as rotons.

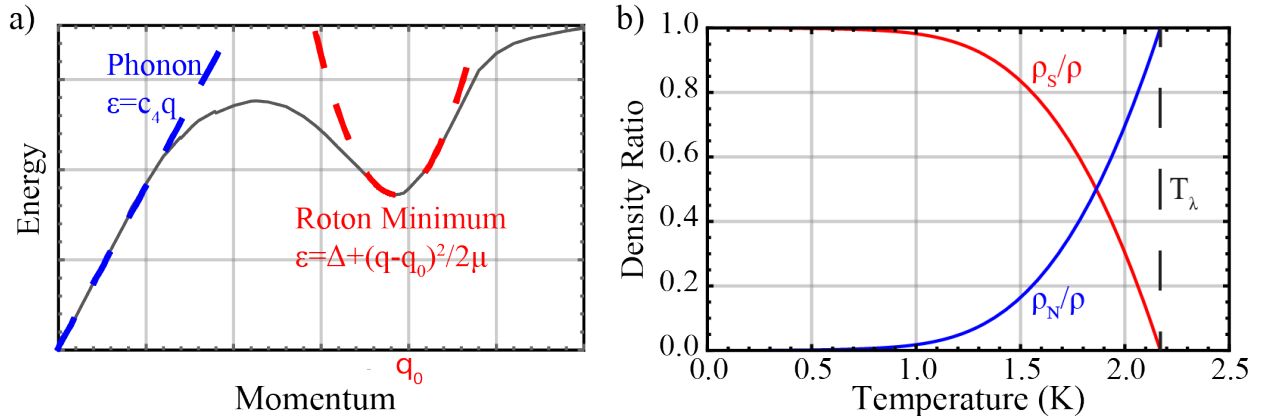


Figure 1.2: a) The dispersion curve of helium II showing the linear phonon contribution (blue) and the roton minimum (red). b) The superfluid (red) and normal fluid (blue) fractions of helium below  $T_\lambda$

The phonon and roton contributions to the normal fluid density are given by [11]

$$\rho_{n,ph} = \frac{2\pi^2 k_B^4}{45\hbar^3 c^5} T^4, \quad (1.12)$$

$$\rho_{n,r} = \frac{2\mu^{1/2}q_0^4}{3(2\pi)^{3/2}(k_B T)^{1/2}\hbar^3} \exp^{-\Delta/k_B T}, \quad (1.13)$$

where  $\Delta$ ,  $q_0$ , and  $\mu$  are defined as above, by neutron scattering experiments. These two contributions are equal at  $\approx 570$  mK; below this temperature the rotons rapidly become irrelevant. When we consider acoustic loss in  $^4\text{He}$  at dilution refrigerator temperatures, we need only consider phonon-phonon collisions because while phonon-roton and roton-roton collisions will also lead to acoustic loss, the roton population is so small as to make their contributions irrelevant. At temperatures below about 450 mK, where  $\rho_{n,r} \ll \rho_{n,ph}$ , we can write:  $\rho_n/\rho \approx 1.2 \cdot 10^{-4}T^4$ . We note that helium-4 is unique among the condensates in that, at experimentally achieved temperatures of  $T < 10$  mK, the fraction of temperature to transition temperature is  $T/T_\lambda < 0.005$ . In comparison, in  $^3\text{He}$ , the lowest achieved temperatures are approximately 200  $\mu\text{K}$ , leading to  $T/T_C < 0.08$  [16]. In atomic Bose-Einstein condensates, the fractional temperature is often  $T/T_C \approx 0.5$  [17]. For helium-4, this small  $T/T_\lambda$  ratio leads to the incredible conclusion that at 10 mK the non-condensate fraction is expected to be only  $\rho_n/\rho \approx 10^{-12}$ .

Finally, we point out that because phonons are the dominant excitation below 570 mK, we can calculate the specific heat of helium from the Debye theory for solids. One finds that the specific heat is given by [11]:

$$C_V = \frac{2\pi^2 k_B^4}{15\rho_4 \hbar^3 c_4^3} T^3 \approx 20.7 \cdot T^3 \text{ J/kg} \cdot \text{K}. \quad (1.14)$$

Note that  $C_V$  has the  $T^3$  dependence that is expected when phonons are responsible for heat conduction. When we consider the difficulty of cooling our sample to low temperatures, it will be important that the heat capacity drops rapidly with decreasing temperature.

## 1.7 Second Sound

Below  $T_\lambda$ , where the two fluid model applies, we expect to find multiple solutions for sound propagation because each fluid has its own velocity field. From the equations of motion

above, one can solve for the ordinary longitudinal pressure modes, modulations of density at constant temperature, which in helium II are known as first sound. Additionally one finds the relation [11]:

$$\frac{\partial^2 S}{\partial x^2} = \frac{\rho_N}{\rho_S} \frac{C}{TS^2} \frac{\partial^2 S}{\partial t^2}, \quad (1.15)$$

where  $C$  is the heat capacity. (In helium, the heat capacity at constant pressure is nearly equal to the heat capacity at constant volume.) Notice that Eqn. (1.15) is also an equation for the propagation of sound, but in this case, the waves are variations in entropy  $S$  or equivalently, temperature  $T$ . Because the superfluid component cannot carry entropy, movement of temperature and mass is linked. The normal fluid component carries the entropy while the superfluid component moves in the opposite direction. These temperature waves are known as second sound and their velocities can be given by [11]:

$$c_2 = \sqrt{\frac{\rho_S TS^2}{\rho_N C}}. \quad (1.16)$$

Like first sound, the absorption of second sound in helium II is well studied both theoretically and experimentally. We introduce second sound because there may be some conversion of first sound to second sound; given the higher attenuation of second sound this may become a relevant loss process in very high Q superfluid acoustic resonators.

## 1.8 Vortices

Finally, we mention that the superfluid can be described by a macroscopic wave function [11]:

$$\psi = e^{i \sum_i s(\mathbf{R}_i)} \phi, \quad (1.17)$$

where  $s(\mathbf{R}_i)$  is a function of position and  $\phi$  corresponds to the ground state at rest. In this description, the velocity of the fluid depends on the gradient of the phase:

$$v_S(\mathbf{R}) = \frac{\hbar}{m} \nabla s(\mathbf{R}). \quad (1.18)$$

Consider what happens to a body of liquid helium-4 set into rotation. An ordinary viscous fluid will rotate as a solid body, but the viscous interactions between atoms are absent in a superfluid. The condition that  $\nabla \times \mathbf{v}_S = 0$ , which is required for the condition of no viscosity in the superfluid, cannot be universally valid as experiments have shown that helium can be set into rotation. As suggested by London and Onsager [18] and later found experimentally, the liquid is permeated by an array of vortex lines which increase the energy but maintain  $\nabla \times \mathbf{v}_S = 0$  over most of the volume. A vortex line is defined by its circulation  $\kappa = \oint \mathbf{v} \cdot d\mathbf{l}$ .

Vortices can be envisaged as holes in the superfluid helium. Imagine a cylinder submerged in the fluid; as one moves away from the cylinder a distance  $r$  the velocity grows as  $v = A/r$  where  $A$  represents a constant. If the cylinder is made small enough, the centrifugal force of the fluid rotation will be strong enough to maintain the hole. The size of the vortex ( $a_0$ ) can be estimated by balancing the surface tension  $T_{surf}$  with the Bernoulli force [11]:

$$a_0 = \frac{\rho \kappa^2}{16\pi^2 T_{surf}} \approx 0.3 \text{ \AA}. \quad (1.19)$$

The vortex is a small region of size  $a_0$  where the macroscopic wavefunction tends to zero.

Because  ${}^4\text{He}$  are bosonic particles, any rotation of the fluid where each atom replaces its neighbor produces a state which is indistinguishable from the initial state. Such a rotation produces a phase change of the macroscopic wave function equal either to zero or an integral multiple of  $\pi$ . This condition leads to the quantization of circulation:  $\oint \mathbf{v} \cdot d\mathbf{l} = 2\pi\hbar n/m$  where  $n$  is an integer value and  $m$  is the mass of a helium atom.

It is not well known how many vortices will be present in a  $50 \text{ cm}^3$  sample of helium such as those which we use. There are ways to limit the vortex population, such as by cooling slowly through the lambda point or by filling a vessel slowly through a sinter. It is also not known how vortices will interact with first sound and what limitations they may ultimately place on the mechanical  $Q$ . The presence of vortices is something we acknowledge and will address if and when it becomes a limiting factor.

# Chapter 2

## Optomechanics

### 2.1 Introduction

Optomechanics is the study of systems with a mechanical mode parametrically coupled to either a microwave or an optical mode (or both). There are several excellent review papers outlining both the underlying physics and the experimental results to date; for a recent review, see Aspelmeyer et al. [19].

The canonical example of a microwave optomechanical system is a parallel RLC circuit where one of the capacitor plates is free to vibrate; for an illustration, see Fig. (2.1). The capacitance of a parallel plate capacitor is  $C = \epsilon_0 A/d$ , where  $A$  is the area of the plates and  $d$  the distance between them. As the capacitor plate vibrates, the distance  $d$  is modulated, changing both the capacitance of the cavity and its frequency  $\omega = 1/\sqrt{LC}$ . Exciting a mechanical mode with frequency  $\omega_M$  in the capacitor plate produces sidebands at  $\omega_C \pm \omega_M$  on the microwave cavity resonance.

The optomechanical Hamiltonian is written as [20]:

$$H = \hbar\omega_C \left( a^\dagger a + \frac{1}{2} \right) + \hbar\omega_M \left( b^\dagger b + \frac{1}{2} \right) + g_0 \hbar (b^\dagger + b) \left( a^\dagger a + \frac{1}{2} \right), \quad (2.1)$$

where  $\omega_C$  and  $\omega_M$  are the frequencies of the microwave and mechanical modes and  $a^\dagger$  ( $a$ ) and  $b^\dagger$  ( $b$ ) are the raising (lowering) operators for the microwave and mechanical modes, respectively.  $g_0$  is the single photon optomechanical coupling rate which describes how much

the frequency of the microwave cavity is pulled by the motion of the mechanics:

$$g_0 = \frac{\partial \omega_C}{\partial x} \Delta x_{ZP}. \quad (2.2)$$

$g_0$  depends on the zero point motion  $\Delta x_{ZP}$  which describes the magnitude of the motion of the mechanical mode in its ground state, where it has a phonon occupation of less than one.  $\Delta x_{ZP}$  depends on the mechanical resonator's mass  $m$  and frequency as:

$$\Delta x_{ZP} = \sqrt{\frac{\hbar}{2m\omega_M}}. \quad (2.3)$$

From this definition we note that smaller masses and larger mechanical resonance frequencies increase the optomechanical coupling rate. As will be elaborated in more detail in Chapter 3, the parametric coupling between the optical and mechanical modes allows one to either "damp" or "drive" the mechanics. With high enough coupling rates, the mechanical mode can be cooled to its ground state, where one expects it may behave quantum mechanically.

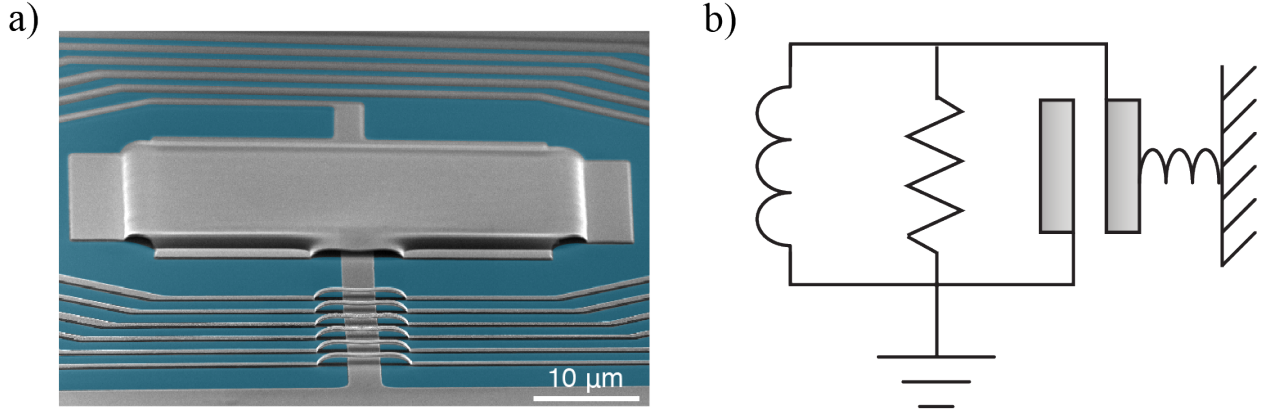


Figure 2.1: a) An SEM of a nanomechanical resonator used in our lab, showing a capacitor with the top plate suspended surrounded by a spiral inductor (courtesy Chan U Lei). b) The canonical example of a microwave optomechanical system: an RLC circuit with a capacitor plate that is free to vibrate.

The field of optomechanics spans a wide range in both frequency and mass, from atomic systems all the way up to LIGO [21]. While the physics of these systems has been well

understood for decades, recent progress in nanofabrication techniques has permitted the manufacture of mechanical oscillators with the parameters necessary to achieve ground states of the mechanics. Ground state cooling was first achieved in 2010 by Andrew Cleland’s lab at UCSB [22]; this was result was quickly repeated in Konrad Lehnert’s group at JILA [23] and Oskar Painter’s lab at Caltech [24].

In the last five years, several experiments have confirmed the quantum nature of these ground state macroscopic oscillators. The following is not a complete compendium of such results but meant to highlight some of the interesting physics that can now be achieved in such systems. In Cleland’s original ground state cooling experiment, a single quantum of energy was exchanged between the GHz mechanical oscillator and a qubit [22]. In 2013, Palomaki et al [25] demonstrated entanglement between the microwave and mechanical modes in a nanomechanical microwave drum resonator. In our lab, Weinstein et al. [26] observed the sideband asymmetry of the mechanical drum resonator shown in Fig. (2.1a). Sideband asymmetry describes the behavior of an oscillator in its ground state where it is able to absorb energy from the environment but no longer able to emit energy. By putting a mode of the drum resonator into its quantum ground state and measuring both sidebands, Weinstein et al. [26] confirmed this physics. Following this result, sideband asymmetry was also measured in an optical system [27]. In another result from our lab, Wollman et al. [28] demonstrated quantum squeezing of the mechanics of a microwave drum resonator. This result has since been replicated in other systems [29,30]. Finally, in 2016 Reidinger et al. [31] demonstrated non-classical correlations between single photons and phonons in a photonic crystal cavity by measuring violations of the Cauchy-Schwarz inequality in the state of the mechanics.

Of future interest to the field of optomechanics are systems which allow the preparation and transfer of quantum states [32]. There is increasing investment in superconducting qubits as scalable building blocks for quantum processing. Qubits operate at microwave frequencies, but microwave cabling is lossy and cannot be used to transfer information over long distances. In contrast optical fibers provide very low loss communication over long length scales. A device that can efficiently and with high fidelity transfer a state between microwave and optical photons is of great importance. Optomechanical systems with low

loss mechanical resonators may also be useful in the storage of quantum states.

## 2.2 Our System

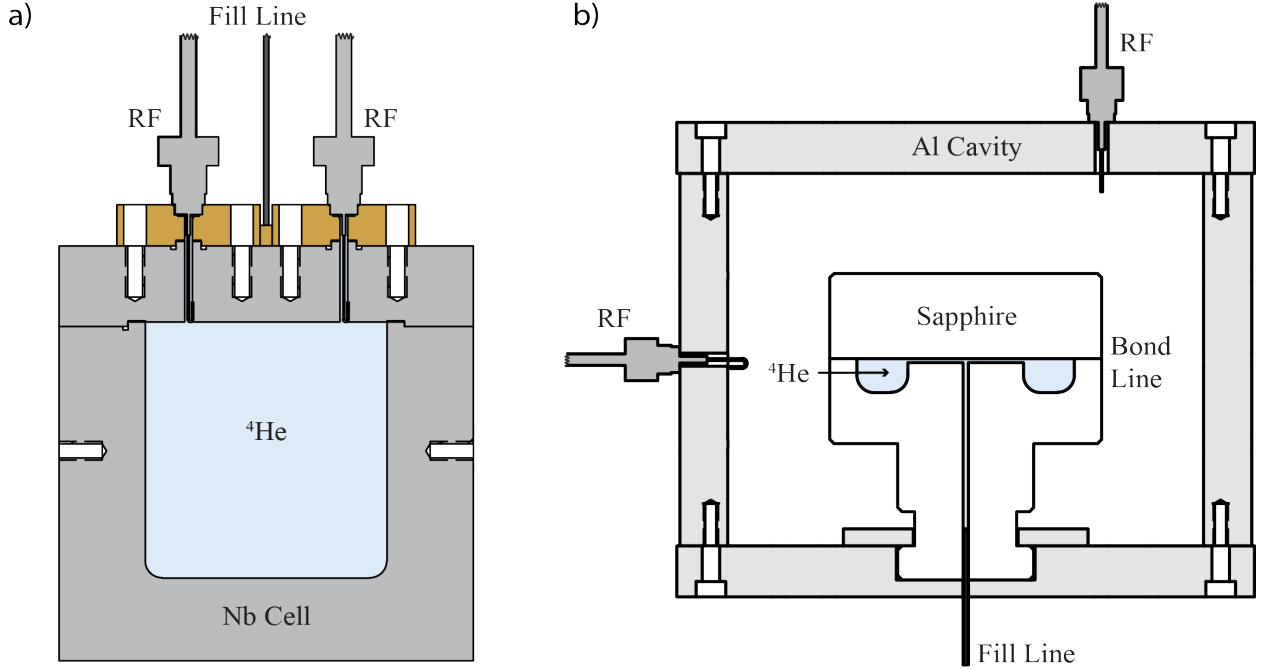


Figure 2.2: Diagrams of our superfluid optomechanical systems: a) the cylindrical niobium cell with an inner diameter of 3.56 cm and height of 3.95 cm. Two hermetically sealed dielectric probes are used to couple microwaves into and out of the cavity. A capillary allows the cell to be filled at low temperatures. b) A vertical slice through the center of the sapphire cavity setup, showing the ring of  ${}^4\text{He}$  and the fill line. The top cylinder, which supports the whispering gallery modes, is 5 cm in diameter and 3.1 cm in height. The helium annulus has an inner diameter of 2.2 cm, an outer diameter of 4 cm, and a height of 0.64 cm. The sapphire and the microwave couplers are mounted to an aluminum cavity which reduces the microwave loss from the evanescent fields.

While the nanomechanical drumhead resonators provide a platform for an intuitive understanding of optomechanical coupling, the results of optomechanics extend to any system where a low frequency acoustic vibration is parametrically coupled to a high frequency microwave mode. In our experiment, we observe acoustic modes in a superfluid filled cavity coupled to microwave modes of the surrounding resonator. Here the density modulation produced by the acoustic modes results in a proportional modulation of helium's permittivity,

which couples to the microwave modes.

We had several reasons for choosing to work with superfluid  $^4\text{He}$ . The first is that we expected to achieve extremely high mechanical  $Q$ s as will be outlined in Chapter 4. High mechanical  $Q$  acoustic modes allow for extremely sensitive force detection with potential applications to gravitational waves (see Section 6.2 and Singh et al. [2]). High  $Q$  modes also have extraordinary number state lifetimes:  $\tau_N = \hbar Q/(k_B T)$  [33]; for  $Q = 10^{10}$  at  $T = 10$  mK, we expect  $\tau_N = 8$  seconds. Additionally, the optomechanical systems which have so far reached the quantum ground state have extremely small masses (order 100 pg), and we were interested to extend these results to a more massive system. Recall that  $g_0 \propto 1/\sqrt{m}$  so that less massive resonators have a higher  $g_0$ . As will be discussed in Chapter 3, in practice the optomechanical coupling rate is enhanced by the microwave pump power. Because of helium's very low dielectric loss tangent, we believe the high pump powers required to overcome a small  $g_0$  are achievable (see Section 6.1).

We designed two systems for studying superfluid optomechanics, shown in Fig. (2.2). The first uses a cylindrical superconducting niobium resonator and the second a cylindrical sapphire whispering gallery mode resonator. While both resonators were fabricated, this thesis will focus primarily on the niobium design because the initial results with the niobium cavity were more promising.

We first briefly describe the sapphire cavity setup shown in Fig. (2.2b). It is made from two pieces of sapphire bonded together. The microwave whispering gallery modes reside in the top cylinder which has a diameter of 5 cm and a height of 3.1 cm. The notched post extending from this cylinder is used only to secure the sapphire inside an aluminum cavity. The aluminum cavity serves two purposes: it holds the microwave couplers and it diminishes the losses from the evanescent fields leaking from the sapphire cavity; it has an inner diameter of 8.9 cm and a height of 7 cm. The helium annulus has an inner diameter of 2.2 cm, an outer diameter of 4 cm, and a height of 0.64 cm. It is connected to the base of the cavity with a drilled hole which serves as a fill line. The sapphire design was not immediately successful because both the bond line and the unpolished annular cavity are located in a high field region of the whispering gallery mode, significantly deteriorating its

microwave  $Q$ .

In contrast to the sapphire setup, we made significant experimental progress with the niobium cylinder design shown in Fig. (2.2a). The niobium cavity is made from two pieces: a U shaped body and a lid, which are sealed together with indium wire. The inner cylindrical cavity is approximately 4 cm in length and 3.6 cm in diameter. We use the  $TE_{011}$  mode of the microwave cavity, which is typically the highest  $Q$  mode in these systems and has a frequency  $\omega_C = 2\pi \cdot 10.6$  GHz when the resonator is filled with  $^4\text{He}$ . Coupling to the microwave mode is achieved via two loops of wire recessed into the cavity lid. The intrinsic loss rate of the  $TE_{011}$  mode is  $\kappa_{int} = 2\pi \cdot 31$  Hz but we have overcoupled the cavity such that  $\kappa_{in} = \kappa_{out} \approx 2\pi \cdot 230$  Hz for the optomechanics experiments. With the niobium cell full of helium, we apply a red detuned microwave pump tone at  $\omega_P = \omega_C - \omega_M$  while driving the acoustic mode at  $\omega_M$  with a piezo transducer attached to the niobium cavity, to produce an upconverted sideband at the microwave cavity resonance [34]; see Section 5.4. We detect acoustic modes in the superfluid at frequencies within 1% of their expected values, and we determine their quality factors by recording the free decay of the acoustic oscillations. Our single photon optomechanical coupling rate is  $g_0 = 2\pi \cdot 10^{-8}$  Hz.

It is worth nothing that while we developed the first optomechanical system using superfluid helium-4 [1], since then the field has expanded to include other such systems, though they are in significantly different parameter regimes. The Harris lab at Yale has developed a helium filled cavity between two optical fibers, held in alignment by a glass ferrule [35]. They observe first sound modes optomechanically coupled to an optical mode. Both modes are at significantly higher frequency than the modes of our design: ( $\omega_C = 2\pi \cdot 195$  THz,  $\omega_M = 2\pi \cdot 318$  MHz,  $g_0 = 2\pi \cdot 3$  kHz). The Bowen lab at the University of Western Australia is working with silica microtoroid whispering gallery mode resonators covered in a film of helium-4 [36]. They observe third sound modes coupled to optical modes of the toroid ( $\lambda = 1551$  nm,  $\omega_M \approx 2\pi \cdot 10$  kHz to  $2\pi \cdot 5$  MHz,  $g_0 \approx 2\pi \cdot 10$  Hz). Both systems have higher optomechanical coupling rates (listed in parentheses above) than we expect for our niobium cell because of their smaller mode masses and higher mechanical frequencies. However, our measured acoustic  $Q$ s are significantly higher than in either of these systems.

## 2.3 Microwave Modes

### 2.3.1 TE Modes of a Cylinder

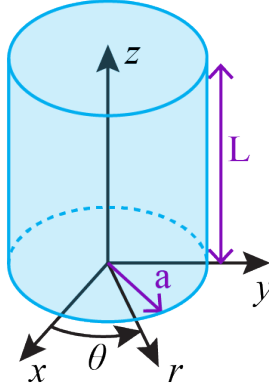


Figure 2.3: Cylinder of height  $L$  and radius  $a$  in cylindrical coordinates.

We will first describe the microwave properties of the niobium cavity design shown in Fig. (2.2a). The electromagnetic eigenmodes of a right cylinder are found by enforcing the appropriate boundary conditions to Maxwell's equations. The details of these calculations are explicitly worked out in many microwave engineering textbooks (see for example Pozar [37]), so only the results are summarized here. The cavity of interest is a cylinder of height  $L$  and radius  $a$ , which is most easily represented in a cylindrical coordinate system  $(r, \theta, z)$  as shown in Fig. (2.3). Electric and magnetic field components are represent by  $E$  and  $H$ , respectively.

Transverse electric (TE) modes are defined such that  $E_z = 0$  and  $H_z$  is a solution to the wave equation:  $\nabla^2 H_z + k^2 H_z = 0$ , where  $k$  is the wave vector. Enforcing the boundary condition that tangential components of  $\mathbf{E}$  must equal zero at the walls ( $\hat{n} \times \mathbf{E} = 0$ , where  $\hat{n}$  is a normal unit vector pointing out of the wall) leads to  $E_\theta(r, \theta, z) = 0|_{r=a}$ ,  $E_\theta(r, \theta, z) = 0|_{z=0,L}$ , and  $E_r(r, \theta, z) = 0|_{z=0,L}$ .

One can use these conditions to solve for the explicit form of the TE modes of a right

cylinder, which are given by [38]:

$$\begin{aligned}
E_r(r, \theta, z) &= \frac{i\eta n}{k_1 r} J_n(k_1 r) \sin(n\theta) \sin(k_3 z), \\
E_\theta(r, \theta, z) &= i\eta J'_n(k_1 r) \cos(n\theta) \sin(k_3 z), \\
E_z(r, \theta, z) &= 0, \\
H_r(r, \theta, z) &= \frac{k_3}{k} J'_n(k_1 r) \cos(n\theta) \cos(k_3 z), \\
H_\theta(r, \theta, z) &= -\frac{nk_3}{kk_1 r} J_n(k_1 r) \sin(n\theta) \cos(k_3 z), \\
H_z(r, \theta, z) &= \frac{k_1}{k} J_n(k_1 r) \cos(n\theta) \sin(k_3 z),
\end{aligned}$$

where  $\eta = \sqrt{\mu/\epsilon}$  is the wave impedance and  $\mu = \mu_R \mu_0$  is the permeability, where  $\mu_R$  is the relative material dependent value and  $\mu_0 = 4\pi \cdot 10^{-7}$  N/A<sup>2</sup> is the permeability of free space. Similarly,  $\epsilon = \epsilon_R \epsilon_0$  is the permittivity, where  $\epsilon_R$  is the relative material dependent value and  $\epsilon_0 = 8.85 \cdot 10^{-12}$  F/m is the permittivity of free space. In helium,  $\mu_R \approx 1$  and  $\epsilon_R \approx 1.05$ . The wavenumber,  $k = \omega \sqrt{\mu \epsilon}$ , is given by:

$$\begin{aligned}
k &= \sqrt{k_1^2 + k_3^2}, \\
k_1 &= \frac{2x'_{nm}}{d}, \\
k_3 &= \frac{\pi l}{L},
\end{aligned} \tag{2.4}$$

where  $x'_{nm}$  is the  $m$ th extrema of the  $n$ th Bessel function of the first kind ( $J'_n(x'_{nm}) = 0$ ). A table of Bessel function extrema can be found in Appendix B.2. The integers  $n$ ,  $m$ , and  $l$  are used to label the modes; they indicate the number of variations azimuthally, radially, and longitudinally, respectively.

Equating  $k = \omega \sqrt{\mu \epsilon}$  with the relation given in Eqn. (2.4), we can solve for the frequencies

of the  $\text{TE}_{nml}$  modes [37]:

$$f_{nml} = \frac{c}{2\pi\sqrt{\mu_r\epsilon_r}} \sqrt{\left(\frac{x'_{nm}}{a}\right)^2 + \left(\frac{l\pi}{d}\right)^2}, \quad (2.5)$$

where we have used the relation  $c = 1/\sqrt{\mu_0\epsilon_0}$  for the speed of light in vacuum.

### 2.3.2 TM Modes of a Cylinder

For the transverse magnetic (TM) modes,  $H_z = 0$  and  $E_z$  is a solution to the wave equation. As in the TE case, we enforce the boundary condition that tangential components of  $\mathbf{E}$  must equal zero at the walls, leading to the conditions:  $E_\theta(r, \theta, z) = 0|_{r=a}$ ,  $E_z(r, \theta, z) = 0|_{r=a}$ ,  $E_\theta(r, \theta, z) = 0|_{z=0,L}$ , and  $E_r(r, \theta, z) = 0|_{z=0,L}$ .

One obtains the following explicit formulas for the TM modes [38]:

$$\begin{aligned} E_r(r, \theta, z) &= -\frac{k_3}{k} J'_n(k_1 r) \cos(n\theta) \sin(k_3 z), \\ E_\theta(r, \theta, z) &= \frac{nk_3}{kk_1 r} J_n(k_1 r) \sin(n\theta) \sin(k_3 z), \\ E_z(r, \theta, z) &= \frac{k_1}{k} J_n(k_1 r) \cos(n\theta) \cos(k_3 z), \\ H_r(r, \theta, z) &= -\frac{in}{\eta k_1 r} J_n(k_1 r) \sin(n\theta) \cos(k_3 z), \\ H_\theta(r, \theta, z) &= -\frac{i}{\eta} J'_n(k_1 r) \cos(n\theta) \cos(k_3 z), \\ H_z(r, \theta, z) &= 0, \end{aligned}$$

where the definitions are identical to the TE case with the exception of the constant  $k_1$ :

$$k_1 = \frac{2x_{nm}}{d},$$

where  $x_{nm}$  is the  $m$ th zero of the  $n$ th Bessel function of the first kind ( $J_n(x_{nm}) = 0$ ). Bessel function zeros are shown in Appendix B.1.

Similarly, the frequencies of the  $\text{TM}_{nml}$  modes are given by:

$$f_{nml} = \frac{c}{2\pi\sqrt{\mu_r\epsilon_r}} \sqrt{\left(\frac{x_{nm}}{a}\right)^2 + \left(\frac{l\pi}{d}\right)^2}, \quad (2.6)$$

where again the only difference from the case of TE modes is the replacement of  $x'_{nm}$  with  $x_{nm}$ .

### 2.3.3 Quality Factor of Cylindrical Microwave Resonators

In a cylindrical microwave cavity resonator, the highest  $Q$  mode is generally the  $\text{TE}_{011}$  because no current flows between the walls of the cylinder and the lid. For practical purposes, this means that using a two piece cavity where the lid must be attached to the cylinder with indium has a less detrimental effect on the  $Q$ . In a right cylinder, the high  $Q$   $\text{TE}_{011}$  mode is degenerate with the lower  $Q$   $\text{TM}_{111}$  mode. This degeneracy can be explicitly broken with a stub in the cavity lid [39], but we found that the asymmetry of our cavity as machined was enough and made no additional modifications.

Microwave quality factors are limited by resistive losses in the walls; the highest  $Q$  values are achieved in superconducting cavities with cleaned and polished inner walls. We considered various materials for our cell before settling on niobium. A common choice is copper, which does not superconduct at any temperature. In copper, microwave quality factors of up to  $3 \cdot 10^5$  have been achieved with an electrolytically polished cavity at 4.2 K [40]. Significantly higher microwave  $Q$ s have been measured with superconducting metals; the highest superconducting microwave  $Q$ s of which I am aware are:  $Q \approx 10^9$  in aluminum ( $T_C = 1.2$  K) [41],  $Q > 10^{10}$  in lead ( $T_C = 7.2$  K) [42], and  $Q > 10^{11}$  in niobium ( $T_C = 9.4$  K) [43, 44]. To achieve the highest  $Q$ s in a cylindrical cavity, the body of the cylinder should be U shaped, and the single lid required should be welded in place, reducing the losses associated with seals. Heat treatments in a vacuum furnace remove impurities and further increase  $Q$  [43].

We chose to work with niobium not only because it has the highest microwave  $Q$  but also because it has the highest  $T_C$  among elemental superconductors. Because the transition

temperature is  $T_C > 9$  K, the microwave properties can be tested in a helium bath at 4.2 K, which is much simpler than using a helium-3 or dilution refrigerator. Even with a lid attached by an indium seal, we found that a simple procedure of polishing the cavity and chemically etching away  $\approx 100$  microns of material was enough to remove the surface layer damaged by machining and produce  $Q > 10^8$  [1]. Importantly for our optomechanical system, which has microwave frequencies of order 10 GHz and acoustic frequencies of order 10 kHz, achieving sideband resolution requires a microwave  $Q \approx 10^7$ , which is not difficult with niobium.

### 2.3.4 Brief Introduction to Superconductivity

Superconductivity was first observed in 1911 by Onnes, who found that the resistance of a sample of mercury abruptly dropped to zero at cryogenic temperatures [5]. For his studies, he was awarded the Nobel Prize in 1913. In 1957, the first theory of superconductivity was presented by Bardeen, Cooper, and Schrieffer [45], who won the Nobel Prize in 1972 for what is commonly known as the BCS theory.

According to the microscopic theory of superconductivity there is a small attractive interaction between the electrons in a metal, which at low enough temperatures will cause the electrons to condense into Cooper pairs. For conventional low temperature superconductors, this attractive interaction is mediated by phonons of the crystal lattice. One can imagine that as an electron moves through the lattice, it will attract ions of positive charge. The resultant deformed lattice then preferentially attracts another electron of opposite spin. Interestingly, strong electron-phonon interaction results in higher resistivity in the normal state; high  $T_C$  elemental superconductors such as niobium and lead are more resistive in the normal state than the excellent conductors gold and copper, which have weak electron-phonon interactions and show no evidence of superconductivity.

Electrons in a metal obey Fermi-Dirac statistics; the probability that a state with energy  $\epsilon$  is occupied by an electron is given by [46]:

$$f(\epsilon) = \frac{1}{e^{(\epsilon - \epsilon_F)/k_B T} + 1}, \quad (2.7)$$

where  $\epsilon_F$  is the Fermi energy. As a consequence, only electrons within  $k_B T$  of the Fermi energy contribute to the macroscopic properties of the metal. Because of the weak attractive interaction between electrons in a superconductor, as the temperature falls, the electron states near the Fermi level get redistributed. Eventually a temperature dependent energy gap,  $2\Delta(T)$ , opens up producing a new lower energy ground state, the superconducting state. BCS theory predicts that the pairing energy (or energy gap) will be given by [46]:

$$2\Delta(0) = 2 \cdot 1.76k_B T_C = 3.12 \text{ meV}, \quad (2.8)$$

where  $T_C$  is the transition temperature. Below  $T_C$ , it will be energetically favorable for two electrons near the Fermi surface to form a pair, which will have lower energy because of the attractive potential. These new particles are known as Cooper pairs, and they have twice the mass and twice the charge of an electron. Pairs form between electrons of opposite spin and momentum, as this pairing produces the minimum energy state. Because Cooper pairs are bosons, the Pauli exclusion principle no longer applies and all pairs can be in the same quantum state.

As noted above, when electrons condense into Cooper pairs, it is only those within  $k_B T_C$  of the Fermi surface that participate. One finds that the range of momenta of the relevant electrons is  $\delta\rho = k_B T_C / v_F$  where  $v_F$  is the Fermi velocity. Using the Heisenberg uncertainty relation for position (we define  $\delta x = \xi_0$ ) and momentum,  $\xi_0 \cdot \delta\rho \approx \hbar$ , one finds that the spatial extent of a Cooper pair, known as the coherence length, is given by [46]:

$$\xi_0 = \frac{\hbar v_F}{k_B T_C}. \quad (2.9)$$

Much like superfluid, a superconductor can be described in terms of a two fluid model. The "superfluid" component consists of Cooper pairs of electrons while the "normal" component consists of the remaining unpaired free electrons. The number of unpaired electrons

$(n_{normal})$  is related to the Boltzmann factor  $e^{-\Delta/k_B T}$ :

$$n_{normal} \propto e^{-\Delta/k_B T}. \quad (2.10)$$

At zero temperature, all electrons are paired; as  $T$  increases, pairs will be broken up creating unpaired electrons and unoccupied states. Therefore increasing  $T$  decreases the size of the energy gap. A good approximation for the temperature dependence of the gap is [47]:

$$\frac{\Delta(T)}{\Delta(0)} = \left( \cos \left( \frac{\pi T^2}{2T_C^2} \right) \right)^{1/2}. \quad (2.11)$$

Notice that this function increases slowly at low  $T$ , so that at  $T = T_C/2$  the energy gap is still 96% of its value at zero. For this reason, achieving temperatures  $T \leq T_C/2$  is considered a good benchmark for observing the expected superconducting properties of a material.

The DC resistance of a superconductor is zero because the Cooper pairs carry current without resistance while the normal electrons remain inert. One way to understand the state of zero resistance is in terms of the de Broglie wavelength ( $\lambda = h/mv$ , where  $m$  is the mass and  $v$  is the drift velocity) of the current carrying Cooper pairs. In a normal metal, the electrons have large drift velocities, and therefore small de Broglie wavelengths, on the order of the crystal lattice. Electrons scatter from imperfections in the crystal lattice, such as impurity atoms, leading to resistance. In a superconductor, the current ( $j = -n2e\Delta v$ , where  $n$  is the number of charge carriers and  $e$  is the charge of an electron) is carried by all the Cooper pairs, so that the drift velocity is very small. Therefore the de Broglie wavelength is much larger than the size of the crystal lattice, so there is no scattering from imperfections and therefore no resistance.

In contrast to the DC case, RF current in a superconductor still experiences finite resistance. Cooper pairs can move without friction but they do have inertia, so in the presence of an RF field, they do not perfectly screen the normal electrons from the applied field. The time varying magnetic field on the surface creates ( $H$ ) an electric field ( $E_{int}$ ) in the skin

depth [46]:

$$E_{int} \propto \frac{dH}{dt} \propto \omega H, \quad (2.12)$$

where  $\omega$  is the frequency of the applied RF field. The electric field in the skin depth acts on the normal electrons and creates a current [46]:

$$j_{int} \propto n_{normal} E_{int} \propto n_{normal} \omega H. \quad (2.13)$$

The movement of the normal electrons leads to a dissipation [46]:

$$P_{diss} \propto E_{int} j_{int} \propto n_{normal} \omega^2 H^2. \quad (2.14)$$

The power dissipated in a microwave cavity can also be written in terms of the surface resistance  $R_S$  [37]:

$$P_{diss} = \frac{1}{2} R_S H^2. \quad (2.15)$$

Using Eqns. (2.14, 2.15) we can find for the surface resistance:

$$R_S \propto n_{normal} \omega^2 \propto A_S \omega^2 e^{-\Delta(0)/k_B T}, \quad (2.16)$$

where  $A_S$  is a material dependent constant depending on the Fermi velocity  $v_F$ , the London penetration depth  $\lambda_L$ , the coherence length  $\xi_0$ , and the mean free path of the electrons. This equation is valid for  $T < T_C/2$ , where, as shown above, the energy gap  $\Delta(T)$  is relatively constant. Eqn. (2.16) includes two important results of superconductivity: the exponential decrease of resistance with temperature and the dependence of the surface resistance on the RF frequency squared.

### 2.3.5 Microwave Quality Factor of Niobium

In general the quality factor  $Q$  of a microwave resonator is given by [46] :

$$Q = \frac{\omega_C W}{P_{diss}}, \quad (2.17)$$

where  $\omega_C$  is the resonance frequency,  $W$  is the energy stored in the electric field and  $P_{diss}$  is the dissipated power. Eqn. (2.17) can be written in the more convenient form  $Q = G/R_S$  where  $G$  is a mode dependent geometric factor:

$$G = \mu\omega \frac{\int_V |H|^2 dV}{\int_S |H|^2 dS}, \quad (2.18)$$

and  $R_S$  is the surface resistance. For a superconductor, we expect a temperature dependent resistance  $R_S(T) = R_{BCS}(T) + R_0$ , where  $R_{BCS}$  is the contribution from the BCS theory and  $R_0$  is the residual resistance from all other sources.

As we have noted earlier, at temperatures below half of the transition temperature the energy gap changes little, and we expect the BCS theory to apply very well. The expected BCS losses for temperatures  $T < T_C/2$  and for frequencies  $f \ll 2\Delta/h \approx 10^{12}$  are given by:

$$R_{BCS} = Af^2 \frac{\exp^{-\Delta(T)/k_B T}}{T}, \quad (2.19)$$

where  $A$  is a constant which depends on the material properties [48]. The exponential can be simplified using measurements of the energy gap in niobium which give  $\Delta(0)/k_B T_C = 1.9$ , where  $T_C = 9.3$  K. There are no general expressions for the constant  $A$ ; however a simplified expression for the BCS resistance in niobium, which is in good agreement with both theory and experiments, is given by [49]:

$$R_{BCS} \approx 2 \cdot 10^{-4} \left( \frac{f}{1.5 \cdot 10^9} \right)^2 \frac{\exp^{-17.67/T}}{T}. \quad (2.20)$$

### 2.3.6 Microwave Modes in Sapphire

As will be discussed in Chapter 4, at low enough temperatures, the acoustic  $Q$  of the  $TE_{011}$  cavity design will ultimately be limited by the container losses rather than the losses in  ${}^4\text{He}$ . (We expect a maximum superfluid acoustic  $Q \approx 10^{11}$  for a niobium container.) One can instead use a cell material with lower acoustic dissipation than niobium; the acoustic  $Q$ s of many materials have been well established in gravitational wave literature in the context of high  $Q$  resonant bar detectors (See Table 4.1). The lowest acoustic loss factors have been measured in sapphire monocrystals [50, 51]. Therefore we also designed a superfluid optomechanical setup using sapphire, as shown in Fig. (2.2b).

Like niobium, sapphire is also an excellent microwave resonator. It has very large dielectric constants ( $\epsilon_{\parallel} = 11.34$  and  $\epsilon_{\perp} = 9.27$  at 15 K [52]) leading to well contained, high quality factor whispering gallery modes. Because of its extremely low dielectric loss tangent, sapphire is a good candidate for ultra-stable microwave sources, and has been thoroughly studied in this context. See for instance the review articles by Locke et al. [53] and McNeilage et al. [54].  $Q$  values as high as  $8 \cdot 10^9$  (measured at 1.6 K) have been achieved in the whispering gallery modes of cylindrical disks of sapphire [55, 56].

The whispering gallery modes are labeled by whether they have predominantly electric (quasi-TM) or magnetic (quasi-TE) fields along the longitudinal direction in the sapphire disk. The "z" direction field equations and frequencies of these modes have been calculated [57, 58], and the radial and azimuthal components can be solved for using Maxwell's equations [59]. The quasi-TM modes are labeled  $WGH_{m,n,p+\partial}$  and the quasi-TE modes are labeled  $WGE_{m,n,p+\partial}$  where  $m$ ,  $n$ , and  $p$  are the number of variations in the azimuthal, radial, and axial directions, respectively<sup>1</sup>.

Quality factors of dielectric cavity resonators are limited by radiation losses. The highest  $Q$  factors have been obtained in modes of high azimuthal number because the fields of such modes are well contained within the sapphire. Surface polishing also limits these losses. The radiative losses can be reduced further by enclosing the resonator within a superconducting

---

<sup>1</sup>Note that this mode numbering convention is different from the convention used for cylindrical cavity resonators.

cavity shield as first suggested by Blair and Jones [60]. The highest quality sapphire is HEMEX (Crystal Systems [61]), which is grown by the heat exchanger method and has extremely low impurity concentrations. The c-axis of HEMEX is aligned parallel to the boule to within 1 degree.

The quality factor for the unloaded  $Q$  of a two port dielectric resonator inside a cavity resonator is [62]:

$$Q^{-1} = Q_{\text{sapphire}}^{-1} + Q_{\text{cavity}}^{-1} = F_c \tan(\delta) + R_s \tau^{-1}, \quad (2.21)$$

where  $F_c$  is a factor defined by the confinement of the EM fields within the dielectric,  $\tan(\delta)$  is the dielectric loss tangent of sapphire,  $R_s$  is the surface resistance of the surrounding cavity, and  $\tau$  is a mode dependent geometric factor of the surrounding cavity. In the best sapphire resonators, the losses are limited by  $\tan(\delta)$ .

## 2.4 Acoustic Modes

In either design of Fig. (2.2), the expected superfluid acoustic modes can be found by solving for the standing waves of the inner cavity. Solutions for acoustic modes are given by solving the Helmholtz equation,  $\nabla^2 p + k^2 p = 0$ , where  $k$  is the wavenumber and  $p = P e^{i\omega_M t}$  is the pressure of a mode with frequency  $\omega_M$ . Working in cylindrical coordinates  $(r, \theta, z)$  we find:

$$\frac{\partial^2 P}{\partial r^2} + \frac{1}{r} \frac{\partial P}{\partial r} + \frac{1}{r^2} \frac{\partial^2 P}{\partial \theta^2} + \frac{\partial^2 P}{\partial z^2} + k^2 P = 0. \quad (2.22)$$

The boundary conditions come from assuming that the walls of the cavity are rigid. For the niobium setup, which is a right cylindrical cavity of radius  $a$  and length  $L$ :

$$\begin{aligned} \frac{\partial P}{\partial z} \bigg|_{z=0,L} &= 0, \\ \frac{\partial P}{\partial r} \bigg|_{r=a} &= 0. \end{aligned}$$

Assuming a solution of the form  $P(r, \theta, z) = R(r)\Theta(\theta)Z(z)$  and using separation of variables, we solve for the pressure [63]:

$$p_{lmn} = A_{lmn} J_m(k_{mn}r) \cos(m\theta + \gamma_{lmn}) \cos(k_{zl}z) e^{i\omega_{lmn}t}, \quad (2.23)$$

where  $k_{zl} = l\pi/L$  and  $k_{mn} = j'_{mn}/a$ . Here  $j'_{mn}$  is the  $n$ th extremum of the  $m$ th Bessel function of the first kind ( $J'_m(j'_{mn}) = 0$ ). A table of Bessel function extrema for the acoustic modes is shown in Appendix B.3. Notice the difference between this table and the table used for the microwave modes: the first value (for  $n = m = 0$ ) is 0, so the first row is displaced by a single column. The integers  $l, m$ , and  $n$  represent the number of nodes in the longitudinal, azimuthal, and radial directions<sup>2</sup>.

From the wavenumber  $k = \omega_M/c_4$  we solve for the frequencies of the acoustic modes:

$$\omega_{lmn} = c_4 \sqrt{k_{mn}^2 + k_{zl}^2} = c_4 \sqrt{\left(\frac{j'_{mn}}{a}\right)^2 + \left(\frac{l\pi}{L}\right)^2}, \quad (2.24)$$

where  $c_4$  is the speed of sound in helium-4.

The profiles of the acoustic modes for the niobium setup ( $a = 1.8$  cm and  $L = 4$  cm) are shown in Fig. (2.4). Every mode is shown up to the  $l = 3, m = 0, n = 1$  mode at 12 kHz, which is the highest frequency mode that we were able to detect experimentally.

---

<sup>2</sup>Note that this convention for the integers  $l, m$ , and  $n$  is different than the convention used for the microwave modes of a right cylinder.

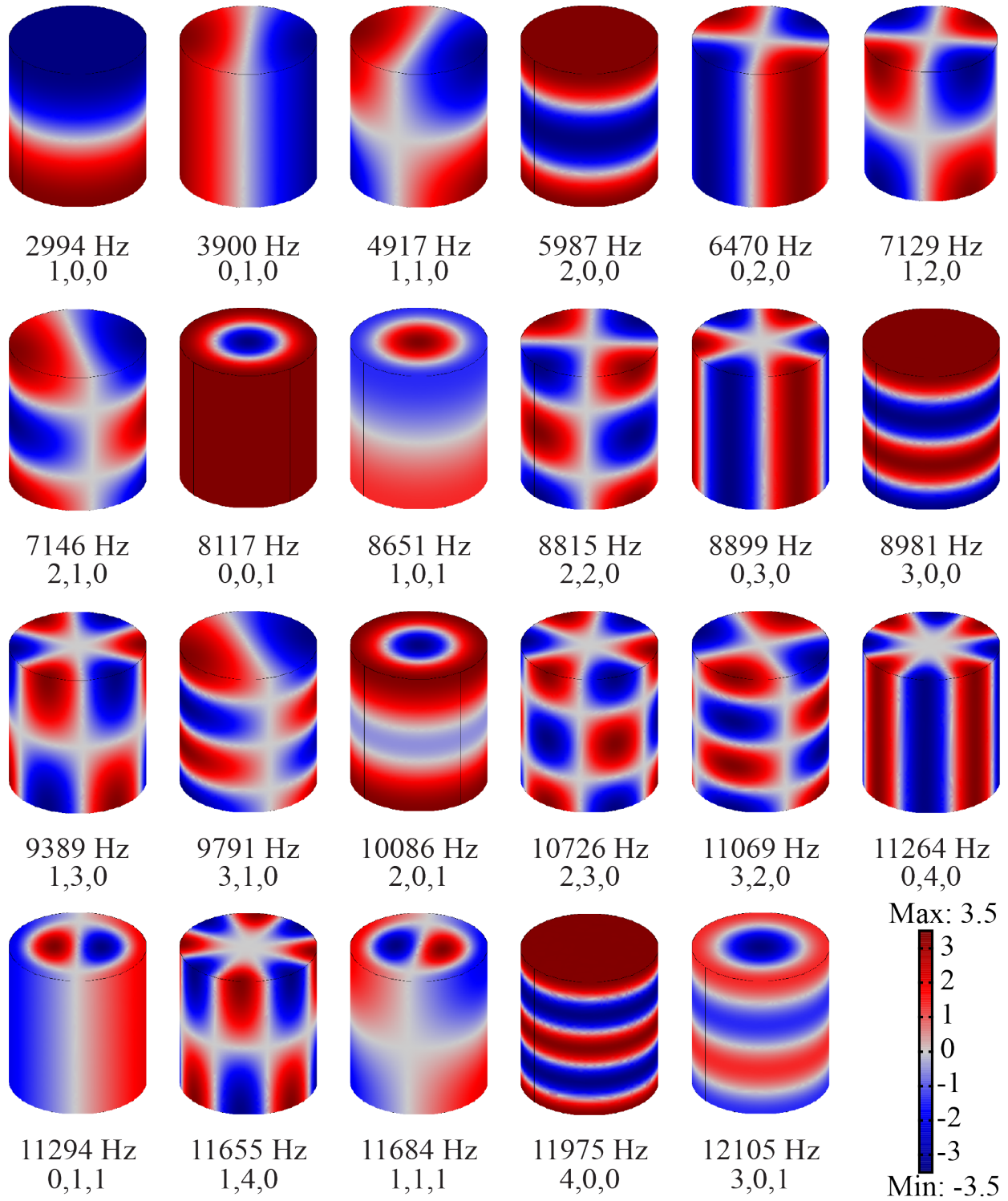


Figure 2.4: The profiles of every superfluid acoustic mode for the niobium cavity design up to a frequency of 12 kHz. Below each mode is its frequency and mode number  $(l, m, n)$ , where  $l$ ,  $m$ , and  $n$  indicate the number of nodes in the longitudinal, azimuthal, and radial directions. The white areas of the profiles indicate node locations.

In the sapphire design, the helium cavity is not a cylinder but an annulus. The acoustic eigenmodes of an annulus can be solved for using the Helmholtz equation as above with rigid boundary conditions at each wall. For an annulus with inner radius  $a$ , outer radius  $b$  and height  $h$ :  $\partial P/\partial z|_{z=0,h} = 0$  and  $\partial P/\partial r|_{r=a,b} = 0$ . The solutions for pressure are given by [64]:

$$p_{lmn}(r, \theta, z) = \left( J_m(k_{mn}r) + \frac{J'_m(k_{mn}a)}{Y'_m(k_{mn}a)} Y_m(k_{mn}r) \right) \cdot \cos(m\theta) \cos(k_{zl}z) e^{i\omega_{lmn}t}, \quad (2.25)$$

where  $Y$  is a Bessel function of the second kind. The frequencies are given by:

$$\omega_{lmn} = c_4 \sqrt{k_{mn}^2 + \left( \frac{l\pi}{h} \right)^2}, \quad (2.26)$$

where  $k_{mn}$  is the  $n$ th value of  $k_r$  satisfying the boundary condition  $J'_m(k_r a) Y'_m(k_r b) - J'_m(k_r b) Y'_m(k_r a) = 0$ . As above  $J$  is a Bessel function of the first kind. Again  $l$ ,  $m$ , and  $n$  are the number of nodes in the longitudinal, azimuthal, and radial directions, respectively.

#### 2.4.1 Acoustic to Microwave Coupling Strength

In both the sapphire and the niobium designs, the acoustic helium mode couples capacitively to the microwave container resonance. We first consider the niobium cylinder design of Fig. (2.2a) because the microwave mode equations are simpler.

A standing wave is nothing more than a spatial pressure variation in the cylinder. Regions of higher pressure will have higher density and higher permittivity, altering the energy stored in the electromagnetic mode of the cavity. Assuming that the electric and magnetic fields are not seriously perturbed, one can approximate the frequency shift caused by the acoustic mode as [37]:

$$\frac{\Delta\omega}{\omega} = -\frac{\int \Delta\mu |\bar{H}_0|^2 + \Delta\epsilon |\bar{E}_0|^2 dV}{\int \mu |\bar{H}_0|^2 + \epsilon |\bar{E}_0|^2 dV}, \quad (2.27)$$

where  $\mu$  and  $\epsilon$  are the permeability and permittivity, respectively, and  $H_0$  and  $E_0$  represent the unperturbed magnetic and electric fields.

To proceed, we first address whether the acoustic coupling to the magnetic or electric

field is larger. On a TM or TE resonance, the energy stored in the electric field equals the energy stored in the magnetic field or half the total stored energy  $W$ :

$$W/2 = \int \mu |\bar{H}_0|^2 dV = \int \epsilon |\bar{E}_0|^2 dV. \quad (2.28)$$

The largest frequency shift will occur if the perturbations in  $\mu$  and  $\epsilon$  are not spatially dependent and can be removed from the integrals. We will compare the coupling to the magnetic field,  $C_M = \Delta\mu \int |\bar{H}_0|^2 dV$ , to the coupling to the electric field,  $C_E = \Delta\epsilon \int |\bar{E}_0|^2 dV$ . Dividing both by  $W/2$  one finds  $C_M = \Delta\mu/\mu_0$  and  $C_E = \Delta\epsilon/\epsilon_0$ . Under the assumption of a linear dependence between density and permeability and between density and permittivity, one finds  $\Delta\mu/\mu_0 = \chi_M \Delta\rho/\rho$  and  $\Delta\epsilon/\epsilon_0 = \chi_E \Delta\rho/\rho$  where  $\chi_M$  and  $\chi_E$  are the magnetic and electric susceptibilities, respectively. Therefore the relative frequency shift caused by the coupling to the magnetic and electric fields is given by the ratio  $C_M/C_E = \chi_M/\chi_E$ . Bruch and Weinhold [65] calculate that the magnetic susceptibility of liquid helium will differ by no more than 0.5 % from the theoretical value for gaseous helium,  $-8.6 \cdot 10^{-7}$ ; the electric susceptibility of helium at millikelvin temperatures is 0.057, giving  $C_M/C_E \approx 10^{-5}$  [66]. Therefore we will neglect the term  $\Delta\mu |\bar{H}_0|^2$  in Eqn. (2.27) and consider only how the acoustic mode couples to the electric field through  $\Delta\epsilon_R$ .

The change in dielectric constant ( $\epsilon_R$ ) due to a change in density ( $\rho$ ) is given by the Clausius-Mosotti equation:

$$\frac{\epsilon_R - 1}{\epsilon_R + 2} = \frac{4\pi\alpha_M\rho}{3M}, \quad (2.29)$$

where  $M$  is the molar mass (4.00 g/mole in  ${}^4\text{He}$ ) and  $\alpha_M$  is the molar polarizability (0.123 cm<sup>3</sup>/mole in  ${}^4\text{He}$ ) [67]. Solving for  $\epsilon_R$ , and differentiating with respect to density, one finds:

$$\frac{\partial\epsilon_R}{\partial\rho} = \frac{3\chi}{(1 - \chi\rho)^2} = \frac{(\epsilon_R + 2)(\epsilon_R - 1)}{3\rho}, \quad (2.30)$$

where  $\chi = 4\pi\alpha_M/3M$ . We can relate the density to the pressure  $P$  through the compressibility  $\kappa = -1/V \cdot \partial V/\partial P$ , where  $V$  is volume. Differentiating  $\rho = m/V$  with respect to

volume, and using the definition of  $\kappa$ , one finds:

$$\partial\rho = \rho\kappa\partial P. \quad (2.31)$$

Finally we will write the pressure of the acoustic mode as  $P \cdot f(r, \theta, z)$  where  $P$  is the amplitude of the mode and  $f(r, \theta, z)$  is a spatially dependent function which is different for each eigenfrequency. Combining Eqns. (2.27), (2.31), and (2.30) and using the fact that equal energy is stored in the magnetic and electric fields, one finds a relation for the change in frequency relative to the amplitude of the pressure wave:

$$\frac{\partial\omega_C}{\partial P} = -\frac{1}{6}\omega_C\kappa(\epsilon_R + 2)(\epsilon_R - 1)\frac{\int f(r, \theta, z) |\overline{E}_0|^2 dV}{\int \epsilon_R |\overline{E}_0|^2 dV}. \quad (2.32)$$

Ultimately we would like to solve for the optomechanical coupling rate  $g_0$  as defined in the Hamiltonian (Eqn. 2.1). Since we are working with pressure instead of displacement, we write:  $g_0 = \partial\omega_C/\partial P \cdot \Delta P_{ZP}$ . The energy stored in an acoustic mode is given by [63]:

$$E = \frac{\kappa}{2} \int (Pf(r, \theta, z))^2 dV. \quad (2.33)$$

We solve for the zero point pressure  $\Delta P_{ZP}$  by equating Eqn. (2.33) with  $\hbar\omega_M/2$ . Letting  $\xi = \int (f(r, \theta, z))^2 dV$ , we find:

$$\Delta P_{ZP} = \sqrt{\frac{\hbar\omega_M}{\kappa\xi}}. \quad (2.34)$$

Using Eqns. (2.32) and (2.34) one can calculate the single photon coupling rate ( $g_0$ ) for an array of acoustic and microwave modes.

We can solve for the coupling constants for the sapphire setup using a similar approach. Because of the difficulty of calculating the EM fields of the whispering gallery modes analytically, we instead use a successful 2D simulation technique for axisymmetric resonators (see reference [68]) to calculate the eigenfrequencies of the resonator. To estimate the coupling, we can calculate the eigenfrequency of a specific mode for a range of dielectric constants in

the helium ring, which gives a value for  $\partial\omega_C/\partial\epsilon_R$ . This method of calculating  $\partial\omega_C/\partial\epsilon_R$  will overestimate the coupling constant because it does not include the overlap integral between the electromagnetic mode and the acoustic mode; including the profiles of both modes in the simulation would yield an exact result. Using Eqns. (2.30) and (2.31) above, one finds a relation for the coupling constant:  $\partial\omega_C/\partial P = \partial\omega_C/\partial\epsilon_R \cdot \kappa/3 \cdot (\epsilon_R - 1) (\epsilon_R + 2)$ . Note that the highest quality factor microwave modes have high azimuthal order but no longitudinal or radial variation, and therefore do not couple to the purely azimuthal acoustic modes. Also note that  $g_0$  for the sapphire setup is limited because the whispering gallery modes primarily reside in the sapphire where they do not interact with the superfluid acoustic mode; in this respect, the niobium setup is superior.

## 2.5 Cavity Heating

### 2.5.1 Thermal Model

In the ideal case where acoustic loss is limited by the three phonon process, the  $Q$  will have a  $T^4$  dependence, and measuring high  $Q$ s will require long periods of temperature stability. In addition, as we will outline in Chapter 3, achieving optomechanical sideband cooling in our system requires large microwave pump powers. In both cases cavity heating may become important; here we consider the effects of heating on the helium temperature.

To estimate the effect of heating in  ${}^4\text{He}$ , we will compare the heating from dielectric losses to the cooling through thermal phonon exchange with the cell. We will justify why this model is appropriate. We focus here on our niobium setup shown in Fig (2.2a), although the results can be generalized to other systems. A thermal model of the helium, niobium cell and mixing chamber is shown in Fig. (2.5). The helium and niobium are represented as capacitances with  $C = c_{mol}n$ , where  $c_{mol}$  is the molar specific heat in J/mol K and  $n$  is the number of moles.  ${}^4\text{He}$  cools through phonon scattering at the cell boundary, which is

mediated by the Kapitza resistance ( $R_k$ ) [5]:

$$R_K = \frac{15\hbar^3 \rho_s c_s^3}{2\pi^2 k_B^4 A \rho_4 c_4 T^3}, \quad (2.35)$$

where  $A$  is the surface area of contact,  $\rho_4 = 145 \text{ kg/m}^3$  and  $c_4 = 238 \text{ m/s}$  are the density and speed of sound in  ${}^4\text{He}$ , and  $\rho_s$  and  $c_s$  are the density and speed of sound in the boundary material. In our case,  $A = 0.0064 \text{ m}^2$ ,  $\rho_s = \rho_{Nb} = 8570 \text{ kg/m}^3$ , and  $c_s = c_{Nb} = 3480 \text{ m/s}$ . Notice one of the reasons that  ${}^4\text{He}$  is notoriously difficult to cool to low temperatures is that  $R_K$  is proportional to the acoustic impedance mismatch between helium and the boundary material ( $Z = \rho_s c_s / \rho_4 c_4$ ); for a metal boundary this impedance mismatch is high because of helium's low density and speed of sound. For our niobium cell, the impedance mismatch is  $Z = 860$  and the Kapitza resistance is  $R_K = 40/T^3$

In turn the niobium cell cools through the suspension system, which in our most successful experiments has been a copper wire. Its resistance will be given by:

$$R_{\text{susp}} = \frac{L_{\text{Susp}}}{\lambda A_{\text{Susp}}}, \quad (2.36)$$

where  $L_{\text{Susp}}$  is the length,  $A_{\text{Susp}}$  is the cross-sectional area, and  $\lambda$  is the thermal conductivity in  $\text{W/m K}$ . Note that both resistances  $R_K$  and  $R_{\text{Susp}}$  have units of  $\text{K/W}$ . One can understand the conductance,  $1/R$ , as follows: one Watt across a conductance of one  $\text{W/K}$  produces a one Kelvin temperature drop.

The suspension system is easily modified from run to run and  $R_{\text{Susp}}$  will depend on the specific design that we use. First we consider material choice. For the excellent and readily available conductors copper and silver, the low temperature thermal conductivity calculated from Wiedemann Franz is given by [5]:

$$\lambda_{Cu} = (RRR/0.76) \cdot T,$$

$$\lambda_{Ag} = (RRR/0.55) \cdot T,$$

where  $RRR$  is the ratio of the electrical conductivity at low temperature to the conductivity at room temperature:  $RRR = \sigma_{4.2K}/\sigma_{300K}$ ;  $RRR$  is a measure of the limit placed on conductivity by defect scattering, and it can be improved in a given sample by vacuum annealing. Notice that in theory silver is the superior conductor; however in practice the low temperature values of thermal conductivity for silver may be  $\approx 30$  times smaller than the predictions from Wiedemann-Franz [69]. In our final planned run, we made an annealed 5N silver suspension wire with length 6.5 cm and diameter 0.1 cm. If we achieved  $RRR = 5000$  through annealing and we use the experimental values from [69], we can expect  $\lambda = 300 \cdot T$  or  $R_{Susp} \approx 280/T$ . Note that this resistance may be reduced by as much as an order of magnitude if the conductivity is in line with Weidemann Franz or if a copper wire is used.

Finally we compare the resistances  $R_K$  and  $R_{Susp}$ . Notice the different temperature dependencies between low temperature phonon ( $R_K \propto T^3$ ) and electron ( $R_{Susp} \propto T$ ) conductivity mean that at low enough temperatures,  $R_K > R_{Susp}$ . For our niobium cell and the silver suspension system assumed above,  $R_K = R_{Susp}$  at  $T \approx 380$  mK, and  $R_K = 10 \cdot R_{Susp}$  at 120 mK. At temperatures below 100 mK where we will operate our experiment,  $R_{Susp}$  can be neglected. Note that these temperatures will be higher if  $R_{Susp}$  is made smaller.

We also note that we have assumed that resistance between the niobium cell and the suspension wire is small compared to other thermal resistances. This assumption may not be obvious given that in niobium far below  $T_C$ , thermal conduction will be dominated by phonons as the electrons are frozen out in Cooper pairs. The boundary resistance between the niobium cell and the suspension wire will be given by the Kapitza boundary resistance where although the impedance mismatch is now  $\approx 1$ , the surface area of contact is also much smaller. If we use a silver suspension with a circular contact area of radius 0.2 cm, we find  $R_{K,Susp} \approx 3/T^3$ , which is an order of magnitude smaller than  $R_K$  between the helium and the cell; we need not consider the contact resistance between the cell and the suspension system here.

Further we can justify ignoring the heat capacity of the niobium cell ( $C_{Nb}$ ) because it will be much smaller than the heat capacity of the helium itself ( $C_{He}$ ). At very low temperatures ( $T < T_C/10$ ), niobium will behave like an insulator because the electrons have frozen into

Cooper pairs and phonons are responsible for heat conduction. In niobium  $T_C = 9.3$  K so our experiments will operate entirely in this temperature range. When the phonon conductivity dominates, the specific heat is given by the Debye approximation, which for niobium is  $C \approx 1944 \times T^3 / \Theta_D^3$  J/mol·K where  $\Theta_D = 275$  K is the Debye temperature [70, 71]. The cell is approximately 14 moles of niobium, so the total heat capacity is  $10^{-3}T^3$  J/K.  $^4\text{He}$  is also an insulator with a Debye law heat capacity proportional to  $T^3$ . However in helium the specific heat per mole is significantly higher than in niobium, primarily because the sound velocity in helium is  $\approx 1/10$  as high. The molar heat capacity of helium has been thoroughly studied experimentally and a good compilation of values can be found on Russell Donnelly's website [72]. At one Kelvin, the heat capacity of the 1.4 moles of helium in the cell will be 0.6 J/K, almost three orders of magnitude higher than the heat capacity of the niobium cell ( $10^{-3}$  J/K). Since we expect a  $T^3$  dependence for both, we can ignore the heat capacity of the niobium cell for our experiments at all lower temperatures as well.

Now for low temperatures ( $T < 120$  mK) we can justify a simpler thermal model where the dominant resistance is the thermal boundary resistance between helium and the niobium cell ( $R_K$ ) and the dominant capacitance is the heat capacity of the helium ( $C_{He}$ ). The thermal time constant for cooling is given by  $\tau = R_K \cdot C_{He} \approx 10$  seconds.

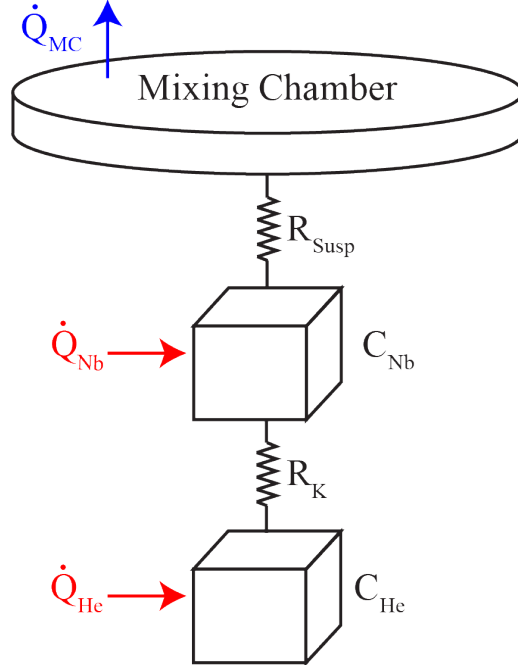


Figure 2.5: A simplified representation of the thermal conduction from the superfluid helium to the mixing chamber. The helium is treated as a capacitance  $C_{He}$  connected to the cell  $C_{Nb}$  through the Kapitza boundary resistance  $R_K$ , and the cell is connected to the mixing chamber through the resistance of the suspension system  $R_{Susp}$ . Arrows represent heating due to dielectric loss in both the niobium ( $\dot{Q}_{Nb}$ ) and the helium ( $\dot{Q}_{He}$ ) and the cooling power of the dilution refrigerator ( $\dot{Q}_{MC}$ ).

### 2.5.2 Dielectric Heating

In general, the power dissipated by dielectric heating is given by  $P = (A^2\omega/2) \cdot \int \epsilon \tan(\delta) |E|^2 dV$  where  $\omega$  is the microwave frequency,  $A$  is the microwave amplitude  $\epsilon = \epsilon_R \epsilon_0$  is the permittivity, and  $\tan(\delta)$  is the loss tangent of the material [37]. Using the energy stored in the electric field  $W_e = n_P \hbar \omega = (A^2 \epsilon / 4) \cdot \int |E|^2 dV$ , we can write the dielectric heating expected in the helium as:

$$\dot{Q}_{He} = n_P \hbar \omega_C^2 \tan(\delta), \quad (2.37)$$

where  $n_P$  is the number of pump photons in the cavity and  $\omega_C$  is the eigenfrequency of the cavity mode. Dielectric loss in helium was studied by Hartung, et. al [73] using high quality factor microwave cavities. Based on their results, a maximum loss tangent value for helium at 1.5 K is  $\tan(\delta) \leq 10^{-10}$ . The results of Hartung, et. al [73] were limited by the

$Q$  of their microwave cavity; in fact  $\tan(\delta)$  in helium is anticipated to be much smaller and we can consider this value to be a "worst case." For the  $\text{TE}_{011}$  mode in our niobium cell  $\omega_C/2\pi = 10.6$  GHz, and we can write  $P_{He} = 5 \cdot 10^{-23} n_P$ .

There will also be dielectric heating at the surface of the niobium cell. If we assume that the internal  $Q$  of the microwave mode is limited by dielectric loss, then  $Q_{int} = 1/\tan(\delta)$  [37] and the power dissipated in the microwave mode will be:

$$\dot{Q}_{Nb} = n_P \hbar \omega_C \kappa_{int}. \quad (2.38)$$

For the  $\text{TE}_{011}$  mode in our cavity we measured  $Q_{int} = 3.6 \cdot 10^8$  (See Chapter 5), so the heating is  $\dot{Q}_{Nb} = 5 \cdot 10^{-22} n_P$ .

Now that we have quantified the expected heating, we consider the rate of cooling. Our Oxford Kelvinox 400H has a cooling power of  $400 \mu\text{W}$  at  $100 \text{ mK}$ . At low temperatures, the cooling power of a dilution refrigerator is proportional to  $T^2$ , so we estimate the cooling power ( $\dot{Q}_{MC}$ ) of our system as:  $\dot{Q}_{MC} \approx 0.04T^2$ . The power from dielectric heating in both the helium and the niobium cell will heat the mixing chamber until the dilution refrigerator cooling power equals the heating. We can solve for the increased fridge temperature,  $T_{MC}$ , from  $\dot{Q}_{Nb} + \dot{Q}_{He} = 0.04T_{MC}^2$ , where we can write  $T_{MC} = T_i + \Delta T$ , with  $T_i$  the starting temperature and  $\Delta T$  the increase in temperature. Assuming the increase in temperature is small ( $\Delta T \ll T_{MC}$ ):

$$T_{MC} = \left( \frac{\dot{Q}_{Nb} + \dot{Q}_{He} + 0.04T_i^2}{0.04} \right)^{1/2}. \quad (2.39)$$

Because of the high thermal resistance between helium and the mixing chamber, the final temperature of the  ${}^4\text{He}$  will be higher than the mixing chamber temperature by an amount:  $\Delta T = R_K \dot{Q}$ . The final temperature of the helium will be

$$T_{He} = \left( \alpha_{R_K} \dot{Q}_{He} + T_{MC}^4 \right)^{1/4}, \quad (2.40)$$

where  $\alpha_{R_K} = 15\hbar^3 \rho_s c_s^3 / 2\pi^2 k_B^4 A \rho_4 c_4$  is the Kapitza resistance without the temperature de-

pendence.

## 2.6 Notes about Temperature Stability

The velocity of sound in helium-4 depends on temperature as [74]:

$$c_4(T) - c_4(0) = \frac{\pi^2}{60} \frac{(G+1)^2}{\rho_4 \hbar^3} \left( \frac{k_B T}{c_4} \right)^4 \ln \left( \frac{1 + (2\omega\tau)^2}{1 + (3\gamma\bar{\rho}\omega\tau)^2} \right), \quad (2.41)$$

where  $G = (\rho/c_4) \partial c_4 / \partial \rho = 2.84$  is the Grüneisen's parameter [74],  $k_B$  is the Boltzmann constant,  $\rho = 145 \text{ kg/m}^3$  is the density,  $\hbar$  is the reduced Planck constant,  $c_4 = 238 \text{ m/s}$  is the speed of sound [74],  $\omega$  is the frequency of the acoustic wave,  $T$  is the temperature,  $\tau = 1/(0.9 \cdot 10^7 T^5)$  is the thermal phonon lifetime [75],  $\bar{\rho} = 3k_B T/c_4$  is the average thermal momentum, and  $\gamma \approx -10^{48} (\text{s/kg}\cdot\text{m})^2$  is the dispersion constant defined in Eqn.(4.1), which characterizes the weak non-linearity of the dispersion relation for low momentum phonons [76, 77].

In order to use the superfluid acoustic mode as a sensitive detector, for instance as a gravitational wave detector, the source of interest must remain within the bandwidth of the helium resonator,  $\Delta f = \omega_M/2\pi Q$ , which will place limits on the temperature stability. As will be discussed in Chapter 4, in the ideal case, the superfluid acoustic  $Q$  will be limited by the three phonon process intrinsic to helium-4. If the three phonon process is the dominant source of loss, shifts to lower temperature will be the limiting case, as the resonator will become more narrowband as the temperature decreases. If the source frequency is originally matched to the frequency of the superfluid acoustic oscillator, the maximum frequency shift for which the source will remain in the oscillator's bandwidth will be one half of the acoustic bandwidth. The maximum frequency shift  $\Delta T$  from a starting temperature of  $T_0$  is given by:

$$f(T_0) - f(T_0 + \Delta T) = \frac{\omega_M}{4\pi} \frac{1}{Q_{3PP}(T_0 + \Delta T)}, \quad (2.42)$$

where  $Q_{3PP} = \omega_M/2c_4\alpha_{3PP}$  and  $\alpha_{3PP}$  is given by Eqn. (4.2). The results of solving for  $\Delta T$

as both an increase and a decrease in temperature are shown in Fig. (2.6)

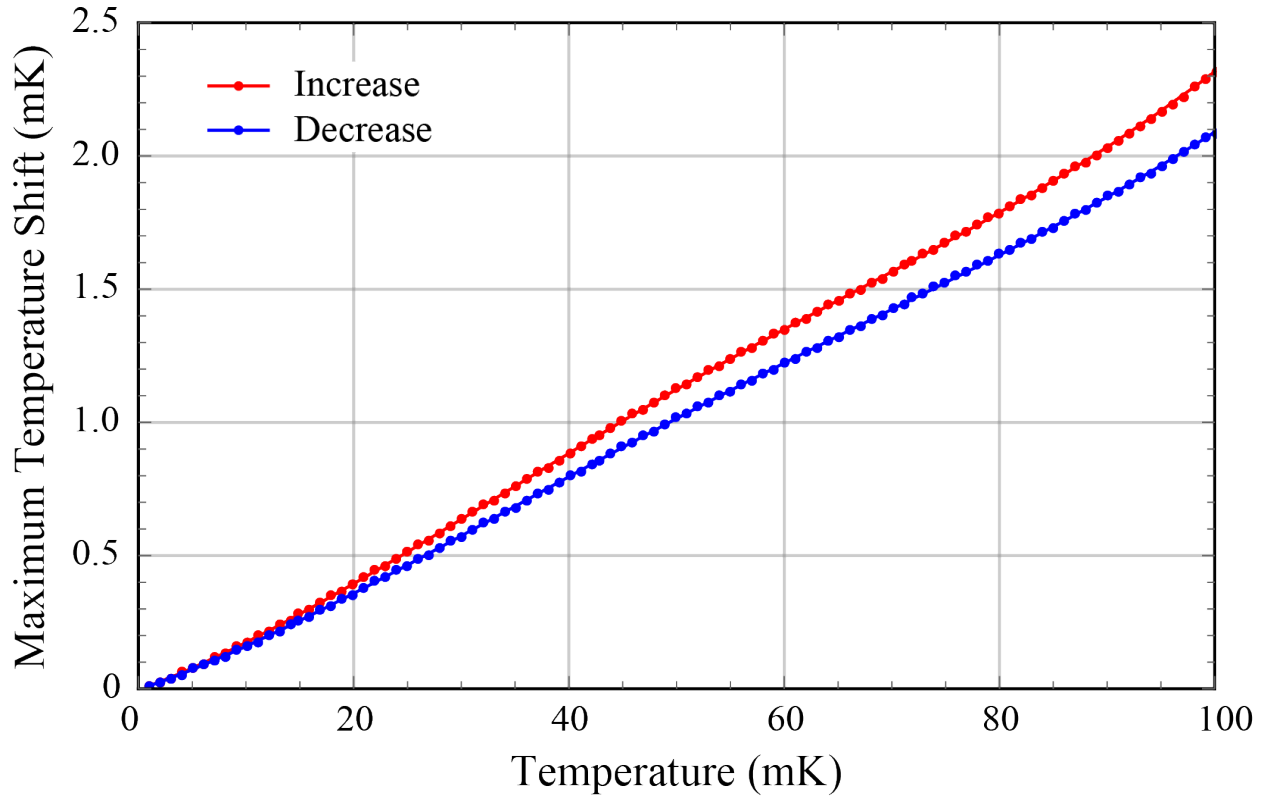


Figure 2.6: The maximum temperature increase (red) and decrease (blue) over which a source originally centered in the superfluid acoustic resonator will remain within the bandwidth of the resonator, assuming that at all temperatures the  $Q$  is limited by the three phonon process.

# Chapter 3

## Circuit Equations

### 3.1 Inductively Coupled RLC Circuit

As introduced in Chapter 2, the niobium microwave cavity can be represented as an RLC circuit, where the effect of the superfluid mechanical mode is a sinusoidally varying capacitance. The basic circuit representation of this setup is shown in Fig. (3.1). The bare cavity inductance, resistance and capacitance are denoted  $L_C$ ,  $R_C$  and  $C_C$ , respectively and the varying capacitance from the superfluid acoustic mode is labeled  $C_M$ . We couple to the cavity inductively with two small loops recessed into the cavity lid, each with inductance  $L$ . The inductance of a loop is given by:  $L = \mu R (\ln (8R/a) - 2)$  where  $R$  is the radius of the loop and  $a$  the radius of the wire. For our coupling loops,  $a = 0.015$  cm and  $R = 0.065$  cm, so we find  $L \approx 3$  nH. The mutual inductance between these loops and the microwave cavity is given by:  $M_{in} = k_1 \sqrt{LL_C}$  and  $M_{out} = k_2 \sqrt{LL_C}$ . Here  $k_1$  and  $k_2$  are the input and output coupling coefficients. We use the subscripts 1 and 2 to avoid confusion with  $\kappa_{in}$  and  $\kappa_{out}$ , the cavity input and output coupling rates. We drive the cavity with a voltage source  $2V_0$  through a 50 ohm transmission line and we detect the output signal on a HEMT amplifier.

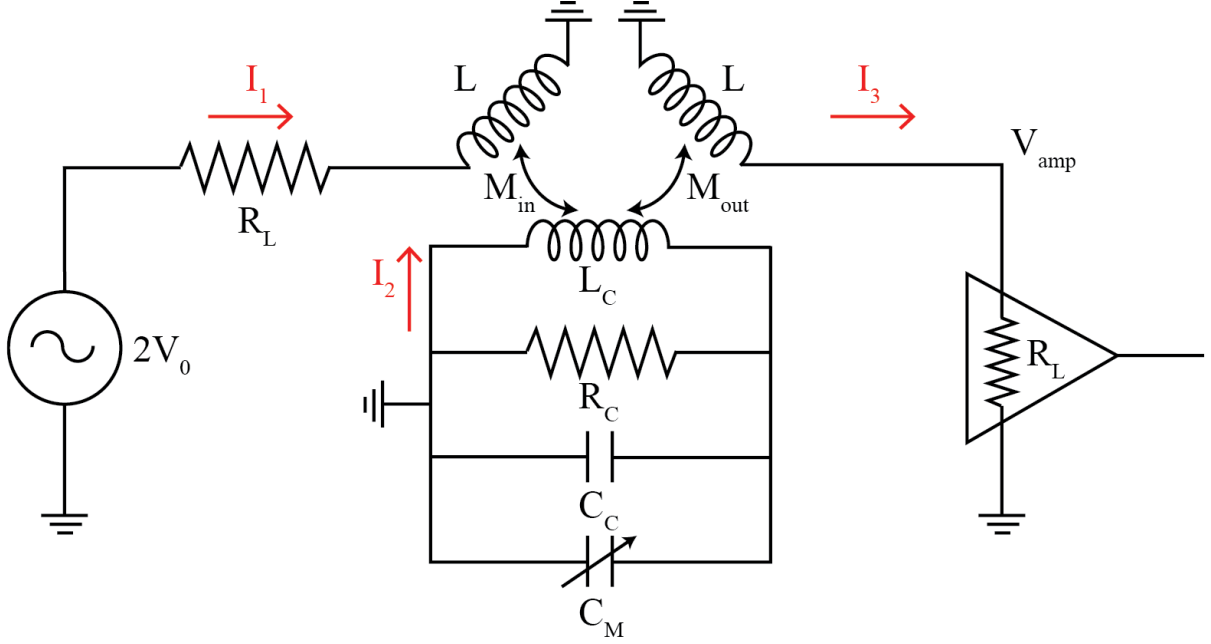


Figure 3.1: The equivalent circuit model for the inductively coupled niobium cavity ( $R_C, L_C, C_C$ ) parametrically coupled to the superfluid acoustic mode ( $C_M$ ).

We can solve for the cavity currents and voltages using Kirchoff's laws. For the input circuit on the left of Fig. (3.1), we write:

$$2V_0 - R_L \cdot I_1 - L \cdot \dot{I}_1 + M_{in} \cdot \dot{I}_2 = 0. \quad (3.1)$$

If we write the currents with their explicit time dependence:  $I = I e^{i\omega t}$ , then we can rewrite Eqn. (3.1) as:

$$2V_0 = (R_L + i\omega L) I_1 - i\omega M_{in} I_2, \\ I_1 = \frac{2V_0 + i\omega M_{in} I_2}{R_L + i\omega L}. \quad (3.2)$$

Similarly the output circuit on the right of Fig. (3.1) is written:

$$- R_L \cdot I_3 - L \cdot \dot{I}_3 + M_{out} \cdot \dot{I}_2 = 0, \quad (3.3)$$

which becomes:

$$0 = -R_L \cdot I_3 - i\omega L I_3 + i\omega M_{out} I_2, \\ I_3 = \frac{i\omega M_{out} I_2}{i\omega L + R_L}. \quad (3.4)$$

Finally the central circuit representing the cavity itself is described by:

$$-L_C \cdot \dot{I}_2 + M_{in} \cdot \dot{I}_1 - I_2 \cdot Z_{RC} + M_{out} \cdot \dot{I}_3 = 0, \quad (3.5)$$

where  $Z_{RC}$  is the combined impedance of the parallel resistor and capacitor elements:

$$\frac{1}{Z_{RC}} = \frac{1}{R_C} + i\omega C_C, \\ Z_{RC} = \frac{R_C}{1 + i\omega C_C R_C}. \quad (3.6)$$

Eqn. (3.5) simplifies to:

$$i\omega (M_{in} I_1 + M_{out} I_3) = \left( i\omega L_C + \frac{R_C}{1 + i\omega C_C R_C} \right) I_2. \quad (3.7)$$

Substituting Eqn. (3.2) for  $I_1$  and Eqn. (3.4) for  $I_3$  into Eqn. (3.7) we find:

$$i\omega \left( \left( \frac{2V_0 + i\omega M_{in} I_2}{R_L + i\omega L} \right) M_{in} + \left( \frac{i\omega M_{out} I_2}{R_L + i\omega L} \right) M_{out} \right) = \left( i\omega L_C + \frac{R_C}{1 + i\omega C_C R_C} \right) I_2 \\ \frac{i\omega M_{in}}{R_L + i\omega L} 2V_0 - \frac{\omega^2 I_2}{R_L + i\omega L} (M_{in}^2 + M_{out}^2) = \left( i\omega L_C + \frac{R_C}{1 + i\omega C_C R_C} \right) I_2 \\ \frac{i2\omega M_{in}}{R_L + i\omega L} \frac{V_0}{I_2} = \frac{\omega^2 (M_{in}^2 + M_{out}^2)}{R_L + i\omega L} + i\omega L_C + \frac{R_C}{1 + i\omega C_C R_C}. \quad (3.8)$$

We will return to this result later. In order to understand Eqn.(3.8) more fully it is helpful to first convert the cavity circuit to its equivalent parallel model.

## 3.2 Equivalent Parallel Circuit Model

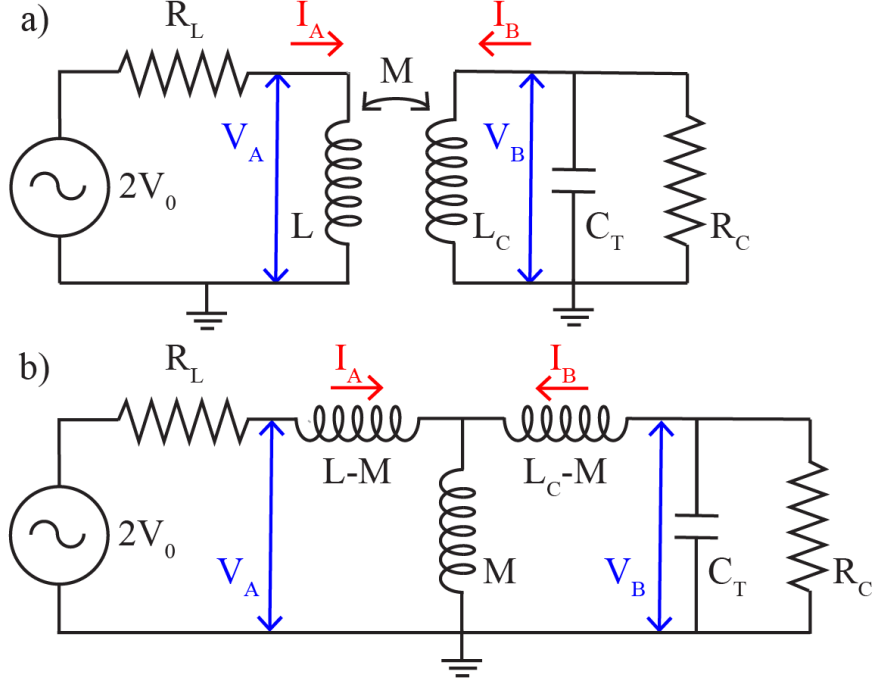


Figure 3.2: a) The input circuit inductively coupled to the microwave cavity and b) its T circuit equivalent.

While we couple to the niobium cavity inductively, the identical circuit with capacitive coupling has been well studied in the field of optomechanics. For instance, Jared Hertzberg's thesis [78] has a thorough treatment of the circuit model for a capacitively coupled transmission line resonator. He begins by converting the circuit to its parallel equivalent, and it will be instructive to do the same for the inductively coupled circuit used here.

We start by converting the coupled inductors into their equivalent T circuit [79]. Taking just the input circuit and the cavity, we have the circuit shown in Fig. (3.2a), where we have combined the cavity capacitors into a single capacitance  $C_T = C_C + C_M$ . The inductors  $L$  and  $L_C$  are coupled through the mutual inductance  $M$ . The equations for the voltage  $V_A$

across the input inductor  $L$  and the voltage  $V_B$  across the cavity inductor  $L_C$  are:

$$V_A = i\omega L I_A + i\omega M I_B,$$

$$V_B = i\omega M I_A + i\omega L_C I_B.$$

By adding zero,  $0 = -M I_A + M I_A$  ( $0 = -M I_B + M I_B$ ), we can rewrite these equations as follows:

$$\begin{aligned} V_A &= i\omega (L - M) I_A + i\omega M (I_A + I_B), \\ V_B &= i\omega M (I_A + I_B) + i\omega (L_C - M) I_B. \end{aligned} \quad (3.9)$$

Eqns. (3.9) are the equations for the T-circuit shown in Fig. (3.2b) with three inductors  $L - M$ ,  $M$  and  $L_C - M$ , demonstrating that the circuits shown in Figs. (3.2a) and (3.2b) are equivalent.

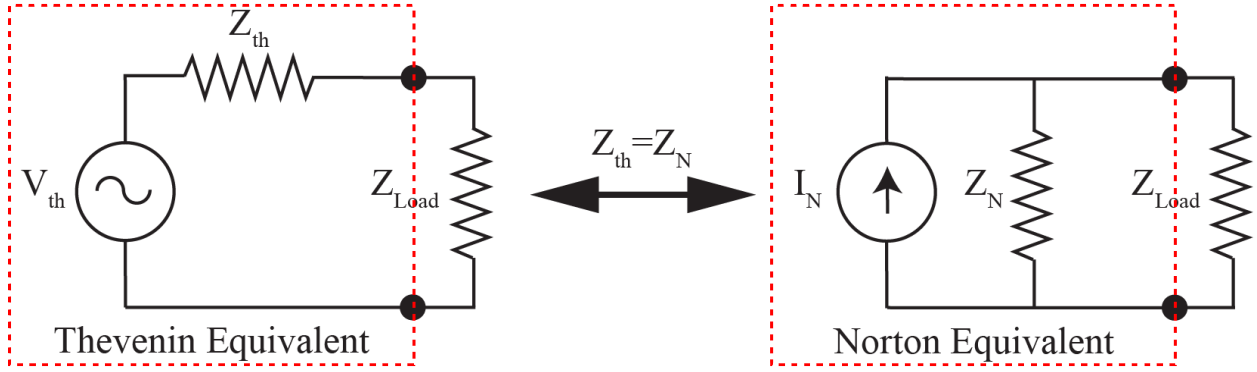


Figure 3.3: The Thevenin (series) and Norton (parallel) equivalent circuits. The impedance  $Z_{th} = Z_N$ .

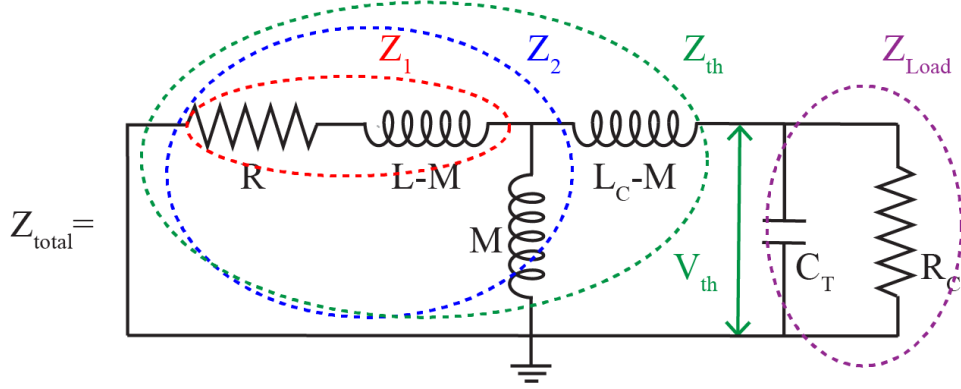


Figure 3.4: Solving for the thevenin impedance ( $Z_{th}$ ) of Fig. (3.2b). The intermediate impedances  $Z_1$  and  $Z_2$  are referenced in the text.

Ultimately we would like to use Norton-Thevenin equivalent circuits (Fig. (3.3)) to find a parallel equivalent for the circuit shown in Fig. (3.2b). The first step in solving for the Thevenin circuit is to deactivate the source and find the resultant equivalent impedance. As shown in Fig. (3.4), we will treat the cavity resistor and capacitor  $R_C$  and  $C_T$  as a load impedance  $Z_{load}$  and solve for the impedance of the remaining circuit  $Z_{th}$ .

We now work through the calculation of  $Z_{th}$ . The first step is to combine the series resistor  $R_L$  and inductor  $L - M$  into their equivalent impedance  $Z_1 = R_L + i\omega(L - M)$ .  $Z_1$  is in parallel with the inductor  $M$ ; we write the combined impedance of these two elements as  $Z_2$  and solve:

$$\begin{aligned} \frac{1}{Z_2} &= \frac{1}{Z_1} + \frac{1}{i\omega M}, \\ \frac{1}{Z_2} &= \frac{1}{R_L + i\omega(L - M)} + \frac{1}{i\omega M}, \\ Z_2 &= \left( \frac{i\omega M + R_L + i\omega(L - M)}{i\omega M(R_L + i\omega(L - M))} \right)^{-1}, \\ Z_2 &= \left( \frac{R_L + i\omega L}{i\omega M R_L - \omega^2 M(L - M)} \right)^{-1}, \\ Z_2 &= \frac{\omega^2 M(M - L) + i\omega M R_L}{R_L + i\omega L}. \end{aligned}$$

The final Thevenin impedance ( $Z_{th}$ ) will be given by the series impedance of  $Z_2$  and the last

inductor  $L_C - M$ . We solve for  $Z_{th}$  as follows:

$$\begin{aligned}
Z_{th} &= \frac{\omega^2 M (M - L) + i\omega M R_L}{R_L + i\omega L} + i\omega (L_C - M), \\
Z_{th} &= \frac{(\omega^2 M^2 - \omega^2 M L + i\omega M R_L) (R_L - i\omega L)}{R_L^2 + (\omega L)^2} + i\omega (L_C - M), \\
Z_{th} &= \frac{\omega^2 M^2 R_L - \omega^2 M L R_L + \omega^2 M L R_L + i(\omega M R_L^2 - \omega^3 M^2 L + \omega^3 M L^2)}{R_L^2 + (\omega L)^2} + i\omega (L_C - M), \\
Z_{th} &= \frac{\omega^2 M^2 R_L}{R_L^2 + (\omega L)^2} + i\omega \left( \frac{M R_L^2 - \omega^2 M^2 L + \omega^2 M L^2}{R_L^2 + (\omega L)^2} + L_C - M \right), \\
Z_{th} &= \frac{\omega^2 M^2 R_L}{R_L^2 + (\omega L)^2} + i\omega \left( L_C + \frac{M R_L^2 - \omega^2 M^2 L + \omega^2 M L^2 - M R_L^2 - \omega^2 M L^2}{R_L^2 + (\omega L)^2} \right), \\
Z_{th} &= \frac{\omega^2 M^2 R_L}{R_L^2 + (\omega L)^2} + i\omega \left( L_C - \frac{\omega^2 M^2 L}{R_L^2 + (\omega L)^2} \right). \tag{3.10}
\end{aligned}$$

Looking at Eqn. (3.10), we see that the total impedance has the form of a resistor and an inductor in series:  $Z_{th} = R_{series} + i\omega L_{series}$  where the values are given by  $R_{series} = \omega^2 M^2 R_L / (R_L^2 + (\omega L)^2)$  and  $L_{series} = L_C - \omega^2 M^2 L / (R_L^2 + (\omega L)^2)$ .

Finally we solve for the voltage  $V_{th}$  using the voltage divider between  $Z_1$  and  $M$ :

$$\begin{aligned}
V_{th} &= 2V_0 \frac{i\omega M}{Z_1 + i\omega M}, \\
V_{th} &= 2V_0 \frac{i\omega M}{R_L + i\omega (L - M) + i\omega M}, \\
V_{th} &= 2V_0 \frac{i\omega M}{R_L + i\omega L}.
\end{aligned}$$

In the above calculation we solved for the impedance of an RLC circuit inductively coupled to an input circuit. In reality our cavity has two coupling ports, one each for input and output. If we had included the output circuit, we would have an additional term for the

output coupling  $M_{out}$  such that the series circuit impedance is:

$$Z = R_{series} + i\omega L_{series},$$

$$R_{series} = \frac{\omega^2 R_L (M_{in}^2 + M_{out}^2)}{R_L^2 + (\omega L)^2}, \quad (3.11)$$

$$L_{series} = L_C - \frac{\omega^2 L (M_{in}^2 + M_{out}^2)}{R_L^2 + (\omega L)^2}. \quad (3.12)$$

Finally we use Norton-Thevenin equivalents as shown in Fig. (3.3) to find the equivalent parallel elements: a resistor  $R_{\parallel}$  and inductor  $L_{\parallel}$ . The impedance of our desired circuit, is given by  $Z_N$  as follows:

$$\frac{1}{Z_N} = \frac{1}{R_{\parallel}} + \frac{1}{i\omega L_{\parallel}},$$

$$\frac{1}{Z_N} = \frac{i\omega L_{\parallel}}{i\omega R_{\parallel} L_{\parallel}} + \frac{R_{\parallel}}{i\omega R_{\parallel} L_{\parallel}},$$

$$Z_N = \frac{i\omega R_{\parallel} L_{\parallel}}{i\omega L_{\parallel} + R_{\parallel}},$$

$$Z_N = \frac{\omega R_{\parallel} L_{\parallel}}{\omega L_{\parallel} - iR_{\parallel}}.$$

From the Norton-Thevenin equivalent,  $Z_{th} - Z_N = 0$ , allowing us to solve for  $R_{\parallel}$  and  $L_{\parallel}$  in terms of  $R_{series}$  and  $L_{series}$ . This calculation gives:

$$L_{\parallel} = L_{series} \left( 1 + \left( \frac{R_{series}}{\omega L_{series}} \right)^2 \right),$$

$$R_{\parallel} = R_{series} \left( 1 + \left( \frac{\omega L_{series}}{R_{series}} \right)^2 \right).$$

Substituting for  $R_{series}$  (Eqn. (3.11)) and  $L_{series}$  (Eqn. (3.12)) and using the definition of

mutual inductance,  $M = k\sqrt{LL_C}$ , we find:

$$R_{||} \approx \frac{\omega^2 LL_C}{(k_1^2 + k_2^2) R_L} \left( \left( \frac{R_L}{\omega L} \right)^2 + 1 \right),$$

$$L_{||} \approx L_C,$$

where the only approximations we have made are  $k_1^2 \ll 1$  and  $k_2^2 \ll 1$ . Now that we have a parallel representation of the input resistor and coupling inductors of Fig. (3.4), we have a full parallel representation of our original circuit in Fig. (3.1). We can write the impedance of this circuit as  $Z_{tot}$ :

$$\frac{1}{Z_{tot}} = \frac{1}{R_C} + i\omega C_C + \frac{1}{i\omega L_C} + \frac{(k_1^2 + k_2^2) R_L}{\omega^2 LL_C} \frac{1}{\left( \frac{R_L}{\omega L} \right)^2 + 1}, \quad (3.13)$$

where the first three terms represent the impedances internal to the cavity and the final term represents the impedance that arises from coupling to external circuits. Because the final term is real, we write it as a resistance,  $1/R_{ext}$ , denoting the loss that arises from external coupling:

$$R_{ext} = \frac{\omega^2 LL_C}{(k_1^2 + k_2^2) R_L} \left( \left( \frac{R_L}{\omega L} \right)^2 + 1 \right). \quad (3.14)$$

We can relate the circuit model to the experimental cavity coupling rates  $\kappa$  through the cavity quality factor  $Q$ . In a parallel RLC circuit,  $Q = R\sqrt{C_T/L_C} = R/\omega_C L$ . The linewidth of the cavity, or its total loss rate, is  $\kappa_{tot} = \omega_C/Q$ , and the cavity frequency is defined by its inductance  $L_C$  and capacitance  $C_T$ :  $\omega = 1/\sqrt{L_C C_T}$ . We write the total cavity Q ( $Q_{tot}$ ) as:

$$\frac{1}{Q_{tot}} = \omega_C L \frac{1}{R_{tot}} = \omega_C L \left( \frac{1}{R_{int}} + \frac{1}{R_{||,in}} + \frac{1}{R_{||,out}} \right). \quad (3.15)$$

We can solve for the internal ( $\kappa_{int}$ ) and external ( $\kappa_{ext}$ ) coupling rates:

$$\begin{aligned} Q_{int} &= \frac{R_C}{\omega_C L}, \\ \kappa_{int} &= \frac{\omega_C}{Q_{int}} = \frac{\omega_C^2 L_C}{R_C}, \\ Q_{ext} &= \frac{R_{ext}}{\omega_C L}, \\ \kappa_{ext} &= \frac{\omega_C}{Q_{ext}} = \frac{\omega_C^2 L_C}{R_{ext}}. \end{aligned}$$

Now we can write the external coupling rate  $\kappa_{ext}$  in terms of the external resistance solved for above in Eqn. (3.14):

$$\kappa_{ext} = \frac{\omega_C^2 L_C}{R_{ext}} = \frac{(k_1^2 + k_2^2) R_L}{L} \frac{1}{\left(\left(\frac{R_L}{\omega L}\right)^2 + 1\right)}. \quad (3.16)$$

Finally, the Norton equivalent current of the parallel circuit is given by  $I_0 = V_{th}/Z_{th}$ :

$$I_0 = \frac{2V_0 \left( \frac{i\omega M_{in}}{R_L + i\omega L} \right)}{\frac{\omega^2 (M_{in}^2 + M_{out}^2) R_L}{R_L^2 + \omega^2 L^2} + i\omega \left( L_C - \frac{\omega^2 (M_{in}^2 + M_{out}^2) L}{R_L^2 + \omega^2 L^2} \right)}. \quad (3.17)$$

Using only the simplifications that  $k_1^2, k_2^2 \ll 1$ , we find that

$$\begin{aligned} I_0 &= \frac{i2M_{in}V_0}{iL_C R_L - LL_C \omega + \omega (M_{in}^2 + M_{out}^2)}, \\ I_0 &= \frac{i2k_1 L V_0}{\sqrt{L L_C} (iR_L + (k_1^2 + k_2^2 - 1) \omega L)}, \\ I_0 &= \frac{2k_1 L V_0}{\sqrt{L L_C} (R_L + i\omega L)}. \end{aligned}$$

We now have expressions for every element of the full parallel circuit model shown in Fig. (3.5).

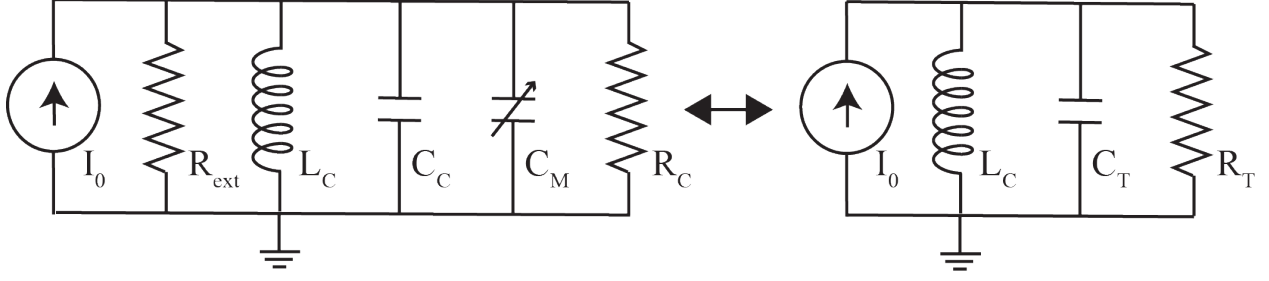


Figure 3.5: The parallel equivalent to Fig. (3.1). On the right the simplified version where the resistors  $R_{ext}$  and  $R_C$  are combined into  $R_T$  and the capacitors  $C_C$  and  $C_M$  are combined into  $C_T$ .

### 3.3 Circulating Cavity Voltage

Using the definitions from the parallel model, we would like to define the experimentally relevant currents and voltages of the system. We return to Eqn. (3.8) describing the full cavity system and rewrite it as follows:

$$\frac{i\omega M_{in}}{R_L + i\omega L} \frac{2V_0}{I_2} = \frac{R_C (1 - i\omega C_C R_C)}{1 + \omega^2 R_C^2 C_C^2} + \frac{\omega^2 (M_{in}^2 + M_{out}^2) R_L}{R_L + i\omega L} + i\omega \left( L_C - \frac{\omega^2 L (M_{in}^2 + M_{out}^2)}{R_L^2 + (\omega L)^2} \right). \quad (3.18)$$

Given the complexity of this equation, we will simplify the right hand side term by term. At the outset we note that  $C_M \ll C_C$ , so we will approximate the total capacitance as  $C_T \approx C_C$  where convenient. To simplify the first term, we remind the reader that the  $Q$  of an RLC circuit can be written:  $Q_{int} = \omega_C C_C R_C$ . Because we work with high  $Q$  cavities, as long as  $\omega \approx \omega_C$ ,  $\omega C_C R_C \gg 1$ . Therefore we can simplify the first term as follows:

$$\begin{aligned} \frac{R_C (1 - i\omega C_C R_C)}{1 + \omega^2 R_C^2 C_C^2} &\approx \frac{R_C (1 - i\omega C_C R_C)}{\omega^2 R_C^2 C_C^2} \\ &= \frac{1}{\omega^2 C_C^2 R_C} - \frac{i}{\omega C_C}. \end{aligned}$$

The second term can be re-written in terms of  $\kappa_{ext}$ :

$$\begin{aligned}
\frac{\omega^2 (M_{in}^2 + M_{out}^2) R_L}{R_L + i\omega L} &= \frac{\omega^2 L L_C R_L (k_1^2 + k_2^2)}{R_L + (\omega L)^2} \\
&= L_C \frac{R_L}{L} \frac{k_1^2 + k_2^2}{\left(\frac{R_L}{\omega L}\right)^2 + 1} \\
&= L_C \kappa_{ext}.
\end{aligned}$$

The third term can also be rewritten in terms of  $\kappa_{ext}$ :

$$\begin{aligned}
i\omega \left( L_C - \frac{\omega^2 L (M_{in}^2 + M_{out}^2)}{R_L^2 + (\omega L)^2} \right) &= i\omega \left( L_C + \frac{\omega^2 L (k_1^2 L L_C + k_2^2 L L_C)}{R_L^2 + (\omega L)^2} \right) \\
&= i\omega L_C \left( 1 + \frac{k_1^2 + k_2^2}{\left(\frac{R_L}{\omega L}\right)^2 + 1} \right) \\
&= i\omega L_C \left( 1 + \frac{\kappa_{ext} L}{R_L} \right).
\end{aligned}$$

Combining the simplifications for all three terms, the right hand side of the circuit equation (Eqn. (3.18)) becomes:

$$\begin{aligned}
&= \frac{1}{\omega^2 C_C^2 R_C} - \frac{i}{\omega C_C} + L_C \kappa_{ext} + i\omega L_C \left( 1 + \frac{\kappa_{ext} L}{R_L} \right) \\
&= L_C \left( \kappa_{int} \frac{1}{(\omega^2 C_C L_C)^2} + \kappa_{ext} \right) + i\omega L_C \left( 1 - \frac{1}{\omega^2 L_C C_C} + \frac{\kappa_{ext} L}{R_L} \right) \\
&= L_C \left( \kappa_{int} \frac{\omega_C^4}{\omega^4} + \kappa_{ext} \right) + i\omega L_C \left( 1 - \frac{\omega_C^2}{\omega^2} + \frac{\kappa_{ext} L}{R_L} \right) \\
&= L_C \kappa_{tot} + i\omega L_C \left( \frac{\omega^2 - \omega_C^2}{\omega^2} + \frac{\kappa_{ext} L}{R_L} \right),
\end{aligned}$$

where we assume in the last step that  $\omega \approx \omega_C$ . With this approximation, we can make one

further simplification as follows:

$$\begin{aligned}\frac{\omega^2 - \omega_C^2}{\omega^2} &= \frac{(\omega + \omega_C)(\omega - \omega_C)}{\omega^2} \\ &\approx \frac{2\omega_C\Delta}{\omega^2}.\end{aligned}$$

Here we define  $\Delta = \omega - \omega_C$ , where  $\omega$  is the frequency of the signal applied to the cavity.

Finally we can write:

$$\begin{aligned}\frac{i\omega M_{in}}{R_L + i\omega L} \frac{2V_0}{I_2} &= L_C \kappa_{tot} + i\omega L_C \left( \frac{2\omega_C\Delta}{\omega^2} + \frac{\kappa_{ext}L}{R_L} \right), \\ \frac{i\omega M_{in}}{R_L + i\omega L} \frac{2V_0}{I_2} &= L_C \left( \kappa_{tot} + i \left( \frac{2\omega_C\Delta}{\omega} + \kappa_{ext} \frac{\omega L}{R_L} \right) \right), \\ \frac{i\omega M_{in}}{R_L + i\omega L} \frac{2V_0}{I_2} &= L_C \left( \kappa_{tot} + i \left( 2\Delta + \kappa_{ext} \frac{\omega L}{R_L} \right) \right), \\ \frac{i\omega M_{in}}{R_L + i\omega L} \frac{2V_0}{I_2} &\approx L_C (\kappa_{tot} + i2\Delta).\end{aligned}\tag{3.19}$$

In the last step we have used the approximation that  $2\Delta \gg \kappa_{ext}\omega L/R_L$ , which can be justified by our system parameters:  $\Delta \approx 10^4$  and  $\kappa_{ext}\omega L/R_L = \omega^2 L/QR_L \approx 10$  using  $\omega \approx \omega_C \approx 10^{10}$ ,  $L \approx 10^{-9}$ ,  $Q \approx 10^8$ , and  $R_L = 50$ . Finally we can rearrange Eqn. (3.19) to explicitly write the current in the cavity  $I_2$  as:

$$|I_2| = 2V_0 \sqrt{\frac{\kappa_{in}}{R_L L_C}} \frac{1}{\sqrt{\kappa_{tot}^2 + (2\Delta)^2}}.\tag{3.20}$$

With an expression for  $I_2$ , we can now solve for the voltage in the cavity,  $V_{cav} = L_C \dot{I}_2 = i\omega L_C I_2$ :

$$V_{cav} = \frac{-\omega^2 M_{in} 2V_0}{R_L + i\omega L} \frac{1}{\kappa_{tot} + i2\Delta}.\tag{3.21}$$

Now if we use the definition of  $\kappa_{in}$  we can write:

$$\begin{aligned}
\frac{\omega M_{in}}{\sqrt{R_L^2 + (\omega L)^2}} &= \frac{\omega k_1 \sqrt{L} \sqrt{R_L}}{\sqrt{R_L}} \frac{1}{\omega L \sqrt{\left(\frac{R_L}{\omega L}\right)^2 + 1}} \\
&= \sqrt{\frac{L_C}{R_L}} \frac{k_1 \sqrt{R_L}}{\sqrt{L} \sqrt{\left(\frac{R_L}{\omega L}\right)^2 + 1}} \\
&= \sqrt{\frac{L_C \kappa_{in}}{R_L}}.
\end{aligned} \tag{3.22}$$

Similarly, using the definition of  $\kappa_{out}$ , we write:

$$\frac{\omega M_{out}}{\sqrt{R_L^2 + (\omega L)^2}} = \sqrt{\frac{L_C \kappa_{out}}{R_L}}. \tag{3.23}$$

Eqn. (3.22) allows us to rewrite Eqn. (3.21) for  $V_{cav}$  as:

$$|V_{cav}| = 2V_0 \sqrt{\frac{\kappa_{in} L_C}{R_L}} \frac{\omega}{\sqrt{\kappa_{tot}^2 + (2\Delta)^2}}, \tag{3.24}$$

where we recognize the Lorentzian line shape in the term  $1/\sqrt{\kappa_{tot}^2 + (2\Delta)^2}$ . As expected for an off resonant drive, most of the power is reflected from the cavity.

The energy in a parallel RLC circuit is given by  $E = \frac{1}{2}CV_{RMS}^2 + \frac{1}{2}L_C I_{RMS}^2 = L_C I_{RMS}^2$  where  $V_{RMS}$  and  $I_{RMS}$  are root mean square time average values. The peak value is related to the RMS value through  $V_{RMS} = V_{pp}/\sqrt{2}$ . Therefore we can solve for the energy stored in the cavity using  $E = \frac{1}{2}L_C |I_2|^2$ :

$$E_{cav} = 2|V_0|^2 \frac{\kappa_{in}}{R_L} \frac{1}{\kappa_{tot}^2 + (2\Delta)^2}. \tag{3.25}$$

The input power is  $W = |V_{0,RMS}|^2/R_L = |V_0|^2/2R_L$  so we can rewrite Eqn. (3.25) as:

$$E_{cav} = 4W_{in} \frac{\kappa_{in}}{\kappa_{tot}^2 + (2\Delta)^2}, \tag{3.26}$$

where  $W_{in}$  is the power incident on the cavity. Finally we can solve for the number of cavity photons ( $n_C$ ) using  $E_{cav} = n_C \hbar \omega_C$ :

$$n_C = \frac{4W_{in}}{\hbar \omega_C} \frac{\kappa_{in}}{\kappa_{tot}^2 + (2\Delta)^2}. \quad (3.27)$$

We would also like an expression for the output voltage at the amplifier,  $V_{amp}$ . With an expression for the current  $I_3$ , we can solve for  $V_{amp} = R_L I_3$ . The current  $I_3$  is related to the current  $I_2$  in the cavity inductor  $L_C$  through the output coupling  $M_{out}$ :

$$\begin{aligned} 0 &= M_{out} \dot{I}_2 - R_L I_3 - L \dot{I}_3, \\ 0 &= i\omega M_{out} I_2 - R_L I_3 - i\omega L I_3, \\ I_3 &= \frac{i\omega M_{out}}{R_L + i\omega L} I_2, \\ |I_3| &= \sqrt{\frac{\kappa_{out} L_C}{R_L}} I_2. \end{aligned} \quad (3.28)$$

where we have used Eqn. (3.23) for  $\kappa_{out}$  to simplify the expression. Substituting (3.20) for  $I_2$  we find:

$$\begin{aligned} |I_3| &= 2|V_0| \sqrt{\frac{\kappa_{out} L_C}{R_L}} \sqrt{\frac{\kappa_{in}}{R_L L_C}} \frac{1}{\sqrt{k_{tot}^2 + (2\Delta)^2}}, \\ |I_3| &= \frac{2|V_0|}{R_L} \frac{\sqrt{\kappa_{out} \kappa_{in}}}{\sqrt{\kappa_{tot}^2 + (2\Delta)^2}}. \end{aligned}$$

The amplifier voltage becomes:

$$|V_{amp}| = 2|V_0| \frac{\sqrt{\kappa_{out} \kappa_{in}}}{\sqrt{\kappa_{tot}^2 + (2\Delta)^2}}. \quad (3.29)$$

It will be more convenient to have an expression for the amplifier voltage in terms of the

cavity voltage. Using  $V_{amp} = R_L I_3$  and Eqn. (3.28) for  $I_3$  we find:

$$V_{amp} = \sqrt{\frac{\kappa_{out} L_C}{R_L}} R_L I_2. \quad (3.30)$$

The cavity voltage is related to  $I_2$  by  $V_{cav} = L_C \dot{I}_2 = i\omega L_C I_2$ , allowing us to write:

$$\begin{aligned} |V_{amp}| &= \sqrt{\frac{\kappa_{out} L_C}{R_L}} \frac{R_L}{\omega L_C} |V_{cav}|, \\ |V_{amp}| &= \sqrt{\frac{\kappa_{out} R_L}{L_C}} \frac{1}{\omega} |V_{cav}|. \end{aligned} \quad (3.31)$$

### 3.4 Sideband Voltages

Using the parallel circuit model, we can easily solve for the sideband voltages that will arise due to the fluctuating capacitance  $C_M$ . Here we work with the simplified parallel circuit of Fig. (3.5), where we write the combined resistance as  $R_T$ , which is defined by  $1/R_T = 1/R_C + 1/R_{ext}$ , and we write the total capacitance as:  $C_T = C_C + C_M$ . The following will be identical to the treatment for the capacitively coupled circuit.

The total current in the circuit,  $I_P$ , can be written as the sum of the currents through each element:

$$I_P = I_{R_T} + I_{L_C} + I_{C_T}. \quad (3.32)$$

Given the definitions for the current in an inductor:  $I_L = \int_0^t V/L_C dt$  and the current through a capacitor:  $I_{C_T} = \partial/\partial t (C_T V)$ , we can write the derivative of the current  $I_P$  as:

$$\begin{aligned} \dot{I}_P &= \frac{1}{R_T} \dot{V} + \frac{1}{L_C} V + \frac{\partial^2}{\partial t^2} (C_T V), \\ \dot{I}_P &= \frac{1}{R_T} \dot{V} + \frac{1}{L_C} V + C_T \ddot{V} + 2 \frac{\partial C_M}{\partial t} \dot{V} + \frac{\partial^2 C_M}{\partial t^2} V. \end{aligned} \quad (3.33)$$

In order to find the time derivatives of  $C_M$  we require an explicit time dependence. Recall that  $C_M$  represents the fluctuating capacitance contributed by the superfluid acoustic mode. To make a circuit model analogy, we use the equation for the capacitance of a parallel plate

capacitor:  $C = \epsilon A/x$ , where  $A$  is the area of the plates and  $x$  the distance between them. The fluctuating capacitance due to the superfluid acoustic mode is analogous to the distance  $x$  fluctuating with sinusoidal time dependence  $x = x_0 \cos(\omega_M t + \phi_M)$  where  $\omega_M$  and  $\phi_M$  are the frequency and phase of the mechanical mode and  $x_0$  is the amplitude of the motion. From the Taylor expansion, we can approximate  $C_M$  as:

$$C_M(x) \approx C_M(x=0) + \frac{\partial C_M(x)}{\partial x}|_{x=0}x. \quad (3.34)$$

For simplicity we will drop the  $|_{x=0}$  on the first derivative. The time derivatives of  $C_M$  are as follows:

$$\begin{aligned} C_M &= \frac{\partial C_M}{\partial x} x_0 \cos(\omega_M t) = \frac{1}{2} \frac{\partial C_M}{\partial x} x_0 (e^{i(\omega_M t + \phi_M)} + e^{-i(\omega_M t + \phi_M)}), \\ \dot{C}_M &= \frac{i}{2} \omega_M \frac{\partial C_M}{\partial x} x_0 (e^{i(\omega_M t + \phi_M)} - e^{-i(\omega_M t + \phi_M)}), \\ \ddot{C}_M &= -\frac{1}{2} \omega_M^2 \frac{\partial C_M}{\partial x} x_0 (e^{i(\omega_M t + \phi_M)} + e^{-i(\omega_M t + \phi_M)}). \end{aligned}$$

Now we let  $I_P = I_P \cos(\omega_P t + \phi_P) = \frac{1}{2} I_P (e^{i(\omega_P t + \phi_P)} + e^{-i(\omega_P t + \phi_P)})$ ; this represents the drive coming from the source, and as such it oscillates at the "pump" frequency  $\omega_P$  with phase  $\phi_P$ . Note that it is acceptable to drop the  $1/2$  and the second exponential as long as only linear operations are performed; for non-linear operations, such as multiplication, both terms must be retained.

With the input current oscillating at  $\omega_P$  and the varying capacitance oscillating at  $\omega_M$  we anticipate a solution of the form:

$$\begin{aligned} V &= \frac{1}{2} V_P (e^{i(\omega_P t + \phi_P)} + e^{-i(\omega_P t + \phi_P)}) + \frac{1}{2} V_D (e^{i(\omega_D t + \phi_D)} + e^{-i(\omega_D t + \phi_D)}) \\ &\quad + \frac{1}{2} V_U (e^{i(\omega_U t + \phi_U)} + e^{-i(\omega_U t + \phi_U)}), \end{aligned}$$

where  $D$  and  $U$  denote the down- and up- converted sidebands, ie.  $\omega_D = \omega_P - \omega_M$  and

$$\omega_U = \omega_P + \omega_M.$$

The derivatives will be given by:

$$\begin{aligned}\dot{V} &= \frac{1}{2}i\omega_P V_P (e^{i(\omega_P t + \phi_P)} - e^{-i(\omega_P t + \phi_P)}) + \frac{1}{2}i\omega_D V_D (e^{i(\omega_D t + \phi_D)} - e^{-i(\omega_D t + \phi_D)}) \\ &\quad + \frac{1}{2}i\omega_U V_U (e^{i(\omega_U t + \phi_U)} - e^{-i(\omega_U t + \phi_U)}), \\ \ddot{V} &= -\frac{1}{2}\omega_P^2 V_P (e^{i(\omega_P t + \phi_P)} + e^{-i(\omega_P t + \phi_P)}) - \frac{1}{2}\omega_D^2 V_D (e^{i(\omega_D t + \phi_D)} + e^{-i(\omega_D t + \phi_D)}) \\ &\quad - \frac{1}{2}\omega_U^2 V_U (e^{i(\omega_U t + \phi_U)} + e^{-i(\omega_U t + \phi_U)}).\end{aligned}$$

In the following we will simplify our notation with the shorthand *c.c.*, which will always denote the complex conjugate of the first exponential term inside the same parenthesis. For instance, we will write  $(e^{i(\omega_M t + \phi_M)} - e^{-i(\omega_M t + \phi_M)})$  as  $(e^{i(\omega_M t + \phi_M)} - \text{c.c.})$ . Substituting the equations for  $I_P$  and  $C_M$  into Eqn. (3.33), and making the simplification that because  $C_M \ll C_C$ ,  $C_T \approx C_C$  we find:

$$\begin{aligned}\frac{1}{2}I_P (e^{i(\omega_P t + \phi_P)} - \text{c.c.}) &= V \left( \frac{1}{L_C} - \frac{1}{2}\omega_M^2 \frac{\partial C_M}{\partial x} x_0 (e^{i(\omega_M t + \phi_M)} + \text{c.c.}) \right) \\ &\quad + \dot{V} \left( \frac{1}{R_T} + i\omega_M \frac{\partial C_M}{\partial x} x_0 (e^{i(\omega_M t + \phi_M)} - \text{c.c.}) \right) \\ &\quad + \ddot{V} \left( C_C + \frac{1}{2} \frac{\partial C_M}{\partial x} x_0 (e^{i(\omega_M t + \phi_M)} + \text{c.c.}) \right).\end{aligned}$$

Multiplying by  $\sqrt{L_C/C}$  and using the definitions  $\omega_C = 1/\sqrt{L_C C_C}$  and  $\kappa_{tot} = \omega_C/Q =$

$\omega_C^2 L_C / R_T$ , we can write:

$$\begin{aligned} \frac{1}{2} \sqrt{\frac{L_C}{C_C}} I_P (e^{i(\omega_P t + \phi_P)} - c.c.) &= \omega_C V \left( 1 - \frac{1}{2} \frac{\omega_M^2}{\omega_C^2} \frac{1}{C_C} \frac{\partial C_M}{\partial x} x_0 (e^{i(\omega_M t + \phi_M)} + c.c.) \right) \\ &\quad + \frac{\kappa_{tot}}{\omega_C} \dot{V} \left( 1 + i\omega_M \frac{1}{\kappa_{tot} C_C} \frac{\partial C_M}{\partial x} x_0 (e^{i(\omega_M t + \phi_M)} - c.c.) \right) \\ &\quad + \frac{1}{\omega_C} \ddot{V} \left( 1 + \frac{1}{2} \frac{1}{C_C} \frac{\partial C_M}{\partial x} x_0 (e^{i(\omega_M t + \phi_M)} + c.c.) \right). \end{aligned}$$

Because  $\omega_M \ll \omega_C$  (in our system,  $\omega_M \approx 10$  kHz compared to  $\omega_C \approx 10$  GHz) we drop the term that goes as  $\omega_M^2 / \omega_C^2$ :

$$\begin{aligned} \frac{1}{2} \sqrt{\frac{L_C}{C_C}} I_P (e^{i(\omega_P t + \phi_P)} - c.c.) &\approx \omega_C V \\ &\quad + \frac{\kappa_{tot}}{\omega_C} \dot{V} \left( 1 + i\omega_M \frac{1}{\kappa_{tot} C_C} \frac{\partial C_M}{\partial x} x_0 (e^{i(\omega_M t + \phi_M)} - c.c.) \right) \\ &\quad + \frac{1}{\omega_C} \ddot{V} \left( 1 + \frac{1}{2} \frac{1}{C_C} \frac{\partial C_M}{\partial x} x_0 (e^{i(\omega_M t + \phi_M)} + c.c.) \right). \end{aligned}$$

Finally substituting for  $V$  we find that the right hand side becomes:

$$\begin{aligned} &\approx \frac{1}{2} \omega_C (V_P (e^{i(\omega_P t + \phi_P)} + c.c.) + V_D (e^{i(\omega_D t + \phi_D)} + c.c.) + V_U (e^{i(\omega_U t + \phi_U)} + c.c.)) \\ &\quad + (\omega_P V_P (e^{i(\omega_P t + \phi_P)} - c.c.) + \omega_D V_D (e^{i(\omega_D t + \phi_D)} - c.c.) + \omega_U V_U (e^{i(\omega_U t + \phi_U)} - c.c.)) \\ &\quad \cdot \frac{i\kappa_{tot}}{2\omega_C} \cdot \left( 1 + i\omega_M \frac{1}{\kappa_{tot} C_C} \frac{\partial C_M}{\partial x} x_0 (e^{i(\omega_M t + \phi_M)} - c.c.) \right) \\ &\quad - (\omega_P^2 V_P (e^{i(\omega_P t + \phi_P)} + c.c.) + \omega_D^2 V_D (e^{i(\omega_D t + \phi_D)} + c.c.) + \omega_U^2 V_U (e^{i(\omega_U t + \phi_U)} + c.c.)) \\ &\quad \cdot \frac{1}{2\omega_C} \cdot \left( 1 + \frac{1}{2} \frac{1}{C_C} \frac{\partial C_M}{\partial x} x_0 (e^{i(\omega_M t + \phi_M)} + c.c.) \right). \end{aligned}$$

Now to solve for the voltage at the upper sideband, collect terms that oscillate at  $\omega_U = \omega_P + \omega_M$ :

$$0 = V_U \omega_C \left( 1 - \frac{\omega_U^2}{\omega_C^2} \right) (e^{i(\omega_U t + \phi_U)} + c.c.) + i V_U \kappa_{tot} \frac{\omega_U}{\omega_C} (e^{i(\omega_U t + \phi_U)} - c.c.) \\ - V_P \frac{\omega_P}{C_C} \frac{\partial C_M}{\partial x} x_0 \left( \frac{\omega_M}{\omega_C} + \frac{\omega_P}{2\omega_C} \right) (e^{i(\omega_U t + \phi_M + \phi_P)} + c.c.). \quad (3.35)$$

Because  $\omega_U, \omega_P \approx \omega_C$  we can make the simplifications that  $\omega_U/\omega_C \approx 1$  and  $\omega_P/\omega_C \approx 1$ , giving:

$$1 - \frac{\omega_U^2}{\omega_C^2} = \left( 1 - \frac{\omega_U}{\omega_C} \right) \left( 1 + \frac{\omega_U}{\omega_C} \right) \approx 2 \left( 1 - \frac{\omega_U}{\omega_C} \right). \quad (3.36)$$

Finally, the last term in Eqn. (3.35) will go as  $\approx (\omega_M/\omega_C + 1/2)$ . Because  $\omega_M \ll \omega_C$ , we can drop the first term in the parenthesis. We find that Eqn. (3.35) simplifies to:

$$V_U (2(\omega_C - \omega_U) (e^{i(\omega_U t + \phi_U)} + c.c.) + i \kappa_{tot} (e^{i(\omega_U t + \phi_U)} - c.c.)) \\ = V_P \frac{\omega_P}{2C_C} \frac{\partial C_M}{\partial x} x_0 (e^{i(\omega_U t + \phi_M + \phi_P)} + c.c.).$$

Returning to trigonometric notation, we have:

$$V_U (2(\omega_C - \omega_U) \cos(\omega_U t + \phi_U) - \kappa_{tot} \sin(\omega_U t + \phi_U)) \\ = V_P \frac{\omega_P}{2C_C} \frac{\partial C_M}{\partial x} x_0 \cos(\omega_U t + \phi_P + \phi_M).$$

Using the addition formula:  $A \cos(xt) + B \sin(xt) = \sqrt{A^2 + B^2} \cos(xt - \arctan(B/A))$ , we find:

$$V_U \sqrt{(2\Delta_U)^2 + \kappa_{tot}^2} \cos \left( \omega_U t + \phi_U - \arctan \left( \frac{\kappa_{tot}}{2\Delta_U} \right) \right) \\ = V_P \frac{\omega_P}{2C_C} \frac{\partial C_M}{\partial x} x_0 \cos(\omega_U t + \phi_P + \phi_M),$$

where we have used the definition:  $\Delta_U = \omega_U - \omega_C$ . Finally, we can write the voltage and

phase of the upconverted sideband:

$$V_U = V_P \frac{\omega_P}{2C_C} \frac{\partial C_M}{\partial x} x_0 \cdot \frac{1}{\sqrt{(2\Delta_U)^2 + \kappa_{tot}^2}}, \quad (3.37)$$

$$\phi_U = \phi_P + \phi_M + \arctan \left( \frac{\kappa_{tot}}{2\Delta_U} \right). \quad (3.38)$$

Similarly, solving for the voltage and phase of the downconverted sideband, we find:

$$V_D = V_P \frac{\omega_P}{2C_C} \frac{\partial C_M}{\partial x} x_0 \cdot \frac{1}{\sqrt{(2\Delta_D)^2 + \kappa_{tot}^2}}, \quad (3.39)$$

$$\phi_D = \phi_P - \phi_M + \arctan \left( \frac{\kappa_{tot}}{2\Delta_D} \right), \quad (3.40)$$

where  $\Delta_D = \omega_D - \omega_C$ .

### 3.4.1 Upconverted Signal Power

We would like to write the upconverted sideband voltage (Eqn. (3.37)) in terms of the optomechanical coupling constant  $g_0 = g\Delta x_{ZP}$  where  $g = \partial\omega_C/\partial x$ . Using the circuit model analogy, the optomechanical coupling results from a change in the position of a capacitor plate, which modulates the cavity frequency  $\omega_C = 1/\sqrt{L_C C_C} \approx 1/\sqrt{L_C C_T}$ . Therefore we can solve for  $g = \partial\omega_C/\partial x$  using the capacitance of a parallel plate capacitor  $C = \epsilon A/x$ :

$$\begin{aligned} g &= \frac{\partial}{\partial x} \frac{1}{\sqrt{L(C_C + C_M)}}, \\ g &= -\frac{1}{2\sqrt{L}} \frac{1}{\sqrt{(C_C + C_M)^3}} \frac{\partial C_M}{\partial x}, \\ g &= -\frac{1}{2\sqrt{L}C_T} \frac{1}{C_T} \frac{\partial C_M}{\partial x}, \\ g &\approx -\frac{\omega_C}{2C_T} \frac{\partial C_M}{\partial x}. \end{aligned} \quad (3.41)$$

Assume that our microwave drive is on the red sideband,  $\omega_P = \omega_C - \omega_M$ , such that the upconverted sideband is located at the cavity frequency,  $\omega_U = \omega_C$  and  $\Delta_U = 0$ , as is the case for all of the data taken in this thesis. For a frequency domain illustration, see the Anti-Stokes drive in Fig. (3.6). Using the relation for  $g$  from Eqn. (3.41), we can simplify Eqn. (3.37) for the voltage in the upconverted sideband:

$$V_U = V_P \frac{\omega_P}{\omega_C} \frac{C_T}{C_C} \frac{x_0 g}{\kappa_{tot}},$$

$$V_U \approx V_P \frac{x_0 g}{\kappa_{tot}}, \quad (3.42)$$

where we have used the approximations that  $C_T/C_C \approx 1$  and  $\omega_P/\omega_C \approx 1$ .

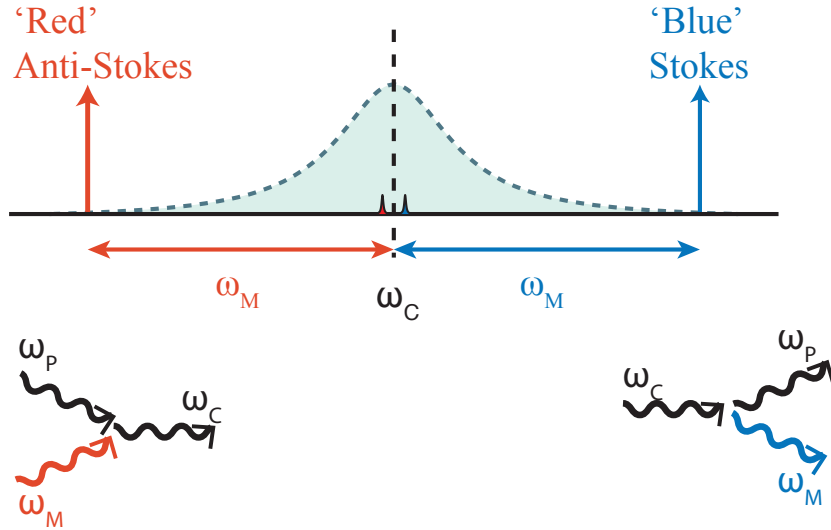


Figure 3.6: The scattering picture for a cavity drive tone ( $\omega_p$ ) applied on either the red or blue sideband. On the red or Anti-Stokes sideband, the pump frequency is  $\omega_p = \omega_C - \omega_M$  and the upper sideband is incident with  $\omega_C$ ; in this case the mechanics is preferentially damped. For a drive on the blue or Stokes sideband the pump frequency is  $\omega_p = \omega_C + \omega_M$ , the lower sideband is incident with  $\omega_C$ , and the mechanics is driven to higher occupations.

Using Eqn. (3.31) for the voltage at the amplifier in terms of a cavity voltage, Eqn. (3.42) for the voltage in the upconverted sideband in terms of the pump voltage in the cavity, and Eqn. (3.24) for the voltage in the cavity in terms of the source voltage, we can write the

upconverted sideband voltage at the amplifier in terms of the source voltage:

$$V_{amp,U} = 2V_0 \frac{gx_0}{\kappa_{tot}} \sqrt{\frac{\kappa_{in}\kappa_{out}}{\kappa_{tot}^2 + (2\Delta)^2}}. \quad (3.43)$$

The power of this upconverted sideband will be given by:

$$W_{amp,U} = 4W_{in} \frac{g^2 x_0^2}{\kappa_{tot}^2} \frac{\kappa_{in}\kappa_{out}}{\kappa_{tot}^2 + (2\Delta)^2}. \quad (3.44)$$

Using  $x_{RMS}^2 = \langle x^2 \rangle = x_0^2/2$  where  $x_0$  is a peak amplitude, we can write:

$$W_{amp,U} = 4W_{in} \frac{2\langle x^2 \rangle g^2}{\kappa_{tot}^2} \frac{\kappa_{in}\kappa_{out}}{\kappa_{tot}^2 + (2\Delta)^2}. \quad (3.45)$$

It is most convenient to have a relation for the signal power in terms of the mechanical and cavity occupations. We can find a relation between the motion of the mechanics and its phonon occupation  $n_M$ . The energy stored in the mechanical mode is  $K\langle x_{RMS}^2 \rangle$  where  $K = m\omega_M^2$  is the spring constant and  $x$  is the RMS position. Now if we equate this with the total energy from phonon occupation of the mode  $\bar{n}_M \hbar \omega_M$ , we find:

$$\begin{aligned} \langle x^2 \rangle &= \frac{\bar{n}_M \hbar}{m\omega_M}, \\ \langle x^2 \rangle &= 2\bar{n}_M \Delta x_{ZP}^2, \end{aligned} \quad (3.46)$$

where we have used the definition for zero point motion  $\Delta x_{ZP} = \sqrt{\hbar/2m\omega_M}$ .

For convenience we would like to write the upconverted signal in terms of the optomechanical coupling rate  $\Gamma_{opt}$  which is given by [19]:

$$\Gamma_{opt} = \frac{4(g\Delta x_{ZP})^2}{\kappa_{tot}} n_P = \frac{4g_0^2}{\kappa_{tot}} n_P, \quad (3.47)$$

where  $n_P$  is the number of pump photons in the niobium cavity, and, as above,  $g_0 = \partial\omega/\partial x$ .  $\Delta x_{ZP}$  is the single photon optomechanical coupling rate which defines the cavity frequency shift resulting from a single pump photon.

Using Eqns. (3.27), (3.46), and (3.47) we can rewrite Eqn. (3.45) in its most convenient form:

$$W_{amp,U} = \hbar\omega_C n_M \Gamma_{opt} \frac{\kappa_{out}}{\kappa_{tot}}. \quad (3.48)$$

We will also need an equation for the occupation of the microwave cavity from phase noise of the source. We have already solved for the occupation  $n_C$  from a single tone microwave drive (Eqn. (3.27)); however, in reality the microwave source is not a delta function. Every source will also have power at frequencies off the carrier tone, known as phase noise. We will define this power as  $S_{noise}$ . The phase noise is defined at each offset frequency from the carrier tone in units of dBc/Hz, meaning the power in dB at the offset frequency relative to the carrier power in a one Hz bandwidth. Because the phase noise is broadband, it will not be filtered by the Lorentzian shape of the cavity. We can find the total occupation of the cavity due to phase noise by integrating  $n_C$  (Eqn. (3.27)) over all frequencies:

$$n_{cav} = \frac{4S_{noise}}{\hbar\omega_C} \kappa_{in} \int_{-\infty}^{\infty} \frac{1}{\kappa_{tot}^2 + (2\Delta)^2} d\omega. \quad (3.49)$$

Using  $\int 1/(a^2 + x^2) = (1/a) \cdot \tan^{-1}(x/a)$ , we find that the integral is equal to  $\pi/2\kappa_{tot}$ . Because phonon number  $n_C$  must be unitless, for a phase noise in its typical units of dBc/Hz, we divide by  $2\pi$ :

$$n_{cav} = \frac{S_{noise}}{\hbar\omega_C} \frac{\kappa_{in}}{\kappa_{tot}}. \quad (3.50)$$

### 3.5 Sideband Cooling

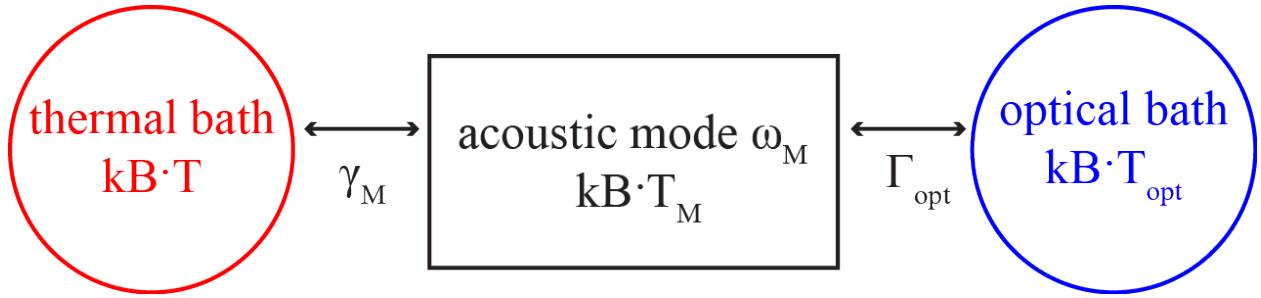


Figure 3.7: The phonon occupation of the mechanical mode is determined by its coupling both to the thermal bath through its intrinsic dissipation  $\gamma_M$  and to the optical bath through the optomechanical coupling rate  $\Gamma_{opt}$ .

With the results from the circuit model, we have all the necessary understanding to calculate the minimum phonon occupation that can be achieved through sideband cooling of the mechanics. As mentioned above, a tone applied on the red sideband preferentially upconverts phonons from the mechanical mode, lowering its occupation. The final number of phonons in the mechanical mode is determined by its coupling to both the thermal bath (through its intrinsic dissipation  $\gamma_M = \omega_M/Q_M$ ) and the optical bath (through  $\Gamma_{opt}$ ). This final occupation is neatly summarized in the detailed balance equation [20]:

$$n_M = \frac{\gamma_M n_M^{th} + \Gamma_{opt} n_M^{opt}}{\gamma_M + \Gamma_{opt}}, \quad (3.51)$$

where  $n_M^{th}$  is the thermal motion of the mode and can be approximated as  $n_M^{th} = k_B T / \hbar \omega_M$  for  $n_M \gg 1$ . Similarly  $n_M^{opt}$  is the occupation of the microwave mode. Because the microwave cavity is high frequency, its thermal occupation will be minimal and instead its occupation will be dominated by phase noise from the microwave source as derived in Eqn. (3.50).

One instructive way of writing the detailed balance equation is in terms of the cooperativity, which is the ratio of the optomechanical and intrinsic damping rates ( $C = \Gamma_{opt}/\gamma_M$ ):

$$n_M = \frac{n_M^{th} + C n_M^{opt}}{1 + C}. \quad (3.52)$$

Now one can clearly see that as  $C \rightarrow \infty$ , the occupation of the mechanics  $n_M$  asymptotes to the occupation of the microwave cavity  $n_M^{opt}$ . Therefore the phase noise of the source will ultimately limit the minimum achievable value of  $n_M$ .

Because  $\gamma_M$  will be fixed in a given system at a given temperature, achieving  $C > 1$  requires large  $\Gamma_{opt}$ . Recall that  $\Gamma_{opt} = 4g_0^2 n_p / \kappa_{tot}$  where  $g_0 = \partial\omega / \partial x \cdot \Delta x_{ZP}$ .  $g_0$  is a fixed parameter and can only be made larger by modifying the mechanical system, for instance by decreasing the mass of the resonator or increasing its frequency. Increases in  $g_0$  of optomechanical devices have been largely responsible for the achievement of ground state cooling, as outlined in Chapter 2. While the nanomechanical resonators shown in Fig. (2.1a) can now achieve  $g_0 \approx 2\pi \cdot 30$  Hz or more, our superfluid resonator has a  $g_0 \approx 2\pi \cdot 10^{-8}$  Hz. To reach large  $\Gamma_{opt}$  in our system we need to achieve much larger pump powers  $n_P$ . With high microwave power, the dielectric heating discussed in Section 2.5 must be considered quantitatively. Heating will elevate the helium bath temperature, increasing  $n_M^{th}$  and decreasing  $\gamma_M$  and may ultimately limit the minimum phonon occupation. Prospects for sideband cooling in our system are described in Chapter 6.

## 3.6 Detection Temperature

Finally, we address the noise temperature of our detection, which we define as the temperature at which the added noise of our detection scheme is equal to the thermal noise amplitude of the superfluid acoustic mode. There are multiple sources of noise in the system, including detection noise of the cryogenic amplifier, phase noise of the microwave source, and heating in the mechanical mode. The final noise detection temperature will include contributions from each of these sources. Given the small dielectric loss tangent of helium and a high  $Q$  microwave resonator, we anticipate that contributions from heating will be negligible, except at very high pump powers.

The noise of the cryogenic amplifier is given by  $4k_B T_{HEMT}$ ; for a typical HEMT amplifier  $T_{HEMT} \approx 5$  K. We will define the phase noise of the source as  $S_{noise}$ , which we can write conveniently as  $S_{noise} = W_{in} \cdot 10^{-x}$ , where  $x$  is the phase noise at a given offset frequency in

dBc/Hz and  $W_{in}$  is the pump power incident on the cavity. We divide these noise sources by the power density of the signal we wish to detect, namely the upconverted mechanical sideband due to the superfluid acoustic mode:  $4W_{amp,U}/\Gamma_{tot}$ .  $W_{amp,U}$  is the power in the upconverted sideband (Eqn. (3.48)) and  $4/\Gamma_{tot}$  is the total bandwidth of the mechanics, where  $\Gamma_{tot} = \gamma_M + \Gamma_{opt}$ . We would like to solve for the temperature of the acoustic mode ( $T_N$ ) required to make the signal power density equal to the noise power density. Because  $W_{amp,U} \propto n_M \propto T_N$ , we can write the noise temperature of our detection scheme as:

$$T_N = \frac{4k_B T_{HEMT} + S_{noise}}{4W_{amp,U}/\Gamma_{tot}}, \quad (3.53)$$

where we divide  $W_{amp,U}$  by  $T_N$  by using a temperature of 1 Kelvin in Eqn. (3.48) for  $W_{amp,U}$ . We can interpret  $T_N$  as follows: when  $T_N = 50$  mK, the added noise of our measurement scheme equals the noise amplitude of the superfluid acoustic mode thermalized to 50 mK.

Finally, we discuss the additional noise that will be added by dielectric heating. Sources of heating and their effect on the helium temperature are addressed in Section 2.5. In the ideal case where the acoustic dissipation ( $\gamma_M$ ) is limited by the three phonon process,  $\gamma_M \propto T^4$ , and small temperature changes can have a significant effect. In this case  $T_N$  will need to be recalculated to include the effects of the elevated helium temperature. However, in the case where  $\Gamma_{opt} \gg \gamma_M$ , changes in  $\gamma_M$  will have little effect on  $\Gamma_{tot}$  or  $T_N$ .

The total temperature for detection includes the thermal contribution from the helium resonator as well as the added noise of the measurement scheme:

$$\text{Total Noise Temperature} = T_{He} + T_N. \quad (3.54)$$

At high pump powers,  $T_{He}$  may be elevated by dielectric heating, increasing the thermal noise and the overall noise temperature.

# Chapter 4

## Acoustic Loss Mechanisms

### 4.1 Attenuation in Pure $^4\text{He}$

From the 1950s through the 1970s, there was a significant amount of work, both theoretical and experimental, toward finding a description for the absorption coefficient of first sound in liquid  $^4\text{He}$  at low temperatures. At temperatures below  $T_\lambda \approx 2.17$  K,  $^4\text{He}$  can be described by the two fluid model, where helium is treated as a composition of two separate and weakly interacting fluids, termed superfluid and normal fluid. As reviewed in Chapter 1, the superfluid component is dissipationless and has no entropy, while the normal fluid acts like an ordinary viscous liquid. The excitations in helium below  $T_\lambda$  are rotons and phonons with normal fluid densities falling proportionally to  $e^{-8.65/T}$  (Eqn. (1.13)) and  $T^4$  (Eqn. (1.12)), respectively [11]. The phonon and roton populations are equal at approximately 0.57 K; at temperatures we consider here ( $T < 100$  mK) only the phonon component of the normal fluid will be relevant.

At very low temperatures in pure  $^4\text{He}$  the only intrinsic mechanism available for absorption of acoustic phonons is phonon-phonon interactions. In early work, there was a question of whether the leading order process was three phonon (leading to a  $T^4$  dependence in the absorption coefficient) or four phonon (leading to a  $T^6$  dependence in the absorption coefficient). For an illustration of the three phonon and four phonon processes, see Fig. (4.1). Elementary arguments show that for the three phonon process (3PP) energy and momentum conservation cannot be satisfied if the dispersion relationship has a negative curvature [77].

The dispersion curve is given by:

$$\epsilon(q) = c_4 q [1 - \gamma \cdot q^2 - \delta \cdot q^4 \dots], \quad (4.1)$$

where  $\epsilon$  and  $q$  are the energy and momentum of an excitation of the condensate,  $c_4$  is the speed of sound in  ${}^4\text{He}$ , and  $\gamma$  and  $\delta$  are constants. Because of the roton minimum, it was presumed that  $\gamma > 0$  giving the dispersion curve a negative curvature and preventing the 3PP. However, experimental data of first sound absorption suggested that the 3PP [80–82] was in fact the dominant process. In 1970, Maris suggested that  $\gamma$  is negative [83], so that the three phonon process is allowed; this hypothesis was later confirmed experimentally [84, 85].

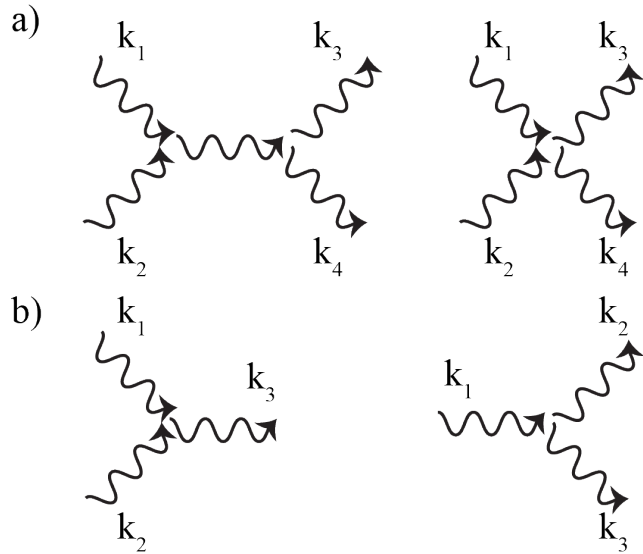


Figure 4.1: Possible a)four phonon and b)three phonon scattering processes.

Many equations are given in the literature for the attenuation coefficient of first sound. While they agree on the  $T^4$  dependence, the constant term varies slightly, agreeing with experiment to within an order of magnitude. The amplitude attenuation coefficient for the 3PP is given by Abraham et al. [86] as:

$$\alpha_{3PP} = \frac{\pi^2}{120} \frac{(G+1)^2}{\rho_4 \hbar^3 c_4^6} (k_B T)^4 \omega (\arctan(2\omega\tau) - \arctan(\Delta E\tau)), \quad (4.2)$$

where  $G = (\rho/c_4) \partial c_4 / \partial \rho = 2.84$  is the Grüneisen's parameter [74],  $k_B$  is the Boltzmann constant,  $\rho = 145 \text{ kg/m}^3$  is the density,  $\hbar$  is the Planck constant,  $c_4 = 238 \text{ m/s}$  is the speed of sound [74],  $\omega$  is the frequency of the acoustic wave,  $T$  is the temperature,  $\tau = 1/(0.9 \cdot 10^7 T^5)$  is the thermal phonon lifetime [75],  $\Delta E = 3\gamma\bar{\rho}^2\omega$  is the energy discrepancy between the initial and final states in the 3PP,  $\bar{\rho} = 3k_B T/c_4$  is the average thermal momentum, and  $\gamma \approx -10^{48} \text{ (s/kg}\cdot\text{m})^2$  is the dispersion constant defined in Eqn.(4.1), which characterizes the weak non-linearity of the dispersion relation for low momentum phonons [76, 77]<sup>1</sup>. Note that Abraham et al. [86] give the absorption coefficient in terms of energy; the amplitude attenuation coefficient, which we quote here, is smaller by a factor of two. In the low temperature limit,  $\omega\tau > 1$ , and the absorption is analogous to the Landau-Rumer regime in solids [87, 88]. Here the arctan functions simplify to a factor of  $\pi/2$  and the quality factor  $Q = \omega/2c_4\alpha$  is frequency independent. For a 6 kHz mode, we will realize this limit for temperatures below 350 mK. At very low temperatures,  $T < 40 \text{ mK}$ , we may reach the limit where  $|\Delta E\tau| \gg 1$ . In this case the second term in Eqn. (4.2) contributes to the attenuation, at most increasing  $\alpha$  by a factor of 2 [89]. This limit could prove difficult to reach, however, as the thermal phonon lifetimes may be limited by boundary scattering. In the high temperature limit of Eqn. (4.2),  $\omega\tau < 1$ , and absorption is in the Akheiser regime [88, 90]. However, this limit is complicated by the effects of roton scattering, which are not included in the above equation and which become important at temperatures above  $\approx 0.6 \text{ K}$ .

Because  $\alpha_{3PP}$  is linearly dependent on  $\omega$ , the quality factor of an acoustic resonator with dissipation dominated by the 3PP will be independent of frequency. Therefore one may consider high frequency resonators, confined in microfluidic channels, which have the advantage of small size and lower thermal occupation. Given the speed of sound in helium of 238 m/s, a resonator with a fundamental mode at 10 (100) MHz would have a dimension of 25  $\mu\text{m}$  (2.5  $\mu\text{m}$ ), easily within the reach of microfabrication techniques [91], and consistent with dimensions typically found in microfabricated superconducting resonators which could be used for detection. However, at high frequencies the container will offer a continuum of modes, making it difficult to isolate the superfluid acoustic mode from the environment and

---

<sup>1</sup> $\epsilon(q) = c_4 q (1 - \gamma q^2 \dots)$ . With this form,  $\gamma < 0$  is known as anomalous dispersion.

ultimately limiting the acoustic quality factor, a subject we will discuss at greater length in Section 4.4. One could imagine a carefully engineered resonator in which the coupling to the continuum is negligible due to interference of the acoustic radiation, as is the case with two-dimensional membranes [92]. In this thesis, we consider only audio frequency acoustic modes which couple weakly to environmental container modes.

Interestingly, Roach, et. al. [93], studying acoustic modes between 15 and 256 MHz, found that the acoustic attenuation decreases as the pressure within the helium cell increases. Jäckle and Kehr [75] have explained this effect as a suppression of the 3PP. Ultrasonic phonons can be absorbed only by thermal phonons of momentum  $q \leq q_C$ , where  $q_C$  is the cutoff momentum, at which the group velocity of thermal phonons is equal to the velocity of the acoustic phonons. The phonon spectrum is pressure dependent, such that at high pressures  $q_C$  is lowered into the range of thermal phonon momentum and the 3PP is suppressed. This process may provide a way to reach lower attenuations at higher temperatures. At low temperatures, where  $k_B T \ll c_4 q_C$ , the 3PP is allowed and the attenuation will be unaffected by the increased pressure. The high pressure limit is 25 bar, where  ${}^4\text{He}$  solidifies.

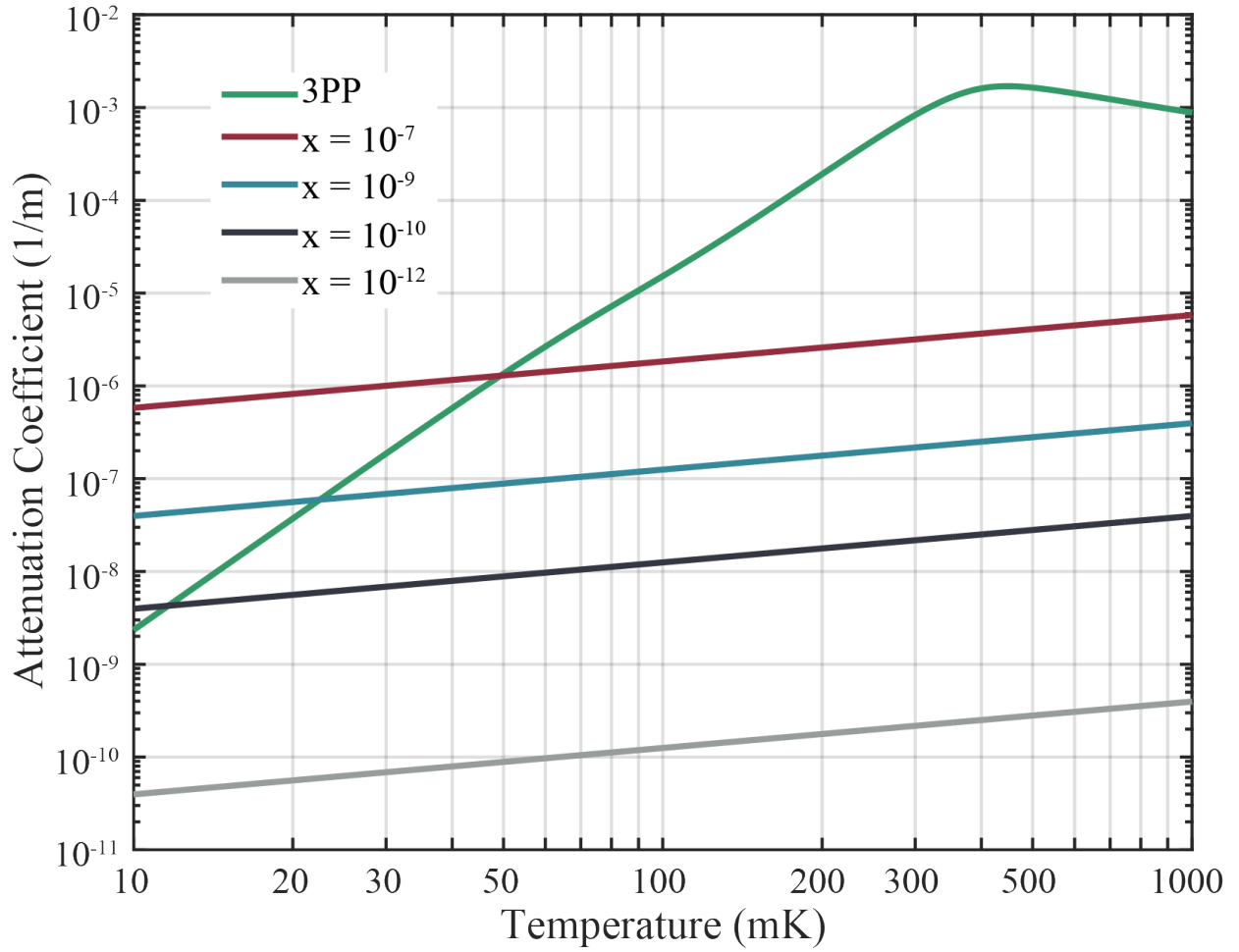


Figure 4.2: shows the expected absorption coefficient for an 8.1 kHz mode from the 3PP (green) and the  $^3\text{He}$  impurity for concentrations  $x =: 10^{-7}$  (red),  $10^{-9}$  (blue),  $10^{-10}$  (black), and  $10^{-12}$  (grey), assuming the mean free path of  $^3\text{He}$  atoms becomes limited by the cell diameter of 3.6 cm.

## 4.2 Attenuation from Impurities

In addition to intrinsic loss processes in  $^4\text{He}$ , we consider the effects of impurities on acoustic absorption. Using cryogenic cold traps, one can freeze all impurities except for  $^3\text{He}$ , which is the only other stable isotope of helium and has a natural abundance of 1.34 ppm ( $x = n_3 / (n_4 + n_3) = 1.34 \cdot 10^{-6}$ , where  $n$  is the number of atoms per unit volume) [8]. We note that the main source of helium is natural gas wells, which tend to have a lower isotopic

impurity, on the order of 0.1 ppm ( $x = 1 \cdot 10^{-7}$ ) [94].

While the acoustic loss in dilute mixtures of  $^3\text{He}$  in  $^4\text{He}$  has been studied both theoretically and experimentally, the bulk of the work has been concerned with mixtures that are in the  $0.0001 \leq x \leq 0.1$   $^3\text{He}$  molar impurity range, well above the concentrations we consider [86, 95–103]. Much of the work is based upon a theoretical outline of  $^3\text{He}$ - $^3\text{He}$  interactions developed by Bardeen, Baym, and Pines (BBP) [104]. They calculate an effective interaction potential for  $^3\text{He}$  atoms using measurements of the spin-diffusion coefficient. Using this interaction, one is able to calculate scattering rates, which allow for the calculation of transport coefficients. Building on this theory, Baym [96] derived an absorption coefficient for first sound in  $^3\text{He}$ - $^4\text{He}$  mixtures at low temperatures (where  $^3\text{He}$ - $^3\text{He}$  interactions dominate damping) which was later extended to higher temperatures by the inclusion of  $^3\text{He}$ -phonon scattering by Baym, Saam, and Ebner [99]. In the low temperature limit ( $T < 100$  mK), they argue the dominant absorptive processes are  $^3\text{He}$  viscosity and the three phonon process in  $^4\text{He}$ , which we have already considered. This theory has reasonable agreement with the absorption data of Abraham, et al. [86, 99] for 5% solutions. The viscosity of dilute  $^3\text{He}$ - $^4\text{He}$  solutions, calculated by Baym and Saam [98] from the same interaction potentials, is also in good agreement with the data of Kuehnold, et al. [101] for solutions with  $0.005 \leq x \leq 0.07$ . However Fu and Pethick [105] argue that the BBP theory is too simple for quantitative agreement with data due to their assumption of a  $^3\text{He}$ - $^3\text{He}$  interaction which is independent of  $^3\text{He}$  concentration. In light of their arguments, Baym’s absorption coefficient cannot be extrapolated to concentrations several orders of magnitude below the data it was developed to explain.

Instead our approach here will be to treat the  $^3\text{He}$  impurities as a very dilute, weakly interacting classical gas. This approach will be valid for temperatures much greater than the Fermi temperature ( $T_F$ ), which for  $^3\text{He}$  atoms at natural isotopic impurity ( $x = 10^{-7}$ ) is  $T_F \approx 0.06$  mK. For isotopically purified samples of helium,  $T_F$  decreases as  $(n_3)^{2/3}$ , where  $n_3$  is the number of  $^3\text{He}$  atoms per unit volume. Therefore in the millikelvin temperature range addressed in this paper, the assumption of  $T \gg T_F$  will always be valid.

The coefficient of absorption for a plane wave traveling in a gas was calculated by Stokes

(viscous contribution) and Kirchoff (thermal conductivity contribution). The combined result is given in standard acoustics texts [106] as  $\alpha = dQ/2I$  where  $I = \rho c |\mu_0|^2$  is the intensity of the wave and  $dQ$  is the energy lost per unit volume per unit time:

$$dQ = \left[ \left( \eta_B + \frac{4}{3}\eta \right) + (\gamma - 1) \frac{\kappa}{c_P} \right] |k\mu_0|^2. \quad (4.3)$$

Here  $\eta_B$  is the coefficient of bulk viscosity,  $\eta$  is the coefficient of shear viscosity,  $\gamma = c_P/c_V$  is the ratio of specific heats ( $\gamma = 5/3$  for a monatomic gas),  $k = \omega/c = 2\pi/\lambda$  is the wave vector,  $\kappa$  is the thermal conductivity, and  $\mu_0$  is the RMS amplitude of the wave. The first two terms (including  $\eta_B$  and  $\eta$ ) represent the viscous loss, while the third term represents the thermal loss. At low temperatures ( $T < 100$  mK) where the  $^3\text{He}$  impurity dominates the normal fluid component of  $^4\text{He}$ , one may ignore the viscous and thermal losses from  $^4\text{He}$ . Since the wave energy will be carried predominantly in the  $^4\text{He}$  we make the simplification that the acoustic intensity,  $I$ , uses only  $^4\text{He}$  parameters. One can make the additional simplification that  $\eta_B = 0$ , which is true for monatomic gases because they have no vibrational or rotational states [106]. Therefore we find for the amplitude attenuation coefficient:

$$\alpha_{^3\text{He}} = \frac{\frac{4}{3}\eta + (\gamma - 1) \frac{\kappa}{c_P}}{2\rho_4 c_4^3} \omega^2, \quad (4.4)$$

where the subscript fours have been added as a reminder to use  $^4\text{He}$  parameters. Based on work by Chapman and Enskog, the viscosity and thermal conductivity of a rarefied gas of hard elastic spheres are given by [107]  $\eta = 0.499l\rho\bar{v}$  and  $\kappa = 2.525\eta c_V$  where  $l = 1/\sqrt{2\pi d^2 n_3}$  is the mean free path and  $\bar{v} = \sqrt{8k_B T/\pi m}$  is the mean molecular velocity,  $d$  is the molecular diameter and  $m$  is the molecular mass. Note that the definition of  $l$  given here is valid only in the viscous flow regime where  $l \gg d$  but much smaller than the smallest container dimension. Substituting for  $\kappa$  we find that the viscous contribution to damping is  $\approx 4/3$  the thermal contribution. Simplification of Eqn. (4.4) leads to:

$$\alpha_{^3\text{He}} \approx \left( \frac{7}{6} \sqrt{\frac{k_B m_3^*}{\pi}} \frac{1}{\sigma} \right) \left( \frac{1}{\rho_4 c_4^3} \right) \left( \sqrt{T} \omega^2 \right), \quad (4.5)$$

where we have introduced the scattering cross section  $\sigma = \pi d^2$  and  $m_3^* = 2.34m_3$  is the effective mass of a  ${}^3\text{He}$  atom at zero concentration [104]. Note that the first term is constant, the second term varies slowly enough to be treated as a constant at temperatures below about 1 K, and the third term shows the dependencies of  $\alpha$ . Because  $\alpha$  is proportional to  $\omega^2$ , thermal and viscous losses become larger at high frequencies, and may limit the  $Q$  of microfabricated acoustic oscillators.

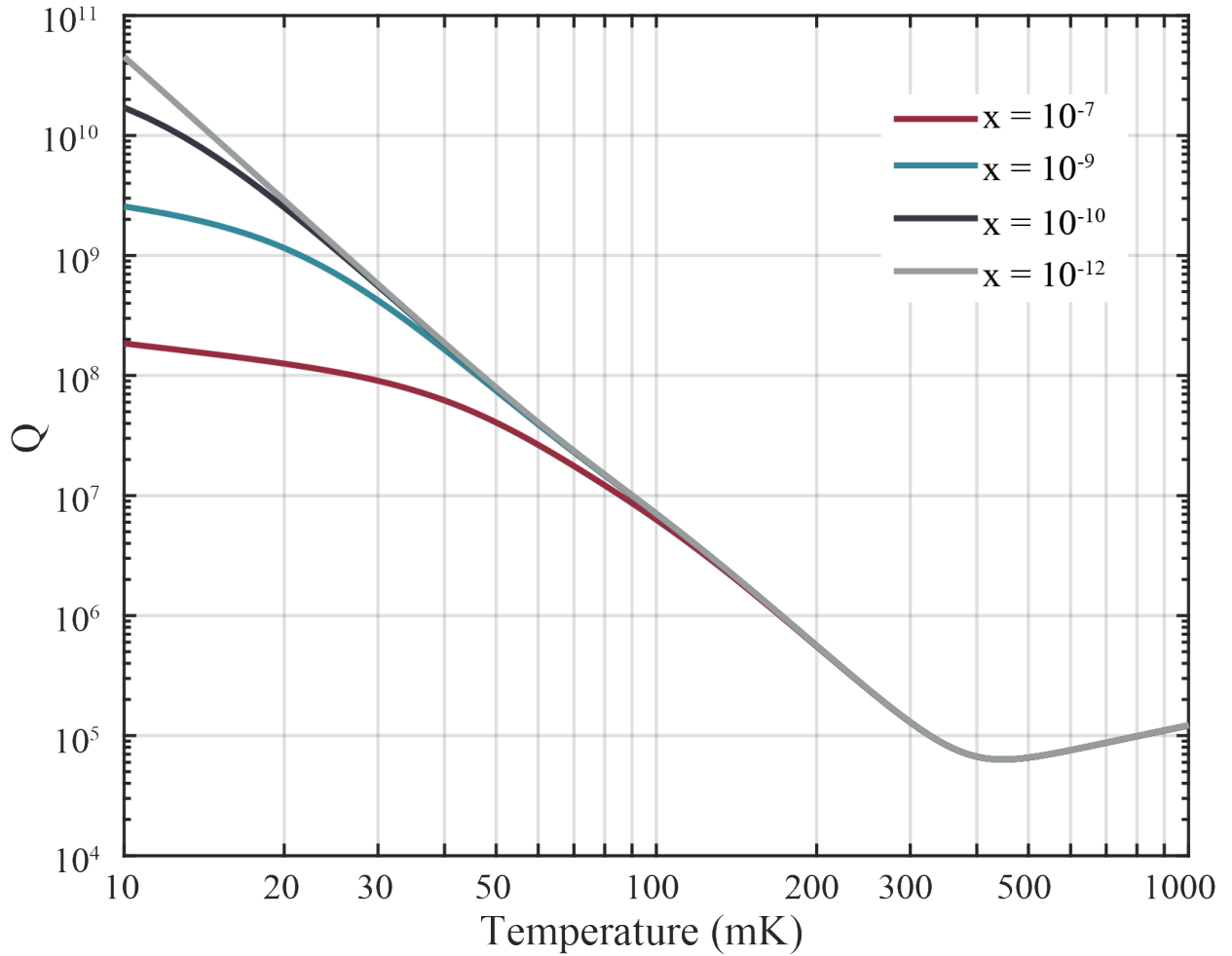


Figure 4.3: shows the expected quality factor versus temperature for an 8.1 kHz mode including effects of both the 3PP and the  ${}^3\text{He}$  impurity for concentrations  $x =: 10^{-7}$  (red),  $10^{-9}$  (blue),  $10^{-10}$  (black), and  $10^{-12}$  (grey), assuming the mean free path of  ${}^3\text{He}$  atoms becomes limited by the cell diameter of 3.6 cm.

### 4.2.1 Lowering Impurity Concentration

For the 8.1 kHz mode of the niobium resonator design shown in Fig. (2.2a), the acoustic loss from the 3PP is approximately equal to the acoustic loss from the  $^3\text{He}$  impurity at 50 mK. For microfabricated resonators of 10 MHz, this transition occurs at 373 mK. To improve the acoustic  $Q$  below these temperatures, the loss from the  $^3\text{He}$  impurity must be lowered. According to Eqn. (4.5), the dissipation from  $^3\text{He}$  is density independent as long as the mean free path is much smaller than the container size. As the density of  $^3\text{He}$  atoms decreases, their mean free path increases as  $1/n_3$ . For instance, when  $^3\text{He}/^4\text{He} = 5 \cdot 10^{-8}$ , the mean free path is already 1 cm, comparable to the dimensions of a 24 kHz resonator.

We modify Eqn. (4.5) by considering what will happen to the mean free path of  $^3\text{He}$  in the limit where classical gas theory gives a result exceeding container size. If reflection from the walls is diffuse, the mean free path will be limited by the container, while if it is specular, it will not. In a study of pure  $^3\text{He}$ , Tholen and Parpia [108] found that the reflection is mostly specular when there are several monolayers of  $^4\text{He}$  coating the container walls. They propose that the monolayers of  $^4\text{He}$  form a superfluid barrier which prevents momentum transfer between  $^3\text{He}$  and the surface.  $^4\text{He}$  preferentially coats the walls of a container because of its larger mass and smaller zero point fluctuations. Based on Tholen and Parpia's results, a reasonable "worst case" scenario would be that only 1 in 100 reflections is diffuse.

Kerscher et al. [109] studied the viscosity of dilute ( $5 \cdot 10^{-5} \leq x \leq 5 \cdot 10^{-7}$ ) solutions of  $^3\text{He}$  in  $^4\text{He}$  by utilizing the Meissner effect to trap a spherical permanent magnet ( $\text{SmCo}_5$ ) in the potential of a superconducting parallel plate capacitor. The drag force is determined by measuring the time constant of the oscillator's decay. They achieve good agreement with their data by assuming the mean free path to be limited to the size of the sphere for the lowest  $^3\text{He}$  ratios. This assumption leads to a viscosity proportional to  $^3\text{He}$  concentration. However, in the case of drag force on a sphere, the difference between specular and diffuse reflection amounts to less than an order of magnitude. Therefore, the results of Kerscher et al. may not indicate that viscosity will become concentration dependent when mean free

path exceeds container size.

If, as a first approximation, one assumes that viscosity becomes concentration dependent when mean free path exceeds container size, the absorption coefficient becomes:

$$\alpha_{3He} = \frac{7}{6} \sqrt{\frac{2k_B m_3^*}{\pi}} \frac{1}{m_4 c_4^3} x L_C \sqrt{T} \omega^2, \quad (4.6)$$

where  $L_C$  is the constant mean free path. The results of the absorption coefficient calculations for the 3PP and  $^3\text{He}$  impurity are shown in Fig. (4.2). We calculate the  $^3\text{He}$  absorption coefficient curves for  $x = ^3\text{He}/^4\text{He}$  concentrations of  $10^{-7}$ ,  $10^{-9}$ ,  $10^{-10}$ , and  $10^{-12}$ . The total quality factor  $Q$  is calculated for the same concentrations using  $Q = \omega/2c_4\alpha$  and  $Q_{\text{total}}^{-1} = Q_{\text{3PP}}^{-1} + Q_{\text{3He}}^{-1}$ . The  $Q$  versus temperature curves are shown in Fig. (4.3).

#### 4.2.2 Isotopic Purification

$^3\text{He}$  exists in sources of  $^4\text{He}$  with a concentration of about 1 in  $10^7$  atoms; however, the unique properites of superfluid  $^4\text{He}$  can be leveraged to isotopically purify the fluid.  $^3\text{He}$  is also a superfluid, but its transition occurs at much lower temperatures:  $T_C \approx 2.5$  mK. Therefore, in a sample of  $^4\text{He}$  below  $T_\lambda$ , the  $^3\text{He}$  atoms move with the normal fluid component.

Superleaks and the heat flush technique can be used to isolate  $^4\text{He}$  from  $^3\text{He}$ . A superleak is a tube through which only superfluid can flow; it can be made with Vycor glass or packed rouge powder. A resistor is placed in front of the superleak as shown in Fig. (4.4), and when the helium bath is heated, the normal component flows away from the heat source carrying impurities such as  $^3\text{He}$  along with it. Because of the counterflow associated with heat transfer in helium II, the superfluid component flows toward the resistor to maintain equal pressures. The superleak does not contribute to the isotopic purification; it only defines the direction in which the normal and superfluid components will flow. Because the superfluid component flows toward the superleak, the helium bath on the opposite side of the superleak will have a lower  $^3\text{He}$  impurity.

Several works have addressed the isotopic purification of  $^4\text{He}$ , and the technique which has

produced the purest product is heat flush. Hendry and McClintock [110] built a continuous flow apparatus preparing purified  ${}^4\text{He}$  gas with  $x_3 < 10^{-11}$  at a rate of 3.3 STP  $\text{m}^3/\text{h}$  (or  $\approx 3.8 \text{ L/h}$  of liquid). Moss et al. [111] discuss a heat flush apparatus of simpler design which produces 0.01 L/h of purity  $x_3 < 10^{-11}$ . A different method of purification, known as differential distillation, utilizes the higher concentration of  ${}^3\text{He}$  in the vapor as compared to the liquid mixture. Tully [112] used differential distillation to achieve  $x_3 \approx 10^{-9}$  in samples ranging from 1 to 25 L.

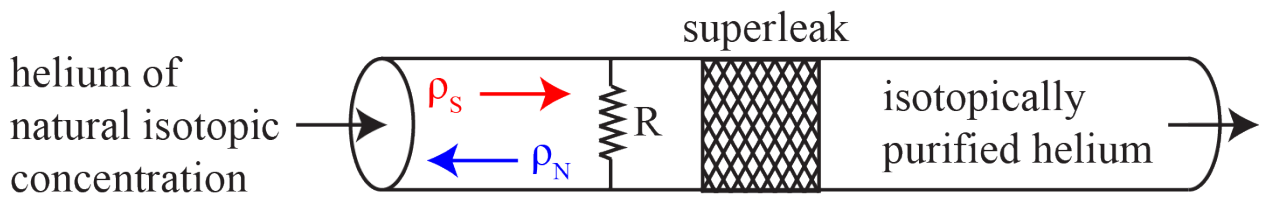


Figure 4.4: A simplified diagram of how helium-4 can be isotopically purified via heat flush. The helium-3 atoms move with the normal fluid component. In the counterflow that is set up when helium II is heated, the normal fluid flows away from the heat source while the superfluid flows toward it. The superleak serves to define the direction with which the normal fluid moves away from the resistor.

### 4.3 Other Acoustic Dissipation Mechanisms in ${}^4\text{He}$

There are a number of mechanisms not considered above. One possibility is the Rayleigh like scattering of phonons from  ${}^3\text{He}$  quasiparticles. Because  ${}^3\text{He}$  quasiparticle velocities are much smaller than the speed of sound in liquid  ${}^4\text{He}$ , quasiparticle-phonon collisions are approximately elastic. The scattering coefficient for this process has been calculated by Baym and Saam [98] (and revised by Baym and Pethick), for phonons of momentum  $q$  (

$q = \hbar\omega/c$ ) as

$$\tau_R(\omega) = \frac{2.45xm_4(\hbar\omega)^4}{8\pi\rho_4c_4^3}, \quad (4.7)$$

where  $x = n_3/n_4$  is the  $^3\text{He}$  molar density and  $m_4$  is the  $^4\text{He}$  mass. The absorption coefficient  $\alpha_R = \tau_R/2c_4 \approx 10^{-175} \cdot x\omega^4$ , so that even in the case of unpurified  $^4\text{He}$  and acoustic modes in the GHz range, this attenuation will be negligible.

We have also not considered what effect vortices in superfluid  $^4\text{He}$  may have on the attenuation. Quantized vortex lines and rings can absorb energy from superflow, an effect clearly observed in flow through small apertures [113]. Although the densities of vortices in thermal equilibrium should be negligible (due to the large energy of the normal core and kinetic energy of the flow) vortices are inevitably produced in macroscopic samples of superfluid as the sample is cooled through the lambda point [114].

## 4.4 Container Loss

While helium itself can be an ultra-low loss medium, difficulties arise in trying to simultaneously isolate superfluid acoustic modes from the environment while also cooling the bulk helium to millikelvin temperatures. One way to avoid losses from coupling to container modes is to levitate a helium droplet. Levitation can be achieved magnetically [115, 116] electrostatically [117], or with a laser trap [118]. Although suspension through electric or magnetic fields avoids direct contact with the fluid, there is contact through the fields which can result in dissipation through the finite losses in the electrical circuit (e.g. in the magnet [119] and electromagnetic environment) in the same way various position detectors, when tightly coupled, can produce damping [120].

Cooling the drop to the lowest temperatures achievable in a dilution fridge may also prove difficult. A levitating drop self cools due to evaporation of vapor, but the heat flow away from the drop is proportional to vapor pressure, which decreases as  $e^{-1/T}$ . The lowest achievable temperature depends on drop size, but large helium clusters ( $\approx 4000$  atoms) have been cooled to a terminal temperature of  $0.37 \pm .05\text{K}$  [121], which is in good agreement with

theoretical predictions [122] and well above the base temperature of a standard dilution refrigerator.

If instead a bulk sample of  $^4\text{He}$  is held in a container, the liquid is cooled by the exchange of high frequency thermal phonons between  $^4\text{He}$  and the container. The full thermal model is described in Section 2.5.1, but we summarize the results here. In the low temperature limit where phonon processes dominate, we expect the cell to cool with a thermal time constant  $\tau = R_K C_{He}$ , where  $R_K$  is the Kapitza resistance and  $C_{He}$  is the total heat capacity of the helium in J/K. For the niobium cavity setup shown in Fig. 2.2, we calculate  $\tau = 10$  seconds.

Although the acoustic coupling between the helium and the container is essential for cooling the sample, it can provide an acoustic loss channel. If the container walls can be approximated as infinitely thick, they will provide a continuum of environmental acoustic modes where the transmitted energy does not return and is lost. For an acoustic plane wave of first sound normally incident on a planar boundary, the energy transmisson coefficient is  $T = 4Z_1Z_2 / (Z_1 + Z_2)^2$ , where  $Z = \rho c$  is the acoustic impedance. For a wave in helium incident on a boundary with copper,  $T \approx 0.004$ , and the quality factor of the acoustic mode in helium will be limited to  $Q \approx 250$ .

This analysis is not appropriate for a container with thin walls (where the wall thickness is less than the wavelength of the frequency of interest in the container) held in vacuum. In this case, standing waves in the container will result in flexure with the internal pressure field. If well designed, the superfluid acoustic mode will not be coincident with any of the container modes, and the container losses can be found from the acoustic loss angle of the material. It is not difficult to choose an acoustic mode well seperated in frequency from the container modes, because the speed of sound in metals is  $\approx 10$  times higher than the speed of sound in  $^4\text{He}$ ; as a result, the mechanical eigenfrequencies tend to be high, e.g. 10 kHz for a hollow cylinder 7 cm long and 6 cm in diameter. Because of work on gravitational wave detectors, loss angles have been measured for a variety of materials at low temperature. For a summary of the best values, see Table 4.1.

Our approach is to treat the entire system (helium and cell), as a harmonic oscillator. We estimate and compare the energy stored in the helium to the energy stored in the metal

cell. The total energy lost per acoustic cycle is then  $E_{LOST} = E_{He}/Q_{He} + E_{Cell}/Q_{Cell}$ . If the system is to be limited by the intrinsic losses in helium, then  $E_{He}/E_{Cell} \cdot Q_{Cell} > Q_{He}$ .

The acoustic energy stored in the helium is given by [63]:

$$E_{He} = \frac{\kappa}{2} \int (P f_{lmn}(r, \theta, z))^2 dV, \quad (4.8)$$

where  $V$  is the cavity volume,  $P$  is the amplitude of the pressure wave, and  $f_{lmn}(r, \theta, z)$  is a spatially dependent function of the mode. We have solved for the acoustic mode profiles in Section 2.4. For a right cylinder see Eqn. (2.23) and for an annulus see Eqn. (2.25).

To calculate the energy stored in finite distortions of the cell, one begins with the elastic energy density in a crystal [70]:

$$E_C = \frac{1}{2} \sum_{\lambda=1}^6 \sum_{\mu=1}^6 C_{\lambda\mu} e_{\lambda} e_{\mu}, \quad (4.9)$$

where  $C_{\lambda\mu}$  are components of the material dependent stiffness matrix and  $e_{\lambda}$  and  $e_{\mu}$  are strain components. While single crystal pieces of copper or niobium are cubic, designs for kHz frequency acoustic modes will employ large pieces of polycrystalline material, which are isotropic. For an isotropic material the energy storage is given by [123]:

$$\begin{aligned} E_C = & \frac{1}{2} (2\mu + \lambda) (e_{xx}^2 + e_{yy}^2 + e_{zz}^2) \\ & + \frac{1}{2} \mu (e_{xy}^2 + e_{yz}^2 + e_{zx}^2) \\ & + \lambda (e_{xx} e_{yy} + e_{xx} e_{zz} + e_{yy} e_{zz}), \end{aligned} \quad (4.10)$$

where  $e_{xx} = \partial u / \partial x$ ,  $e_{yy} = \partial v / \partial y$ ,  $e_{zz} = \partial w / \partial z$ ,  $e_{xy} = \partial u / \partial y + \partial v / \partial x$ ,  $e_{yz} = \partial v / \partial z + \partial w / \partial y$ , and  $e_{zx} = \partial u / \partial z + \partial v / \partial x$ . Here  $u$ ,  $v$ , and  $w$  represent position dependent deformations in the  $\hat{x}$ ,  $\hat{y}$ , and  $\hat{z}$  directions respectively. Finally, the constants  $\mu = Y/2(1+\nu) = G$  and  $\lambda = Y\nu/(1+\nu)(1-2\nu)$  are Lamé parameters, where  $Y$  is the Young's modulus,  $G$  is the shear modulus, and  $\nu$  is Poisson's ratio. For polycrystalline copper at 4 K:  $Y = 1.386 \cdot 10^{11}$  N/m<sup>2</sup>,  $G = 0.517 \cdot 10^{11}$  N/m<sup>2</sup>, and  $\nu = 0.340$  [124]. For polycrystalline niobium at room temperature:  $Y = 1.049 \cdot 10^{11}$  N/m<sup>2</sup>,  $G = 0.375 \cdot 10^{11}$  N/m<sup>2</sup>, and  $\nu = 0.397$  [125].

Note that stiffness constants are not strongly temperature dependent.

Sapphire is an anisotropic crystal with trigonal symmetry belonging to point group  $3\bar{m}$ . For trigonal symmetry the energy density simplifies to [126]:

$$\begin{aligned}
 E_C = & \frac{1}{2}C_{11}(e_{xx}^2 + e_{yy}^2 + \frac{1}{2}e_{xy}^2) + C_{12}(e_{xx}e_{yy} - \frac{1}{4}e_{xy}^2) \\
 & + C_{13}(e_{zz}(e_{xx} + e_{yy})) + C_{33}e_{zz}^2 \\
 & + C_{14}(e_{yz}(e_{xx} - e_{yy}) + e_{zx}e_{xy}) \\
 & + C_{44}(e_{yz}^2 + e_{zx}^2).
 \end{aligned} \tag{4.11}$$

For sapphire at room temperature, the stiffness constants are:  $C_{11} = 4.975$ ,  $C_{12} = 1.627$ , and  $C_{13} = 1.155$ ,  $C_{14} = 0.225$ ,  $C_{33} = 5.033$ , and  $C_{44} = 1.474$  in units of  $10^{11}\text{N/m}^2$  [127].

Material	Quality Factor	Frequency (kHz)	Temperature (K)
Sapphire [128]	$5 \cdot 10^9$	35	4.3
Silicon [129]	$2 \cdot 10^9$	20	3.5
Quartz [130]	$2 \cdot 10^9$	1560	0.018
Niobium [131]	$2.3 \cdot 10^8$	0.7	5
Helium-4	$1.35 \cdot 10^8$	8.1	0.044
Silicon Nitride [132]	$1.27 \cdot 10^8$	242	0.014
Aluminum 5056 [133]	$6.7 \cdot 10^7$	1	0.05
Vanadium [134]	$3.9 \cdot 10^7$	1	0.05
Beryllium Copper [135]	$7.8 \cdot 10^6$	1	0.144
Aluminum 6061 [136]	$7.4 \cdot 10^6$	1	0.05
Fused Silica [137]	$5 \cdot 10^5$	14	0.01
OFHC Copper [135]	$1.1 \cdot 10^5$	1	0.1

Table 4.1: The highest measured mechanical quality factors of several high  $Q$  materials. Also shown are the frequency of the measure mode and the temperature at which the measurement was taken.

To make quantitative estimates of container loss, the helium cells were modeled in COM-SOL (See Fig. (4.5)). The pressure wave is simulated as a sinusoidally time dependent force

applied to the inner walls of the cylinder. The energy density (Eqn. (4.11)) is integrated over the deformed container shape to find the total energy stored in the cell. For the cylindrical design, using the  $l = 0, m = 0, n = 1$  acoustic mode, COMSOL simulations suggest that  $E_{He}/E_{Cell} \approx 10^3$ , which would limit the quality factor of a copper resonator to  $\approx 10^8$ , assuming we can achieve the mechanical  $Q$  listed in Table 4.1. For niobium, the maximum achievable  $Q$  given by acoustic losses in the cell improves to  $10^{11}$ . For the sapphire design, using the first azimuthal mode, we find an expected maximum  $Q \approx 10^{14}$ .

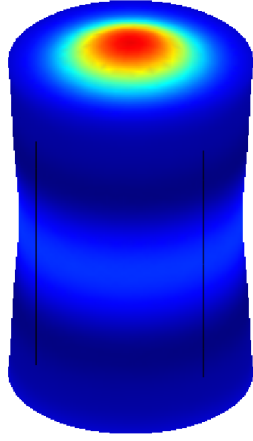


Figure 4.5: COMSOL simulation showing distortions of the niobium cell due to the  $l = 1, m = 0, n = 0$  superfluid acoustic mode with a frequency of 5984 Hz.

For a given cell material, we believe it is not possible to substantially lower the rate of acoustic losses. One can arrive approximately at this conclusion from the equations of motion for a driving force on a plate. Take, for instance, the acoustic mode ( $l = 2, m = 0, n = 0$ ) which will fit one full wavelength in the cylinder, so that the two end caps will experience a driving sinusoidal force. A harmonic driving force of the form  $Fe^{-i\omega t}$  acting transversely on a circular plate leads to a displacement [106]:

$$Y(r) = \frac{F}{T\rho\omega^2} \frac{I_1(\gamma a) (J_0(\gamma r) - J_0(\gamma a)) + J_1(\gamma a) (I_0(\gamma r) - I_0(\gamma a))}{I_1(\gamma a) J_0(\gamma a) + J_1(\gamma a) I_0(\gamma a)}, \quad (4.12)$$

where  $J$  represents Bessel functions of the first kind,  $I$  represents hyperbolic Bessel functions and  $\rho$ ,  $T$ , and  $a$  are the density, thickness, and radius of the plate. Therefore a linear

increase in plate thickness leads to a linear decrease in displacement. From Eqn. (4.11), one finds that energy density is approximately proportional to the deformation squared and therefore inversely proportional to the thickness squared. However, volume is proportional to thickness, so ultimately the energy stored in the plate decreases linearly with increased plate thickness. This result leads one to consider a container design with thick walls, but the walls must remain thin enough that the acoustic resonances of the container are well above the helium mode frequency. These results were validated in our simulations. Modeling different acoustic modes did not change the energy storage substantially. In order to build a resonator with an acoustic quality factor limited by intrinsic losses in helium, one must choose a low loss material for the cell.

Losses from the suspension system must also be considered, but this topic has been studied extensively in gravitational wave literature with several works focusing on the best methods to hold cylindrical objects. Impressively, Braginsky et al. [50] achieved  $Q > 10^9$  in a sapphire cylinder with a wire loop suspension. It is also true that the frequency of the phonons that are responsible for cooling the sample ( $\approx 200$  MHz phonons at 5mK) can be far different from the acoustic mode which one wishes to isolate (kilohertz in the designs in this thesis). One may be able to exploit this large separation of frequencies to allow transmission of high frequencies for cooling and thermal contact, while limiting the coupling at lower frequencies to achieve isolation and low dissipation. An acoustic band-gap structure may be useful for achieving this effect [138, 139]

In addition to the suspension system, one has the additional constraint of filling the cell with liquid  $^4\text{He}$ . Having a continuous fill line from the cell to the fridge will add another channel for energy in the acoustic mode to couple into the environment. This problem may be solvable by pre-filling the cell or by adding a superfluid leak tight valve [140–142] allowing the fill line to be disconnected from the fridge after filling. For the cell to be filled with liquid  $^4\text{He}$  at 4.2 K requires a pressure of  $2.3 \cdot 10^7$  Pa (230 bar) at 77 K which is a pressure of  $9 \cdot 10^7$  Pa (900 bar) at room temperature.

The coaxial cable connections for the microwave mode will also provide an acoustic loss channel, as they are directly connected to the cell. One advantage of using a dielectric

resonator is that these connections will be rigidly attached to the superconducting shielding can instead of the dielectric. It is also possible to capacitively couple the microwaves into the TE<sub>011</sub> resonator with no rigid mechanical connections [143].

# Chapter 5

## Experimental Details and Results

### 5.1 Niobium Cavity Description

The microwave cavity is machined from two pieces of high grade niobium. The cylindrical body is made from RRR grade material purchased from ATI Wah Chang in Albany, Oregon [144]. The material used for the lid is from Fine Metals Corporation in Ashland, Virginia [145] and has a minimum purity specification of 99.8%. The inside of the cavity is a hollow cylinder, 3.556 cm in diameter and 3.955 cm in length. Detailed CAD drawings of the body and the lid are shown in Appendices C.1 and C.2, respectively. The lid is sealed to the body with an indium wire seal.

The lid of the cavity has three ports, one for the helium fill line and two for microwave couplers. In the initial design, the fill line is located at a radius of 1.397 cm and the microwave ports are located at a radius of 1.143 cm, which is equal to  $0.64a$  ( $a$  is the cavity radius), the location of the maximum of the magnetic field. In the second design, used beginning with Run 3, all three ports are located at the position of the radial node (for all acoustic modes with a single radial node), which is a radius of  $0.63a$  or 1.12 cm.

The inner surfaces of both the lid and the body are mechanically polished on a lathe, first with a Scotch Brite abrasive pad to remove machining tool marks, and then with successively finer grades of abrasive paste, to give the inner surface a mirror finish. Following the mechanical polish, 100  $\mu\text{m}$  of the inner cavity surface is chemically removed with a BCP etch. The BCP etch is 25% HF (using the bottle concentration of 50%), 25%  $\text{HNO}_3$  (using

the bottle concentration of 69.5%), and 50%  $\text{HPO}_4$  (using the bottle concentration of 85%). At room temperature, the BCP etch removes  $2.5 \mu\text{m}$  of material per minute. During the etch, the niobium pieces are secured in Teflon holders because Teflon is resistant to the acids. The cavity's larger tapped holes (#4-40) are filled with Teflon screws; however, nylon screws are used in the smaller tapped holes (#2-56) because Teflon is unavailable. Nylon is slowly melted by the BCP etch so one must be careful not to ruin the (#2-56) tapped holes in the lid.

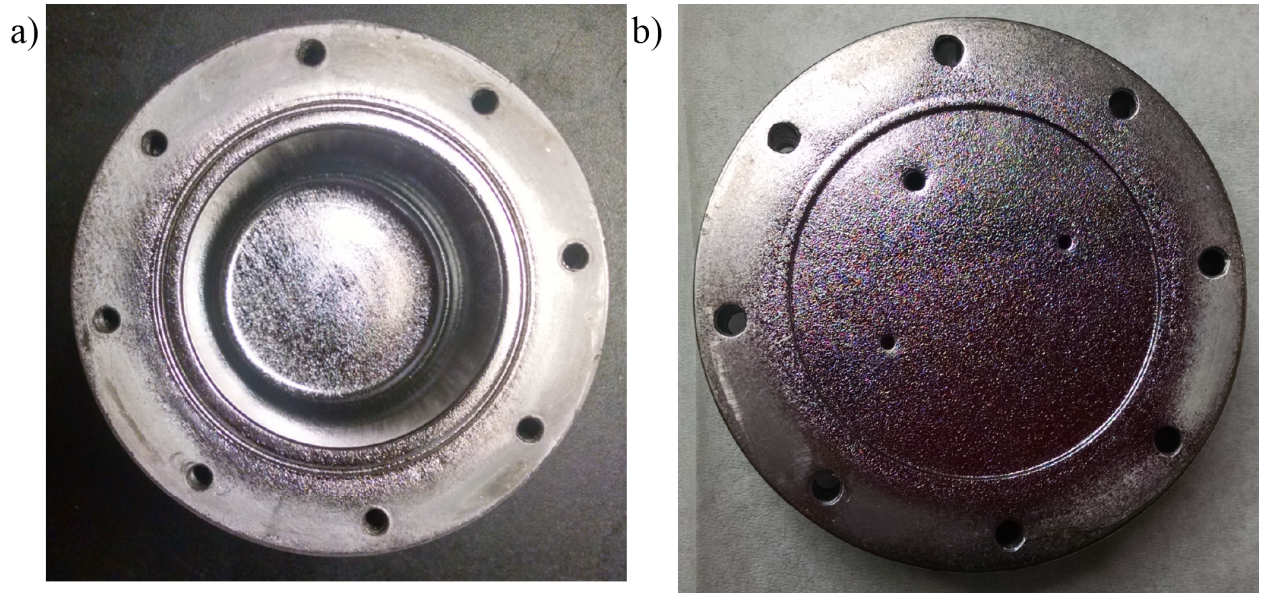


Figure 5.1: Pictures of the niobium microwave cavity after etching, showing a mirror finish: (a) the cell body and (b) the cell lid.

The caps to attach the microwave couplers to the niobium lid are made from OFHC copper and sealed to the lid with indium. The final design of the SMA caps is shown in Appendix C.3. The SMA cap is designed to be used with microwave components purchased from Southwest Microwave [146]: hermetic seals (part number: 290-02G) and 2 hole SMA connectors (part number: 214-522SF). The hermetic seals have a glass (7070) to metal (Kovar) connection which is leak tight from room temperature to cryogenic temperatures because the thermal contractions of the two materials are reasonably well matched. In assembling the microwave ports, the first step was to solder a piece of  $305 \mu\text{m}$  diameter phosphor bronze 5% wire (California Fine Wire Company) to the end of the hermetic seal

launch pin with a high temperature solder (60/40 tin/lead). The wire is covered with a Teflon tube (560  $\mu\text{m}$  ID) to prevent contact between the wire and the SMA cap or niobium lid. Finally, the hermetic seal is soldered to the copper SMA cap with a low temperature solder to produce a seal leak tight to superfluid helium. After assembly is complete, the 305  $\mu\text{m}$  wire is bent to form a coupling loop and its length is adjusted by trial and error to achieve the desired coupling to the  $\text{TE}_{011}$  cavity. The bends in the two coupling loops are made such that the loops are oriented parallel to one another and perpendicular to the magnetic field of the  $\text{TE}_{011}$  mode. It is easiest to assemble the microwave couplers with the cavity lid unattached to the body so that the positioning of the loops can be confirmed and adjusted as necessary. After the microwave couplers are mounted properly, the lid and body of the niobium cell are joined by an indium seal.

The fill line is attached to the cavity with an additional OFHC copper cap, which is also sealed to the lid with indium wire. A stainless steel capillary (125  $\mu\text{m}$  ID) is soldered into the through hole, forming a seal leak tight to superfluids. The small diameter of the capillary limits acoustic losses from the cell to the fridge.

The cell is assembled and the microwave coupling is adjusted at room temperature. Even though a leak tight seal is not required for tests of the microwave coupling loops, it is imperative that indium be used for the connections between the copper SMA mounts and the cell's lid and between the cell's lid and body. The indium seals ensure consistent transmission through the cavity on repeated trials. On initial assembly, it is difficult to perfectly adjust the microwave couplers at 300 K. Ideally the cavity is coupled such that it reaches  $Q \approx Q_{\text{int}}$  at low temperatures with minimal transmission loss. In our case the cavity consistently reaches  $Q_{\text{int}} \approx 100 \cdot 10^6$  at temperatures below two Kelvin, so to be conservative we try to overcouple to achieve  $Q \approx 50 \cdot 10^6$ . From repeated low temperature tests of the cavity, we find that at 300 K the cavity should be undercoupled so that the transmission loss is of order 80 dB.

Once the coupling is approximately right, an initial 300 K leak check is performed. When the room temperature leak check is successful, the cell is attached to a vacuum probe and dipped into a liquid helium bath at 4.2 K. The superconducting temperature of niobium

is  $T_C = 9.3$  K, so a helium bath is sufficient to reach  $T < T_C/2$ . At 4.2 K, the intrinsic microwave  $Q$  is about  $15 - 20 \cdot 10^6$ , and the amount of under or over coupling is more clear. If the one K pot is used to achieve  $T < 2$  K,  $Q_{int}$  will exceed  $100 \cdot 10^6$ , and the  $Q$  should be limited by our microwave couplers. Once the microwave measurements are finished, a 4 K leak check is performed by pressurizing the cavity with helium while the leak detector is attached to the probe vacuum space.

After warming up from the initial cool down, the cavity often shrinks a small amount, so the mode frequencies are slightly lower. This process of adjusting the microwave couplers and leak checking is repeated until the coupling is satisfactory and the leak checks are negative; at this point, the cell can be mounted to the dilution refrigerator.

### 5.1.1 Niobium Cavity Results

Following the procedure outlined above, we assembled the niobium cavity and measured the microwave spectrum at room temperature. Initially stub couplers were used for the microwave connections, but the stubs did not couple to the desired high  $Q$   $TE_{011}$  mode, so we switched to using loop couplers. The microwave spectra measured with each coupling setup are shown in Fig. (5.2); it is evident that the loops couple to a greater number of modes. The frequencies of the microwave modes of a cylindrical cavity are given in Chapter 2 but repeated here for convenience [37]:

$$f_{nml} = \frac{c}{2\pi\sqrt{\mu_R\epsilon_R}} \sqrt{\left(\frac{x'_{nm}}{a}\right)^2 + \left(\frac{l\pi}{L}\right)^2}, \quad (5.1)$$

$$f_{nml} = \frac{c}{2\pi\sqrt{\mu_R\epsilon_R}} \sqrt{\left(\frac{x_{nm}}{a}\right)^2 + \left(\frac{l\pi}{L}\right)^2}, \quad (5.2)$$

for the TE and TM modes, respectively.  $\mu_R$  and  $\epsilon_R$  are the relative permeability and permittivity of the medium inside the cavity,  $a$  and  $L$  are the radius and diameter of the cavity,  $x'_{nm}$  is the mth root of the nth Bessel function of the first kind ( $J'_n(x'_{nm}) = 0$ ), and  $x_{nm}$  is the mth zero of the nth Bessel function of the first kind ( $J_n(x_{nm}) = 0$ ). The frequencies we

measure in our niobium cavity are shown in Table (5.1) and are in close agreement with our expectations from these equations.

As elaborated in Chapter 2, niobium is a type II superconductor and at temperatures  $T < T_C/2$  we expect the microwave losses to be explained by the BCS theory as given in Eqn. (2.20). We measured the superconducting quality factor of the microwave modes on the temperature controlled stage of a 1 K probe. At the probe's lowest temperature, about 1.6 K, the highest  $Q$  mode was the  $TE_{011}$ ; this result is expected because the  $TE_{011}$  mode has no currents between the cylinder body and lid, minimizing the losses from the indium seal. The low temperature frequency of the  $TE_{011}$  is 10.894 GHz, and the highest measured  $Q = 3.6 \cdot 10^8$  is shown in Fig. (5.3a). We measured  $Q$  versus temperature for the  $TE_{011}$  mode by warming the probe in stages and using a vector network analyzer to find the cavity spectral linewidth at each step. The resulting curve is shown in Fig. (5.3b) along with the expected loss from BCS theory. The data fit reasonably well to a total resistance  $R = R_{BCS} + R_0$  where  $R_0 = 2 \mu\Omega$  is the residual resistance calculated from the lowest temperature data point, where BCS losses should be negligible. The deviation from the curve at higher temperatures is probably due to inadequate thermalization time at each temperature step.

Finally we note that indium, which is used to seal the cavity lid to the body, is also a superconductor with  $T_C = 3.4$  K. It is possible that being at temperatures below  $T < T_C/2$  for indium further improves the microwave  $Q$ .

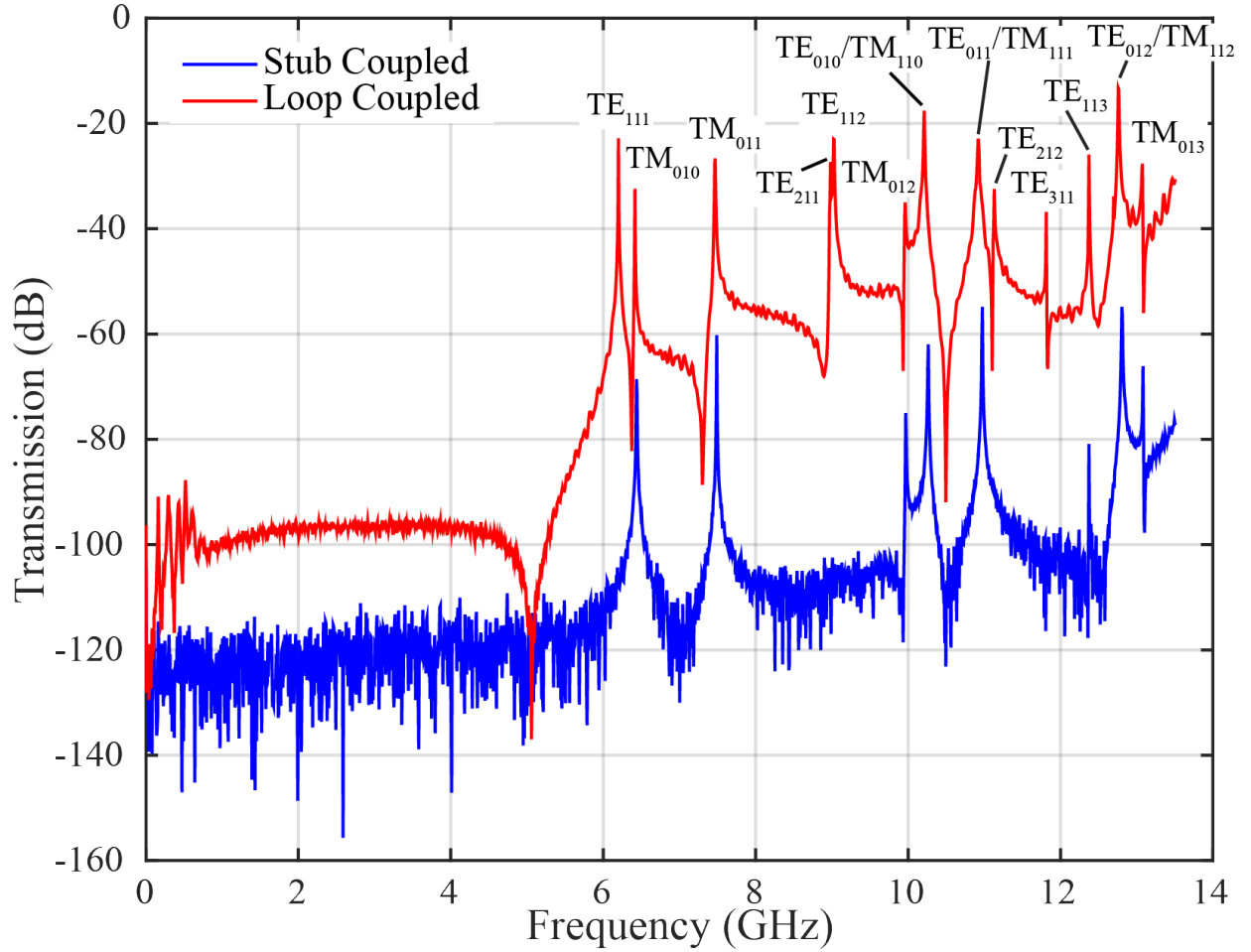


Figure 5.2: Transmission spectrum of the niobium cavity at 300K for stub couplers (blue) and loop couplers (red). In both the loop and stub coupled cavities, the couplers are located on the lid at a radius  $r = 0.64a$  ( $a$  is the cavity radius), where the TE<sub>011</sub> magnetic mode is maximum. Modes are labeled by TE or TM and the mode number (n,m,l). There are three sets of degenerate modes: TE<sub>010</sub>/TM<sub>110</sub>, TE<sub>011</sub>/TM<sub>111</sub> and TE<sub>012</sub>/TM<sub>112</sub>.

Mode Numbers (n,m,l)	Expected Frequency (GHz)	Frequency at 300 K (GHz)	Percent Difference
TE <sub>110</sub>	4.91	-	-
TE <sub>111</sub>	6.19	6.20	0.11
TM <sub>010</sub>	6.42	6.42	0.05
TM <sub>011</sub>	7.44	7.47	0.37
TM <sub>210</sub>	8.15	-	-
TE <sub>211</sub>	8.98	8.98	0.00
TE <sub>112</sub>	9.00	9.03	0.32
TM <sub>012</sub>	9.90	9.96	0.58
TE <sub>010</sub> /TM <sub>110</sub>	10.22	10.21	-0.14
TE <sub>011</sub> /TM <sub>111</sub>	10.90	10.92	0.21
TE <sub>212</sub>	11.10	11.13	0.24
TE <sub>310</sub>	11.21	-	-
TE <sub>311</sub>	11.83	11.81	-0.14
TE <sub>113</sub>	12.33	12.37	0.30
TE <sub>012</sub> /TM <sub>112</sub>	12.70	12.76	0.43
TM <sub>013</sub>	13.01	13.07	0.49

Table 5.1: The TE and TM mode frequencies up to 13.5 GHz for the niobium cavity. The expected frequencies are calculated from Eqns. (5.1) and (5.2) for a cavity with a diameter of 3.556 cm and length of 3.955 cm. The frequencies were measured with a vector network analyzer at 300 K and the spectrum is given by the red line shown in Fig. (5.2). The final column shows the difference between expected and measured frequencies:  $(f_{exp} - f_{meas}) / f_{exp} \cdot 100$ . The only experimentally missing modes are the TE<sub>110</sub>, TE<sub>210</sub>, and TE<sub>310</sub>.

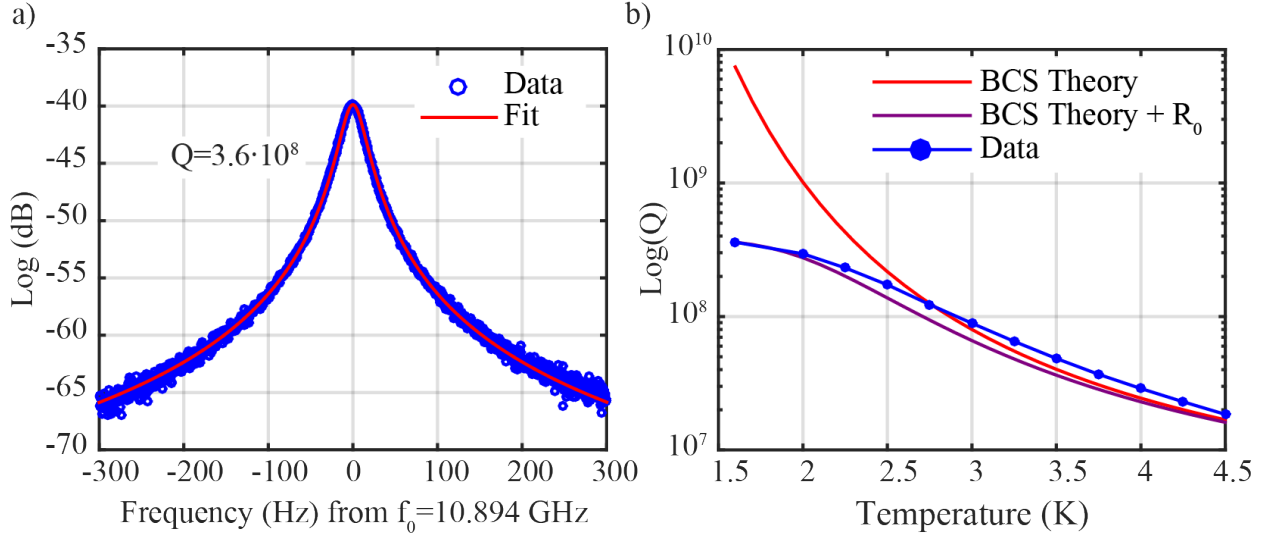


Figure 5.3: (a) S21 measurement of the TE<sub>011</sub> mode at 1.6 K, demonstrating a microwave  $Q$  of  $3.60 \cdot 10^8$  or a cavity linewidth of 30 Hz. (b)  $Q$  of the TE<sub>011</sub> mode versus temperature. Data is represented by blue circles and the connecting line is a guide to the eye only. The red line is the expected quality factor from the BCS losses of Eqn. (2.20). The purple line is the expected quality factor including both the BCS loss and the residual resistance  $R_0$ , where  $R_0$  is calculated from the highest  $Q$  data point and found to be  $2 \mu\Omega$ .

## 5.2 Description of Experimental Setup

As outlined in Chapter 2, our superfluid optomechanical system consists of a hollow niobium cell which is held from the mixing chamber of a dilution refrigerator and filled with liquid  $^4\text{He}$ . A fill line is required to transfer helium from a room temperature cylinder to the cell on the mixing chamber. To this end, we have constructed a room temperature plumbing panel to convey helium from gas cylinders through a liquid nitrogen (LN2) cold trap to the fridge. A picture of this panel is shown in Fig. (5.4). The panel has three gauges for different pressure ranges, one rough compound gauge (30 in Hg vacuum to 1 bar), one convection gauge ( $1.3 \cdot 10^{-4}$  to 1333 mbar), and one ion gauge ( $1.3 \cdot 10^{-9}$  to  $6.7 \cdot 10^{-2}$  mbar). A relief valve protects the ion gauge from exposure to high pressures. The panel has two ports which can be used to evacuate it to vacuum. It is also connected to two helium cylinders, one research grade  $^4\text{He}$  (99.9999% helium) [147] and one sample of isotopically purified helium ( $^3\text{He}$  concentration =  $2 \cdot 10^{-10}$ ) [148]. After the panel is adequately pumped to vacuum, helium from one of these cylinders is flowed through the LN2 cold trap and

into the fridge. The LN2 trap consists of a copper cylinder filled with activated charcoal, immersed in liquid nitrogen. The large surface area of the charcoal is sufficient to freeze most impurities. However, if other gases with low freezing points, such as hydrogen or neon, are present in the helium gas, these will continue through the LN2 trap and freeze on the fill line walls inside the fridge.

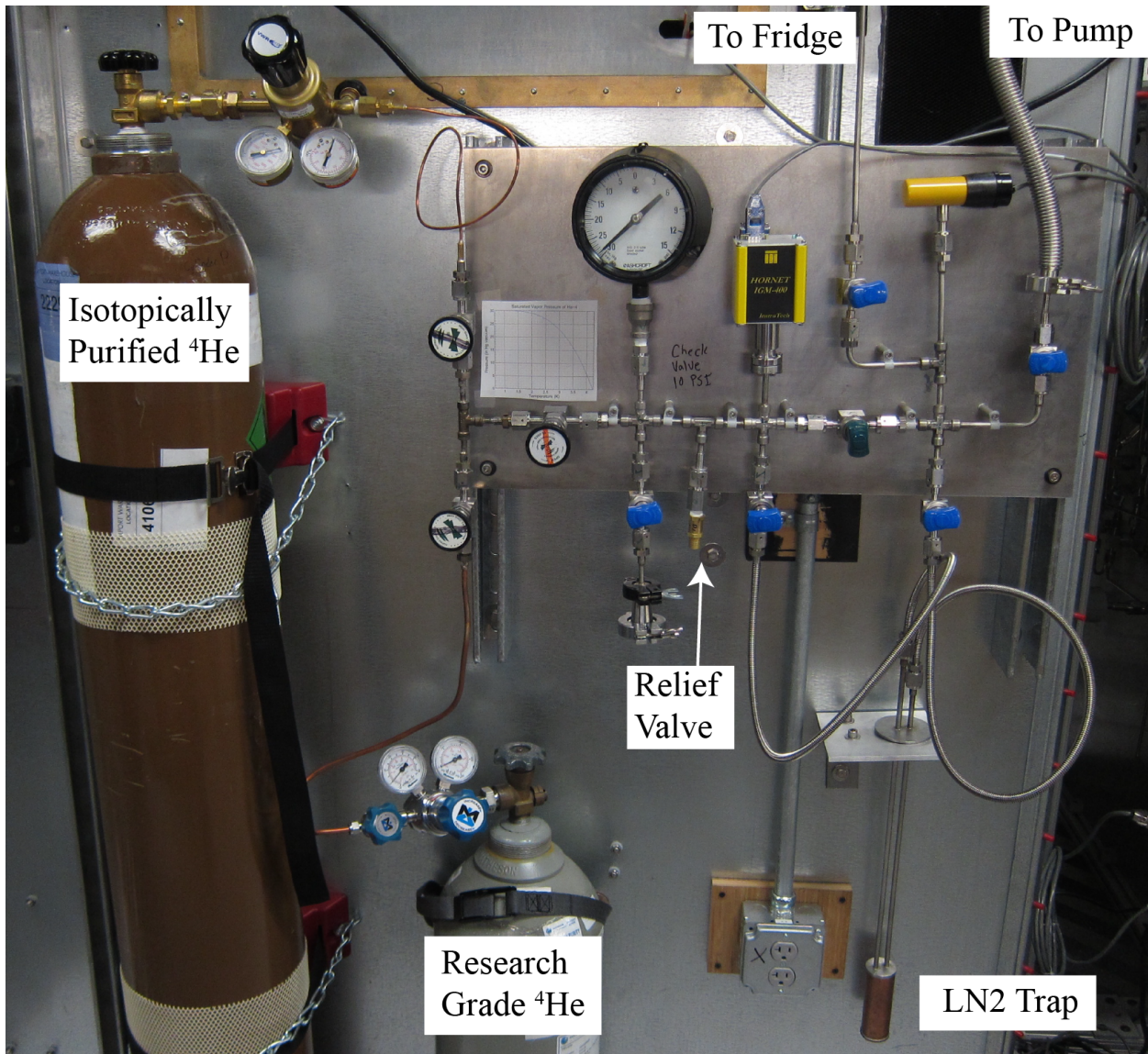


Figure 5.4: The plumping panel used to fill the niobium cavity with helium.

After the helium exits the LN2 trap, it is conducted to the top of the dilution refrigerator, where there is an additional valve on the fill line. Oxford provides experimental lines from

this valve down to the 1 K plate, terminated with an indium seal. From there, we add a custom fill line which is thermally anchored to each stage of the fridge with sintered-silver heat exchangers. This fill line is designed to be long enough and small enough in diameter to limit thermal conductivity through the helium between stages. When the fill line reaches the mixing chamber, it first passes through a cryogenic valve, then a blow off valve, and finally two heat exchangers. Ideally the cryogenic valve is leak tight to superfluid, allowing the helium filled cell and heat exchangers to be thermally isolated from the higher temperature stages. A picture of the experimental setup on the dilution refrigerator is shown in Fig. (5.5).

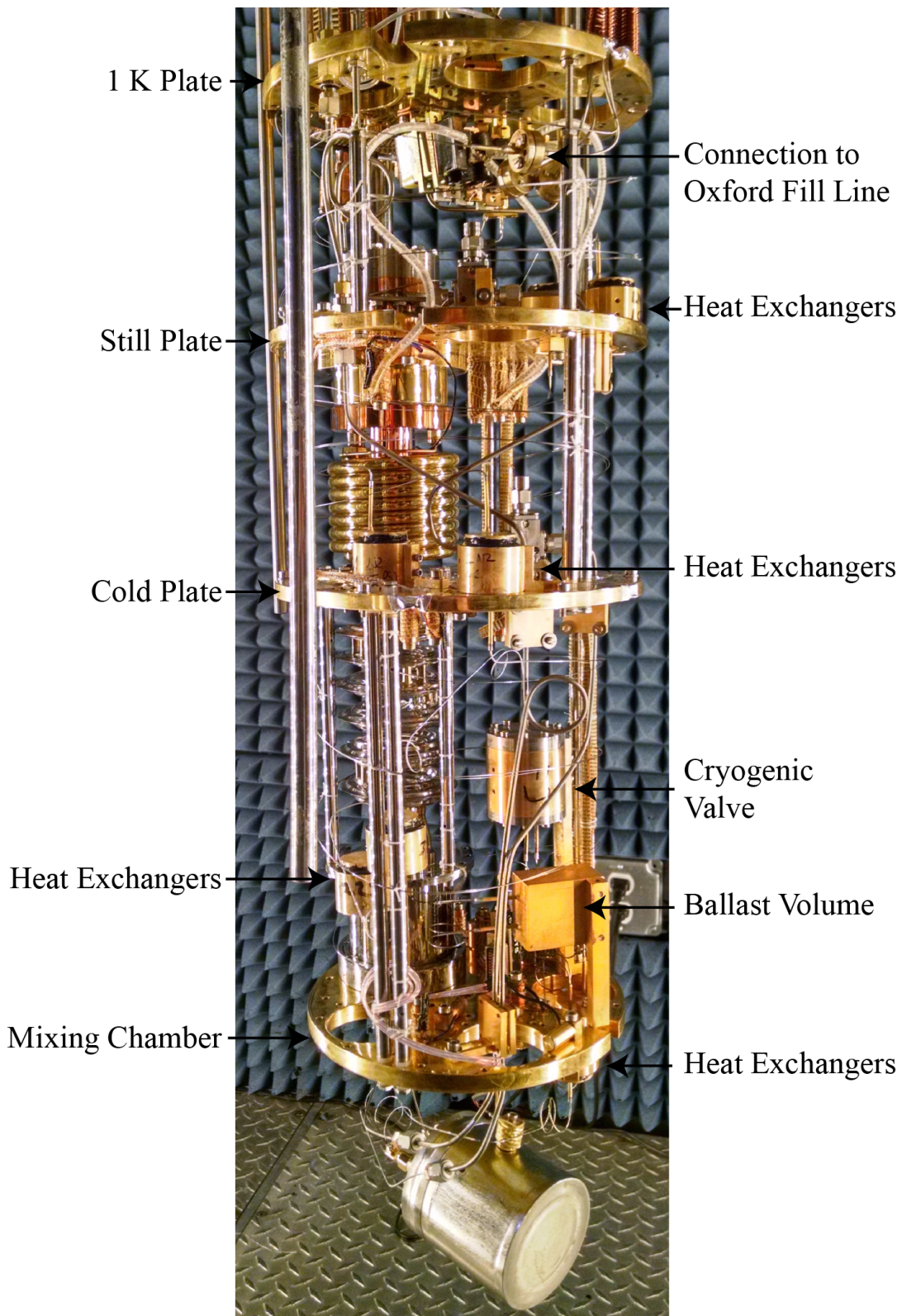


Figure 5.5: The helium fill line from the 1 K plate to the niobium cell. The line is thermally anchored at each stage with sintered-silver heat exchangers.

The sintered-silver heat exchangers used on the fill line are designed to overcome the poor Kapitza boundary conductance between helium and metals (see Eqn. (2.35)) by providing a large surface area for thermal contact. They are custom made following recipes from literature [149–151]. They consist of two gold plated copper pieces: a lid and a body, which is a hollowed out cylinder with a central cylindrical post. Detailed drawings are shown in Appendix E. Silver powder from Inframet Advanced Materials [152] is packed around the central post. Two powder sizes are used, either particles with an average size of 100-500 nm or particles with an average size of 300-1000 nm. The silver powder is first cleaned in acetone, IPA, and methanol and then dried. The desired amount of powder is weighed and then sifted into the heat exchanger body in 5-6 batches. Each batch of powder is compressed into the copper body with a brass mating piece, and the entire assembly is squeezed in a vice. A packing fraction of 50% is used, meaning the total density of the packed powder is 50% of the density of solid silver. When the sinters are packed, each has about 6.6 grams or  $1.2 \text{ cm}^3$  of powder. Following packing, the sinters are heat treated in a helium atmosphere at  $100^\circ\text{C}$  for an hour. The heat treatment fuses the separate silver particles together like a sponge and compresses the silver so that it squeezes onto the central post. After heat treatment, the pieces are cleaned in an IPA bath with sonication to remove any loose powder. Finally a piece of filter paper is placed over top of the sintered silver to prevent loose powder from plugging the fill line. The heat exchanger lid is then fixed to the body with Stycast 2850, and the final assembly is leak checked at room temperature and 77 K. The BET adsorption isotherm technique [153] can be used to measure the final surface area of the sintered-silver powder. We did not measure the surface area, but from similar work by Busch, et. al. [150] and Keith and Ward [151], we estimate it would be about  $0.5 \text{ m}^2/\text{g}$ , giving each of our heat exchangers a total surface area of about  $3.3 \text{ m}^2$ .

The blow off valve, which is located on the mixing chamber, serves two purposes. For one, a blow off is necessary because helium expands upon heating and vaporization, potentially creating a "bomb" which will burst if the fridge warms up unexpectedly. In this case, the blow off is made to burst first, at low pressures, preventing damage to the niobium cell. In our setup, this blow off valve also doubles as a ballast volume. After the cell line is completely

filled, we allow the fridge to cool from 4 K; as the helium cools, it contracts, placing the fill level inside this ballast volume. We make the ballast from a hollowed out piece of copper, with an inner volume of about  $7.4 \text{ cm}^3$ . A copper foil is soldered over the hole, which has a surface area of  $5.4 \text{ cm}^2$ . On multiple trials, this solder joint failed at  $\approx 7 \text{ bar}$ . Ideally this bursting pressure should be lower to prevent potential damage to the niobium cavity.

Also located on the mixing chamber is the cryogenic valve, which requires its own fill line because it is actuated by pressure. We built a second plumbing panel to transfer helium from a cylinder to the fridge for the valve. It is very similar to the panel for filling the cell except that it is made to withstand high pressure because the valve actuation pressures can be above 100 PSI (6.9 bar). The panel has both a vacuum and a high pressure side, isolated from one another with a valve. The vacuum side of the panel has two gauges, which are further protected by a 10 PSI blow off valve: a rough compound gauge (30 in Hg vacuum to 1 bar) and a convection gauge ( $1.3 \cdot 10^{-4}$  to 1333 mbar). These gauges are used to determine if the plumbing panel and valve actuation line have been adequately evacuated to vacuum through the pump out port. The high pressure side of the panel has a gauge which ranges from 0 to 500 PSI (0 to 34.5 bar) and an LN2 cold trap. When in use, research grade helium (99.9999%) [147] is fed through the LN2 trap and toward the fridge. As with the fill line used for the cell, at the top of the fridge there is an additional valve, and inside the fridge the Oxford experimental line is used down to the 1 K plate. From there, the line is composed of stainless steel capillaries anchored at each stage with sintered-silver heat exchangers. On the mixing chamber, the line passes through two heat exchangers before being attached to the actuation port of the valve. All fill line joints are made with solder or with Stycast 2850 so they can withstand high pressure. The heat exchangers on the valve line were leak tested at 77 K with minimum pressures of 150 PSI (10.3 bar) to ensure they would not burst.

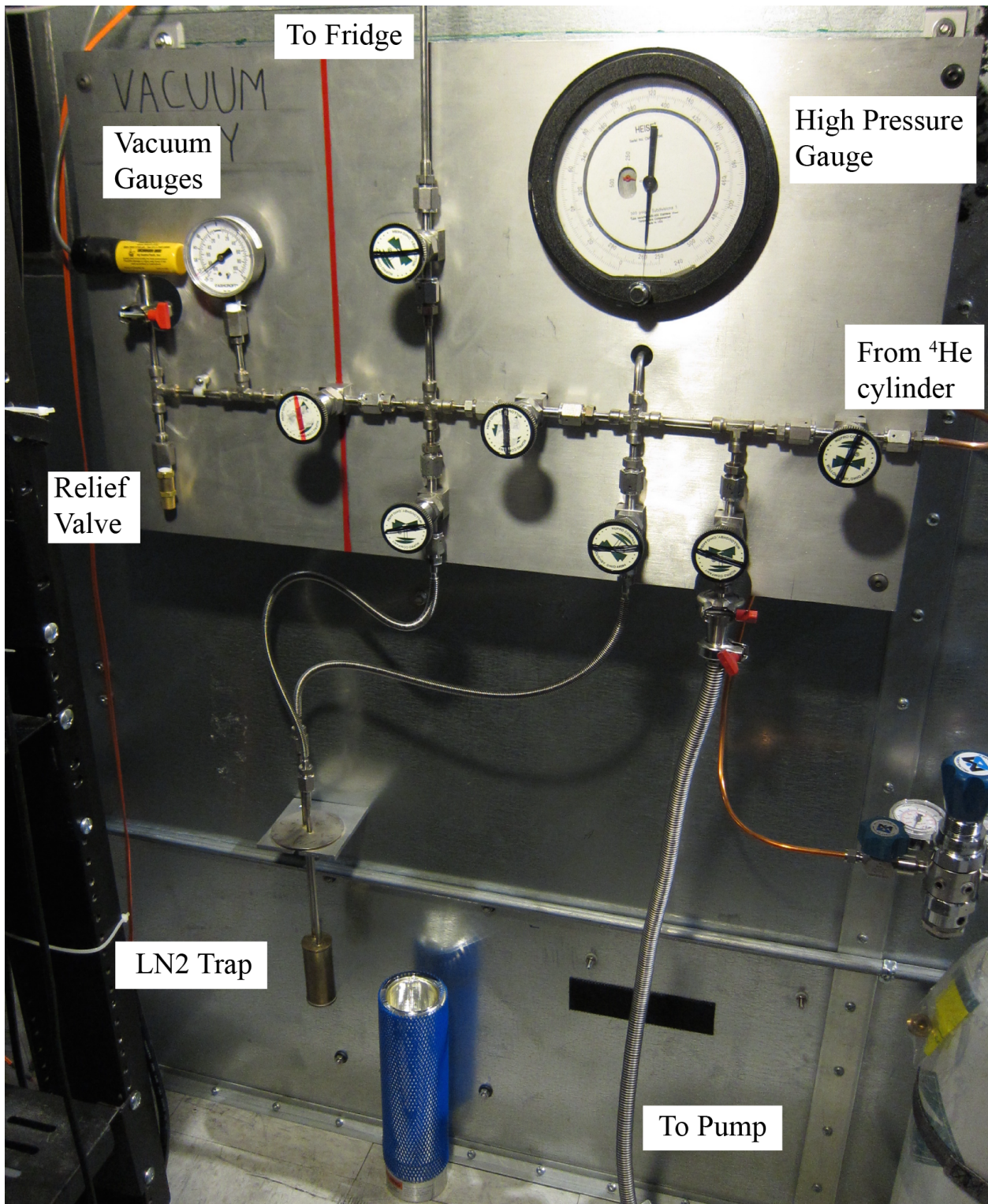


Figure 5.6: The plumbing panel used to actuate the cryogenic valve.

### 5.3 Experimental Run Procedure

Once the niobium cell is prepared and mounted to the dilution refrigerator, the first step in cooling down is to flow dry nitrogen ( $N_2$ ) gas through the fridge fill line. At this point, the fill line is not yet attached to the cell, and one should check that the line is not plugged by inserting the final capillary into a beaker of IPA and looking for bubbles. If a cryogenic valve is being used, the valve line can be checked for plugs in the same manner. If both the valve and cell lines are clear, dry  $N_2$  gas should be flowed through the lines overnight, to ensure that they are free of moisture. Water vapor can be trapped in the large surface areas of the heat exchangers in each line.

After an overnight flush of the fill lines, the final solder joint to the valve actuation port can be made. One can check that the valve is actuating by applying a very small amount of pressure ( $< 15$  PSI or  $< 1$  bar) to the valve and seeing that the bubbling from the cell line slows. However, one must be very careful during this process because if too much pressure is applied, the valve tip will deform and the valve will not seat properly at low temperatures. With a valve known to be leak tight at cryogenic temperatures, it may be best to avoid this step.

The last step in the plumbing is to make the final indium joint to the cell. Before closing the IVC, we ensure that the fill line to the cell is clear by watching the resonance frequency of the cell shift as it is pumped to vacuum and filled with helium. All  $^4\text{He}$  entering the cell is first flowed through an LN2 cold trap to remove impurities.

The frequency shift expected from filling the cell with helium gas can be found from the dielectric constant ( $\epsilon_R$ ) of helium because the cell's frequency varies as  $f \propto 1/\sqrt{\epsilon_R}$  (Eqn. (5.1)). For liquid helium, the dielectric constant is well known and at 4 K,  $\epsilon_R = 1.05$ . From the Clausius Mosotti relation,

$$\frac{\epsilon_R - 1}{\epsilon_R + 2} = \frac{4\pi\alpha_M\rho}{3M}, \quad (5.3)$$

we can relate the dielectric constant at one density to the dielectric constant at a second (primed) density:  $(\epsilon_R - 1) / (\epsilon'_R - 1) \approx \rho/\rho'$ . Helium expands 866 times from liquid at 1 K to gas at 300 K [5], so we find an expected dielectric constant of gaseous helium of

$\epsilon_R \approx 1.000058$ , which would result in a frequency shift from vacuum of about 300 kHz for our  $\text{TE}_{011}$  mode at 10.87 GHz. Fig. (5.7a), which was taken prior to Run 4, shows the frequency shifts as we fill the cell with one bar of helium. The total shift is about 350 kHz, in line with our expectations. Notice, with the high impedance of our fill line, it takes  $\approx 30$  minutes to fill our cell to one bar with  $^4\text{He}$  gas.

Fig. (5.7b) shows how much pumping time is required to again evacuate the cell to vacuum. It was common, as in Fig. (5.7b) that the final frequency of the cell in vacuum would not agree perfectly with the previous vacuum frequency of the cell. There are two potential explanations for this; one is that after a single pump and flush cycle, a smaller fraction of the residual gas left in the cell is air, which is composed mainly of nitrogen and has a higher dielectric constant than helium. This removal of air will result in an overall lower dielectric constant, leaving the cell at a higher frequency. Another possibility is that the temperature of the cell fluctuates over the couple of hours required to complete a pump and flush cycle. For example, at higher temperatures, the gas inside the cell expands, lowering the dielectric constant, and increasing the cell's frequency.

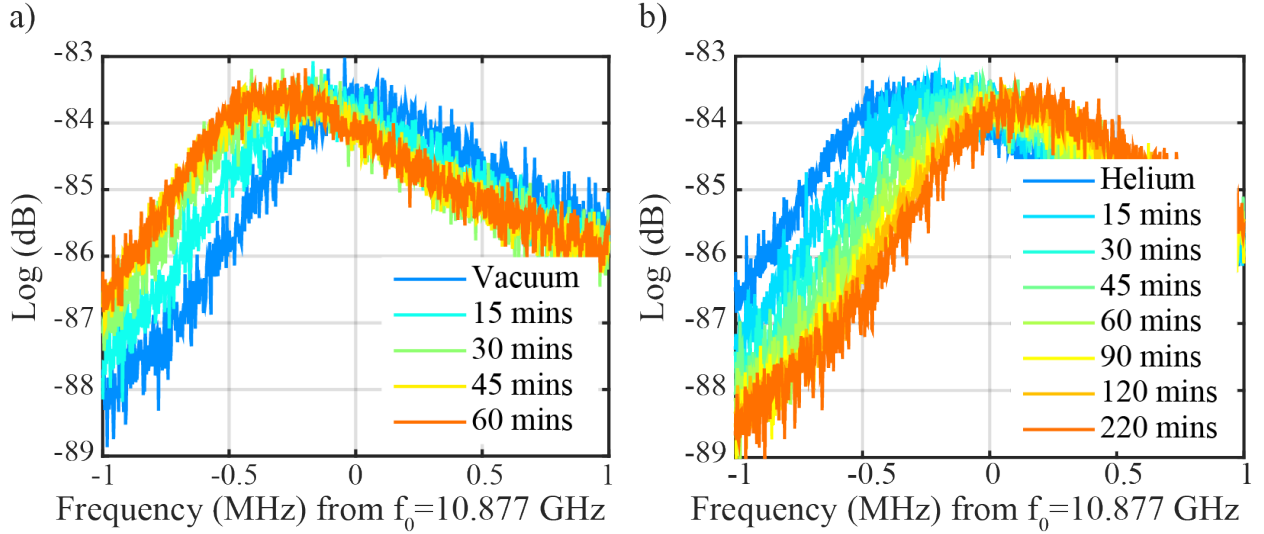


Figure 5.7: From Run 4, January 2015: a) With the cell on the fridge and initially under vacuum, frequency shifts of the  $TE_{011}$  mode while filling the cell with  ${}^4He$  gas. The cell is filled by applying  $\approx 1.2$  bar of pressure from the helium cylinder attached to the plumbing panel. Notice the impedance of the fill line is such that filling requires  $\approx 30$  minutes. b) With the cell on the fridge and initially filled with about one bar of  ${}^4He$  gas, frequency shifts of the cell while evacuating to vacuum. After 90 minutes of pumping, the cell's frequency has returned approximately to the starting vacuum frequency from a). An additional 30 minutes or even 130 minutes of pumping do not appear to shift the frequency any further.

Checking the frequency shifts of the cell also provides a test of the microwave circuit and HEMT amplifier inside the dilution refrigerator. The total transmission loss through the circuit should be consistent with expectations from the measured cable and cavity transmission loss and the gain of the HEMT. Because most of the circuit remains unchanged from run to run, it is helpful to compare the total loss to that measured in previous runs.

Once it is clear that the fill line is unblocked and the microwave circuit is functioning as expected, the IVC is closed and both the cell and IVC are evacuated to vacuum. The cell line is continuously pumped out and flushed with  ${}^4He$  gas for about two days, or 10-12 cycles. Figs. (5.7a) and (5.7b) are used to determine appropriate amounts of time for pumping and flushing the cell. To ensure adequate time is allotted, the cell is filled for 45 minutes and evacuated for about 90 minutes. If a cryogenic valve is used, the valve is filled to  $< 1$  bar and emptied again, all while the cell is filled with helium gas, to ensure that the Torlon needle is not damaged. The valve line is easier to evacuate to a clean vacuum because the total volume of gas is only  $\approx 7$  cm $^3$ , including the volume of the heat exchangers.

During one of these pump and flush cycles, a room temperature leak check is performed on both the cell and the valve. Leak detector background rates on the IVC of  $\approx 10^{-8}$  mbar litre $^{-1}$  s $^{-1}$  are routinely achieved. Assuming no leaks are found in the experimental circuit, a leak check and throughput test of the dilution circuit are also performed.

After the setup is thoroughly tested at 300 K, the fridge is cooled to 77 K (the boiling temperature of liquid nitrogen), and low temperature leak checks of the cell line, the valve actuation line, and the dilution circuit are performed. It is common for the low temperature mode spectrum of the cell to look different from the room temperature spectrum (see Fig. (5.8)). When the TE<sub>011</sub> appears as a dip in the S21 spectrum, it is easier to check that the cell line is not plugged using a different microwave mode. We use the TM<sub>111</sub> mode which is nominally degenerate with the TE<sub>011</sub> and in practice is within 50 MHz in frequency.

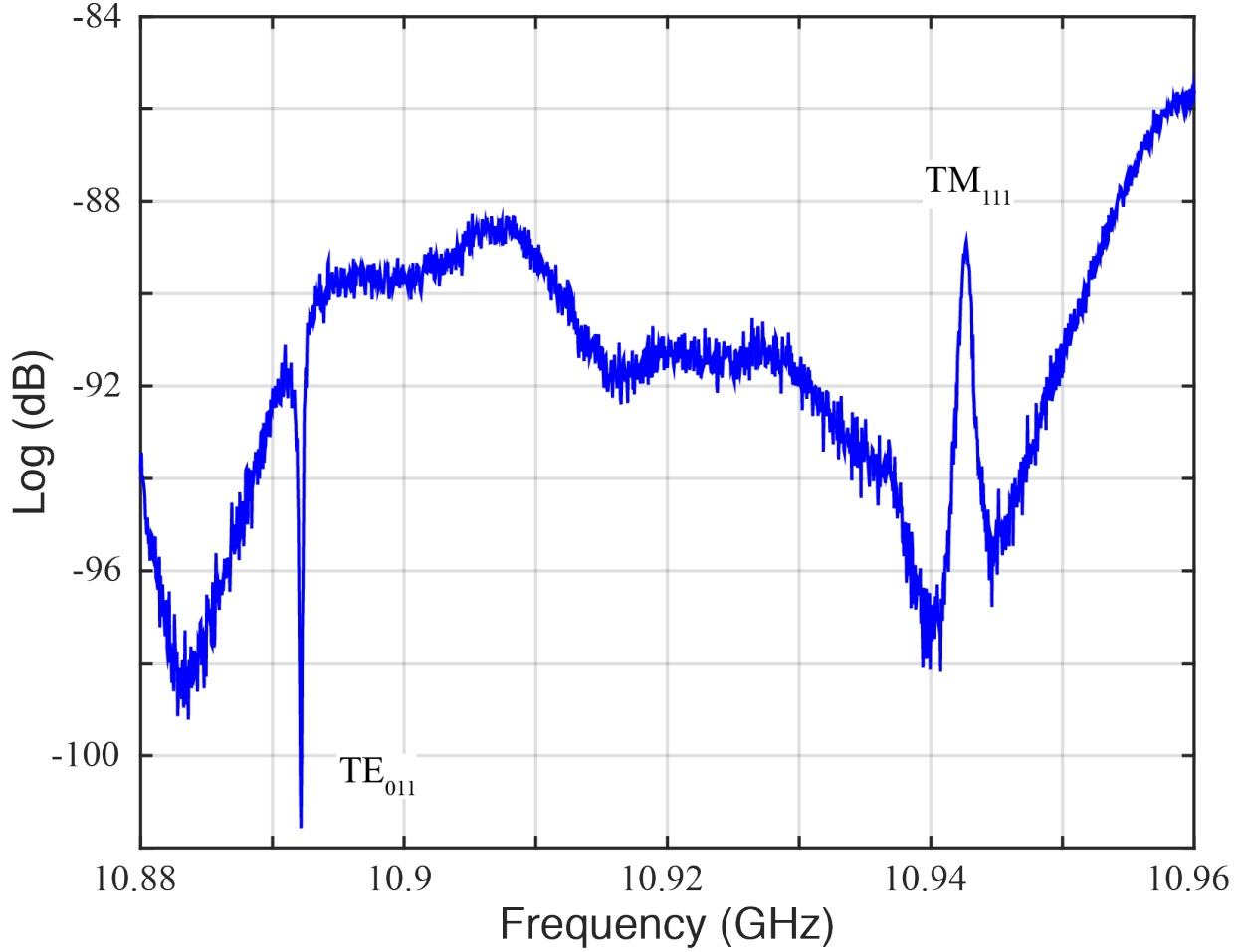


Figure 5.8: From Run 4, January 2015: The  $TE_{011}$  and  $TM_{111}$  modes at 77 K. Notice that the  $TE_{011}$  appears as a dip rather than a peak. Checking the frequency shifts is easier using the  $TM_{111}$  mode in this case.

Typical cell frequency shifts at 77 K are shown in Figs. (5.9a) and (5.9c). The frequency shifts are larger than at room temperature because the helium gas is denser. As above we can estimate the expected frequency shift from:  $(\epsilon_R - 1) / (\epsilon'_R - 1) \approx \rho/\rho'$ . The low temperature (77 K) density of helium is higher than the room temperature (300 K) value by approximately the ratio of the temperatures. At 77 K we find  $\epsilon_R = 1.00022$ . For a mode at 10.94 GHz, we expect a frequency shift of 1.2 MHz for one bar of helium gas or 1.6 MHz for 1.35 bar of helium gas, which was the pressure typically used at the room temperature gas cylinder. In Fig. (5.9a) we see a shift of  $\approx 1.5$  MHz, consistent with these expectations.

If the cryogenic valve is being used, it can safely be closed at 77 K, where the Torlon

needle is stiff and will not be deformed by contact with the stainless steel seat. While the leak detector is attached to the inner vacuum can (IVC) of the dilution refrigerator, the cell is filled with about one bar of helium gas. The valve is then actuated by applying pressurized  $^4\text{He}$  gas in small increments up to 158 PSI (10.9 bar). After the final pressure is reached, we wait for 30 minutes to ensure that the pressure is stable. Fig. (5.9b) shows the result of pumping on the cell fill line while the valve is closed. As expected the frequency remains constant as helium is trapped in the cell. The valve is opened by evacuating the actuation line, and then the cell is evacuated before cool down to 4 K (the boiling temperature of liquid helium).

At 77 K, the most common problem is to find that the cell line is plugged from frozen residual water vapor. The last capillary to the cell is only 125  $\mu\text{m}$  in inner diameter and can be blocked by as little as  $10^{-6} \text{ cm}^3$  of ice. In the case of a blocked capillary, the only solution is to drop the dewar and warm the IVC to 300 K, so that additional pumping and flushing of the cell line can be performed. After one is confident that the fill line is clear of impurities, the process of cooling to 77 K and leak checking can be repeated.

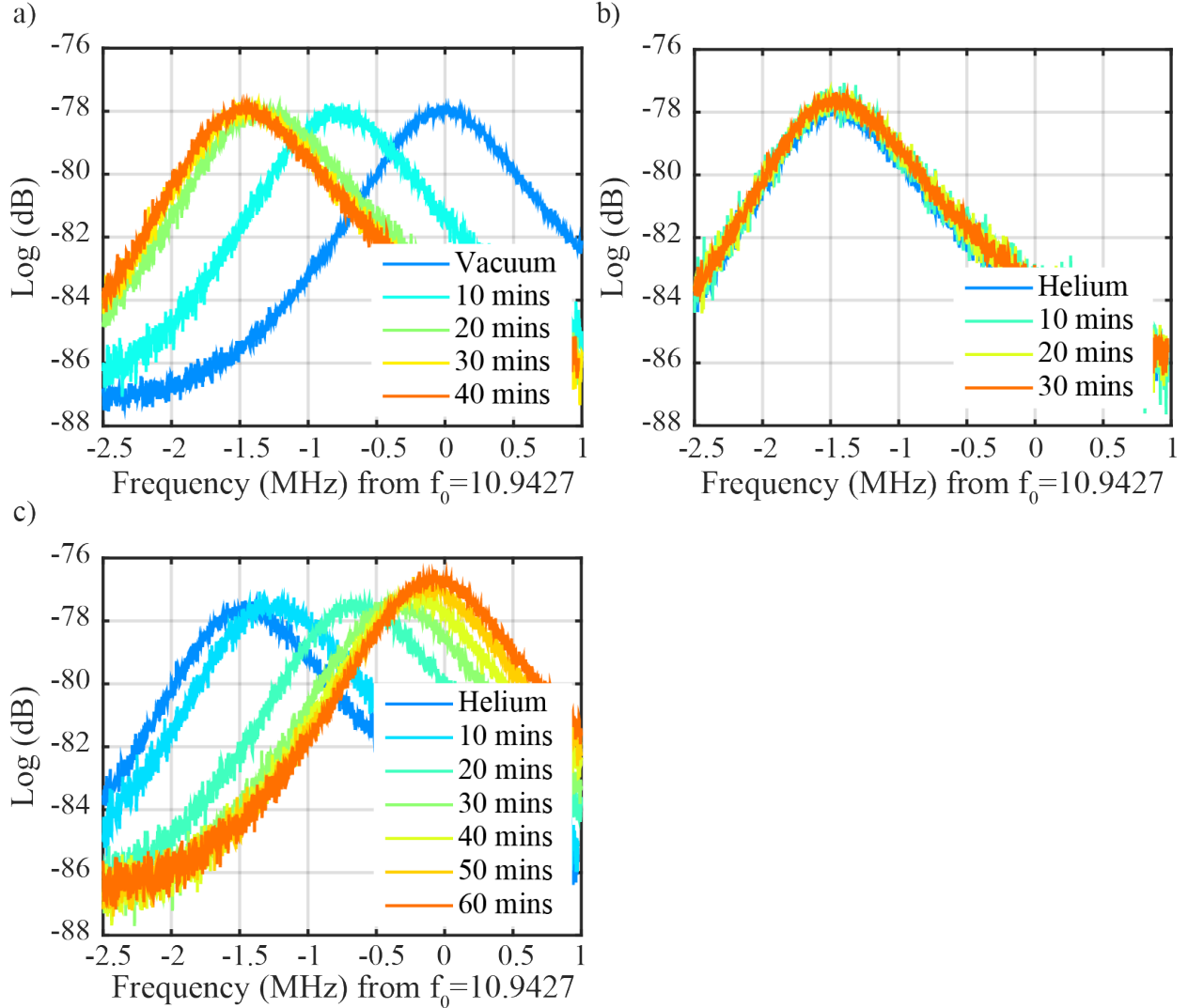


Figure 5.9: From Run 4, January 2015: a) Frequency shifts of the TM<sub>111</sub> mode as the cell is filled with <sup>4</sup>He gas, starting with the cell in vacuum and thermalized to  $\approx 77$  K. Notice that the total frequency shift is greater than at 300 K because helium is denser at lower temperatures. Also note that the frequency shifts more quickly because the conductance of capillaries improves at lower temperatures as the background pressure drops. b) Pumping on the cell at 77K with the cryogenic valve closed. The TM<sub>111</sub> mode frequency remains constant as expected if no helium is exiting the cell. c) Pumping on the cell at 77K with the cryogenic valve open. The frequency shifts back to the vacuum value within about an hour.

Once the 77 K leak checks are complete, the fridge is cooled to liquid helium temperatures, 4 K. Final leak checks of the cell, valve and dilution circuit are performed before proceeding with the experiment.

Assuming no leaks, the next step is to run the dilution refrigerator with the cell empty so that the base temperature and cooling power can be checked. With our Oxford Kelvinox

400H, we expect base temperatures  $< 10$  mK and a cooling power of  $400 \mu\text{W}$  at  $100$  mK. Once these numbers are confirmed, most of the mix can be removed to the keg. To provide the cooling power necessary to fill the cell, the fridge is run with only about 20% of the mix, so that it behaves much like a  $1$  K pot. The cell is then filled using the plumbing panel until the pressure at  $300$  K is just over one bar. Below  $T_\lambda$ , helium flows into the cell with the superfluid critical velocity of  $\approx 1$  cm/s for a  $\approx 100 \mu\text{m}$  capillary [11], and the cell fills in under 4 hours.

With a working cryogenic valve, the procedure from here is straightforward. One can heat the fridge to  $T_\lambda = 2.2$  K, where superfluid  $^4\text{He}$  is at its densest, and close the cryogenic valve. The fill line from the mixing chamber up can then be evacuated overnight. After the line is empty, one can circulate the mix and run the fridge to its base temperature. As the helium expands on cooling, it is assured that the cell will be completely full.

If one does not have a cryogenic valve, one can take advantage of the expansion of liquid helium at temperatures above  $T_\lambda$  to achieve a helium level on the mixing chamber. As shown in Fig. (5.10b), the density of helium above the lambda point decreases with increasing temperature. If one fills the cell line to the top of the fridge near the boiling point, then closes the room temperature valve and cools the fridge, the helium inside the line will contract such that the fill level sits in the ballast volume on the mixing chamber. In this way, it is ensured that the cell will be filled but the fill line connecting the mixing chamber to higher temperature stages will be empty, except for superfluid film flow.

In our system, the cell volume is  $39.3 \text{ cm}^3$ , the ballast volume is  $7.4 \text{ cm}^3$  and the total volume of the cell, mixing chamber heat exchangers, and ballast combined is about  $50 \text{ cm}^3$ . The remaining fill line above the mixing chamber has a total volume of  $< 3 \text{ cm}^3$ . If this volume is completely full at a temperature of  $3.50$  K ( $4.10$  K) and then cooled to  $< 1$  K, it will contract by 6% (12%) or about  $3.3 \text{ cm}^3$  ( $6.5 \text{ cm}^3$ ). This contraction will be sufficient to bring the helium in the fill line down into the ballast volume. In practice, this is accomplished by stopping the  $1$  K pot and slowly warming the fridge to  $\approx 4.1$  K, while  $^4\text{He}$  is evacuated from the fill line as necessary to maintain a pressure just above one bar on the plumbing panel. It is important not to increase the temperature beyond  $4.2$  K where helium boils in case

the expansion creates too much pressure and causes a leak in the fill line. While the cell is heated, its temperature can be inferred from its frequency and the pressure on the plumbing panel. If the starting low temperature frequency is 10.593 GHz, the frequency at 4.1 K will be 10.629 GHz. The helium temperature can be confirmed from its vapor pressure, which increases with temperature as shown in Fig. (5.10a). The vapor pressure is measured with a rough vacuum gauge on the cell plumbing panel. Once the desired temperature has been reached, the valve at the top of the fridge is closed. At this point, the 1 K pot is started, the mix condensed, and the fridge is cooled to its base temperature.

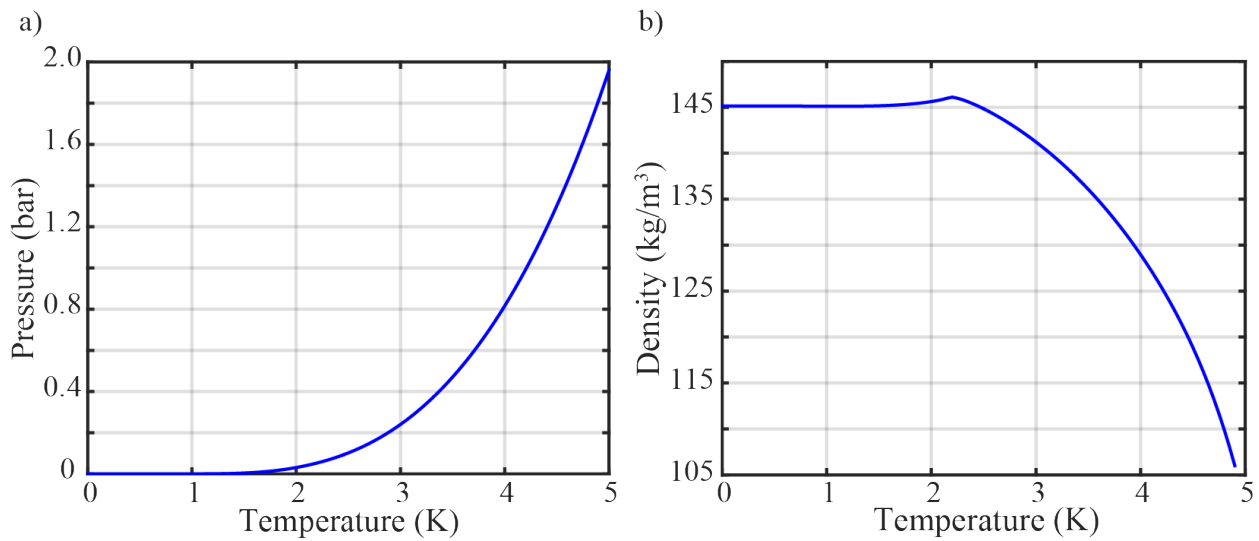


Figure 5.10: a) The vapor pressure of helium versus temperature and b) the density of helium versus temperature.

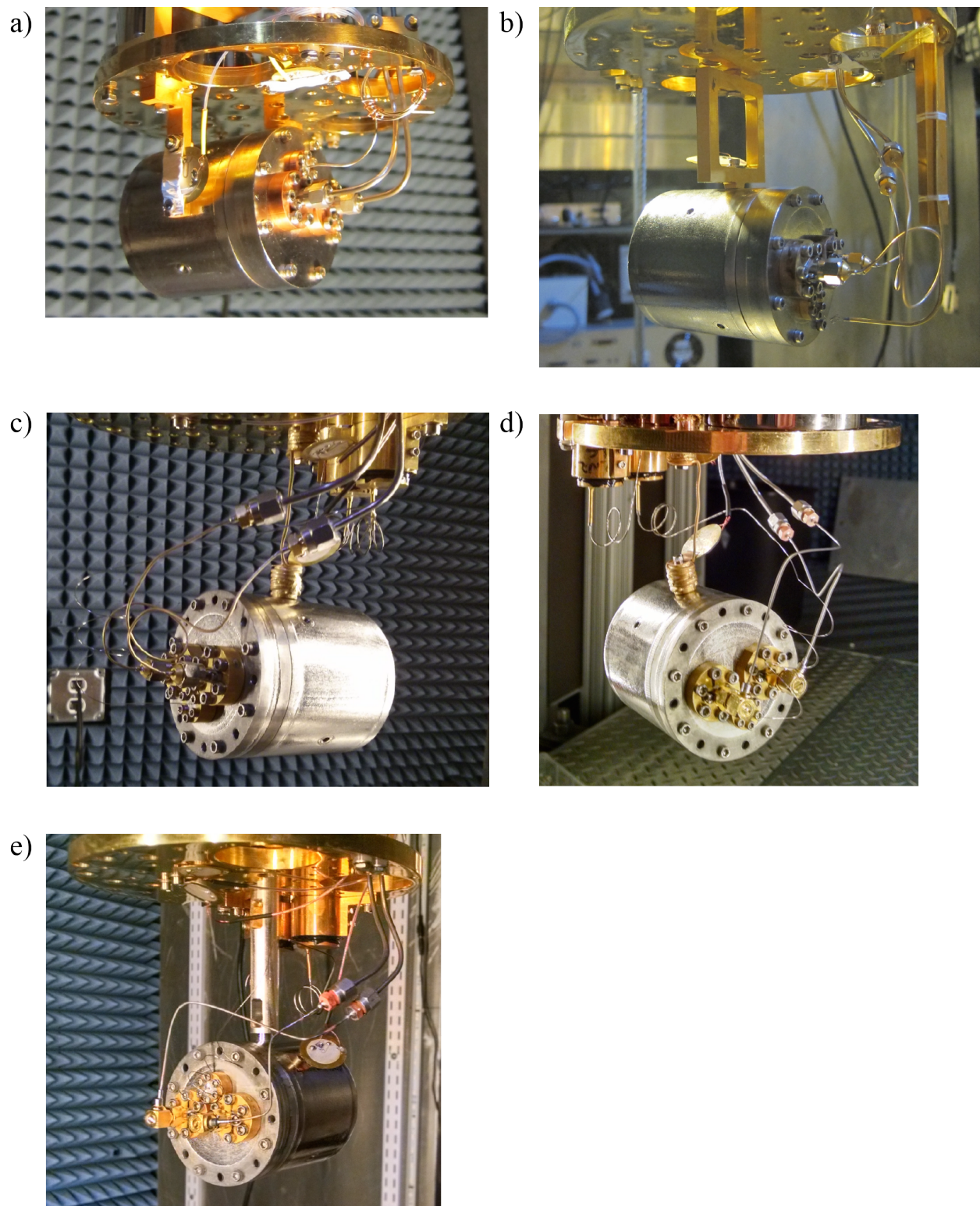


Figure 5.11: Pictures of the cell for each run of the fridge with complete descriptions given in the text: a) Run 1, b) Run 2, c) Run 3, d) Run 4, and e) Run 5.

## 5.4 Measurement Procedure

Once the cell is full and the fridge has reached a stable temperature, we can begin to look for acoustic modes. We know the approximate acoustic mode frequencies from Eqn. (2.24) for a right cylinder, where we use the density ( $\rho_4 = 145 \text{ kg/m}^3$ ) and speed of sound ( $c_4 = 238 \text{ m/s}$ ) in helium-4. We search for the acoustic modes by pumping the cavity with a microwave source, red-detuned from resonance ( $\omega_p = \omega_C - \omega_M$ ) and looking for an up-converted sideband appearing at the cavity frequency [34]. We drive the acoustic motion with a piezoelectric transducer attached near the cavity. We scan the piezo drive frequency near an expected acoustic frequency in increments of  $\approx 10 \text{ Hz}$  until we see a peak appearing, indicating that we are driving the acoustic mode on resonance. The resonances we detect agree within 1% to the expected frequencies (see Table (5.2)). Once a mode is located, we use a ring down measurement to determine its  $Q$ , as shown in Fig. (5.12). While pumping the microwave cavity, we first excite an acoustic mode with the piezo, then turn off the piezo drive and record the free decay, obtaining a curve like Fig. (5.18). We can fit the decaying voltage to an exponential  $V(t) = A_0 \exp(-t/\tau) + V_0$  with three fit parameters:  $A_0$ , which is the amplitude,  $V_0$ , which is an offset voltage that is very close to zero, and  $\tau = 2Q/\omega_M$ , which is the ring down time constant. Knowing the frequency  $\omega_M$ , we can directly solve for  $Q$  from  $\tau$ .

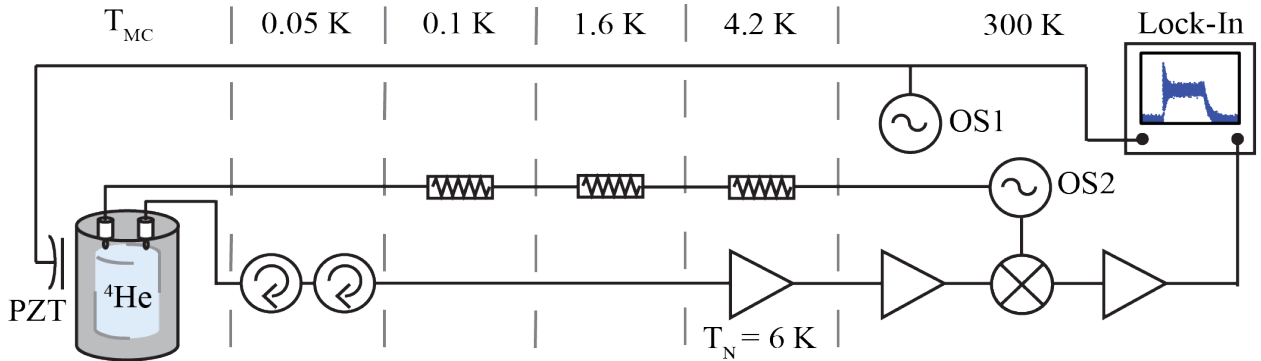


Figure 5.12: A schematic of the microwave measurement circuit. OS2 is a microwave signal generator used to pump the niobium cavity on the red sideband ( $\omega_p = \omega_C - \omega_M$ ). OS1 is an audio frequency generator used to drive the piezoelectric actuator (PZT) which excites the acoustic mode. The upconverted signal from the superfluid acoustic mode is mixed down to an audio signal and measured on a lock-in amplifier.

Mode (l,m,n)	Frequency (Hz)	Degenerate	(Hz, Run 4)	Percent	Highest Q (/10 <sup>6</sup> )
(1,0,0)	2994	no	2990	0.12	0.015
(0,1,0)	3900	yes	3908	-0.20	0.31
(1,1,0)	4917	yes	4998	-1.65	0.04
(2,0,0)	5987	no	5984	0.05	13
(0,2,0)	6470	yes	6461,6469	0.14, 0.01	0.047,0.14
(1,2,0)	7129	yes	7144 ?	-0.21	0.4
(2,1,0)	7146	yes	7144 ?	0.02	0.4
(0,0,1)	8117	no	8115	0.02	135
(1,0,1)	8651	no	8669	-0.21	25.5
(2,2,0)	8815	yes	8803	0.14	0.02
(0,3,0)	8899	yes	8951	-0.58	0.293
(3,0,0)	8981	no	9030	-0.55	0.17
(1,3,0)	9389	yes	-	-	-
(3,1,0)	9791	yes	-	-	-
(2,0,1)	10086	no	10113	-0.27	27.5
(2,3,0)	10726	yes	-	-	-
(3,2,0)	11069	yes	-	-	-
(0,4,0)	11264	yes	-	-	-
(0,1,1)	11294	yes	-	-	-
(1,4,0)	11655	yes	-	-	-
(1,1,1)	11684	yes	-	-	-
(4,0,0)	11975	no	-	-	-
(3,0,1)	12105	no	12167	-0.51	6.9

Table 5.2: A table of the superfluid acoustic modes up to and including the highest frequency mode found experimentally. The first column gives the mode numbers, the second the expected frequency from Eqn. (2.24). The third column indicates whether or not the mode is degenerate. The fourth column is the experimentally measured frequency of the mode from Run 4 at the base temperature of fridge; for most of the degenerate modes, only one peak could be found, and many modes were altogether not detectable. The fifth column is the highest Q measured in any run for the given mode.

## 5.5 Notes on Each Run

### 5.5.1 General Notes

For convenience, notable changes to the setup are summarized in Table (5.4) and pictures illustrating each run are shown in Fig. (5.11).

While the acoustic mode frequencies are in close agreement with Eqn. (2.24), they do vary with temperature (Eqn. (2.41)) and pressure in the fill line. Therefore in each run of the experiment, and even at different times throughout an experimental run, the frequencies of the acoustic modes are slightly different. For ease of reference, the modes are referred to by the frequency which was experimentally measured at the base temperature during Run 4. These frequency values are summarized in Table (5.2).

In each experimental run, the cell was mounted from its center, lengthwise. As shown in Fig. (2.4), of the acoustic modes that we measure experimentally, the 2990, 8669, 9030, and 12167 Hz modes have a longitudinal node at the midline of the cavity. We expected that mounting at a node would decrease suspension loss for these acoustic modes, but often the highest  $Q$  for a given run was measured in a different mode.

The intrinsic loss rate of the  $TE_{011}$  mode is  $\kappa_{int} = 2\pi \cdot 31$  Hz as shown in Fig. (5.3a), but for the following experiments, we overcoupled the cavity such that  $\kappa_{in} = \kappa_{out} \approx 2\pi \cdot 230$  Hz.

Because the experiment is operated without a cryogenic valve, the superfluid film flow up the fill line provides a significant heat leak, which can have two effects: heating the fridge stages above their base temperature values and preventing thermalization of the cell to the mixing chamber. While the size of the the heat leak is difficult to quantify, it will be a function of both the length and diameter of the fill line. If we take as an approximation a capillary completely filled with  $^4\text{He}$ , we can estimate the heat flow using the thermal conductivity of  $^4\text{He}$  below 400 mK:  $\lambda_{He} \approx 2 \cdot 10^5 d T^3$  W/K·m, where  $d$  is the diameter of the capillary in meters [5]. We can estimate the thermal resistance of the fill line as  $R = L/\lambda_{He} A = 4L/\lambda_{He} \pi d^2$ , where  $L$  and  $A$  are the length and cross-sectional area of the capillary. Therefore, at low temperatures we expect  $R = 2L/\pi 10^5 d^3 T^3$ . The heat conducted

through the line can be estimated from  $\dot{Q} = \Delta T / R$ , where  $\Delta T$  is the temperature difference across the section of fill line in question. If we assume the helium in the fill line is thermalized to a temperature midway between the stage temperatures, and use  $d = 0.02$  cm and  $L = 1$  m, we calculate  $\dot{Q} \approx 0.6 \mu\text{W}$  arriving at the cold plate from the still and  $\dot{Q} \approx 4 \text{nW}$  arriving at the mixing chamber from the cold plate. Given the cooling power of our dilution refrigerator (400  $\mu\text{W}$  at 100 mK), we do not expect 4 nW to have any effect on the temperature of the mixing chamber. However, the cold plate operated above base temperature for all of our experimental runs, so we believe the heat leak from the still is significant.

As mentioned above, during our experiments, the fill line capillary is not completely filled with helium-4. Instead the helium fill level is located in a ballast volume on the mixing chamber, and the heat leak arises from superfluid film flow. The heat conduction of a superfluid film is more complicated because the film conducts heat as it flows; the superfluid film can flow with critical velocities up to 0.3 m/s [11], and the heat conduction is not well quantified. For instance, we cannot expect the heating from higher stages to decrease linearly with the length of the fill line, as is the case for phonon or electron heat conduction. We do expect the total conduction to depend on the film's volume, which will depend on the circumference of the capillary  $\pi d$ . However the film thickness is only a weak function of the length as it depends on the gravitational potential,  $mgh$ , where  $g = 9.8 \text{ m/s}^2$  is the gravitational acceleration and  $h$  is the height of the film above the helium bath. For thin films, the thickness is a weak function of height:  $h^{1/3}$  [5]. This height is fixed by the construction of the dilution refrigerator, so we can only decrease the heat load by making the capillaries thinner. Since we could not accurately quantify the heat leak, we adjusted the diameter and the length of the fill line by trial and error. For very thin, long capillaries, the experimental limitation is the ability to remove all residual water vapor from the cell at room temperature.

While the diameter and lengths of the fill line are enumerated in the following text, for ease of comparison, they are summarized in Table (5.3).

		Run 1		Run 2	
		d (μm)	L (m)	d (μm)	L (m)
1 K to still		500	0.15	250	0.3
still to CP		500	0.15	250	0.3
CP to MC		500	0.2	250	0.4
MC to cell		500	0.2	0.13, 0.17, 0.05	250, 900, 125

		Run 3		Run 4		Run 5	
		d (μm)	L (m)	d (μm)	L (m)	d (μm)	L (m)
1 K to still		250	0.30	200	1	200	1
still to CP		250	0.3	200	1	150	1
CP to MC		250	0.5	200	1	200	1
MC to cell		250 to 125	0.2 to 0.02	200 to 125	0.3	125	0.3

Table 5.3: Table describing the approximate diameter (d) in  $\mu\text{m}$  and length (L) in m of the fill line between the 1 K plate, still, cold plate (CP), mixing chamber (MC), and cell for each run of the experiment. Not shown is the capillary connecting the room temperature valve at the top of the fridge to the 1 K stage, which is  $300 \mu\text{m}$  in diameter and  $\approx 1.3 \text{ m}$  in length; this line was provided by Oxford and has remained unaltered. Over time, the capillaries below 1 K have been increased in length and decreased in diameter in order to limit thermal conduction and acoustic losses.

Run	Suspension	Final Microwave Connection	Other Notes
Run 1	Copper L brackets	Nb-Nb coax, 2.2 mm OD	-
Run 2	Copper square	BeCu-BeCu coax, 0.9 mm OD	-
Run 3	Copper wire	BeCu-BeCu coax, 0.9 mm OD	Sintered-silver heat exchangers, New cell lid
Run 4	Copper wire	NbTi-NbTi coax, 0.9 mm OD	Fixed continuous heat exchanger
Run 5	Silver rod	NbTi-NbTi coax, 0.9 mm OD	-

Table 5.4: Table summarizing the changes in the experimental setup for all fridge runs, including the choice of cavity suspension, the final coaxial cabling to the cell, and other important notes.

## 5.5.2 Run 1

In the initial run of the experiment, the cell was bolted rigidly to the mixing chamber with copper L brackets (drawings shown in Appendix F.1). As pictured in Fig. (5.11a), the brackets were secured to the cell halfway along its length, with one on each side. The midpoint of the cell is a good choice for mounting the suspension system because several acoustic modes have a longitudinal node at this location, including the modes at 2990, 8669, 9030, and 12167 Hz (see Fig. (2.4)). The final microwave connections to the cell were made with  $50\ \Omega$ , niobium-niobium, 2.2 mm diameter semi rigid coax (Coax Co., SC-219/50-Nb-Nb) [154]. The fill line, from the 1 K stage to the mixing chamber, was a continuous piece of 500  $\mu\text{m}$  ID nickel capillary with length approximately equal to the length of the fridge, 0.5 m (see Table (5.3)). The line was secured at each stage by soldering the outside of the capillary into a 0.32 cm thick copper piece which was bolted to fridge. On the mixing chamber the fill line was soldered into the ballast volume. The final connection from the ballast volume to the cell was about 0.2 m long and was made with the same 500  $\mu\text{m}$  ID nickel capillary.

Data from Run 1 is shown in Fig. (5.13). For the higher  $Q$  modes, at temperatures between  $\approx 150$  and 300 mK, we note that the  $Q$  is  $T^4$  dependent, as expected from the three phonon process (see Eqn. (4.2)). However the  $Q$ s saturate around 100 mK and the highest measured  $Q$  is only  $6.9 \cdot 10^6$  in the 12 kHz mode. It is also worth noting that at "base" temperature, the mixing chamber was above 30 mK and the cold plate and still temperatures were 230 mK and 1.04 K, respectively. These temperatures are far above those measured in the fridge installation run, where no experimental cabling or capillaries were present. At base temperature during the installation run, the mixing chamber temperature was 5.5 mK (measured with a Co-60 nuclear orientation thermometer), the cold plate temperature was 52 mK, and the still temperature was 915 mK. The higher temperatures during Run 1 were attributed to the heat load of the helium fill line.

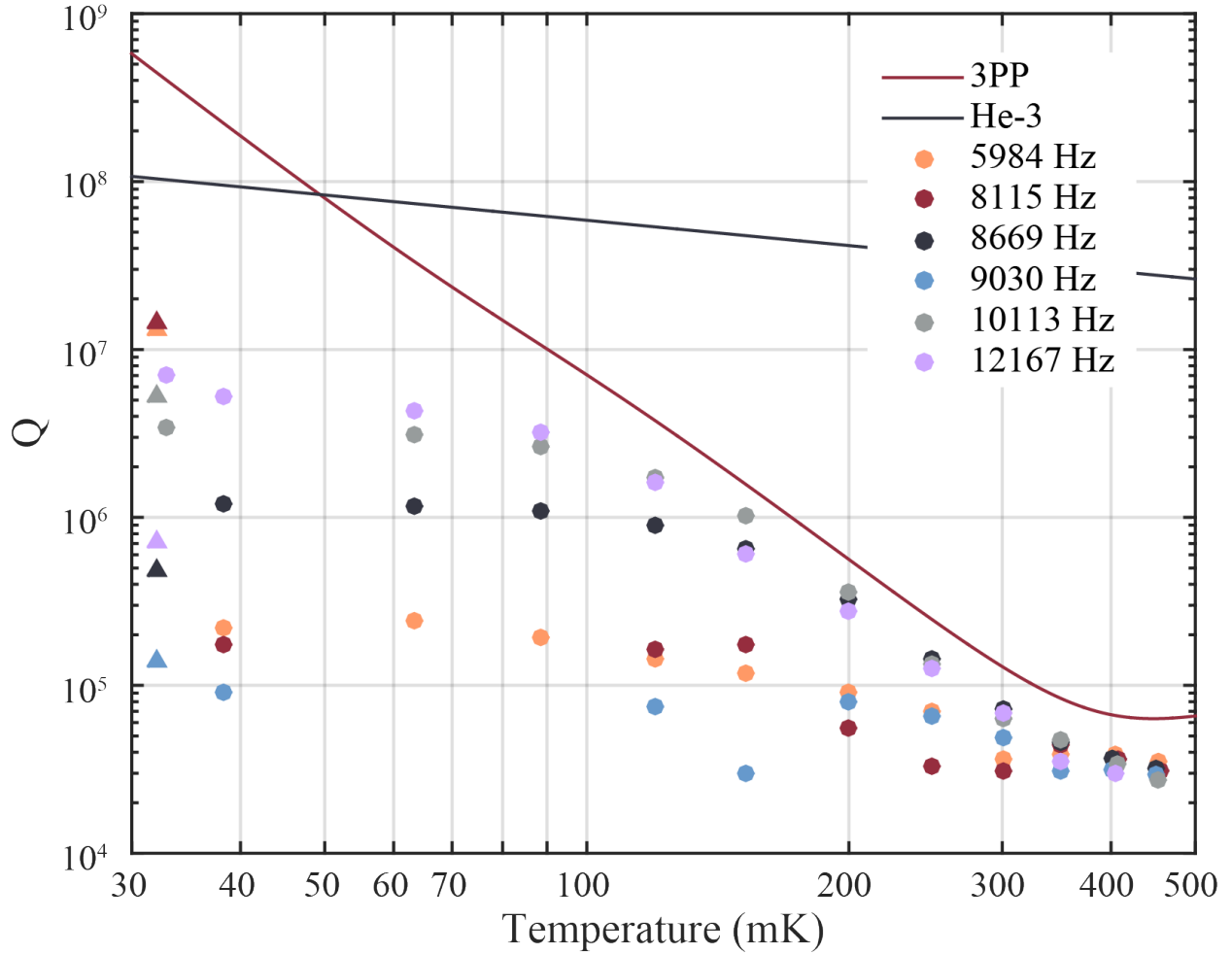


Figure 5.13: Superfluid acoustic  $Q$  versus mixing chamber temperature for the first run (circles) and second run (triangles) of the experiment. Each color denotes a different mode, as shown in the legend. The red line shows the expected loss from the 3PP (Eqn. (4.2)) and the blue line shows the expected loss from the helium-3 impurity (Eqn. (4.5)), assuming  $\omega_M/2\pi = 8115$  Hz.

### 5.5.3 Run 2

In the second run of the experiment, we focused on improving the suspension losses of the acoustic mode. Instead of copper L brackets, the cell was attached to the mixing chamber with a square copper bracket bolted to the center of the niobium cell (see Fig. (5.11b)). A drawing of this bracket is shown in Appendix F.2. In addition, the 2.2 mm diameter niobium coaxial cables used to make the final microwave connection to the cell were replaced with beryllium copper-beryllium copper coaxial cables, with a diameter of 0.9 mm. Beryllium

copper is significantly more flexible than niobium; we thought that the increased flexibility of the cables, coupled with their thinner diameter, would reduce the acoustic losses from the cell to the mixing chamber.

To decrease the heat load from the helium fill line, the nickel capillary was replaced with stainless steel (SS) capillaries of half the diameter (250  $\mu\text{m}$  ID) and twice the length between stages (see Table (5.3)). At each stage the capillaries were again soldered into a copper piece bolted to the dilution refrigerator. The final connection, from the mixing chamber ballast volume to the cell, was made with three sections of capillary: 12 cm of SS with a 250  $\mu\text{m}$  ID, followed by 17 cm of brass with a 900  $\mu\text{m}$  ID, followed by 5 cm of SS with a 125  $\mu\text{m}$  ID. As one can see from the mode profiles (Fig. (2.4)), the superfluid acoustic modes will force helium in and out of the cell through the fill line connection. The final 125  $\mu\text{m}$  ID capillary was used in order to limit acoustic losses from this process.

Data from Run 2 is shown as triangles in Fig. (5.13); because there was no significant improvement in  $Q$ , only low temperature points were taken for each mode. The highest  $Q$  improved by about a factor of 2, to  $14 \cdot 10^6$  in the 10113 Hz mode. In Run 2, the mixing chamber, cold plate, and still reached temperatures of 30, 140, and 955 mK; as in Run 1, these temperatures are above base for the dilution refrigerator and suggest a heat leak.

#### 5.5.4 Run 3

Multiple changes aimed at reducing acoustic loss were made to the setup in Run 3. First, a new niobium cell lid was fabricated, where the helium fill line and microwave couplers were moved to the location of the single radial node in the acoustic modes at 8115, 8669, and 10113 Hz, thereby reducing loss from acoustic radiation into the fill line (see Fig. (2.4)). As with the original cell lid, the new lid was polished and etched following the procedure described in Section 5.1. Microwave  $Q$ s of over  $10^8$  were again measured in the  $\text{TE}_{011}$  mode at  $T < 2$  K.

Additionally, the suspension loss was reduced by replacing the rigid copper mounting block with a copper wire, 0.13 cm in diameter and 6.7 cm long. At each end, the wire

was wrapped around a copper cylinder and brazed in place with silver solder. The copper cylinders were machined with through holes, allowing them to be bolted to the fridge or cell. As with the square bracket, the copper mounting wire was attached to the midpoint of the cell, as shown in Fig. (5.1c). We note here that the use of a wire for mounting also decreases the thermal conductance between the niobium cell and the base plate, making it more difficult to cool the cell (see Section 2.5.1). The thermal resistance of a wire is given by  $R = L/\lambda A$  where  $\lambda$  is the thermal conductivity and  $L$  and  $A$  are the length and cross-sectional area of the wire. For our mounting wire, which was not high purity copper and was given no heat treatment, we expect modest  $RRR$  values; a reasonable estimate is  $RRR \approx 50$ . Therefore we find a low temperature thermal conductivity of  $\lambda = 65 \cdot T$  W/m·K and a resistance of  $R = 770/T$  K/W. From our thermal model in Section 2.5.1, the resistance of the suspension wire will equal the Kapitza resistance ( $R_K$ ) between the helium and the cell at  $T = 228$  mK and the resistance of the suspension wire will equal  $R_K/10$  at 72 mK. At 1 K, the conductance of the suspension wire will be  $1/R = 0.0013$  W/K, meaning that 0.0013 Watts across the wire produces a 1 K temperature drop.

Our final improvement was to add sintered-silver heat exchangers to the fill line at three stages: the still, cold plate, and mixing chamber. The heat exchangers lower the Kapitza boundary resistance between the helium in the fill line and the dilution refrigerator. As discussed in Section 2.5.1, because the acoustic impedance mismatch between helium and metals is high, large surface areas are required to achieve small values of  $R_K$ ; we added  $\approx 6.6$  m<sup>2</sup> of surface area to the base plate, and an additional  $\approx 3.3$  m<sup>2</sup> at 100 mK and 975 mK. By thermally anchoring the fill line at each stage, heat leaks through the helium from higher stages of the fridge are limited. We also increased the thermal resistance of the fill line between stages of the DR by using capillaries of smaller diameter (250  $\mu$ m), and longer length (1 m between each stage).

Fig. (5.15) shows the data from Run 3 as circles. The high temperature data points were extended from 450 mK to 1000 mK showing a turn around in dissipation for both the 8115 and 10113 Hz modes. At temperatures above 1 K, the  $Q$  was not measured because the acoustic modes became too difficult to find. At low temperatures, where the arctan

functions of Eqn. (4.2) simplify to a factor of  $\pi/2$ , we see the expected frequency independent  $Q$ , increasing as  $1/T^4$ . In this regime  $\omega\tau > 1$ , and the absorption is analogous to the Landau-Rumer regime in solids [87, 88]. Here  $\omega$  is the acoustic mode frequency and  $\tau = 1/(0.9 \cdot 10^7 T^5)$  is the thermal phonon lifetime.

As temperature increases, the thermal phonon lifetime decreases and  $\omega\tau$  will eventually pass through one. For the 8115 Hz and 10113 Hz modes, the temperature where  $\omega\tau = 1$  is 355 or 371 mK, respectively. At this temperature we may expect an increase in dissipation due to the resonance with the acoustic mode frequency. From our data, we see a clear dip in  $Q$  at  $\approx 600$  mK; this is within a factor of two of our expectations. Considering the phonon-phonon collisions only, as in Eqn. (4.2), we expect a turn around in dissipation after  $\omega\tau$  crosses one. In Fig. (5.15) we see the dissipation in the 8115 and 10113 Hz modes starts to decrease above 600 mK. In this high temperature limit,  $\omega\tau < 1$ , and absorption is in the Akheiser regime [88, 90]. However, we note that Eqn. (4.2) is derived assuming phonons are the only relevant excitation. The roton population increases exponentially with temperature, and at about 570 mK, the density of rotons is equal to the density of phonons. Once the roton population becomes relevant, roton-phonon and roton-roton collisions also contribute to the dissipation and we no longer expect Eqn. (4.2) to be valid.

During Run 3, we noticed an interesting effect at the higher temperature data points: the piezo modified the frequency of the  $TE_{011}$  mode. It became apparent around 450 mK as the amplitude peaks of the ring down measurements decreased over the data set, and the effect was more pronounced as temperature increased. Looking at the frequency of the  $TE_{011}$  mode showed that the piezo was responsible for driving the frequency shift; see data from 550 mK in Fig. (5.14). Before the piezo is turned on, the microwave cavity is stable. After the drive starts ( $3 V_{pp}$  is applied to the piezo), it takes about 50 minutes for the cavity to stabilize to a new frequency, and when the drive is removed, it takes about 55 minutes for the cavity to return to the original frequency. The cause of this effect is not clear, but a higher frequency indicates an effectively smaller cavity or a lower density of helium in the cell. We note that, at higher temperatures, the density of helium changes more quickly with temperature, and a larger amplitude drive is required on the piezo because of the lower  $Q$  of

the acoustic mode. At 550 mK, a 1 kHz shift in the microwave cavity frequency is a relative change of about  $10^{-5}\%$  which corresponds to a change in dielectric constant of  $\approx 2 \cdot 10^{-5}\%$  or a change in helium density of  $\approx 4 \cdot 10^{-4}\%$ . This would be consistent with an increase in temperature of about 20 mK. In the future, it would be interesting to measure frequency shift versus piezo power and temperature.

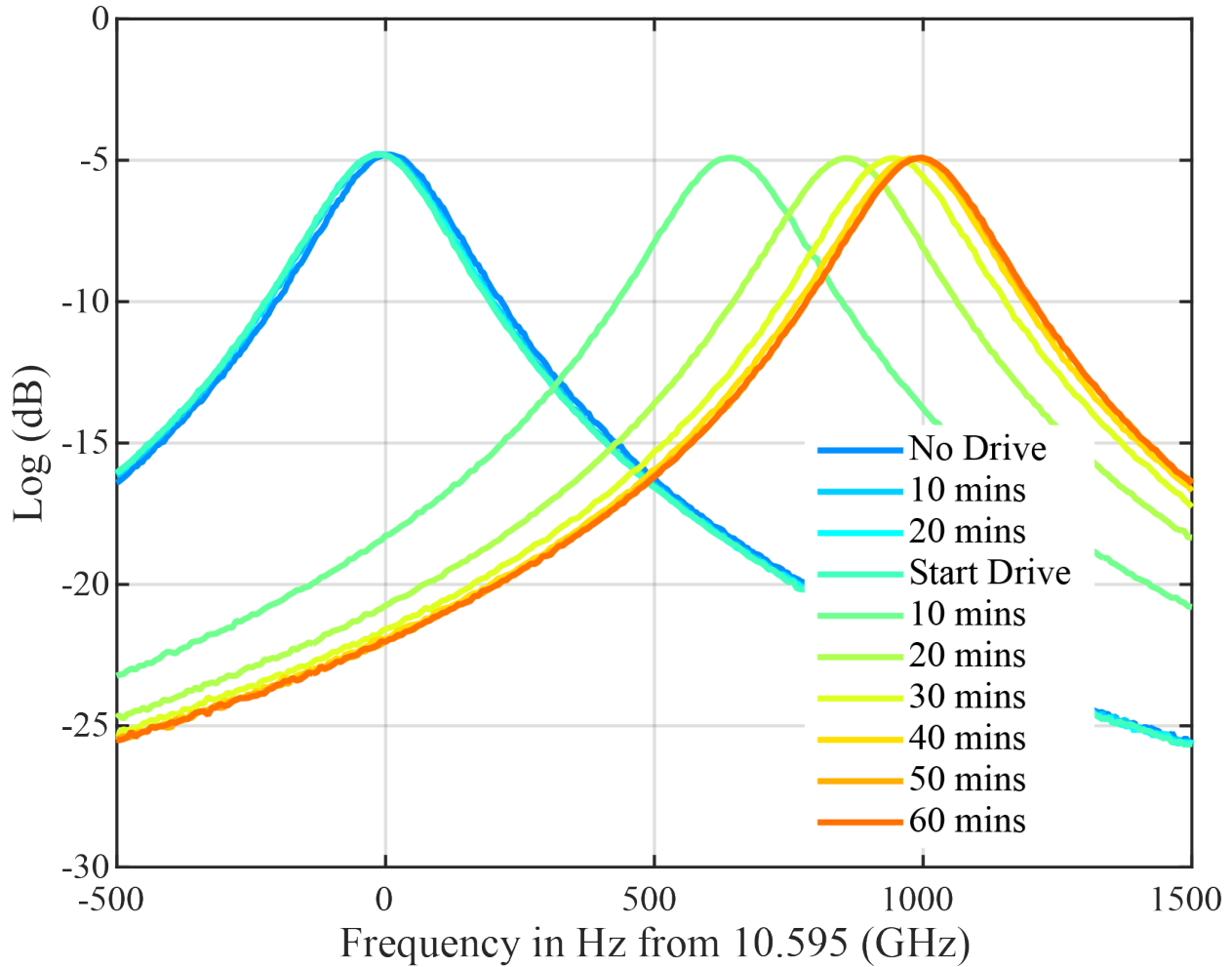


Figure 5.14: The frequency of the  $TE_{011}$  mode at 550 mK before and after the  $3 V_{pp}$  piezo drive for the 10 kHz mode is turned on. Notice that, before the drive, the frequency is stable (the 10 and 20 minute plots are on top of each other), but after the drive is turned on, the mode shifts up in frequency until it reaches a new stable value (the 50 and 60 min plots are on top of each other). The new value is about 1 kHz above the original frequency, or  $\approx 3$  cavity linewidths.

As in Run 2, the highest acoustic  $Q$  improved; this time to  $30 \cdot 10^6$  in the 8115 Hz mode. In all three high  $Q$  modes, the acoustic quality factors between 100 and 300 mK improved to

fit the expected values from the three phonon process (3PP); compare the data in Fig. (5.15) to the data in Fig. (5.13). We attribute this improvement to better thermalization of the superfluid helium to the mixing chamber, probably due to the addition of sintered-silver heat exchangers. Note that the three highest  $Q$  modes (8115, 8669, and 10113 Hz) are the three modes with a radial node. Because of the similarity of their maximum  $Q$  values (ranging from  $23 - 30 \cdot 10^6$ ), and because we expect a frequency independent  $Q$  from the 3PP, we were hopeful that temperature was limiting the acoustic  $Q$ . Again the fridge temperatures were well above their expected base values, with the mixing chamber at 40 mK, the cold plate at 290 mK, and the still at 1050 mK.

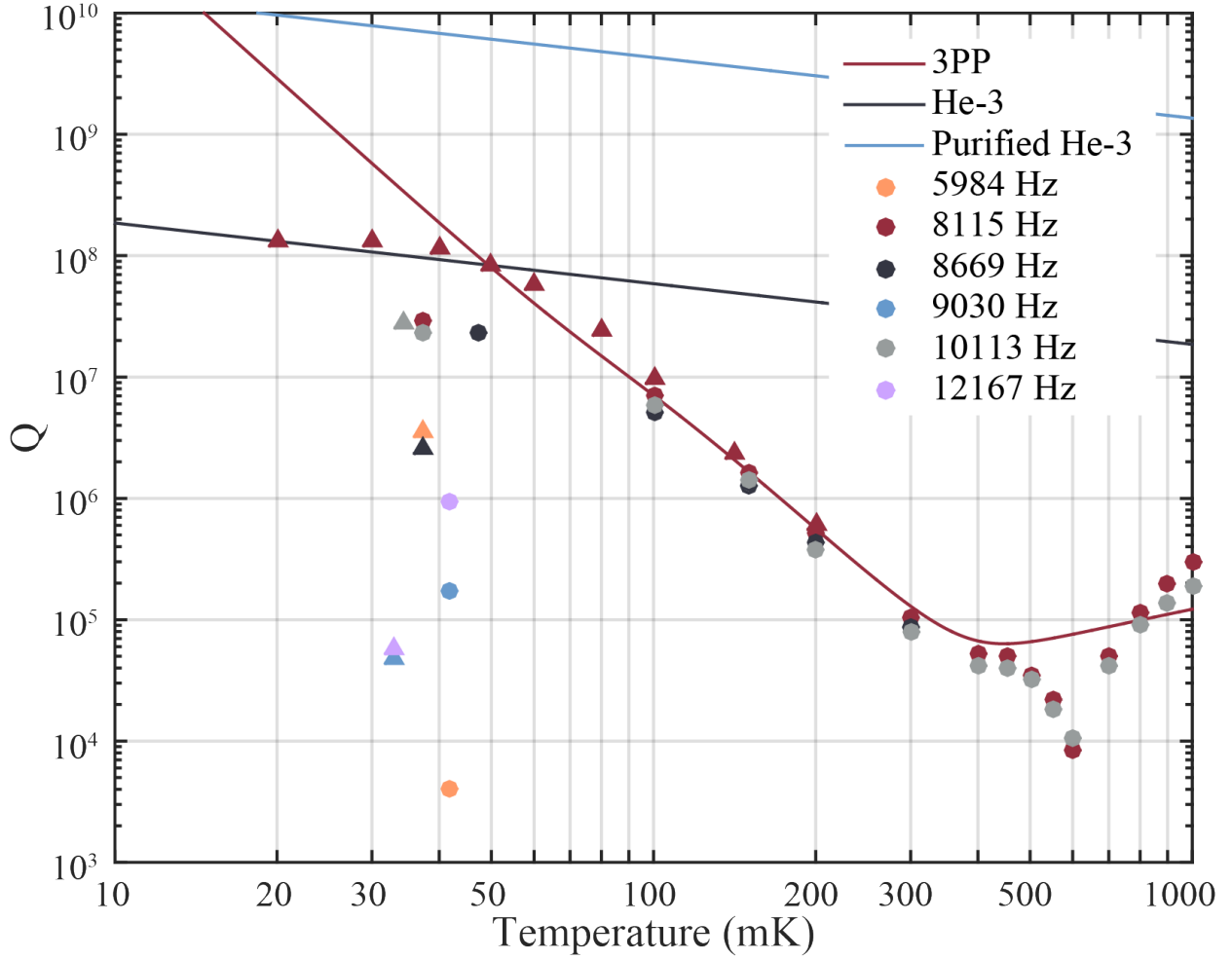


Figure 5.15: Superfluid acoustic  $Q$  versus mixing chamber temperature for the third run (circles) and fourth run (triangles) of the experiment. Each color denotes a different mode, as shown in the legend. The red line shows the expected loss from the 3PP (Eqn. (4.2)), while the navy blue and light blue lines show the dissipation expected from  $^3\text{He}$  impurities at concentrations of  $10^{-6}$  (Eqn. (4.5)) and  $2 \cdot 10^{-10}$  (Eqn. (4.6)), respectively, assuming in all cases a mode frequency of 8115 Hz.

### 5.5.5 Run 4

The experimental setup for Run 4 was very similar to the setup used in Run 3. However, the final microwave connections were made with  $50 \Omega$ , niobium titanium-niobium titanium coaxial cables with a diameter of 0.86 mm (SC-086/50-NbTi-NbTi) [154]. Niobium titanium (NbTi) has a superconducting transition temperature of 9.3 K; at temperatures below 1 K we expected these cables to have no dielectric loss, and therefore we hoped to reduce heating

in the microwave connections.

In Run 4, we also added a cryogenic valve to the mixing chamber. The valve is described more fully in Section 5.6.1, but its operation is summarized here. To close the valve, a bellows is expanded by pressurization with  $^4\text{He}$  gas to force a Torlon needle into a stainless steel seat. This actuation requires a separate helium line be added to the dilution refrigerator. Because the volume in the valve is small ( $\approx 3 \text{ cm}^3$ ), the fill line can be made narrow and long to limit heat leaks without concerns about the difficulty of removing residual water vapor. The actuation line was made with 1 meter of  $150 \mu\text{m}$  ID stainless steel capillary between each stage. It was thermally anchored with sintered-silver heat exchangers with a surface area of  $6.6 \text{ m}^2$  on the mixing chamber and  $3.3 \text{ m}^2$  each on the cold plate and still. The heat exchangers were tested to 150 PSI (10.3 bar) to ensure they would survive the valve actuation pressure.

During Run 4, the cell was first filled at low temperatures and then heated to around  $T_\lambda$ , where liquid helium is densest. The cryogenic valve was closed, the fill line was evacuated, and the fridge was allowed to run to base. Unfortunately, upon following this procedure, we found that the valve was not leak tight to superfluid helium. As illustrated in Fig. (5.16), the  $\text{TE}_{011}$  frequency continued to shift over time as long as the fill line was being pumped on. We waited for three days with the experiment in this configuration to see if the cell frequency would stabilize. The frequency continued to shift until the room temperature valve on the fill line was closed. However, the cryogenic valve serves little purpose in this configuration because one of the major advantages of such a valve is the ability to evacuate the fill line above the mixing chamber, thus eliminating the thermal conduction from superfluid film flow. Consequently, while a cryogenic valve was added in Run 4, because it was not leak tight to superfluid, it did nothing to improve the base temperature of the fridge or the superfluid acoustic  $Q$ .

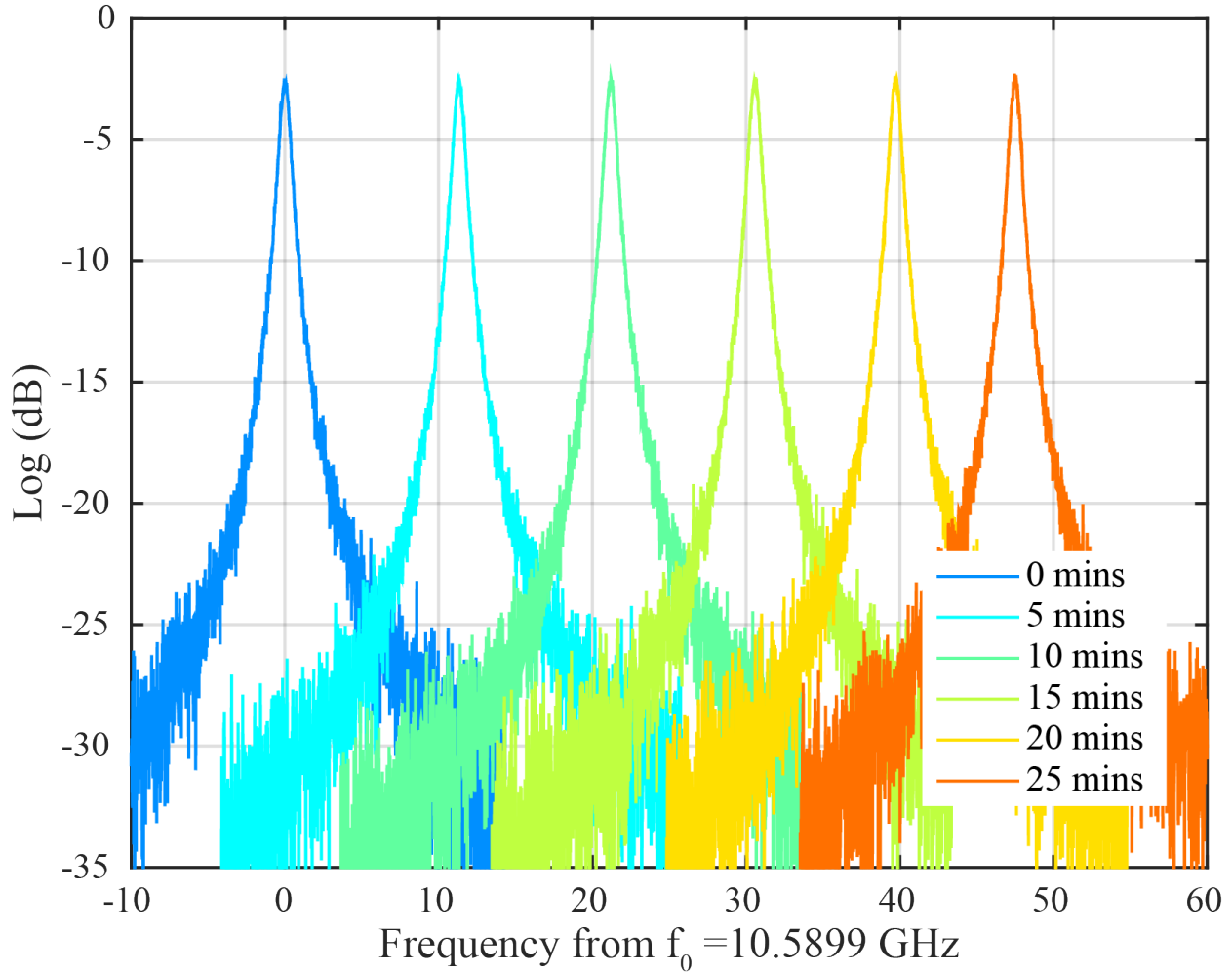


Figure 5.16: The frequency of the TE<sub>011</sub> mode with the cell full of helium, cryogenic valve closed, and fridge at its base temperature while the fill line from the cryogenic valve to room temperature was evacuated with a rough pump. Notice that the cell frequency continued to shift upward indicating that the cell was slowly emptying and the cryogenic valve was not leak tight to superfluid <sup>4</sup>He.

The most important modification for Run 4 was to improve the cooling power of the dilution refrigerator. We found that the tubes of the continuous heat exchanger (located between the 1 K plate and the still) had been inadvertently pressed together creating a thermal short. This problem was solved by putting thin Teflon shims between tubes of the exchanger; see Fig. (5.17). The shims effectively eliminated the thermal short and increased the cooling power at 100 mK (with the cell empty) from 250  $\mu$ W at the end of Run 3 to 450  $\mu$ W at the beginning of Run 4.

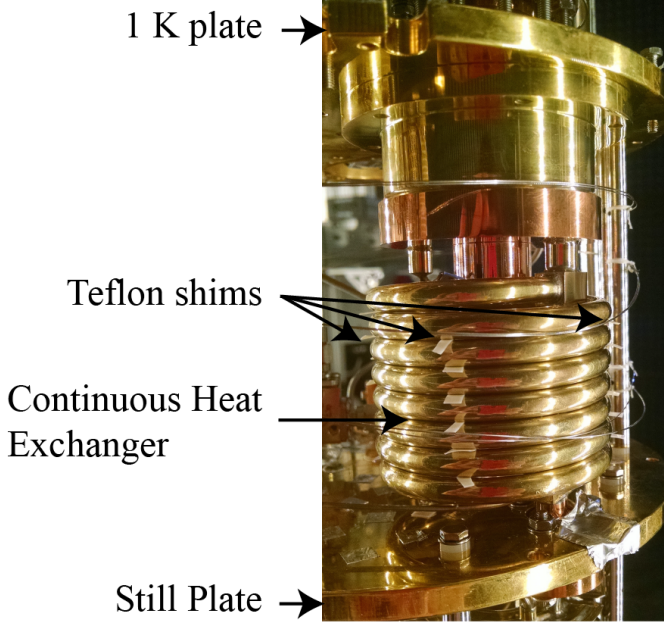


Figure 5.17: The continuous heat exchanger of our Kelvinox 400H dilution refrigerator with Teflon shims inserted between each coil at 90 degree increments.

The final improvement was to replace the standard purity helium ( $x_3 \approx 10^{-6}$ ) with an isotopically purified sample ( $x_3 \approx 2 \cdot 10^{-10}$ ). The switch was made only after initially filling the cell with standard helium and measuring acoustic  $Q$ s approaching  $10^8$ . When we realized that the  $Q$  might be limited by the  $^3\text{He}$  impurity, the cell was emptied and warmed to above 4 K to ensure all liquid was removed. The cell was then refilled with the isotopically purified sample of  $^4\text{He}$ .

The result of these changes on the superfluid acoustic  $Q$ s is shown as triangles in Fig. (5.15). With Run 3 and Run 4 together, the  $T^4$  trend in acoustic attenuation is extended from temperatures of about 400 mK down to 50 mK. In Run 4, the fridge temperatures were notably improved, with the mixing chamber, cold plate, and still measured at  $< 20$ , 108, and 991 mK, respectively. The quality factor of the 8115 Hz mode increased from  $30 \cdot 10^6$  to  $135 \cdot 10^6$ . If the acoustic  $Q$  was limited by the three phonon process in each case, the helium temperature dropped from 65 to 44 mK. The highest quality factor ring down was taken with the fridge temperature at 30 mK and is shown in Fig. (5.18).

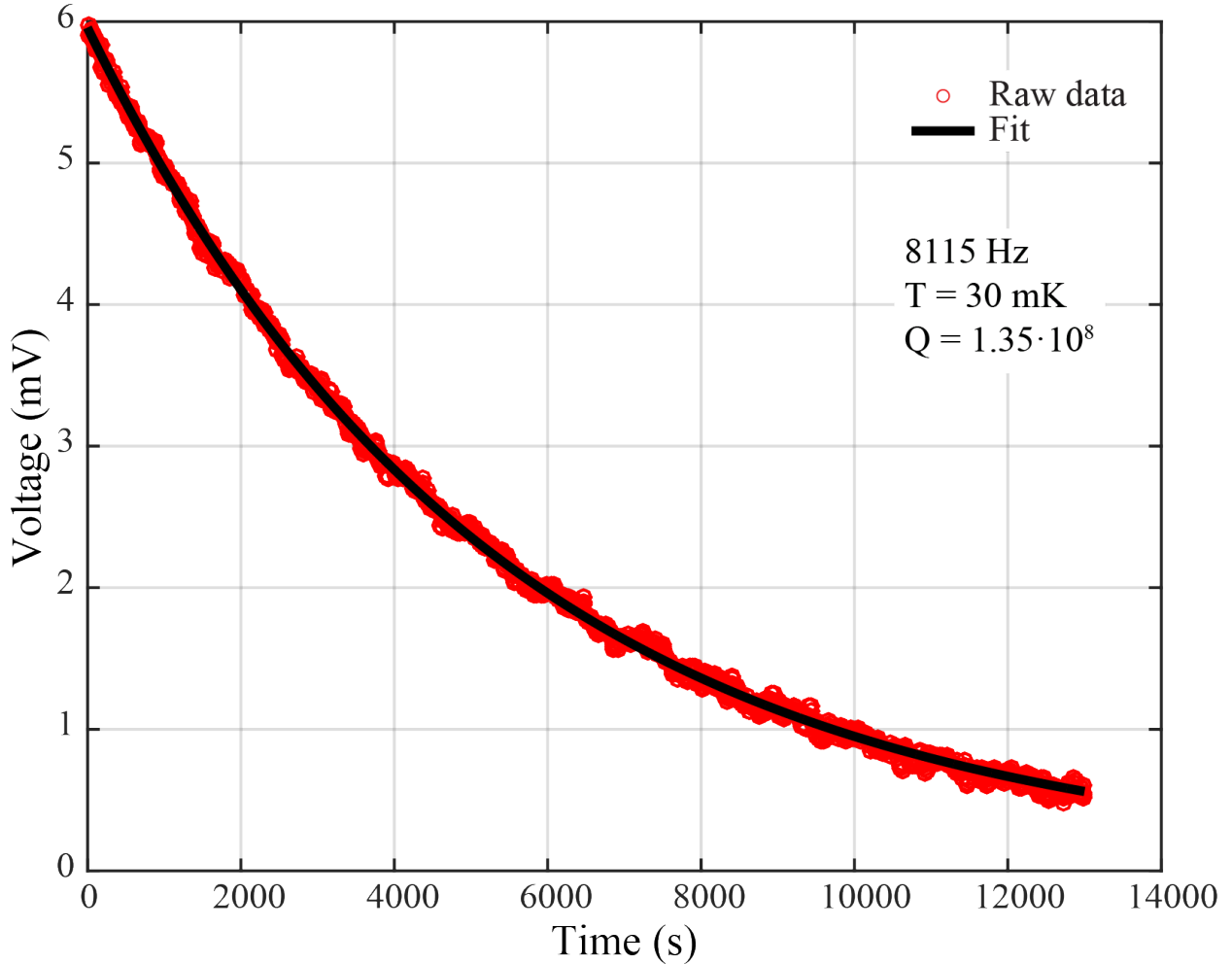


Figure 5.18: A ring down of the 8115 Hz mode, showing the highest quality factor we have measured:  $1.35 \cdot 10^8$ . The mixing chamber temperature was 30 mK, but if the  $Q$  is limited by the 3PP as given in Eqn. (4.2), the helium temperature is 44 mK.

Even with the improvements to the fill line and the dilution refrigerator, we found that at low temperatures, our helium sample had much longer thermalization times than expected (From Section 2.5.1, we expect  $\tau = 10$  seconds). At the lowest fridge temperature, the superfluid  $Q$  continued to improve slowly day by day, suggesting a long term thermal relaxation. Quality factor versus temperature measurements were made by heating the fridge from its lowest temperature, where the thermometry read  $< 20$  mK and the helium was thermalized to 44 mK according to the 3PP. As the fridge was warmed in stages, the  $Q$  was measured versus time. An exponential fit to these data gives a thermal time constant.

Data for warming the mixing chamber from 40 to 50, 50 to 60, 60 to 80, and 141 to 200 mK are shown in Fig. (5.19) along with the exponential fits. It would have been ideal to place a few more points on the higher temperature curves, but nonetheless it is obvious that the time constants become an order of magnitude smaller between 50 and 200 mK; see Fig. (5.20). These data suggest there is a problem with thermalizing the helium-4 sample at low temperatures.

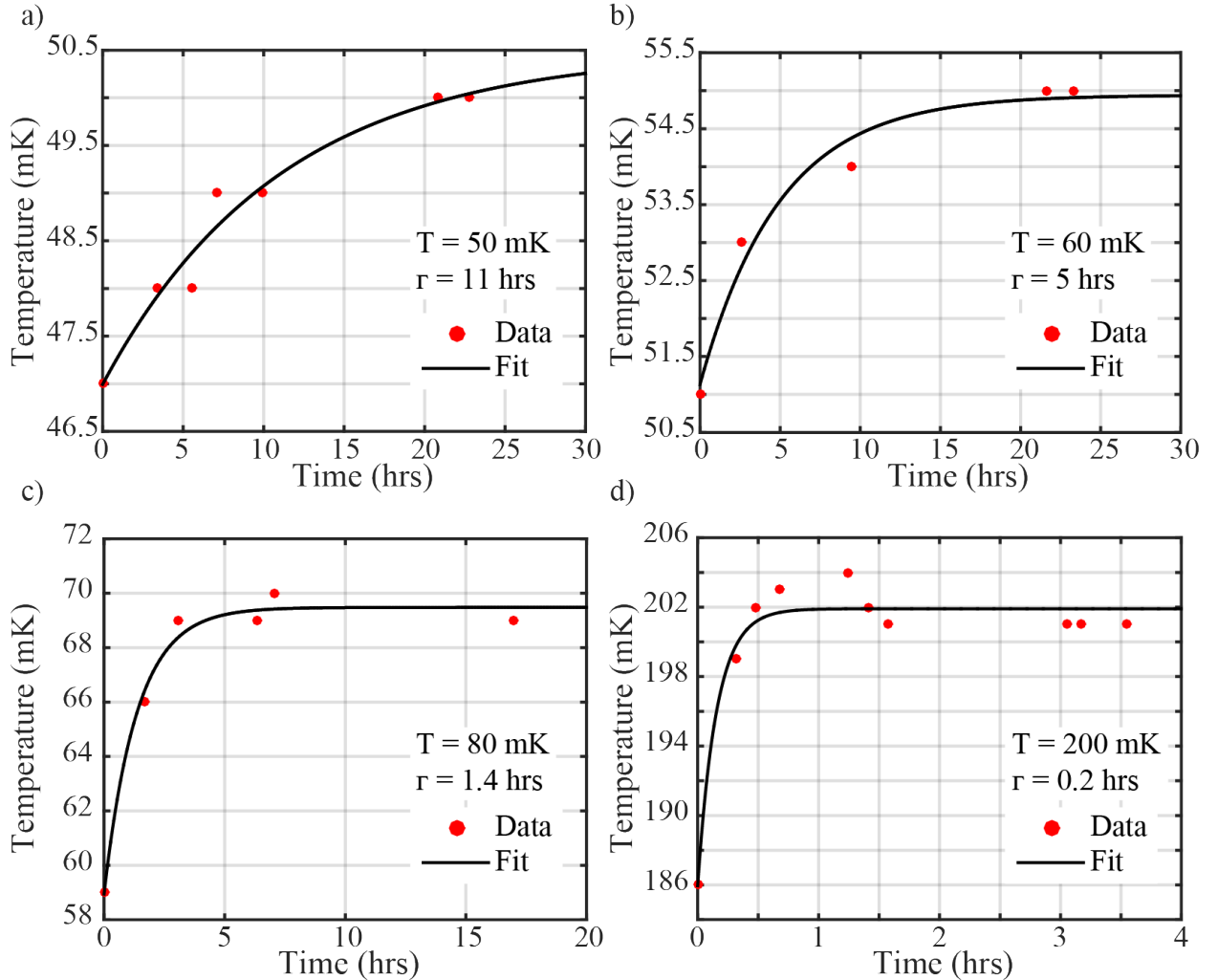


Figure 5.19: Thermalization curves for the superfluid helium, extracted from the quality factor of the 8115 Hz mode by assuming  $Q$  is limited by the 3PP, upon heating the fridge to a) 50 mK, b) 60 mK, c) 80 mK, and d) 200 mK. Data points are shown as red circles; the black line is an exponential fit to the data. The final fridge temperature and the time constant of the exponential fit are shown on each figure. Notice that the final temperature of the helium in some cases differs from the mixing chamber temperature.

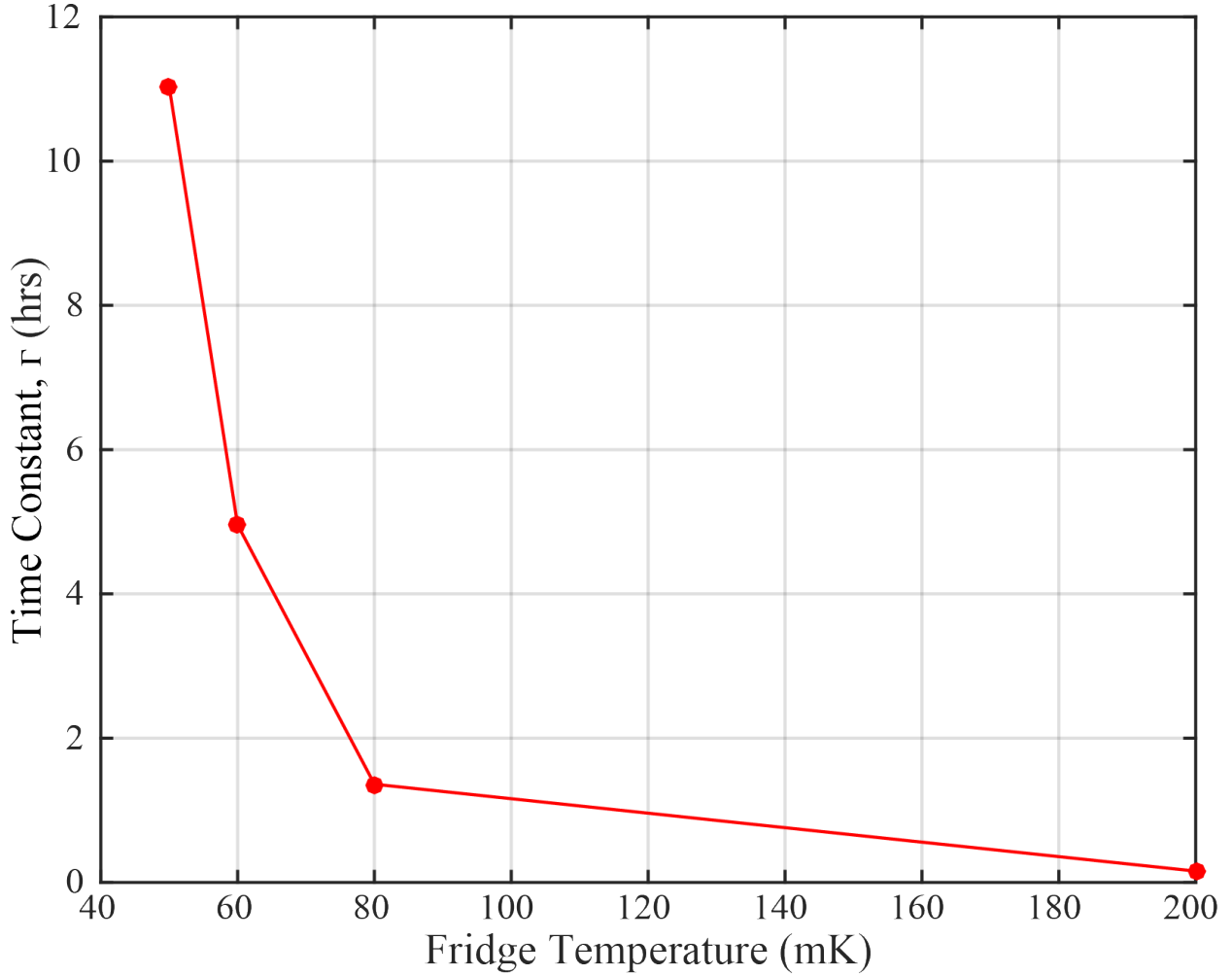


Figure 5.20: The thermal time constants calculated from the exponential fits in Fig. (5.19) plotted versus the final fridge temperature for each data set. The connecting line serves as a guide to the eye only. Notice that the time constants at low temperatures are extremely long.

Additionally, more work must be done to understand what mechanism limits the quality factor in the different acoustic modes. Note that of the three modes with a node located at the fill line, between Runs 3 and 4 the 8119 Hz mode increased in  $Q$ , the 10113 Hz mode remained about the same, and the 8669 Hz mode dropped in  $Q$  by almost an order of magnitude. Of the modes without a radial node, both the 9033 Hz and 12201 Hz mode decreased in  $Q$  while the mode at 5984 Hz saw an increase in  $Q$  by almost three orders of magnitude! All of this is surprising given that the only change in the suspension system between Runs 3 and 4 was to modify the material (but not the diameter) of the final coaxial

cables from beryllium copper to niobium titanium, which is mechanically stiffer.

Finally, in Run 4 we examined the acoustic frequency versus pressure applied to the cell; this measurement would demonstrate the tunability of our superfluid oscillator. The expected change in frequency can be estimated from the compressibility  $K = -1/V \cdot \partial V / \partial P$  and the Grüneisen constant  $G = \rho/c_4 \cdot \partial c_4 / \partial \rho = 2.84$ . Differentiating the density  $\rho = m/V$  with respect to  $V$  and using the definition of  $K$ , one finds that a change in the pressure applied to the cell will change the density as:  $\partial \rho = \rho K \partial P$ . The Grüneisen constant relates this change in density to a change in the speed of sound from which one can estimate the frequency shift of the superfluid modes:  $\Delta f/f = \Delta c_4/c_4 = KG\Delta P \approx 3.5 \cdot 10^{-7} \Delta P$ .

While trying to measure this relation experimentally, a difficulty arose because the microwave frequency (and hence also the acoustic frequency) was not stable over time with pressure applied to the cell. While we have considered the modification to the acoustic frequency, changes in pressure and helium density also modify the microwave frequency through the dielectric constant. In our setup, the instability arises because, with the cell pressurized above one atmosphere, the helium fill line is full of liquid helium up to and above the 4 K plate. From the 4 K stage, the fill line is contained in a thin vacuum tube that passes through the helium bath up to 300 K. Therefore the thermal environment around the helium liquid level in the fill line is constantly changing, introducing a significant instability into the system. A working cryogenic valve would eliminate these issues and enable a frequency versus temperature measurement.

### 5.5.6 Run 5

From Run 4, we learned that despite our improvements, the superfluid cell was still not thermalized to the base temperature of the dilution refrigerator. In Run 5, we addressed thermalization by replacing the copper wire used to suspend the cell with a 4N silver rod [155], approximately 1.27 cm in diameter and 6.6 cm in length. A drawing of the rod is shown in Appendix F.3. After the rod was machined, it was annealed in a helium atmosphere at 850 °C for four hours to increase its thermal conductivity. Assuming we achieved  $RRR = 1000$ ,

we expected a thermal conductivity of  $\lambda = 61 \cdot T$  W/m·K and a resistance of  $R = 9$  K/W. This thermal resistance is about a factor of 100 lower than the resistance of the copper wire suspension used in Runs 3 and 4. The thermal resistance of the silver rod equals the Kapitza resistance between the helium and the niobium cell ( $R_K$ ) at 2 K and equals  $R_K/10$  at 670 mK. Therefore we fully expected the final helium temperature to be limited by  $R_K$ .

To ensure good thermal connections in the suspension, the silver rod was cleaned, and annealed 25  $\mu\text{m}$  thick, 99.95% gold foil was pressed between the rod and the cell and the rod and the fridge. The rod was attached on both ends with brass bolts and tungsten washers. A brass bolt is used because its relative linear thermal expansion coefficient from 300 K to 0 K is  $\alpha_{Brass} = \Delta L/L \cdot 100 = 0.384\%$ , very similar to that of silver,  $\alpha_{Ag} = 0.410\%$ . In tungsten, the value,  $\alpha_W = 0.086\%$ , is much smaller, so as the system cools down, the brass bolt contracts onto the tungsten washer, and the silver rod is pressed more tightly against the cell and the fridge, ensuring good thermal contact.

The fill line was identical to Run 4 except the section between the still and the cold plate was replaced with a 150  $\mu\text{m}$  ID capillary (see Table (5.3)). We made this change because, even in Run 4, the cold plate was well above the temperature from the test run of the dilution refrigerator (102 mK compared to 56 mK). As discussed in Section 5.5.1, because the thermal conductivity of  ${}^4\text{He}$  falls as  $T^3$ , we expected the lower temperature sections of the fill line to provide very little heat conduction, so we left them unchanged. The result was that the mixing chamber, cold plate and still reached temperatures of < 20, 118, and 965 mK, respectively, which was very similar to Run 4.

The data from Run 5 are shown in Fig. (5.21). Notice that the highest  $Q$  was limited to  $1.3 \cdot 10^7$ , in the 6 kHz mode, approximately one order of magnitude below the highest  $Q$  measured in Run 4. In the 8115 Hz mode, which had the highest  $Q$  in Run 4, we measured a  $Q$  two orders of magnitude below that maximum value. Because the suspension was the only change between Run 4 and Run 5, we infer that the drop in quality factors is due to increased suspension loss from using a rigid connection as opposed to a copper wire.

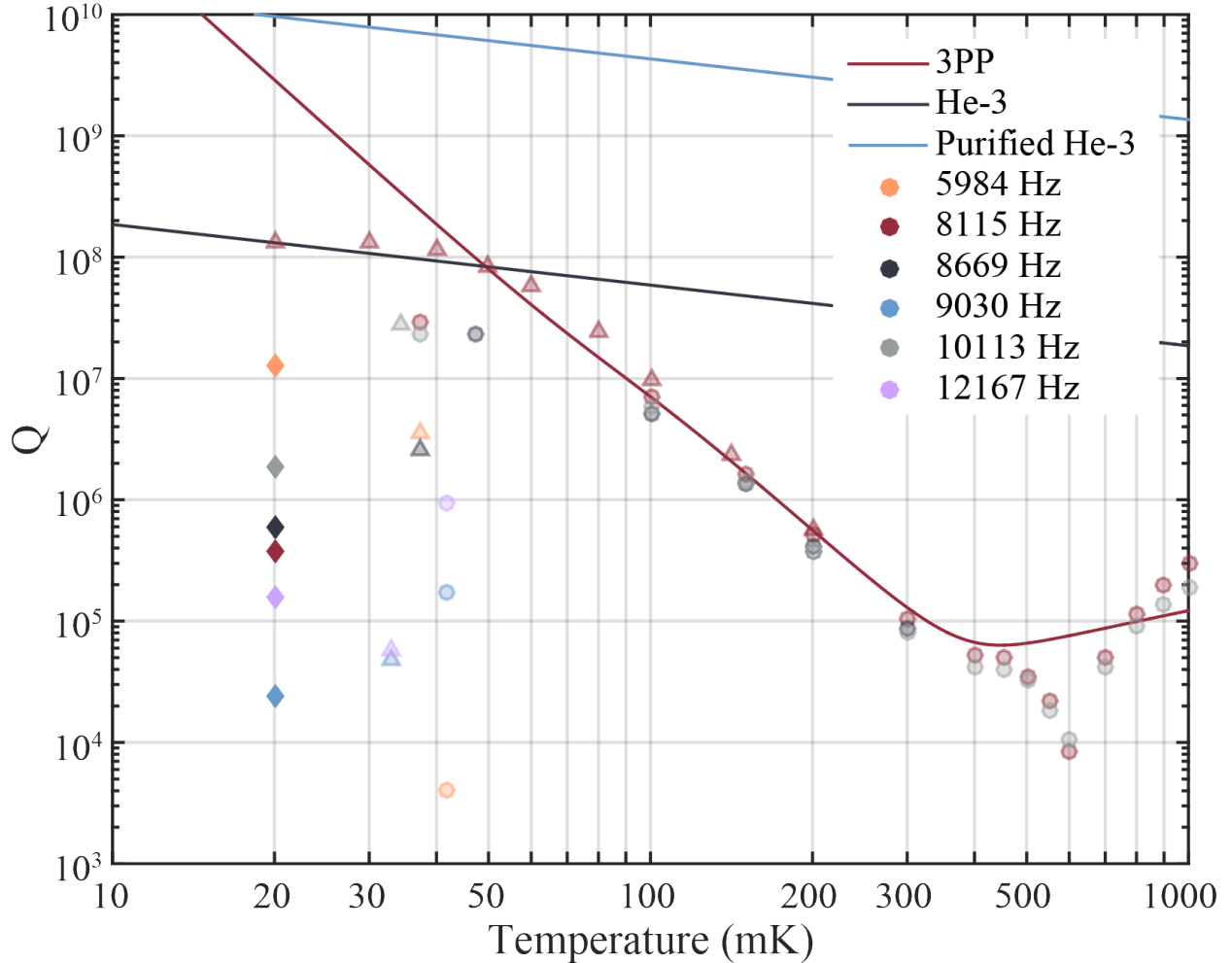


Figure 5.21: Superfluid acoustic  $Q$  versus mixing chamber temperature. Data from Run 5 are shown as diamonds at 20 mK. For comparison the data from Runs 3 and 4 are shown as faded circles and triangles, respectively. Each color denotes a different mode, as shown in the legend. The red line shows the expected loss from the 3PP (Eqn. (4.2)), while the navy blue and light blue lines show the dissipation expected from  $^3\text{He}$  impurities at concentrations of  $10^{-6}$  (Eqn. (4.5)) and  $2 \cdot 10^{-10}$  (Eqn. (4.6)), respectively, assuming in all cases a mode frequency of 8115 Hz.

In Runs 4 and 5, we also measured heating from dielectric loss by increasing the microwave pump power and measuring the  $Q$  of the acoustic mode with the lowest acoustic loss. As the helium heats up, the  $Q$  decreases; the helium temperature can be inferred if it is assumed that the  $Q$  is limited by the 3PP (Eqn. (4.2)). In Run 4, these measurements were done with the 8115 Hz mode (minimum temperature of 44 mK); in Run 5, we used the 5984 Hz mode (minimum temperature of 83 mK). Note that in Run 4, the cell was held from a copper

wire,  $R \approx 770$  K/W, whereas in Run 5 the cell was held from a silver rod,  $R \approx 9$  K/W. The results of this test are shown in Fig. (5.22). The silver rod used in Run 5 does appear to limit the heating more effectively than the copper wire used in Run 4. In either case, heating is evident at incident pump powers  $< 1\mu\text{W}$ , which is at least three orders of magnitude below the powers required to achieve  $\Gamma_{opt} > \Gamma_M$  and demonstrate sideband cooling with our current parameters. These data indicate that we have much more dielectric heating than we would expect from the high  $Q$  of our niobium cavity and the low dielectric loss tangent of  $^4\text{He}$  (see Section 2.5). For instance, at an incident pump power of  $0.4 \mu\text{W}$  ( $n_P \approx 3 \cdot 10^{10}$ ), we expect  $\dot{Q}_{He} \approx 10^{-12} \text{ W}$  (from Eqn. (2.37)) using the maximum possible value of helium's dielectric loss tangent,  $\tan(\delta) = 10^{-10}$ . However, because in both runs the helium reached a temperature of  $\approx 110$  mK and the mixing chamber remained at base, the difference in temperature between the helium and base stage is about 90 mK. Therefore the heating we find experimentally is  $\dot{Q}_{He} \approx 10^{-6} \text{ W}$ , a difference of six orders of magnitude! We conclude that more work must be done to limit the dielectric heating, and improving the thermal connection through the suspension is not an adequate solution.

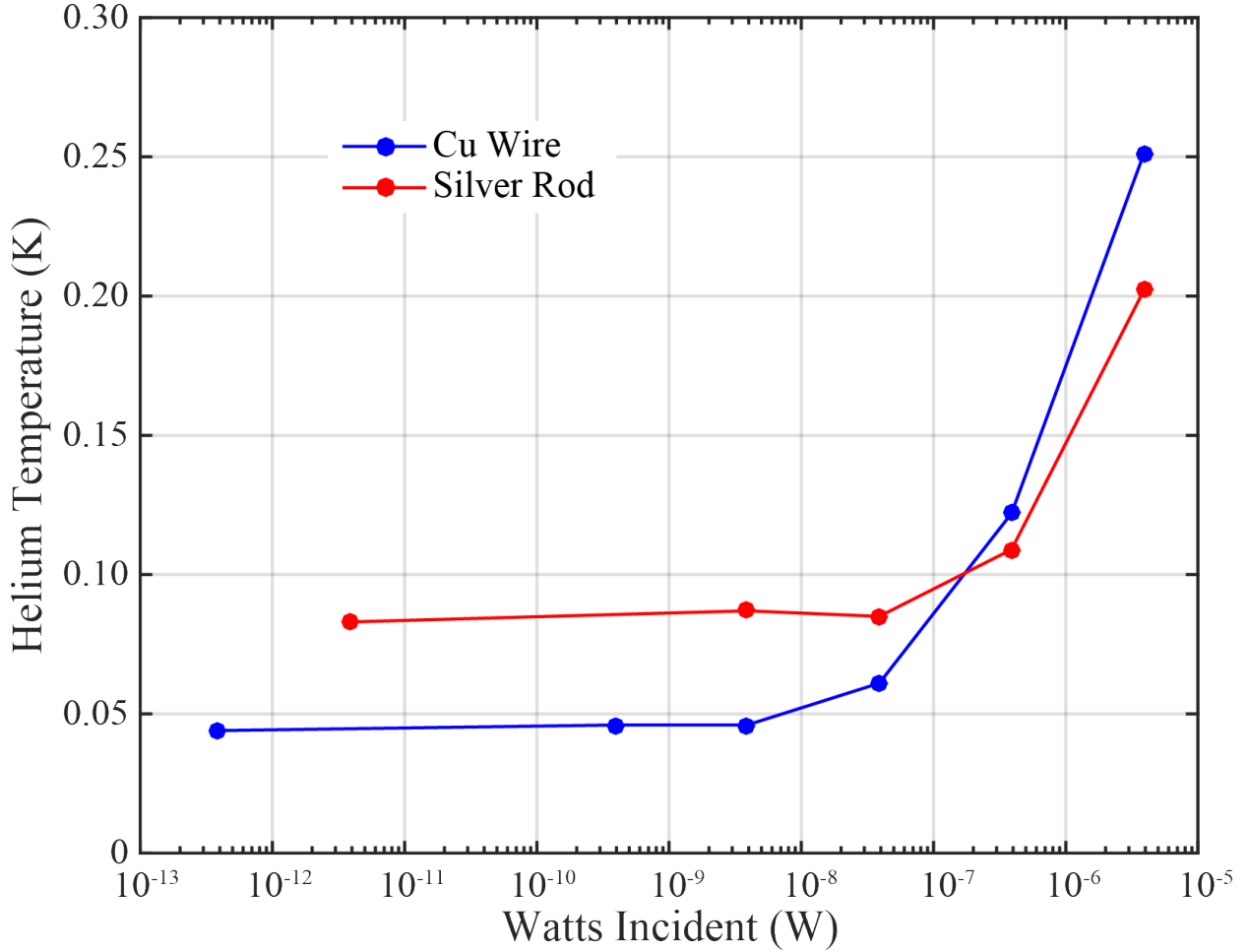


Figure 5.22: Helium temperature inferred from the measured superfluid acoustic quality factor versus power incident on the cavity. The blue and red lines indicate that the cell is attached to the mixing chamber with a copper wire (Run 4) or a silver rod (Run 5), respectively. Note that while the heating is reduced with the silver rod, the difference between the two setups is not substantial.

In Run 5, we also tested the Pound Drever Hall (PDH) technique as a way of following changes in the frequency of the microwave oscillator due to pressure or temperature fluctuations in the cell. The circuit we used is shown in Fig. (5.23a). We added 500 Hz sidebands to the microwave drive with an AM modulator. If the frequency of the cell is constant, the sidebands will be reflected equally, but as the cell frequency changes, it will move closer to one of the sidebands and further from the other, and they will be reflected asymmetrically. Therefore the power in the transmitted sidebands contains information about the detuning between the source and the cavity. The output from the cavity is mixed down to the 500 Hz

sideband frequency before it is measured on a lock-in amplifier. The lock-in is adjusted so that all of the signal is placed into one quadrature to be used as the error signal. One can check that as the source frequency passes through the cavity resonance, the error signal is linear and passes through zero. The output of this signal from the lock-in is fed into a PID controller and ultimately used to feedback on the microwave source frequency. The error signal from our lock-in as we sweep the microwave generator through the cavity frequency is shown in Fig. (5.23b). It is linear through zero, as expected. The PDH technique could be useful for measurements of the acoustic  $Q$  when the cell is pressurized and the frequency is unstable.

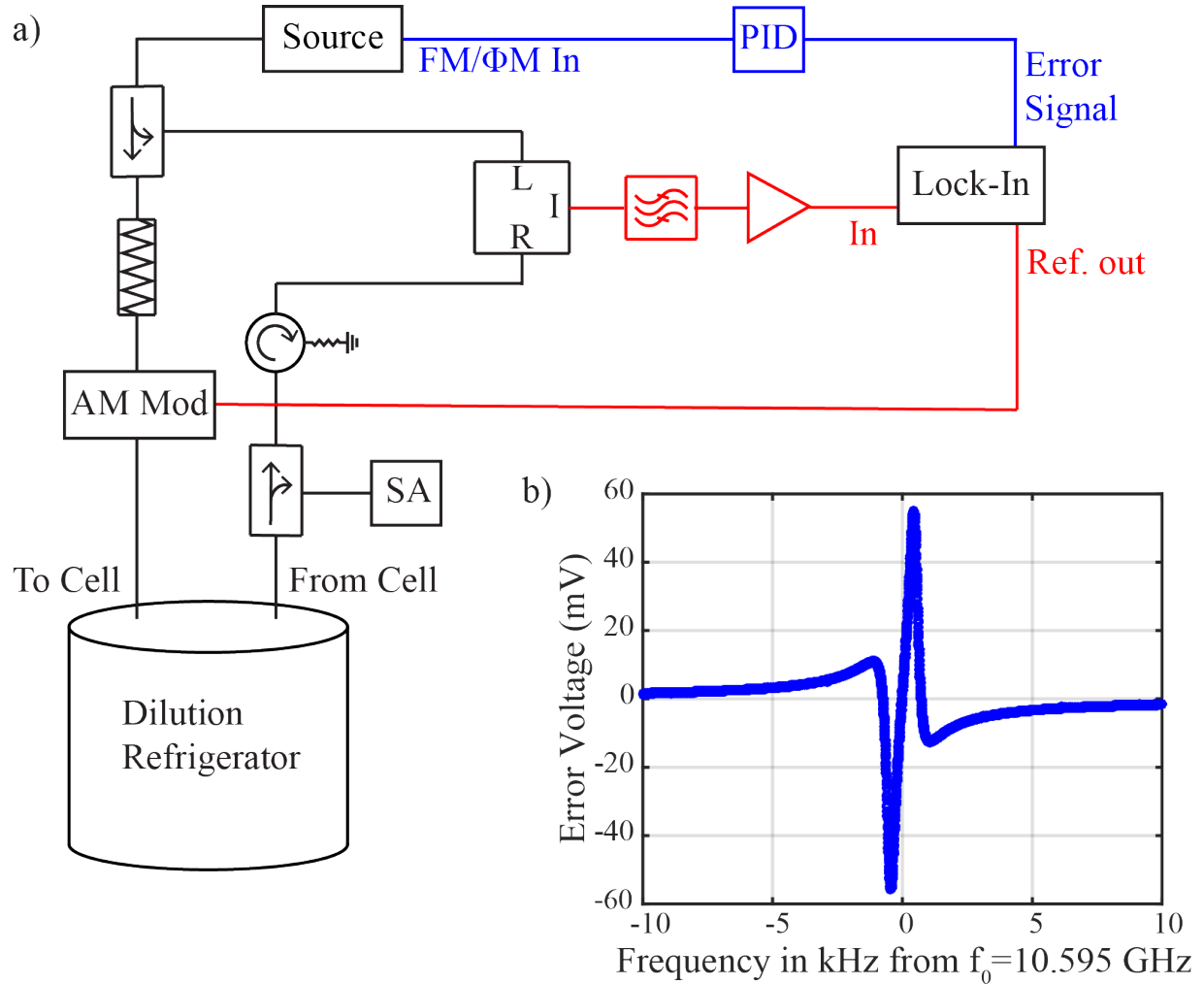


Figure 5.23: a) the Pound Drever Hall frequency stabilization circuit. AM modulation is used to add sidebands to the source before it is incident on the cavity. The signal from the cavity is split in two: one branch is measured on a spectrum analyzer (SA) and the second is mixed down to the sideband frequency and measured on a lock-in. One quadrature of the signal from the transmitted sidebands is used as an error signal, which is first fed into a PID controller and then input to the FM modulation on the source. The red circuit is at acoustic frequencies and the blue circuit is the error signal. b) the PDH error signal from the lock-in.

### 5.5.7 Planned Runs

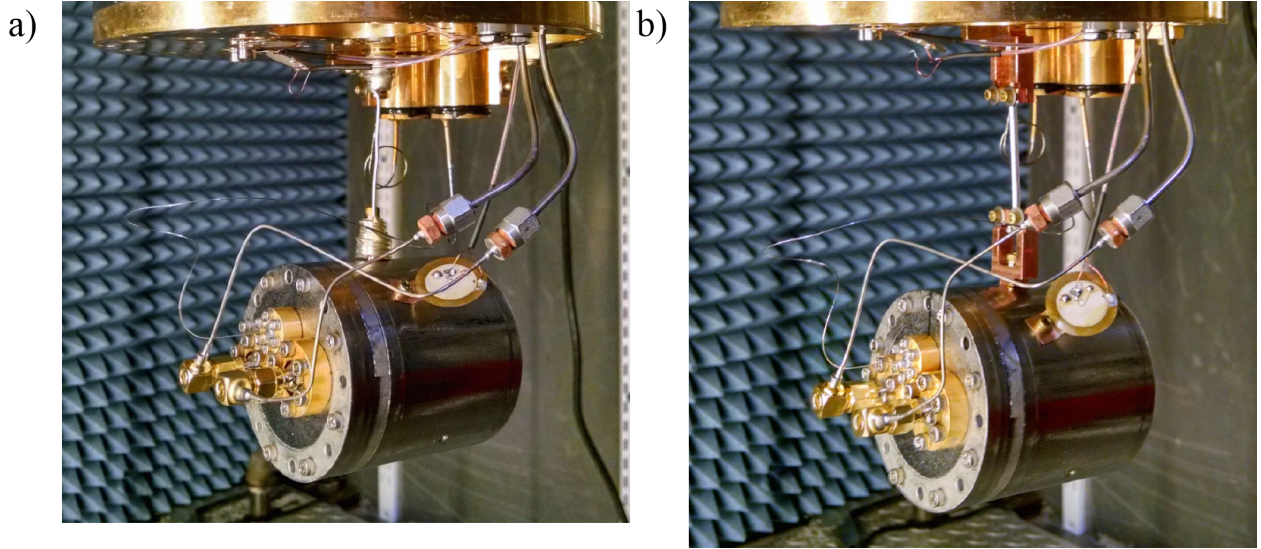


Figure 5.24: Pictures of the cell planned for future runs: a) is similar to the copper wire setup used in Runs 3 and 4, but with an annealed 5N silver wire with a diameter of 0.10 cm. The copper tubes to which the wire is soldered are machined with a smaller diameter section at the top (0.635 cm) so that the wire exits closer to the cell's center keeping the cell level. b) shows a different approach to attaching the wire to the the cell and fridge. One copper piece is bolted to cell (or fridge), and a second copper piece is used to clamp onto the 0.23 cm diameter silver wire.

After run 5, a sixth run was planned to achieve higher  $Q$  values and lower dielectric heating. The cell was to be suspended with an annealed 5N silver wire rather than a copper wire, improving the thermal conductivity of the suspension system. (For instance, a silver wire with diameter 0.10 cm and length 6.6 cm with  $RRR = 5000$  will have a thermal resistance of only  $R = 280$  K/W. See Section 2.5.1 for discussion.) The coupling loops in direct contact with the helium, which were previously made from phosphor bronze, were to be replaced with superconducting NbTi cable with the intention of reducing heating from dielectric loss as discussed in Section 5.5.6. Finally, the fill line and cell were to be cleaned at room temperature with an isotopically purified sample of helium, to ensure that  ${}^3\text{He}$  impurities were adequately removed.

However, no further experiments were done because we ran into difficulty achieving leak tight seals in the niobium cell after taking it apart. Niobium is a malleable metal, and over time and repeated trials, the copper caps used for the microwave connections had formed

depressions in the niobium lid as shown in Fig. (5.25). We believe this is the cause of multiple low temperature leaks which prevented operation of the experiment. The lid was sent for re-machining, and in the future leak tight indium seals should again be achievable.

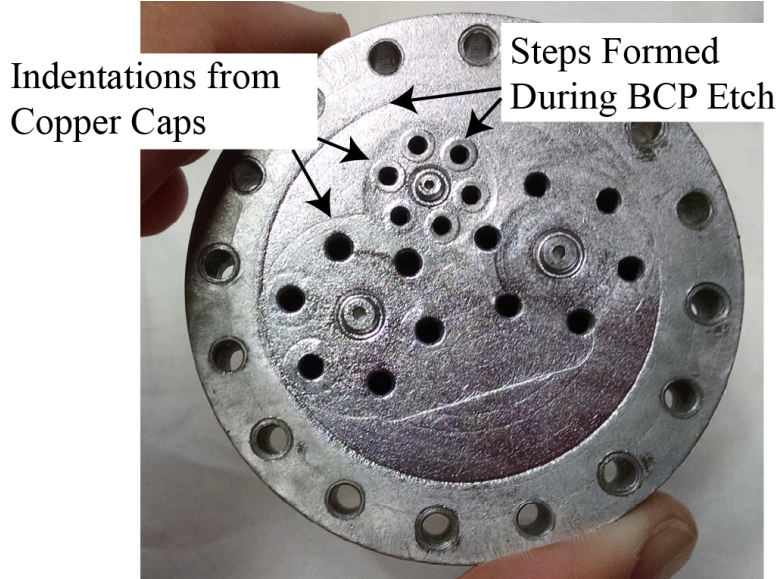


Figure 5.25: Damage to the niobium lid preventing leak tight operation of the cell

## 5.6 Future Improvements

### 5.6.1 Superfluid Valve

Ultimately, to limit the thermal conduction between dilution refrigerator stages caused by superfluid film flow, a leak tight cryogenic valve will be required. The valve will allow the fill line to be evacuated above the mixing chamber. An empty fill line will enable the dilution refrigerator to reach lower temperatures and remove the heat leak to the cell from higher temperature stages.

We worked on two valve designs during my PhD. The first design was assembled and tested for Run 4, where it failed to create a seal leak tight to superfluid. Based on experience with the first design, a second, improved design was conceived and machined; however, it was never tested.

The valve is comprised of six pieces: the needle, plunger, bellows, guide, seal, and housing. The final design is shown in Fig. (5.26) and detailed drawings are in Appendix D. The valve is actuated by pressure, which expands a bellows, forcing a Torlon needle into a stainless steel seat and creating a leak tight seal. When the valve is fully assembled, the needle is threaded into the stainless steel plunger which is inserted into the stainless steel guide for alignment. The nickel bellows (Servometer FC-13-L [156]) are sealed to both the plunger and the guide with a low temperature solder. A brass actuation tube is brazed into the guide, and when gas flows into this tube, the bellows is filled. The housing is used to hold the valve together; both the guide and the seal are secured to the housing with indium seals. The brass tubes used for flowing gas into and out of the valve are brazed into holes in the seal. When the valve is closed, the Torlon needle is forced into one of these ports, closing it off from the other.

To assemble and test the valve one first cleans the guide, plunger, and bellows with IPA and methanol. (Acetone can eat through metals and should be used only cautiously with the thin metal bellows). These pieces should be cleaned well as the actuation volume will not be accessible after the bellows are soldered in place. After cleaning, a fluxless low temperature solder can be used to attach the bellows to both the plunger and the guide. The solder joints must be leak checked both at room temperature and 77 K. If they are not leak tight, the actuation gas will slowly leak into the interior of the valve, and the valve will not close. When leak checking these joints, great care must be taken not to deform the bellows by applying too much differential pressure to the interior. For instance, an atmosphere of pressure difference will expand the bellows past its deformation point.

For the valve to be leak tight to superfluid, the Torlon tip must be machined very well, with a clean, smooth finish. To ensure that the angle of the needle is correct, the lathe should be the last tool ever to touch the Torlon. Additionally, the hole in the stainless steel seal where the Torlon needle makes contact should be polished after the seal is machined. The polishing can be done with a wooden toothpick and polishing paste. Start with coarser grits of polish and move to finer grits until the surface is scratch free under an optical microscope. The polishing process is a very time consuming but essential step.

Next the valve must be checked for alignment. Proper alignment between the needle and seal is essential for the valve to close and is one of the biggest difficulties in making a mechanical valve. Slip fits are required between the guide and housing, plunger and needle, and housing and seal to keep the seal parallel to the plunger. In design 2, the plunger is fitted into the guide with 0.002" of clearance to allow the needle some play in making the seal.

One way to check for alignment at room temperature is to ink the seal with a permanent marker, assemble the valve, and close the needle with just enough pressure to make contact. The ink from the seal will form a ring on the needle. If that ring is unbroken, the alignment is satisfactory. On most trials, the ring will be an incomplete circle and either a different orientation of the seal can be tried, or different needle and seal combinations can be experimented with. The room temperature ink test requires great caution as the Torlon needle can be deformed at room temperature if too much pressure is applied. Once the needle is deformed it will never seat correctly again.

When the valve is aligned at room temperature, it should be re-assembled and leak checked at 300K and 77K. If the valve is leak tight one can also check that it closes at 77 K where Torlon is no longer deformable and will not be damaged by contact with the seal. All leak tests were done on a probe with three fill lines. A line designed to handle high pressure was connected to the actuation port of the valve, and the other two lines were connected to the input and output of the valve. In this way, all three ports of the valve could be checked for leaks into the probe and the closure of the valve could be checked separately. Helium gas was flowed from the input to the output of the valve with the output capillary emerged into IPA. Initially, we looked for a rough closure by observing the speed of the bubbling into the IPA. When the bubbling stopped, the output was connected to a leak detector for a final test of valve closure. To ensure the valve will be leak tight during our experiment, this test must be repeated with superfluid helium on the input line; however we did not have an easy way of doing that test without assembling the system on the dilution refrigerator.

The bellows acts like a spring; for the Servometer FC-13-L the spring rate is 40.33 lb/in. With this spring rate, the surface area of our plunger ( $\approx 0.43 \text{ in}^2$ ), and the distance between

the needle tip and seal, we can estimate the pressure required to shut the valve. Assuming a linear spring, the force  $F$  is related to displacement  $x$  through the spring constant  $k$  by Hooke's law,  $F = kx$ . Pressure is defined as  $P = F/A$ , where  $A$  is the area, so eliminating  $F$  we find that the total displacement of the plunger will be  $x = P \cdot A/k$ .

In the first design, assuming the indium seals did not add height to the valve, the needle traveled about 0.050" to make contact with the seal. Given the bellows spring rate of 40.33 lb/in., this distance required about 5 PSI (0.3 bar) of actuation pressure. The circumference of the needle at contact was 0.070". During trial and error with the ink test, we found that the needle could make a good seal only when the plunger had more play inside the guide, so we modified the design from one with a slip fit to one with 0.002" of clearance. This modification yielded a valve which appeared to close (no bubbling from the output capillary immersed in IPA) at room temperature with 24 PSI (1.7 bar) applied to the actuation port. At 77 K, 50 PSI (3.4 bar) of actuation pressure was required to see a significant decrease in bubbling. At 85 PSI (5.9 bar) the valve was connected to the leak detector and the leak rate was  $8 \cdot 10^{-5}$  mbar l<sup>-1</sup> s<sup>-1</sup>. As the actuation pressure was increased, the leak rate decreased, until a pressure of about 130 PSI (9 bar) where the leak rate was  $4.2 \cdot 10^{-7}$  mbar l<sup>-1</sup> s<sup>-1</sup>. The leak rate slowly dropped over time but further increases in pressure did not lead to noticeable decreases in leak rate. The valve appeared to make a leak tight seal at 77 K; however, the pressure required was much higher than we expected. As the actuation pressure was removed from the valve, at about 120 PSI (8.3 bar) the leak rate noticeably increased again. The valve was cycled to room temperature and back to 77 K, the leak test was repeated, and the valve again closed. This valve was mounted to the mixing chamber of the dilution refrigerator for use in Run 4. While the valve was again leak tight at 77 K, it was not leak tight to superfluid helium. Actuation pressures up to 185 PSI (12.8 bar) were tried, but to no avail.

Because we found unexpectedly high pressures were necessary to close design 1 of the valve, we reduced the circumference of the sealing contact area in design 2, from 0.070" to 0.020". We also decreased the travel distance for the tip to only 0.005", requiring a pressure of < 1 PSI (< 0.07 bar). Finally we simplified the design of the Torlon needle tip, making it

easier to machine a quality surface.

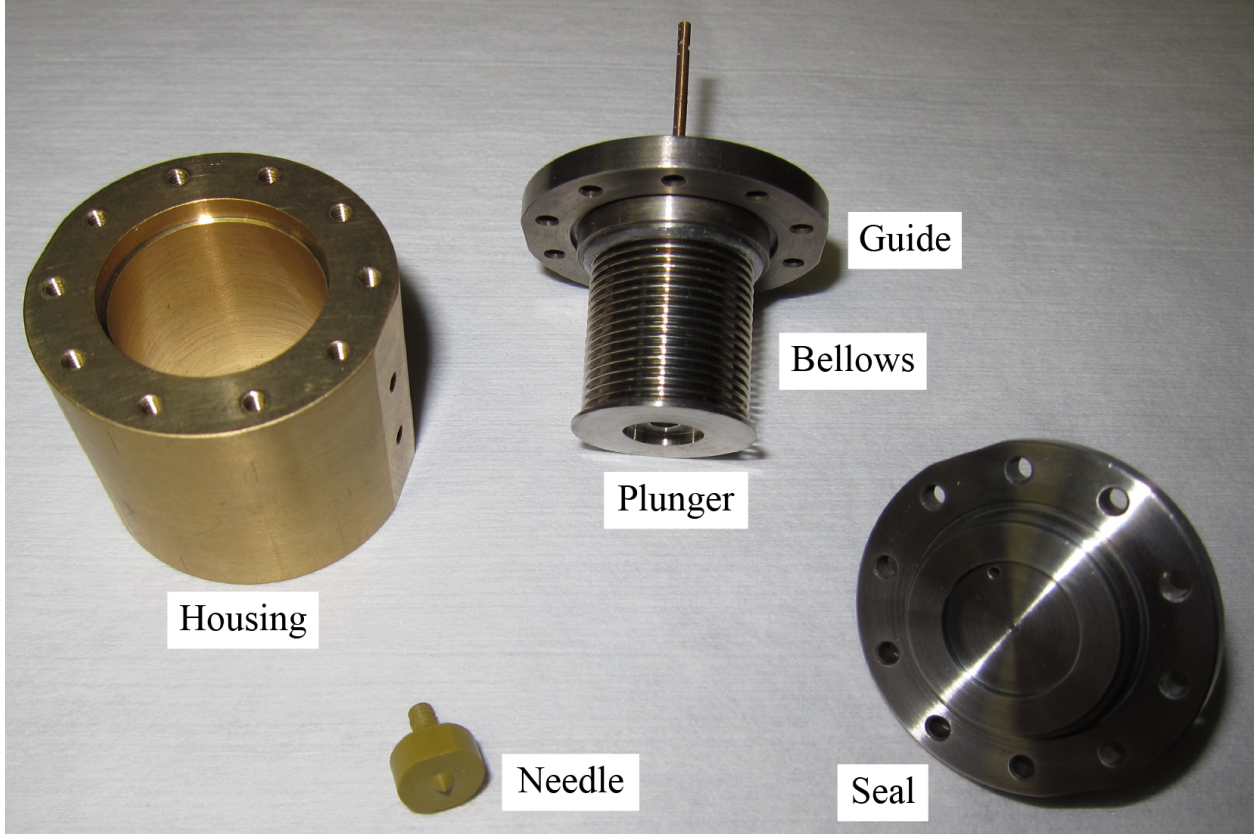


Figure 5.26: Pictures of machined valve pieces for design 2. The housing is brass, the guide, plunger, and seal are stainless steel, the needle is Torlon, and the bellows are nickel. Here the bellows have already been soldered to the plunger and guide.

### 5.6.2 Decreasing Suspension Loss

Improving the acoustic  $Q$  beyond  $10^8$  may also require limiting clamping losses. In our current setup, there are four mechanical connections to the cell: one each for the suspension and the fill line and two for microwave connections. A simple way to reduce suspension loss is to replace the copper suspension wire with a higher  $Q$  material (such as silver) [50]. Additionally, it is possible to eliminate one microwave connection by operating the niobium cavity in reflection or to eliminate both microwave connections by using antenna coupling [143]. The fill line can be removed by welding the cavity lid in place and pre-filling the cell to a pressure of  $2.3 \cdot 10^7$  Pa (230 bar) at 77 K or  $9 \cdot 10^7$  Pa (900 bar) at 300 K. Alternatively,

the fill line and suspension wire can be combined to a single connection.

### 5.6.3 Decreased Dielectric Heating

In order to limit the dielectric heating observed at high pump powers as described in Section 5.5.6 and shown in Fig. (5.22), we will eliminate all normal metals in the microwave lines. We have a new design for coupling to the cell using only aluminum (superconducting  $T_C = 1.2$  K) and StyCast 1266, which has excellent machinability. In this design, a circular StyCast piece with a center hole is sealed with StyCast to an aluminum cap which is sealed to the niobium lid with indium. A superconducting coaxial cable (such as NbTi-NbTi) is stripped down to its inner conductor and inserted through the StyCast piece. The cable is held in place with a U shaped clamping piece while the microwave coupling is tested. The cable can be moved further into the cavity or pulled further out until the desired microwave coupling strength is obtained; StyCast is then used to make the final seal between the inner conductor of the coax and the circular StyCast piece. The downside of this design is that three seals (two StyCast and one indium) must be made leak tight for each microwave coupler.

## 5.7 Sapphire

As described in Section 2.3.6, we also investigated an optomechanical design using a sapphire whispering gallery mode resonator as the microwave cavity. Inside the sapphire resonator is a hollow annulus which is filled with superfluid  $^4\text{He}$ . The cavity was made from two separate pieces of sapphire: a bottom piece, machined with the annular helium cavity and a fill line (Fig. (5.27a)) and a top piece which is a simple cylinder (Fig. (5.27b)). Detailed CAD drawings for the sapphire design are shown in Appendix G. The final sapphire resonator was made by bonding together the top and bottom pieces; a van der Waals bond will form between clean, polished pieces of sapphire that are pressed together and heated. This bonding process is available commercially from Onyx Optics [157] under the trademarked name Adhesive Free Bond. The final bonded and polished cavity is shown in Fig. (5.28).

Fig. (5.27c) shows the test piece which was made with the same final dimensions as the bonded cavity. The test piece was used to understand the microwave properties of the sapphire resonator. Transmission measurements of a whispering gallery mode (WGM) resonator are made by coupling to the evanescent microwave fields. The sapphire resonator was held in an aluminum cavity so that the microwave couplers could be conveniently mounted near the sapphire and adjusted. The aluminum cavity also limits the microwave losses from leakage of the evanescent fields of the WGM resonator. Microwave  $Q$ s of  $2 - 4 \cdot 10^6$  were measured with the test piece at 77K. Data from 300K (where the mode frequency is 10.97 GHz) and 77K (11.06 GHz) are shown in Fig. (5.29a). Each whispering gallery mode is degenerate, comprised of modes propagating in the clockwise and counterclockwise directions. In the case of Fig. (5.29a) the degeneracy is broken at 77K and the two modes are separated by about 60 kHz.



Figure 5.27: The sapphire pieces after machining: a) the bottom piece of the cavity design, showing the annular cavity that will be filled with helium, b) the top piece of the cavity design, c) the test piece of equal size to the final bonded piece, before polishing.

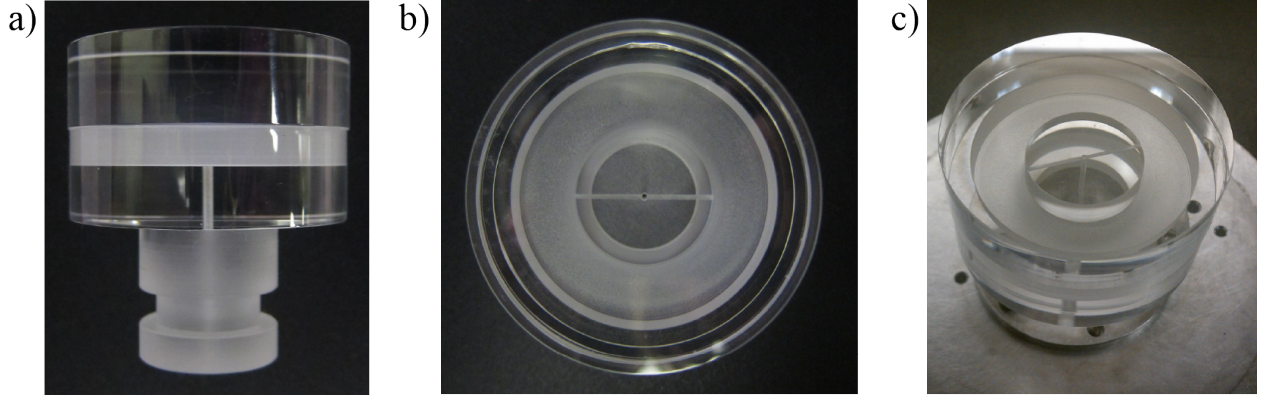


Figure 5.28: The bonded and polished sapphire cavity: a) side view. Note the discontinuity in the outer edge at the location of the bond line, b) top view, c) view from the top edge with the cavity sitting in the base of the aluminum shielding cavity. Notice the fill line connecting the annular cavity to the base of the sapphire mushroom.

While the microwave modes of the test piece had reasonable  $Q$  factors, measurements of the microwave spectrum of the bonded cavity showed only very lossy modes. The modes were so low  $Q$  that they were difficult to locate; an example is shown in Fig.(5.29b). One explanation for the low  $Q$  is the discontinuity of the bond line, which is clearly noticeable in Fig. (5.28a). One can also see the effect of the bond on incident light at the top and bottom edges of the piece in Fig. (5.28b). In addition, the inner annular cavity surface is not polished. These imperfections exist in regions where the microwave field amplitude is high and must contribute significantly to the loss tangent.

Finally we note that a problem with the sapphire design is that the optomechanical coupling is  $\approx 100$  times smaller than in the niobium cavity design. The smaller coupling arises because the WGM is mainly located within the sapphire, where it does not overlap with the helium acoustic modes. Given that the optomechanical coupling rate is already a difficulty in the niobium cavity setup, it would be best to alter the sapphire design to improve this parameter.

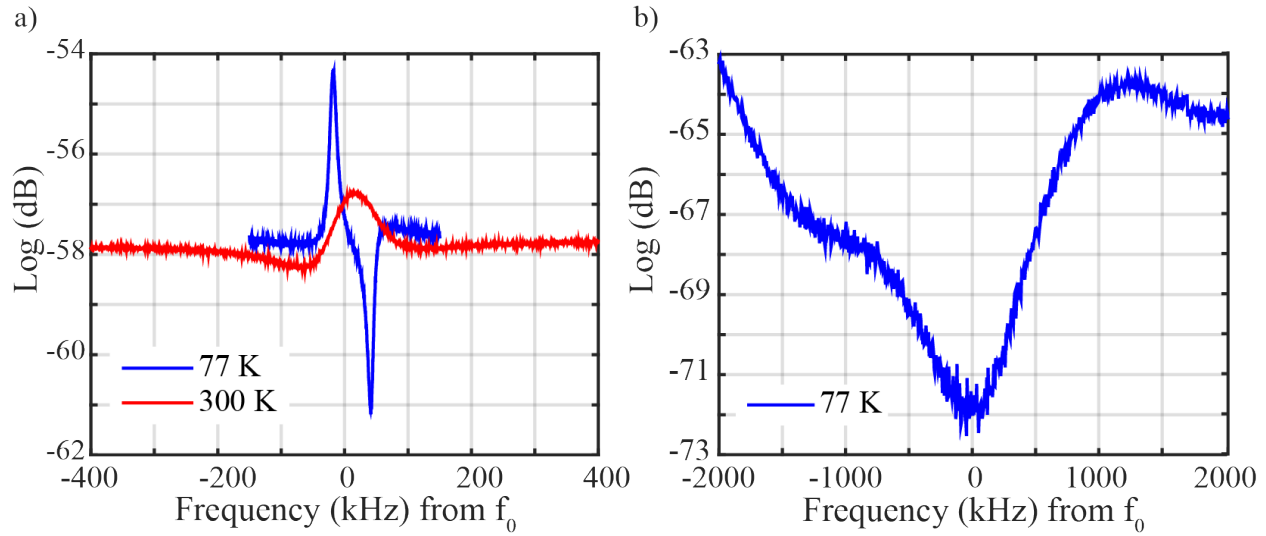


Figure 5.29: a) Transmission measurements of the highest  $Q$  mode of the test resonator (no annular cavity) at both 300K (red,  $f_0 = 10.97$  GHz) and 77K (blue,  $f_0 = 11.06$  GHz). At 300 K, the  $Q$  is  $66 \cdot 10^3$ , and at 77 K the  $Q_s$  of the left and right peaks are  $2.4 \cdot 10^6$  and  $2.8 \cdot 10^6$ , respectively. b) The highest quality factor "mode" that could be found at 77K in the spectrum of the bonded resonator,  $f_0 = 11.05$  GHz.

# Chapter 6

## Outlook

### 6.1 Ground State Cooling

As discussed in Chapter 2, one of the most interesting directions in the field of optomechanics has been the ability to cool macroscopic oscillators to their quantum ground state and to observe quantum limited behavior. Here we address the prospects for achieving ground state cooling in our superfluid acoustic resonator.

As discussed in Chapter 3, in the absence of heating limitations, the final occupation of the mechanical mode is given by:

$$n_M = \frac{n_M^{th} + C \cdot n_M^{opt}}{1 + C}, \quad (6.1)$$

where  $n_M^{th}$  is the thermal occupation of the mechanics,  $n_M^{opt}$  is the occupation of the optical mode,  $C = \Gamma_{opt}/\gamma_M$  is the cooperativity,  $\Gamma_{opt} = 4g_0^2/\kappa_{tot} \cdot n_P$  is the optomechanical coupling rate,  $\kappa_{tot}$  is the microwave cavity linewidth,  $g_0 = \partial\omega/\partial x \cdot \Delta x_{ZP}$  is the single photon optomechanical coupling rate,  $n_P$  is the number of pump photons in the cavity,  $\gamma_M = \omega_M/Q_M$  is the intrinsic loss rate of the mechanics,  $\omega_M$  is the mechanical frequency, and  $Q_M$  is the mechanical quality factor. As the cooperativity increases, the occupation of the mechanics asymptotes to the occupation of the optical mode. In our niobium cavity, the TE<sub>011</sub> mode frequency is 10.6 GHz; from the Boltzmann relation,  $n^{th} = 1/(e^{\hbar\omega/k_B T} - 1)$ , this mode is easily in its ground state even at 700 mK. While our intrinsic  $g_0$  is small, (currently  $g_0 = -10^{-8} \cdot 2\pi$

Hz in the 8115 Hz mode),  $C$  can be made large by increasing the number of pump photons  $n_P$ . As discussed in Section 2.5, we expect to be able to achieve large pump powers without heating the system.

The biggest difficulty we face is that the microwave cavity will be occupied far above its thermal value, for instance by phase noise of the sideband cooling tone. As detailed in Chapter 3, this occupation will be given by:  $n_M^{opt} = S_{noise}/\hbar\omega_C \cdot \kappa_{in}/\kappa_{tot}$ . Therefore increasing  $n_P$  of the sideband cooling tone will eventually result in an increase in mechanical occupation.

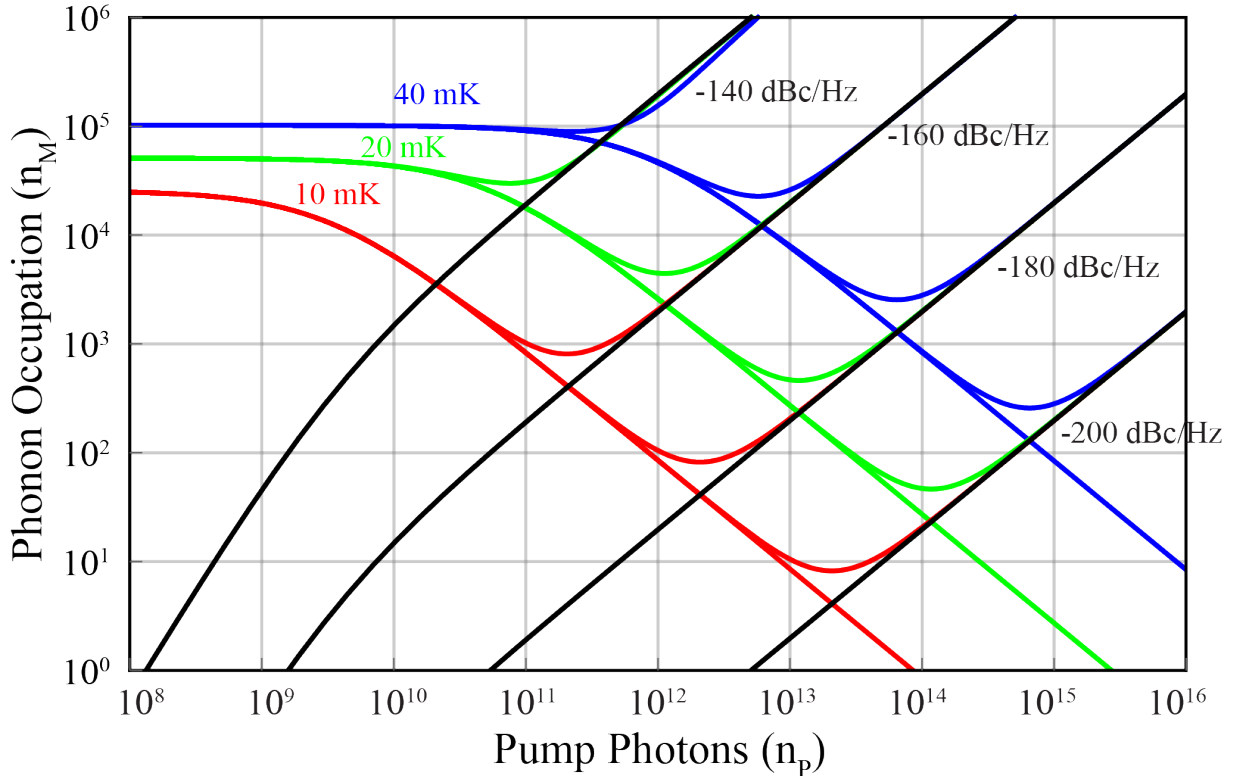


Figure 6.1: The phonon occupation of the superfluid acoustic mode versus the number of pump photons ( $n_P$ ) in the sideband cooling tone, ignoring the effects of dielectric heating, for three starting temperatures: 40 (blue), 20 (green) and 10 mK (red), assuming that  $Q$  is limited by temperature. In each case, the curve that continues to drop with increasing photon number ignores the effect of source phase noise, while the curve that reaches a local minimum includes the effect. The black curves denote sources of various phase noise ( $-140, -160, -180, -200$  dBc/Hz), as labeled on the figure.

The phonon occupations that can be achieved with our current system, assuming that mechanical  $Q$  is limited by temperature through the 3PP and that we can achieve an internal microwave  $Q$  of  $10^9$  (where  $\kappa_{in} = \kappa_{out} = \kappa_{int}$ ), are shown in Fig. (6.1). Note that here we

have ignored the effects of dielectric heating. The occupation resultant from the phase noise of the microwave source is shown for sources with four different phase noise floors:  $\mathcal{L}(10\text{ kHz}) = -140, -160, -180, \text{ and } -200\text{ dBc/Hz}$ . For reference, with the parameters we have assumed, the conversion between pump photon number ( $n_P$ ) and power incident on the cavity ( $W_{in}$ ) is about  $W_{in} = 5 \cdot 10^{-16}n_P$ .

Finally, we address heating from dielectric loss in the system. The power dissipated in the niobium cell will be given by Eqn. (2.38) where we assume  $Q_{int} = 10^9$ . Similarly, the dielectric loss in the helium itself will be given by Eqn. (2.37) where we assume  $\tan(\delta) = 10^{-10}$ . We note, however, that this is only the best limit which has been placed on the helium loss tangent experimentally; in fact  $\tan(\delta)$  is expected to be much lower, so we can consider this a "worst case" value. In Section 2.5, we calculated the time constant of thermalization between the helium and the niobium and the cooling power of the fridge. With these relations, plus the equations for dielectric heating, we can calculate how much the helium temperature will increase using Eqn. (2.40). We use this increased helium temperature to calculate the occupation of the acoustic mode ( $n_M^{th}$ ) and the mechanical damping rate ( $\gamma_M$ ). The phonon occupations which are obtained including both the source phase noise and the effects of dielectric heating are shown in Fig. (6.2) for initial temperatures of 10, 20, and 40 mK and phase noise values of  $\mathcal{L}(10\text{ kHz}) = -140, -160, -180, \text{ and } -200\text{ dBc/Hz}$ . Notice that even with a starting temperature of 10 mK, and a "worst case" assumption of  $\tan(\delta) = 10^{-10}$ , dielectric heating does not increase the acoustic mode occupation until  $n_P > 10^{12}$ . If we can remove all sources of dielectric loss aside from the helium and the niobium cell, achieving large pump powers in this system looks very promising.

Note that the lowest phase noise source available in the lab during the time-frame of this work has a phase noise of  $\mathcal{L}(10\text{ kHz}) \approx -110\text{ dBc/Hz}$ . The best commercially available source is the Agilent E8257D PSG with low phase noise options [158], which has a phase noise on a 10 GHz carrier of  $\mathcal{L}(10\text{ kHz}) \approx -130\text{ dBc/Hz}$ . However, as we note from Fig. (6.1), achieving sideband cooling in the superfluid acoustic resonator requires a source with a phase noise lower than the best commercially available source can provide. Because of the phase noise requirements, ground state cooling in our superfluid optomechanical system with

its current parameters does not look promising. If we increase  $g_0$  by building a less massive oscillator, ground state cooling may be possible.

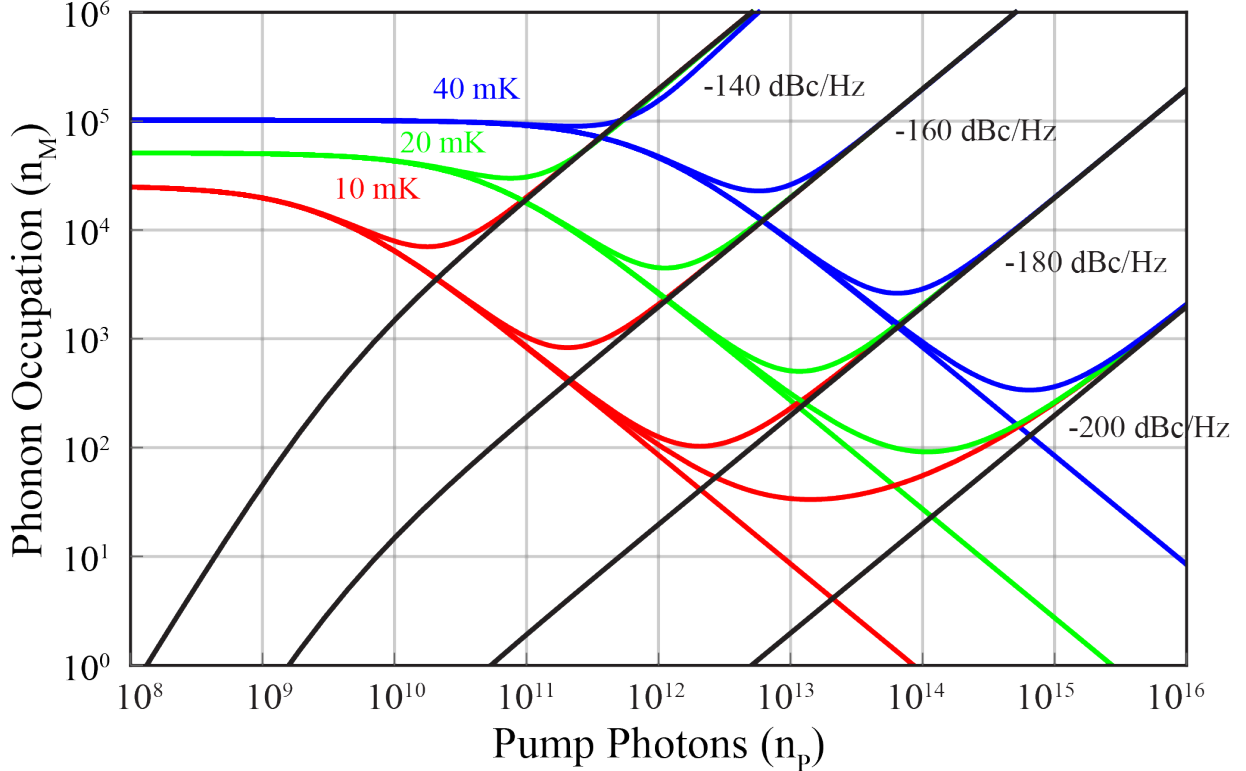


Figure 6.2: The phonon occupation of the superfluid acoustic mode versus the number of pump photons ( $n_p$ ) in the sideband cooling tone, including the effects of dielectric heating, for three starting temperatures: 40 (blue), 20 (green) and 10 mK (red), assuming that  $Q$  is limited by temperature. In each case, the curve that continues to drop with increasing photon number ignores the effects of heating and source phase noise, while the curve that reaches a local minimum includes both effects. The black curves denote sources of various phase noise ( $-140, -160, -180, -200$  dBc/Hz), as labeled on the figure.

### 6.1.1 Low Phase Noise Microwave Source

Low phase noise microwave sources have a broad range of applications, from time keeping [159] to tests of fundamental physics [160]. There are many different implementations, including sources based on microwave frequency sapphire whispering gallery modes [161–163], sources based on optical frequency division of lasers [164], and sources based on multiplying up a low phase noise low frequency microwave crystal [165].

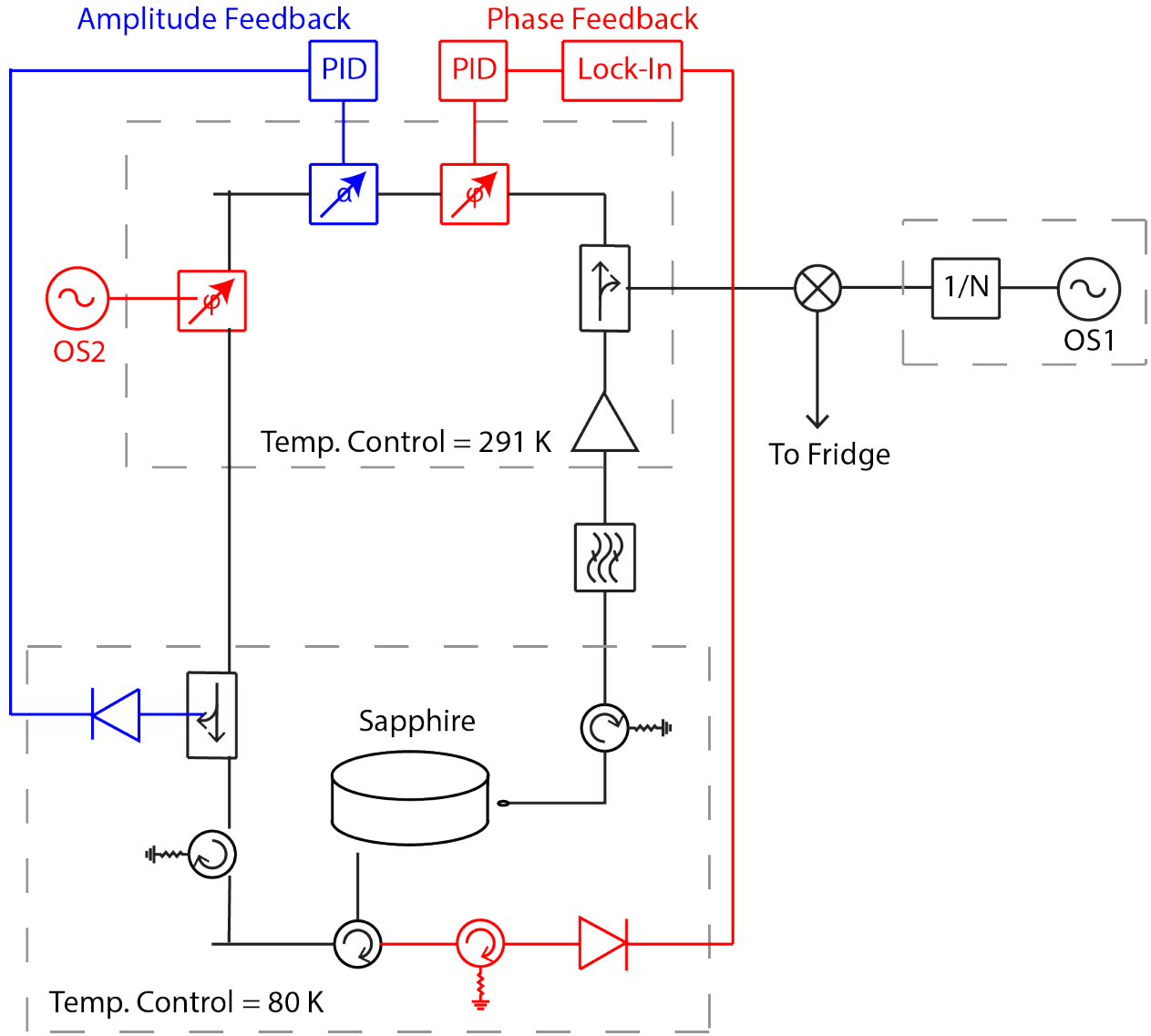


Figure 6.3: A schematic of our low phase noise microwave source as described in the text. The left circuit is the self resonant loop of a sapphire whispering gallery mode resonator, with control loops for both phase (red) and amplitude (blue). The right circuit consists of a microwave source and a divider and provides tunability to the source.

Because we require lower phase noise than any commercially available source can provide (see Fig. 6.1), we worked on a custom low phase noise source. It is based on the self resonant loop of a sapphire whispering gallery mode oscillator; a diagram of our source is shown in Fig.

(6.3). In the ideal case, the phase noise of such a source is governed by Leeson's equation:

$$\mathcal{L}(f_{off}) = 10 \log \left( \left( \frac{Fk_B T}{2P_{in}} \right) \left( 1 + \left( \frac{f_0}{2f_{off}Q} \right)^2 \right) \left( 1 + \frac{f_C}{f_{off}} \right) \right), \quad (6.2)$$

where  $f_{off}$  is the frequency from carrier,  $F$  is the noise figure of the amplifier,  $P_{in}$  is the power incident on the sapphire,  $f_C$  is the flicker frequency of the amplifier, and  $f_0$  and  $Q$  are the frequency and quality factor of the sapphire WGM resonator. To our knowledge, Tobar [162] has built the lowest phase noise microwave source of this type. It displays a phase noise of  $\mathcal{L}(10 \text{ kHz}) = -170 \text{ dBc/Hz}$  on a 10 GHz carrier. Assuming our current best acoustic  $Q_M = 10^8$  at a temperature of 44 mK, and assuming we can achieve a microwave  $Q_C = 10^9$  with  $n_P = 10^9$ , this source would lower our detection noise temperature from 370 K (with the best source in the lab) to 20 mK. A detection temperature of 20 mK would enable us to measure the thermal motion of our superfluid acoustic modes.

A diagram of our source is shown in Fig. (6.3). The self resonant loop provides a low phase noise source at a single frequency, one of the eigenfrequencies of the sapphire disk, as chosen by a bandpass filter. To maintain a stable frequency and amplitude over time, the sapphire disk is temperature regulated at 80 K while the room temperature electronics are temperature regulated at about 291 K. The frequency is further stabilized with a Pound Drever Hall (PDH) feedback loop. The PDH sidebands are applied using a voltage controlled phase shifter. The sidebands reflect from the sapphire cavity and, if the phase of the loop has changed, there will also be a reflected signal at the previous sapphire cavity eigenfrequency. The reflected signals are detected with a power diode. From the power diode, the signal is measured on a lock-in amplifier to produce an error signal which tunes a second voltage controlled phase shifter through a PID controller. This phase shifter corrects for any change in phase as given by the error signal. The amplitude is stabilized with a separate loop. The first step is to measure a fraction of the power incident on the sapphire cavity. This measured power is fed into a PID which adjusts a voltage controlled attenuator to maintain a constant power.

The entire self resonant loop can provide a source only at a single frequency; in our setup

that frequency is 10.583 GHz, which is about 20 MHz away from the frequency required for the superfluid optomechanics experiment. To get to the final required frequency, the source has a second arm which provides tunability; this tuning frequency is mixed with the sapphire frequency to achieve the final frequency needed for the experiment:  $\omega_{SF} = \omega_{WGM} + \omega_{tune}$ . This second arm is low phase noise because of its low frequency. We take a commercially available low phase noise microwave source and divide it down until we achieve the  $\approx 20$  MHz signal. Each division lowers the microwave phase noise by 6 dB. For example, if we begin with a 1 GHz signal with a phase noise of  $-135$  dBc/Hz, we can divide the frequency five times and end with a 20 MHz signal with a phase noise  $-165$  dBc/Hz.

While we expect this custom built source to have very low phase noise, it is still a work in progress. During the timeframe of this thesis, it was not able to produce a frequency stable, low phase noise signal that could be used for the optomechanical experiment.

It is also possible to filter the phase noise of the microwave source using a superconducting filter cavity such as the niobium resonator used for the cell. The amount of filtering that can be achieved will be determined by the linewidth of this cavity  $\kappa_F$  and the offset frequency (for sideband cooling,  $\Delta = \omega_M$ ) at which the filtering is required. The filtered power ( $W_{filter}$ ) will be related to the input power ( $W_{in}$ ) as:

$$W_{filter} = \frac{W_{in}}{1 + (2\Delta/\kappa_F)^2}. \quad (6.3)$$

A reasonable achievable microwave  $Q$  in niobium is  $Q = 10^9$  and our mechanical mode frequency is  $\omega = 2\pi \cdot 8115$  Hz.

## 6.2 Gravitational Wave Detector

Given the relatively large mass of our system ( $m = 6$  g), the zero point motion at low temperatures is quite small. For instance at 10 mK,  $x_{th} = \sqrt{k_B T / \hbar \omega_M} \approx 10^{-16}$  m. If we imagine the helium as a mass on a spring within the niobium resonator, the motion of the spring is described by the frequency and quality factor of the superfluid acoustic resonator.

Because the motion of the cell is coupled to the motion of the helium through this spring, we expect the amplitude of vibration to be  $Q$  times greater for the helium mass than for the cell. Therefore if the amplitude of the helium's motion is limited by temperature, and we reach a superfluid acoustic  $Q \approx 10^{10}$ , we expect motion of the cell on the order of  $10^{-26}$  m, or a strain on the order of  $10^{-25}$ . With displacement sensitivities on this scale, one naturally considers using the system as a sensitive force detector.

One area of recent interest is gravitational wave astronomy, giving the exciting first detection of gravitational waves by the LIGO collaboration [166]. Both LIGO interferometers detected the signal of two black holes coalescing, separated by the 10 ms travel time between them, in September 2015. While LIGO is a broadband detector, ideal for detecting short term, high strain events, there are many astrophysical sources of gravitational waves.

Here we consider using the superfluid optomechanical system as a resonant bar detector, much like a Weber bar [167], for sources of continuous gravitational waves. We are specifically interested in pulsars, which are stars with a misalignment between their spin and electromagnetic axes. For an asymmetric distribution of mass around their spin axis, pulsars are thought to emit gravitational radiation at frequencies  $f_{GW} = 2f_S$  where  $f_S$  is the frequency at which they spin. Pulsars are an ideal source because their frequencies are well known and stable. Additionally, their frequencies range above 1 kHz, where we could feasibly build a helium resonant detector. The frequencies of pulsars will vary over time, not only from Doppler shifts from the relative motion of the Earth and the pulsar but also due to random glitches. The frequency stability is about  $\delta f/f \approx 10^{-6} - 10^{-11}$  but older pulsars are more stable. [168] LIGO and VIRGO have searched unsuccessfully for over 100 pulsars [169], setting a maximum strain limit of  $h \approx 10^{-25}$ .

Pulsars emit gravitational waves because of their asymmetric mass distribution. The power of the emitted waves is [170]

$$P \propto \frac{G \cdot \ddot{Q}_{ij}^2}{c^5}, \quad (6.4)$$

where  $Q_{ij} = \rho \int_{\text{body}} x_i x_j dV$  is the third time derivative of the quadrupole moment. Owing to the small values of this power, gravitational strain fields at Earth are extremely small and

have proven difficult to detect.

In order to compare gravitational antennas, it is helpful to have a generalized treatment of their sensitivity. Hirakawa et al. [171] developed such a framework and it is briefly described here. They write the displacement field for the antenna,  $\mathbf{u}(r, t)$ , in terms of a generalized coordinate  $\xi(t)$  which satisfies  $\mathbf{u}(r, t) = \xi(t) \mathbf{w}(\mathbf{r})$ . Here we are assuming the antenna's motion is of a single eigenmode, so that  $\mathbf{w}$  represents the spatial profile of that mode and  $\xi$  represents the amplitude of displacement.

In terms of this displacement field  $\mathbf{u}(r, t)$  the equation of motion for a gravitational antenna is given by [172]:

$$\mu \left( \ddot{\xi} + \frac{\omega_m}{Q_m} \dot{\xi} + \omega_m^2 \xi \right) = \frac{1}{4} \sum_{ij} \ddot{h}_{ij} q_{ij}, \quad (6.5)$$

where  $\mu = \int \rho \mathbf{w}^2 dV$ , is the reduced mass of the mode. The term on the right hand side represents the force acting on the mode from the passing gravitational field, where  $h_{ij}$  is the metric perturbation and  $q_{ij}$  is the dynamic part of the quadrupole moment of the antenna eigenmode:

$$q_{ij} = \int \rho \left( w_i x_j + x_i w_j - \frac{2}{3} \delta_{ij} \mathbf{w} \cdot \mathbf{r} \right) dV. \quad (6.6)$$

The effective area of such an antenna, meaning the area which actively couples to a gravitational wave, is given by:

$$A_G = \frac{2}{\mu M} \sum q_{ij}^2, \quad (6.7)$$

where  $M$  is the mass of the antenna. Notice  $A_G$  is independent of choice of  $\xi$ . To incorporate both the polarization of the gravitational wave and the orientation of the antenna's quadrupole, we write polarization matrices  $\mathbf{e}(\mathbf{k})^A$  where  $A$  defines the polarization of the GR ( $A = +$  or  $\times$ ).  $\mathbf{k}(\theta, \phi, \psi)$  incorporates the incident direction of the waves  $(\theta, \phi)$  and the polarization of the antenna  $(\psi)$ , which is the rotation of its  $x - y$  plane along the source's

line of sight [173]. The directivity function is then defined as:

$$d^A(\theta, \phi) = \frac{5}{4} \frac{\left(\sum q_{ij} e_{ij}^A(\mathbf{k})\right)^2}{\sum q_{ij}^2}. \quad (6.8)$$

In keeping with our current niobium cavity design, we work with a cylindrical detector. Since we search for sources of continuous waves, longer measurement times ( $\tau_{\text{int}}$ ) lead to lower strain sensitivities. For such an antenna, the minimum detectable strain field with  $2\sigma$  certainty is [174]:

$$h_{\min} \approx 2 \sqrt{\frac{S_{hh}[\omega]}{\tau_{\text{int}}}} = \sqrt{\frac{320k_B(T + T_e)}{M\omega_G^3 A_G d^A Q_m \tau_{\text{int}}}}, \quad (6.9)$$

where  $T$  is the thermal bath temperature and  $T_e$  is the added noise temperature of the measurement system.

We will consider two cylindrical geometries (defined as G1 and G2), with radius  $a = 10.8$  cm and lengths  $L1 = 50$  cm or  $L2 = 3$  m. This design and its sensitivity are described more fully in Singh et al [2]. We focus on the  $l = 0, m = 2, n = 0$  acoustic mode because of its large quadropole moment. In both considered geometries, the  $l = 0, m = 2, n = 0$  has a frequency  $\omega_M = 1071 \cdot 2\pi$  Hz. There are three pulsars within 15 Hz of this frequency, namely pulsars J0034-0534, J1301+0833, and J1843-1113. The effective area  $A_G = 0.629\pi r^2$  in both designs. The effective mass is  $\mu = 0.625M$  for G1 and  $\mu = 0.625M$  for G2. The minimum strain sensitivities (thermal noise limited) that can be achieved with G1 and G2 are shown in Fig. (6.4), along with the current strain limit set by LIGO and the strain limit expected from advanced LIGO.

We now evaluate the experimental parameters required to achieve the strain sensitivities shown in Fig. (6.4). Note that we are assuming for our minimum strain sensitivities that all other noise sources (aside from thermal and detection noises) have been eliminated; most importantly, we assume the difficult task of isolating the cell from environmental vibrations has been achieved. In the following, we focus on the  $L1 = 50$  cm design. The best optomechanical coupling is achieved to the  $TM_{110}$  mode, which has a frequency  $\omega_C = 1.6 \cdot 10^9 \cdot 2\pi$  Hz. The single photon coupling rate is  $g_0 = \partial\omega/\partial P \cdot \Delta P_{ZP} = -8 \cdot 10^{-11} \cdot 2\pi$  Hz. To achieve

a  $Q = 10^{11}$  requires temperatures  $T \approx 4$  mK and  $n_3/n_4 < 3 \cdot 10^{-11}$ . At 4 mK the  $Q$  expected from the three phonon process is  $Q > 10^{12}$ ; with lower  $^3\text{He}$  impurities,  $Q \approx 10^{11}$  could be achieved at higher temperatures; with the best known sample  $n_3/n_4 \approx 10^{-12}$ ,  $Q = 10^{11}$  at  $T = 8$  mK. Assuming a HEMT amplifier with  $T_N = 5$  K, to limit the noise detection temperature to 1 mK, meaning that the added noise of our detection scheme is equal to the thermal noise of the helium oscillator at 1 mK, requires pump photon powers  $n_P \approx 7 \cdot 10^{10}$  and a source with phase noise  $\mathcal{L}(1\text{kHz}) \approx -145 \text{ dB}_c/\text{Hz}$ . To achieve sideband cooling in this system is quite difficult. For instance, one can begin to damp the oscillator when  $C > 1$ ; here this requires  $n_P = 7 \cdot 10^{11}$ .

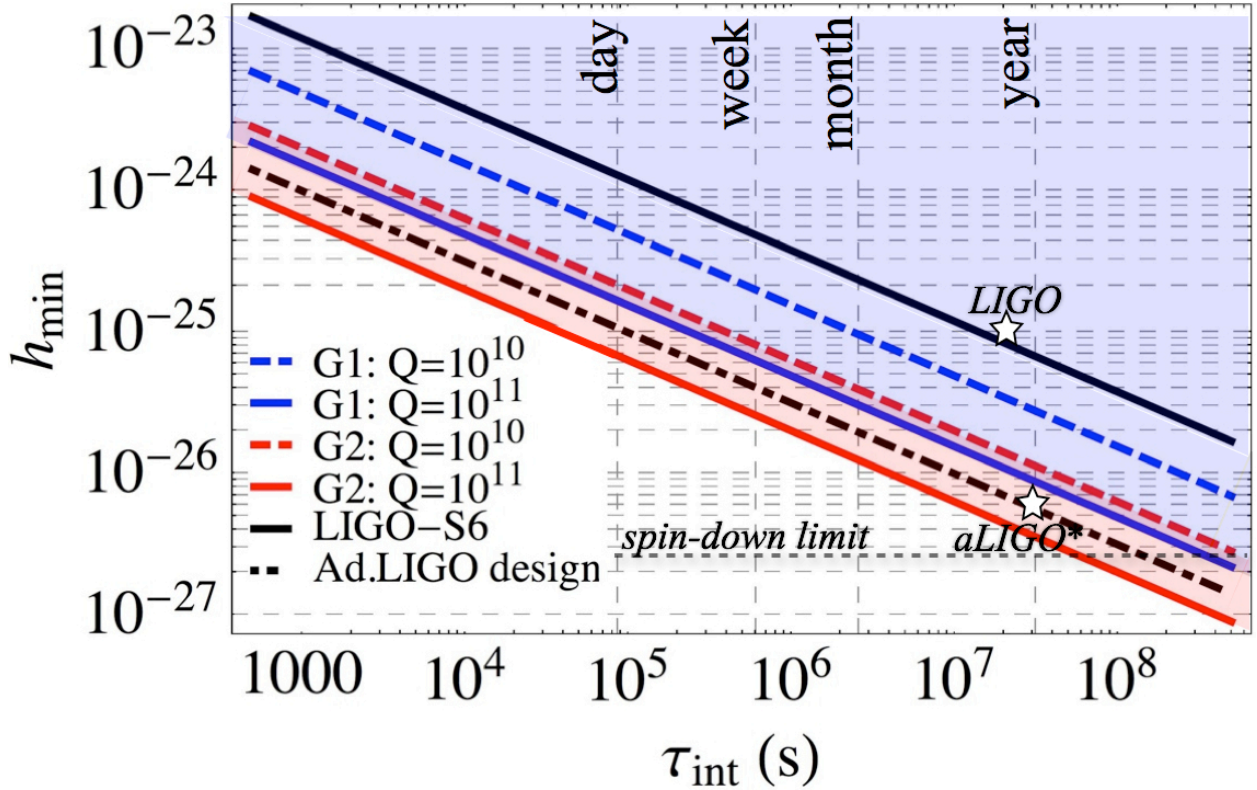


Figure 6.4: The minimum detectable strain  $h_{min}$  versus integration time  $\tau_{int}$  for our superfluid acoustic detectors [2], G1 (blue) and G2 (red) assuming mechanical  $Q$  of  $10^{10}$  (dotted) and  $10^{11}$  (solid). Also shown is the achieved strain sensitivity of LIGO-S6 (solid, black) and the design sensitivity of advanced LIGO (dotted black). The stars indicate the limit set by LIGO and the limit expected from advanced LIGO. The spin down limit of the pulsar J1301+0833 is also shown as the dotted horizontal line.

Finally we note a couple of advantages of the helium detector as opposed to past Weber bar realizations. The frequency of a helium resonant bar detector will be tunable by pressur-

ization. Because 25 bar is required to solidify helium, frequencies can be tuned by up to 50% with pressure [175]. For instance, if the pulsar frequency changes over time, the superfluid acoustic mode could be tuned via pressurization to remain resonant. Additionally, optomechanical sideband cooling would broaden the resonator, increasing its bandwidth. Finally, the  $Q/T$  values for a helium oscillator are significantly better than values for metal Weber bars which have been used in the past [2].

### 6.3 Testing Minimum Length Scales

While general relativity and quantum theory are each highly successful at explaining phenomena at their respective scales, there is as yet no accepted theory which unifies the two. The search for a theory of quantum gravity is difficult in part because of the lack of experimental results in a meaningful parameter regime. The phenomena that may inform such a theory are expected to become important only at the Planck scale, either lengths on the order of the Planck length,  $L_p = \sqrt{\hbar G/c^3} = 1.6 \cdot 10^{-35}$  m or energies on the order of the Planck energy  $E_p = \sqrt{\hbar c^5/G} = 1.2 \cdot 10^{19}$  GeV, where  $G = 6.67 \cdot 10^{-11}$  m<sup>3</sup>/kg·s<sup>2</sup> is the gravitational constant.

In many theories of quantum gravity, quantization of space leads to a minimum length scale equal to the Planck length, below which position can not be meaningfully defined. This minimum length requires a modification of the canonical uncertainty relation from quantum mechanics:  $\Delta x \Delta p \geq \hbar/2$ , which constrains only the product of position and momentum. One way of modifying the relation, which appears in several quantum gravity proposals, is as follows [176, 177]:

$$\Delta x \Delta p \geq \frac{\hbar}{2} \left( 1 + \beta_0 \left( \frac{\Delta p}{M_p c} \right)^2 \right), \quad (6.10)$$

where  $M_p = \sqrt{\hbar c/G} \approx 22 \mu\text{g}$  is the Planck mass and  $\beta_0$  is a constant that quantifies the amount of modification. The minimum length scale is then defined as  $\Delta x_{min} = L_P \sqrt{\beta_0}$ , so that if  $\beta_0 = 1$ , the minimum length is constrained to the Planck length.

Experimentally, the lowest limit that has so far been set is  $\beta_0 < 10^{33}$  [178] in the center of mass mode of the AURIGA detector, an 1100 kg aluminum bar cooled to an occupation of  $n_M = 2 \cdot 10^4$ . For comparison, LIGO's position measurements place a limit of  $\beta_0 \approx 10^{34}$  [179]. Other limits are set by the lack of any deviation measured at the electroweak scale ( $\beta_0 \approx 10^{34}$  [180]) and the hydrogen 1S-2S energy difference ( $\beta_0 < 4 \cdot 10^{34}$  [181]).

Because the modified commutator changes the minimum energy of a harmonic oscillator, one way to place a limit on the minimum length scale is by measuring the energy of a normal mode:  $E_{exp} = \hbar\omega_M(n_t + 1)$ , where  $n_t$  is the phonon occupation of the mode and  $\omega_M$  is its frequency. Thermal occupation is given by  $n_t = 1/(e^{\hbar\omega_M/k_B T} - 1)$ , which reduces to  $n_t \approx k_B T/\hbar\omega_M$  at high temperatures.

Defining the position and momentum operators as  $x = \sqrt{\hbar/m\omega_M}X_M$  and  $p = \sqrt{\hbar m\omega_M}P_M$ , where  $X_M$  and  $P_M$  are dimensionless parameters, we can rewrite the commutation relation as:

$$\Delta X_m \Delta P_M \geq \frac{1}{2} (1 + \beta (\Delta P_M)^2), \quad (6.11)$$

where  $\beta = \beta_0 \hbar m \omega_M / (M_{PC})^2$ . Then the limitation given by measuring an energy  $E_{exp}$  will be  $E_{min} < E_{exp}$  where  $E_{min}$  is the modified ground state energy:

$$E_{min} = \frac{\hbar\omega_M}{2} \left( \sqrt{1 + \frac{\beta^2}{4}} + \frac{\beta}{2} \right) \approx \frac{\hbar\omega_M}{2} \beta. \quad (6.12)$$

If our superfluid acoustic oscillator is in its ground state with its current parameters ( $m = 0.006$  kg and  $\omega_M = 2\pi \cdot 8115$  Hz), the limitation placed by this constraint is  $\beta_0 < 4 \cdot 10^{33}$ , which is not an improvement on the current state of the art. Notice that more massive objects cause larger deformations to the commutation relations.

Pikovski et al. [3] have proposed a tabletop optomechanical scheme whereby lower constraints can be placed on  $\beta_0$ . They propose a measurement of the center of mass mode of the oscillator via its optomechanical coupling with a cavity optical field. Optomechanical systems are ideal because of their relatively large mass. In Pikovski et al.'s scheme [3], the center of mass mode of the oscillator is displaced in phase space via a set of optical pulses.

The phase of the optical field is changed by the resonator's commutator such that a deformation in the commutator can be accessed by measuring the mean of the optical field interferometrically.

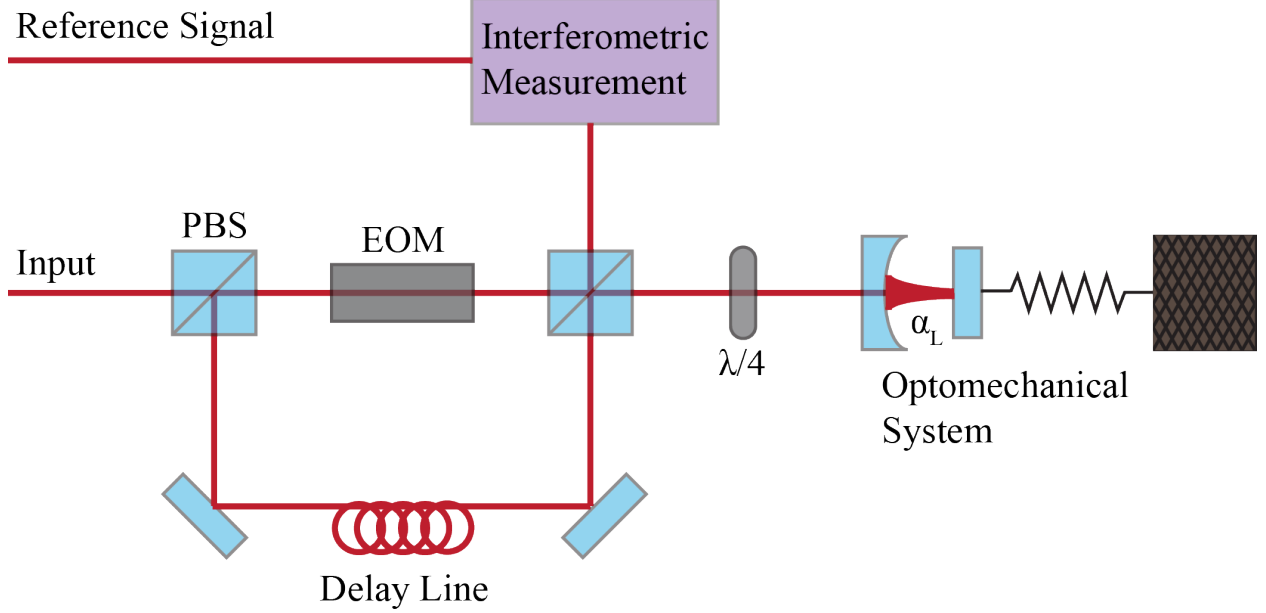


Figure 6.5: The experimental scheme proposed by Pikovski et al. [3] to measure the commutator's deformation. An input signal is incident on a polarizing beam splitter, then an electro optic modulator and a second beam splitter. The field reflects from the optical cavity and enters the delay line. The length of the delay line is such that the mechanical oscillator evolves by one quarter of a mechanical period between each interaction. After all four interactions, the signal is measured interferometrically with the reference.

The optical field interacts with the mechanical resonator through the optomechanical interaction of strength  $\lambda = g_0/\kappa = \partial\omega/\partial x \cdot \Delta x_{zp}/\kappa$  where  $g_0$  is the single photon coupling rate and  $\kappa$  is the optical cavity linewidth. Pikovski et al. [3] suggest a series of pulses that will produce four displacements in phase space, described by the operator:

$$\xi = e^{i\lambda n_L P_m} e^{-i\lambda n_L X_m} e^{-i\lambda n_L P_m} e^{i\lambda n_L X_m}. \quad (6.13)$$

In a classical field, these operations would cancel out with no effect on the optical field or the mechanical oscillator, but because  $X_M$  and  $P_M$  don't commute, the optical field picks up a phase difference which will depend on the deformation of the commutator.

If the commutator is described by Eqn. (6.10), then to first order  $\beta = \beta_0 \hbar \omega_M m / (Mpc)^2$ .

For large cavity occupations  $N_p \gg 1$  and for phonon occupations  $n_m \ll \lambda N_p$ , the mean of the optical field is given by:

$$\langle a_L \rangle = \alpha e^{-i\lambda^2 - N_p(1 - ie^{-i2\lambda^2})} e^{-i\Theta}. \quad (6.14)$$

The additional phase given by the contribution of  $\beta_0$  is:

$$\Theta(\beta) \approx \frac{4}{3} \beta N_p^3 \lambda^4 e^{-i6\lambda^2} = \frac{4}{3} \beta_0 \frac{\hbar\omega_M m}{(M_P c)^2} N_p^3 \lambda^4 e^{-i6\lambda^2}. \quad (6.15)$$

Notice that the change in phase is larger when  $\lambda$  is large. In order to be able to resolve  $\Theta$ , the imprecision in the measurement of phase must obey  $d\langle\Theta\rangle < \Theta$ . For interferometric measurements, the imprecision is given by:

$$d\langle\Theta\rangle = \frac{\sigma_{out}}{\sqrt{N_p N_r}}, \quad (6.16)$$

where  $N_r$  is the number of experimental runs and  $\sigma_{out}$  is the quadrature width of the optical state which is approximately equal to 1/2. Therefore one can solve for the limit on the resolution of  $\delta\beta_0$ , which in the case of measuring "zero" ultimately limits the value  $\beta_0$ :

$$\delta\beta_0 < \frac{1}{2\sqrt{N_p N_r}} / \frac{4}{3} \frac{\hbar\omega_M m}{(M_P c)^2} N_p^3 \lambda^4 e^{-i6\lambda^2}. \quad (6.17)$$

In the case of our current device,  $m = 0.006$  kg,  $\omega_M = 2\pi \cdot 8115$  Hz,  $g_0 = -2\pi \cdot 10^{-7}$  Hz, and  $\omega_C = 2\pi \cdot 10.6$  GHz. Assuming the niobium cavity has an internal  $Q$  of  $10^9$ , with  $\kappa_{in} = \kappa_{out} = \kappa_{int}$ , the total cavity linewidth  $\kappa = 2\pi \cdot 30$  Hz and  $\lambda = g_0/\kappa = 5.2 \cdot 10^{-10}$ . With these parameters, setting a bound of  $\delta\beta_0 \approx 1$  requires  $N_p = 10^{19}$  and  $N_r = 5 \cdot 10^6$ . However, setting a bound below the current limit of  $\delta\beta_0 \approx 10^{33}$  requires only  $N_p = 5 \cdot 10^9$  and  $N_r = 10^6$ . It is important to note that, as stated above, this scheme assumes  $n_m \ll \lambda N_p$ , which for  $N_p = 5 \cdot 10^9$ , requires  $n_M \ll 3$ . However, achieving such low mechanical occupations in our system requires high pump powers in the sideband cooling tone at  $\omega_P = \omega_C - \omega_M$ . Given the difficulty of achieving high pump powers without heating the system, it is of interest to

minimize the total number of pump photons in the cavity: the combined occupation of  $n_p$  from the sideband cooling tone and  $N_P$  for the phase space manipulations. Fig. (6.6) shows the value of both pump fields required to achieve  $n_m \ll \lambda N_p$ . The total pump power (blue line) will be minimum at  $\approx 3 \cdot 10^{12}$ .

Finally, we note that the quoted level of imprecision in  $\delta\beta_0$  can be achieved only if other noise sources are eliminated. This requires [3] both low temperatures ( $T < 100$  mK), which we achieve with our system on the dilution refrigerator, and low occupations of the mechanical resonator  $n_M < 30$ , which, with the parameters stated above, requires a sideband cooling tone with  $3 \cdot 10^{13}$  photons.

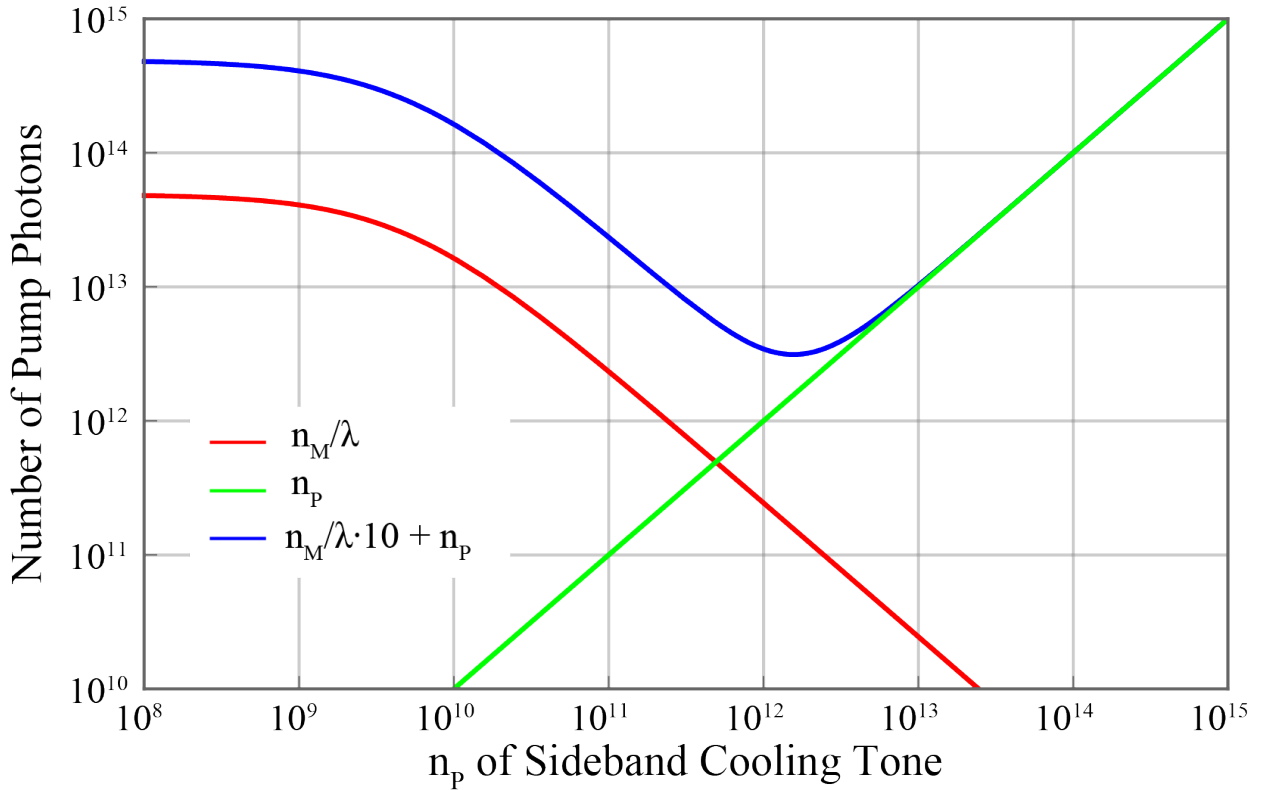


Figure 6.6: The minimum required pump power to achieve  $n_M \ll \lambda N_p$ . The red line shows  $n_M/\lambda$  resulting from the sideband cooling tone with pump photons  $n_p$ .  $n_p$  from the sideband cooling tone is shown with the green line. The blue line shows the total of  $n_p$  from the sideband cooling tone plus  $N_P = n_m/\lambda \cdot 10$  (fulfilling  $N_P \gg n_m/\lambda$ ) for the phase space manipulations of Pikovski et al.'s [3] scheme.

# Appendix A

# Table of Variables

Symbol	Definition
general definitions	
$k_B$	Boltzmann constant
$\hbar = h/2\pi$	reduced Planck constant
optomechanics variables	
$\omega_M$	mechanical frequency
$Q_M$	quality factor of the mechanical mode
$\gamma_M = \omega_M/Q_M$	intrinsic loss rate of the mechanics
$n_M$	occupation of the mechanics
$\omega_C$	microwave cavity frequency
$\kappa_{tot}, \kappa_{int}, \kappa_{ext}$	cavity loss rates: total, internal, and external
$g_0 = \partial\omega/\partial x \cdot \Delta x_{ZP}$	the single photon optomechanical coupling rate
$\Delta x_{ZP} = \sqrt{\hbar/2m\omega_M}$	the zero point motion of the mechanics
$\Gamma_{opt}$	optomechanical coupling rate
$C = \Gamma_{opt}/\gamma_M$	cooperativity
$n_P$	number of pump photons in the cavity
$\epsilon = \epsilon_R \epsilon_0$	permittivity
$\mu = \mu_R \mu_0$	permeability

---

Symbol	Definition
helium variables	
$T_\lambda$	temperature at lambda point
$\rho_S, \rho_N$	superfluid density, normal fluid density
$\rho_4$	density of helium-4
$c_4$	speed of sound in helium-4
$G = \rho_4/c_4 \partial c / \partial \rho$	Gruneisen parameter for helium-4
$\tau$	thermal phonon lifetime in helium-4
$\gamma, \delta$	constants in the dispersion relation for helium-4
$q$	momentum in dispersion relation
$\Delta E$	energy discrepancy between initial and final states in phonon process
$\kappa = 1/\rho_4 c_4^2$	compressibility
$m_3, m_4$	mass of ${}^3\text{He}$ atom, ${}^4\text{He}$ atom
$m_3^* = 2.34m_3$	effective mass of ${}^3\text{He}$ atom
$\sigma$	scattering cross section of ${}^3\text{He}$ atom
$x = n_3 / (n_3 + n_4)$	${}^3\text{He}$ impurity fraction

---

Table A.1: Table of variables

# Appendix B

## Bessel Functions

### B.1 Zeroes of Bessel Functions of the First Kind

The  $m$ th zero of the  $n$ th Bessel function is given by:  $J_n(x_{nm}) = 0$ .

$n \setminus m$	1	2	3	4	5	6	7
0	2.4048	5.5201	8.6537	11.7915	14.9309	18.0711	21.2116
1	3.8317	7.0155	10.1743	13.3237	16.4706	19.6159	22.7601
2	5.1356	8.4172	11.6198	14.796	17.9598	21.117	24.2701
3	6.3802	9.7610	13.0152	16.2235	19.4094	22.5827	25.7482
4	7.5883	11.0647	14.3725	17.6160	20.8269	24.019	27.1991
5	8.7715	12.3386	15.7002	18.9801	22.2178	25.4303	28.6266
6	9.9361	13.5893	17.0038	20.3208	23.5861	26.8202	30.0337
7	11.0864	14.8213	18.2876	21.6415	24.9349	28.1912	31.4228

Table B.1: Bessel function zeros.

## B.2 Extrema of Bessel Functions of the First Kind

The mth extrema of the nth Bessel Function is given by:  $J'_n(x'_{nm}) = 0$ .

n\m	1	2	3	4	5	6	7
0	3.8317	7.0156	10.1735	13.3237	16.4706	19.6159	22.7601
1	1.8412	5.3314	8.5363	11.7060	14.8636	18.0155	21.1644
2	3.0542	6.7061	9.9695	13.1704	16.3475	19.5129	22.6716
3	4.2012	8.0152	11.3459	4.5858	17.7887	20.9725	24.1449
4	5.3175	9.2824	12.6819	15.9641	19.1960	22.401	25.5898
5	6.41562	10.5199	13.9872	17.3128	20.5755	23.8036	27.0103
6	7.50127	11.7349	15.2682	18.6374	21.9317	25.1839	28.4098
7	8.57784	12.9324	16.5294	19.9419	23.2681	26.545	9.7907

Table B.2: Bessel function extrema, microwave modes.

### B.3 Extrema of Bessel Functions of the First Kind, Acoustic

The  $n$ th extrema of the  $m$ th Bessel function is given by:  $J'_m(j'_{mn}) = 0$ . Notice that in comparison to the table of extrema for the microwave modes, for the acoustic mode the first row is displaced.

$m \setminus n$	1	2	3	4	5	6	7
0	0	3.8317	7.0156	10.1735	13.3237	16.4706	19.6159
1	1.8412	5.3314	8.5363	11.7060	14.8636	18.0155	21.1644
2	3.0542	6.7061	9.9695	13.1704	16.3475	19.5129	22.6716
3	4.2012	8.0152	11.3459	4.5858	17.7887	20.9725	24.1449
4	5.3175	9.2824	12.6819	15.9641	19.1960	22.401	25.5898
5	6.41562	10.5199	13.9872	17.3128	20.5755	23.8036	27.0103
6	7.50127	11.7349	15.2682	18.6374	21.9317	25.1839	28.4098
7	8.57784	12.9324	16.5294	19.9419	23.2681	26.545	9.7907

Table B.3: Bessel function extrema, acoustic modes.

## Appendix C

# Niobium Cylinder Drawings

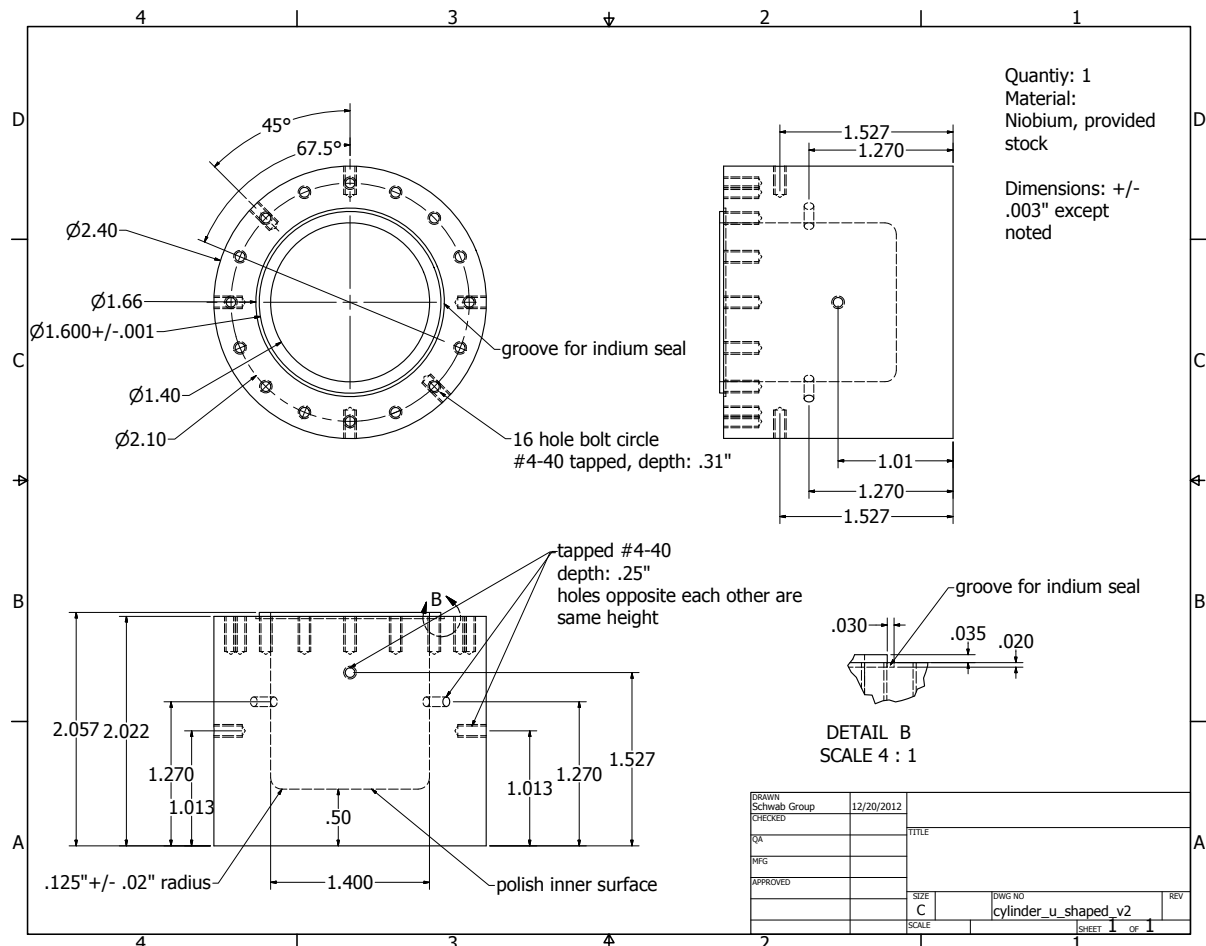


Figure C.1: Drawing of the cylinder body, machined from RRR grade niobium.

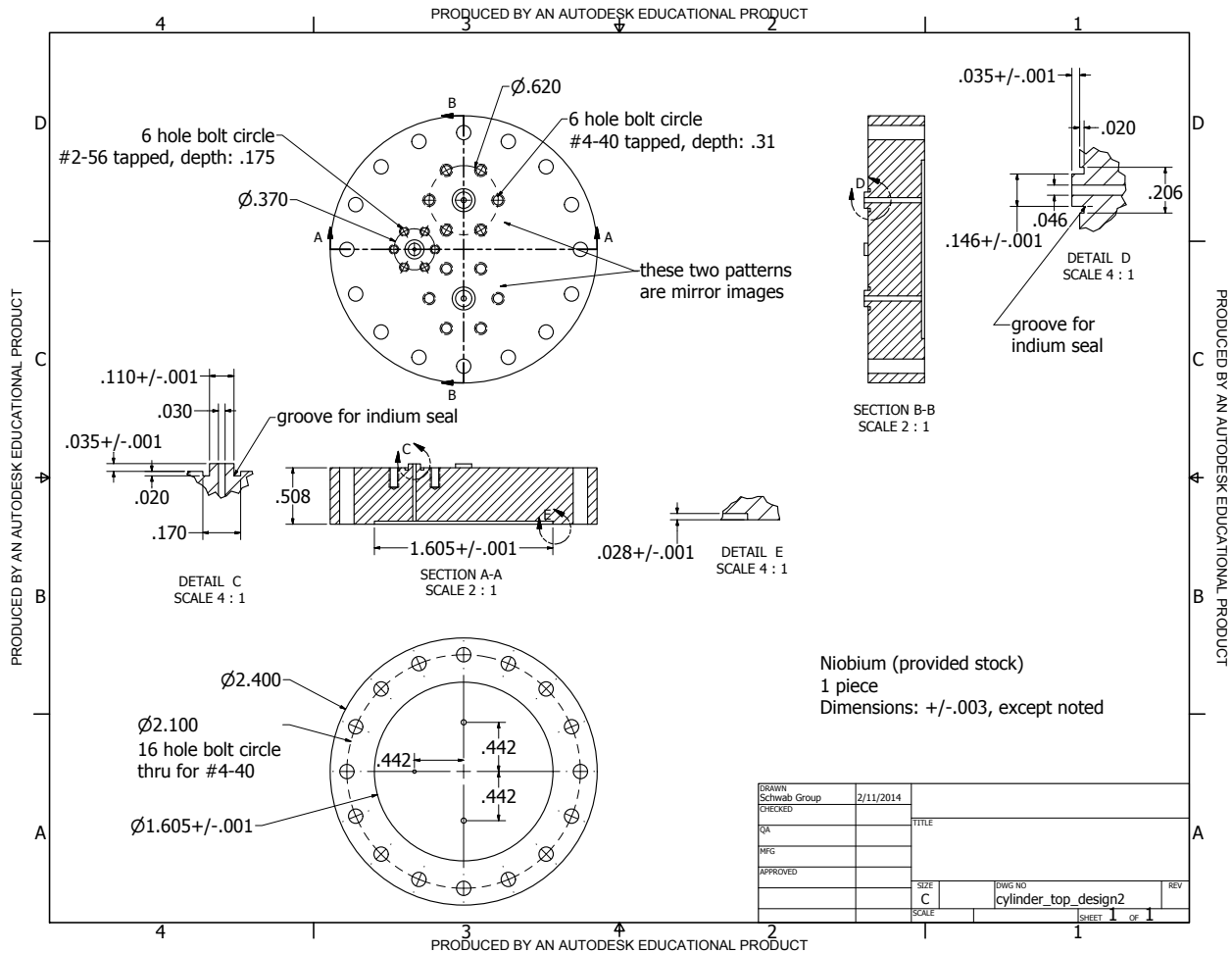


Figure C.2: Drawing of the cylinder top, machined from niobium with a minimum purity of 99.8%. Shown here is the final design with the fill line and microwave ports located at the position of the radial node in helium modes with only one radial node.

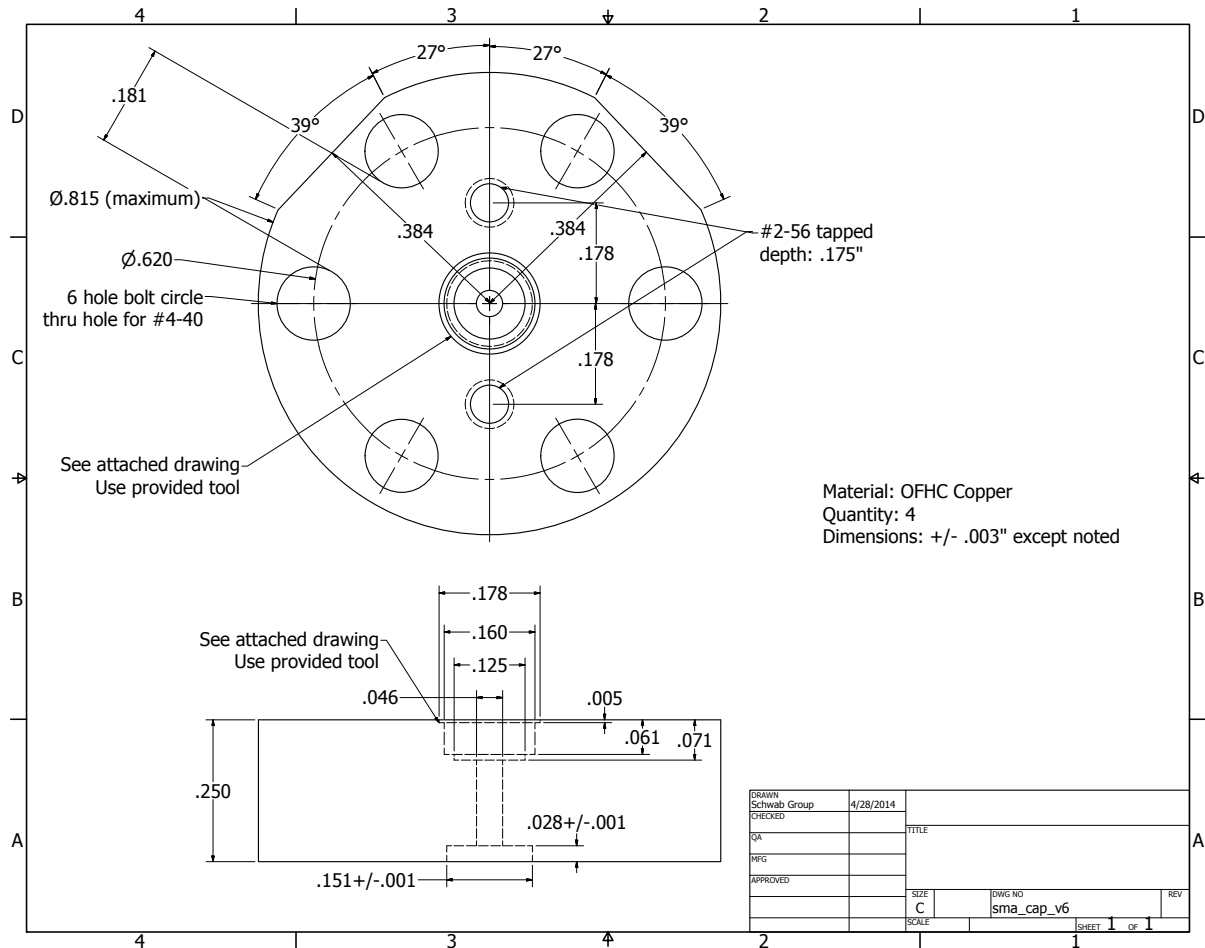


Figure C.3: Drawings of the cap for the microwave ports of niobium cavity. Shown is the final design with cutouts to allow all the pieces to fit on the niobium cavity lid.

# Appendix D

## Valve Drawings

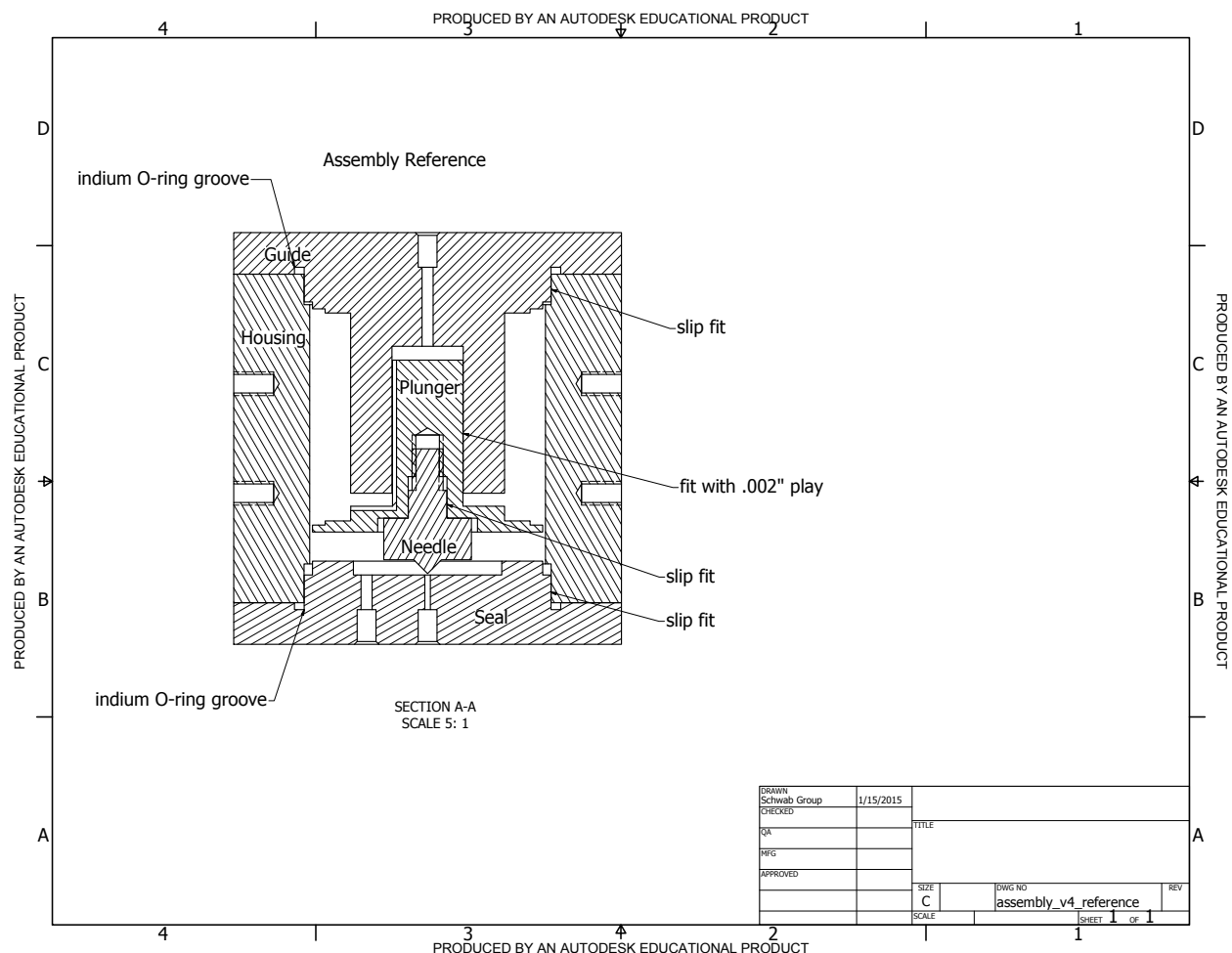


Figure D.1: Drawing of the valve assembly.

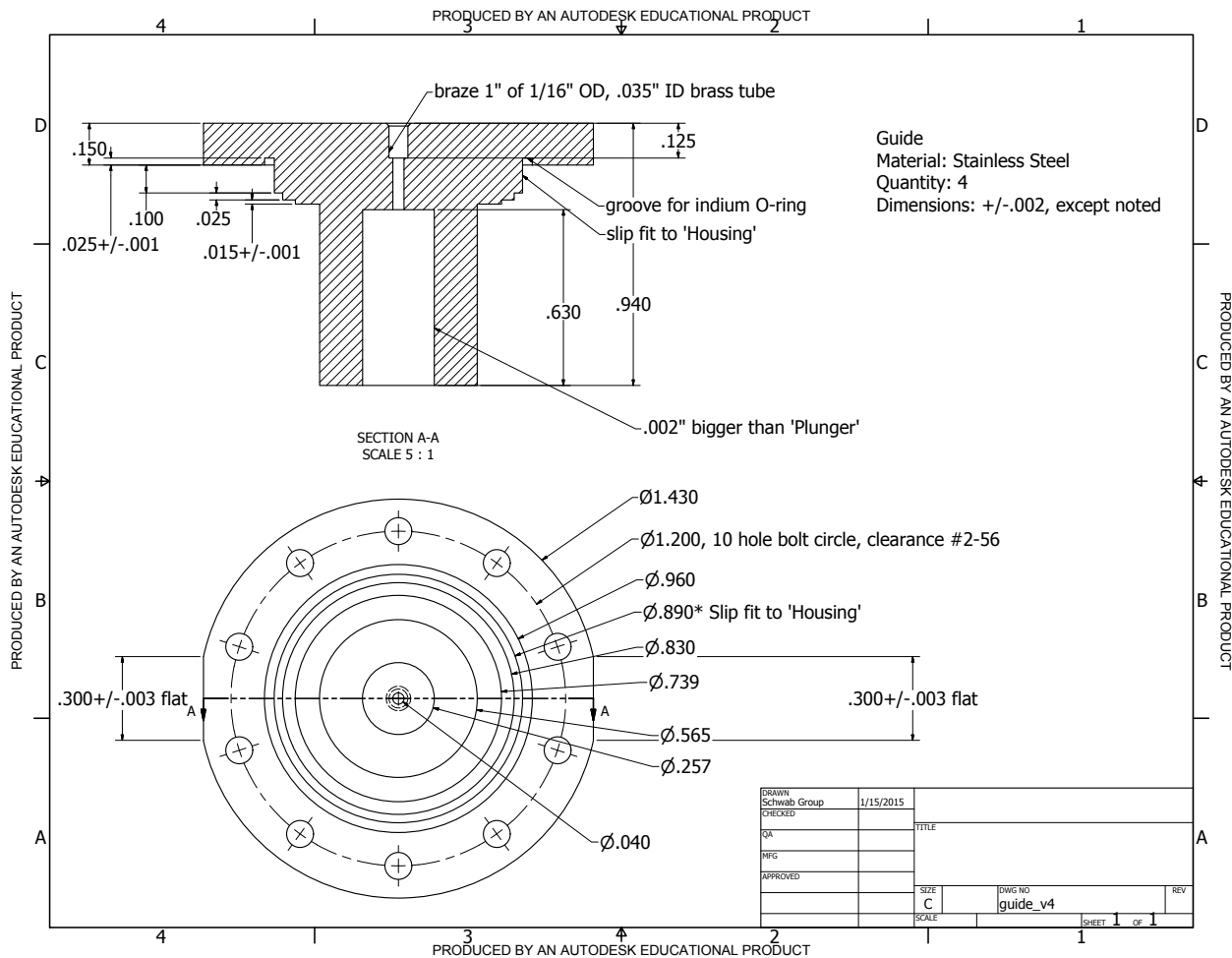


Figure D.2: Drawing of the guide, which is made from stainless steel.

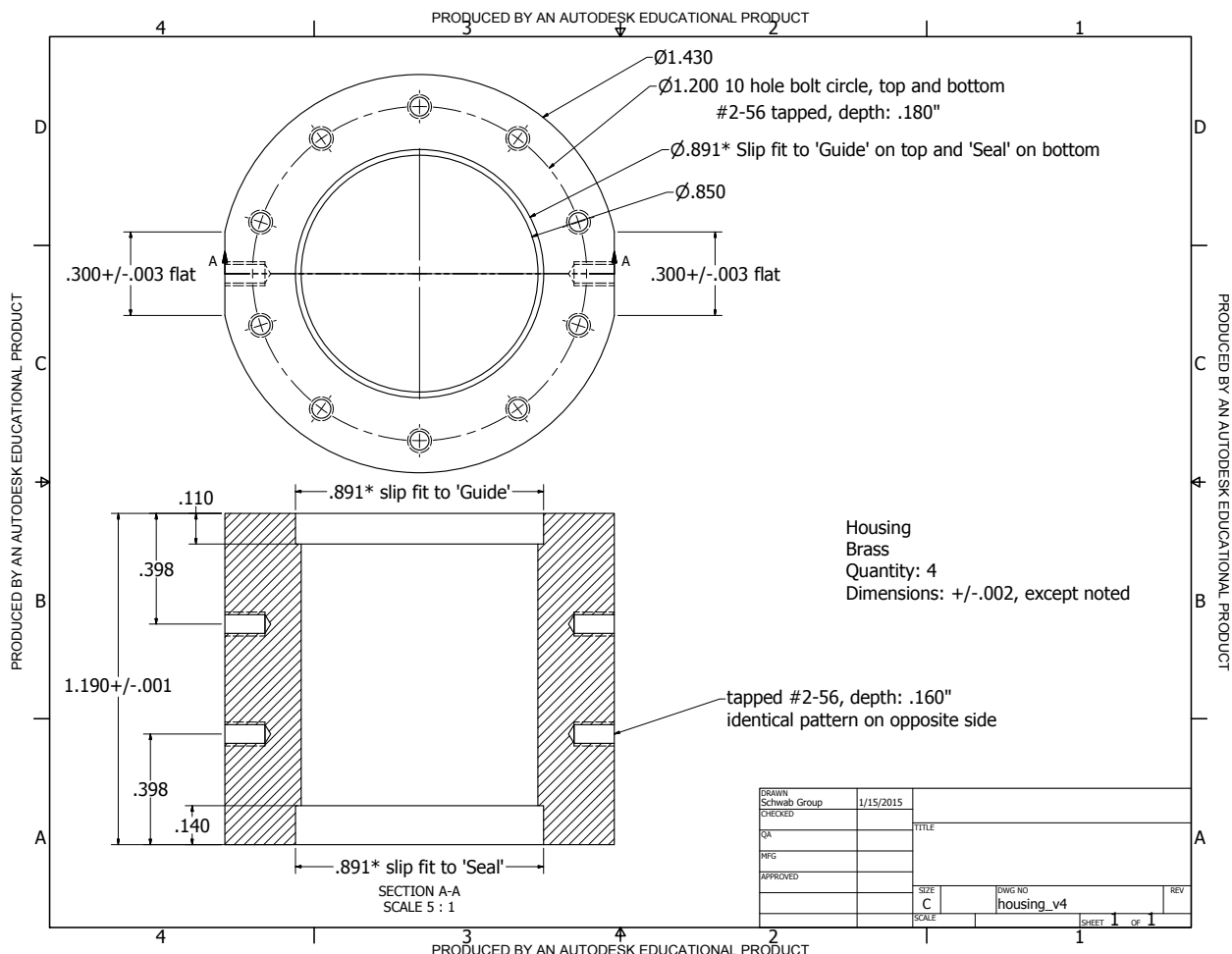


Figure D.3: Drawing of the housing, which is made from brass.

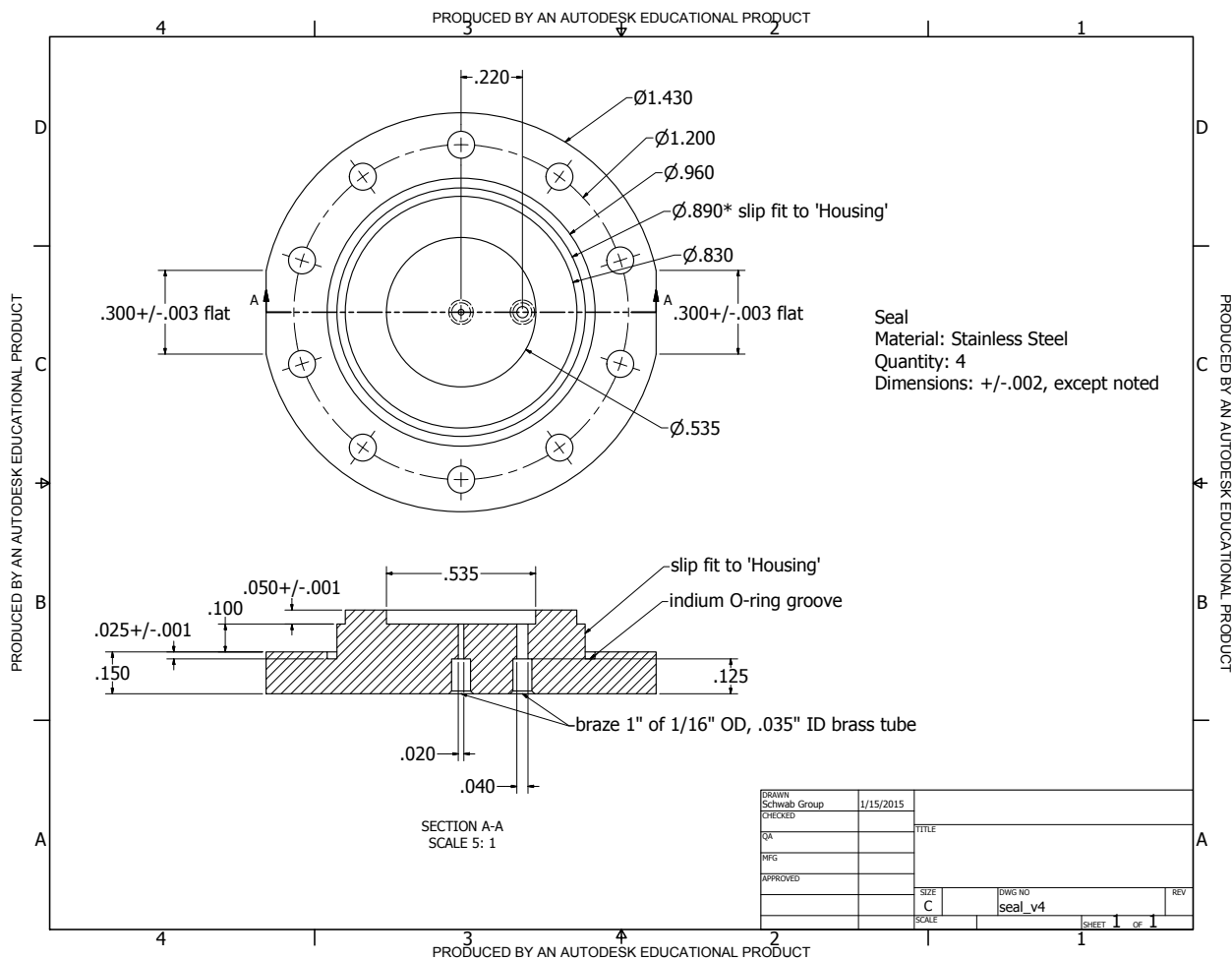


Figure D.4: Drawing of the seal, which is made from stainless steel.

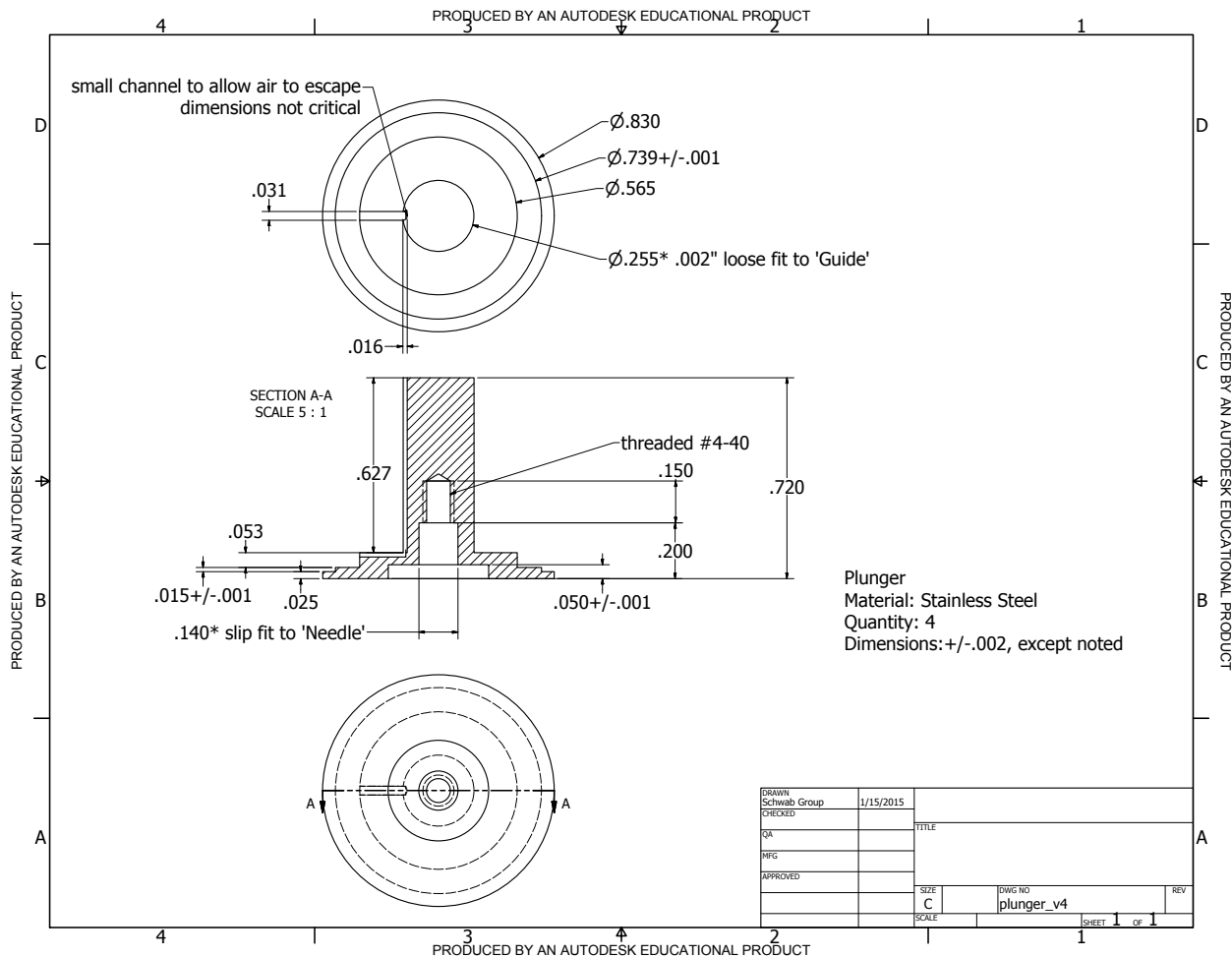


Figure D.5: Drawing of the plunger, which is made from stainless steel.

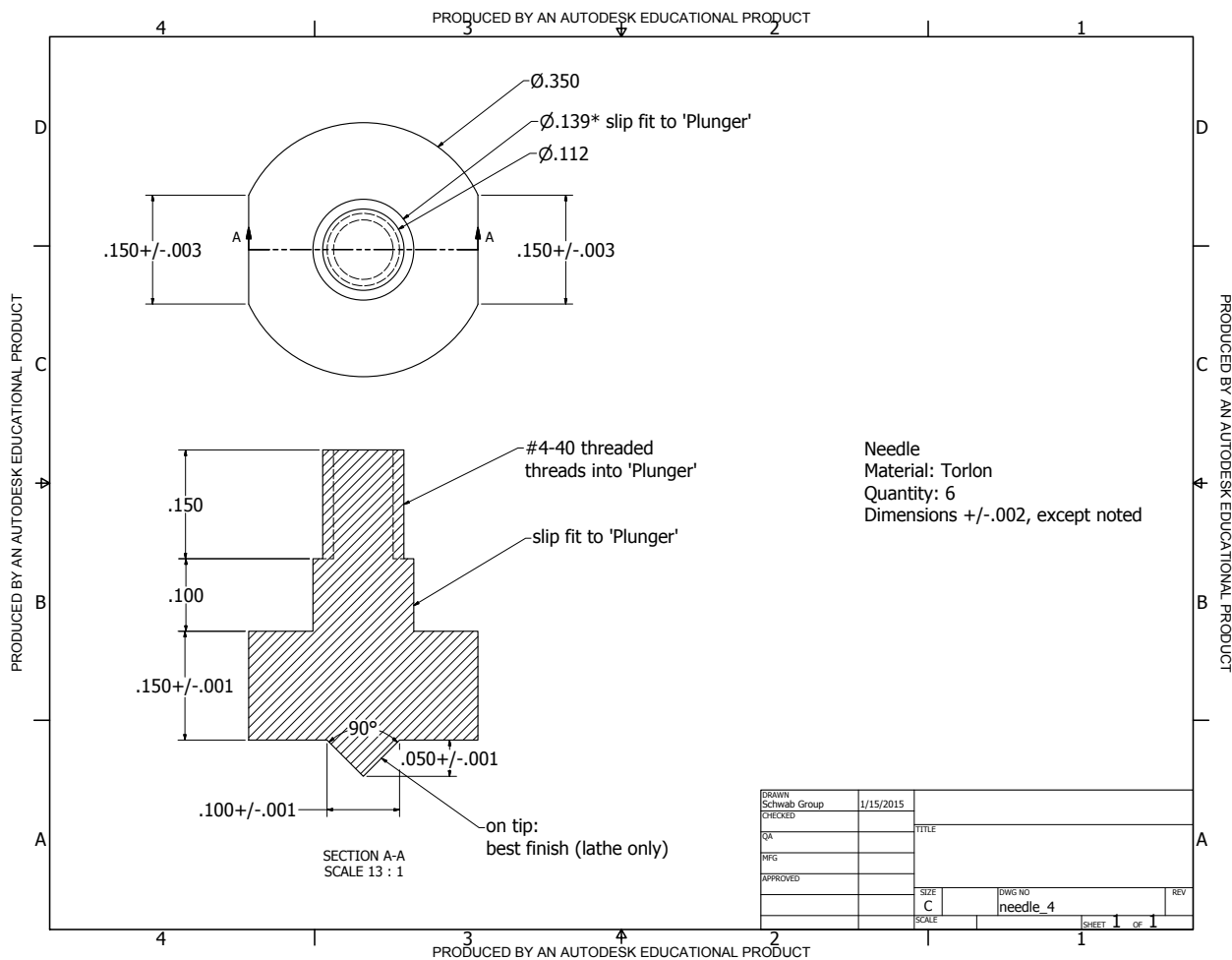


Figure D.6: Drawing of the needle, which is made from Torlon, a stiff plastic that does not easily deform at low temperatures.

# Appendix E

## Sinter Drawings

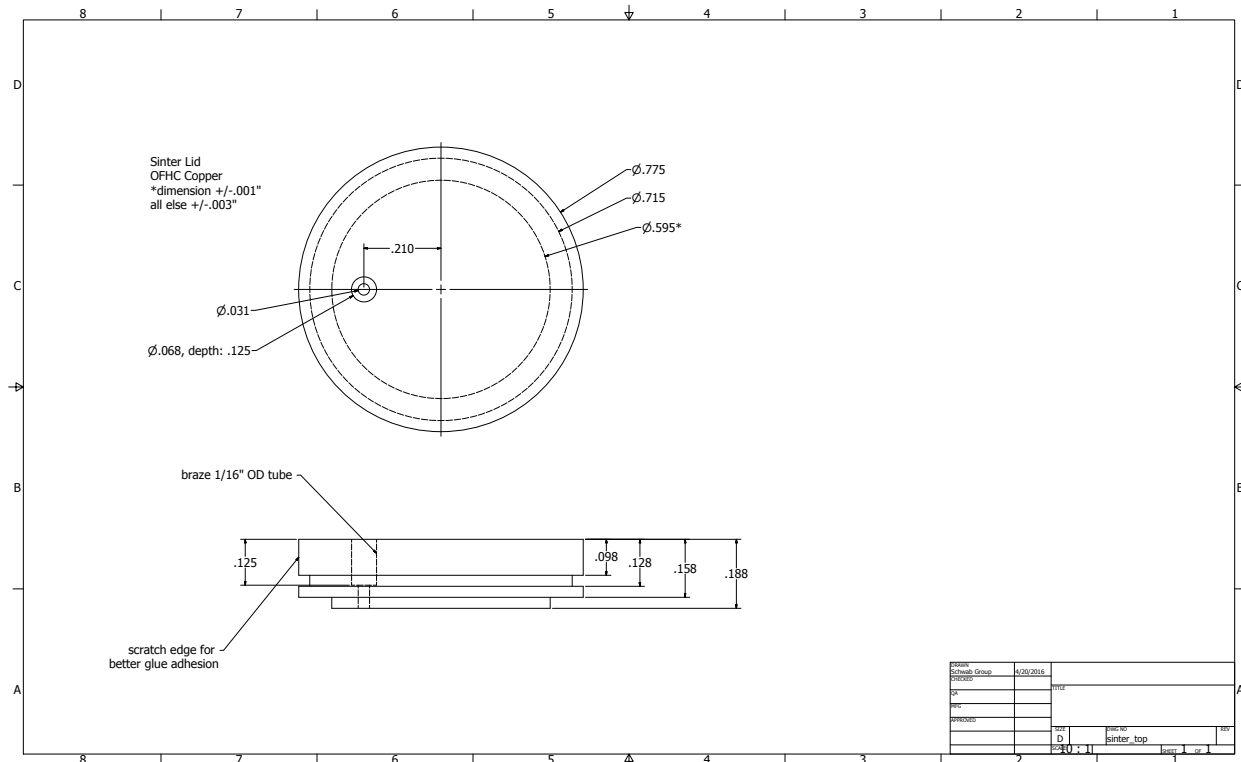


Figure E.1: Drawing of the top for the sintered-silver heat exchangers.

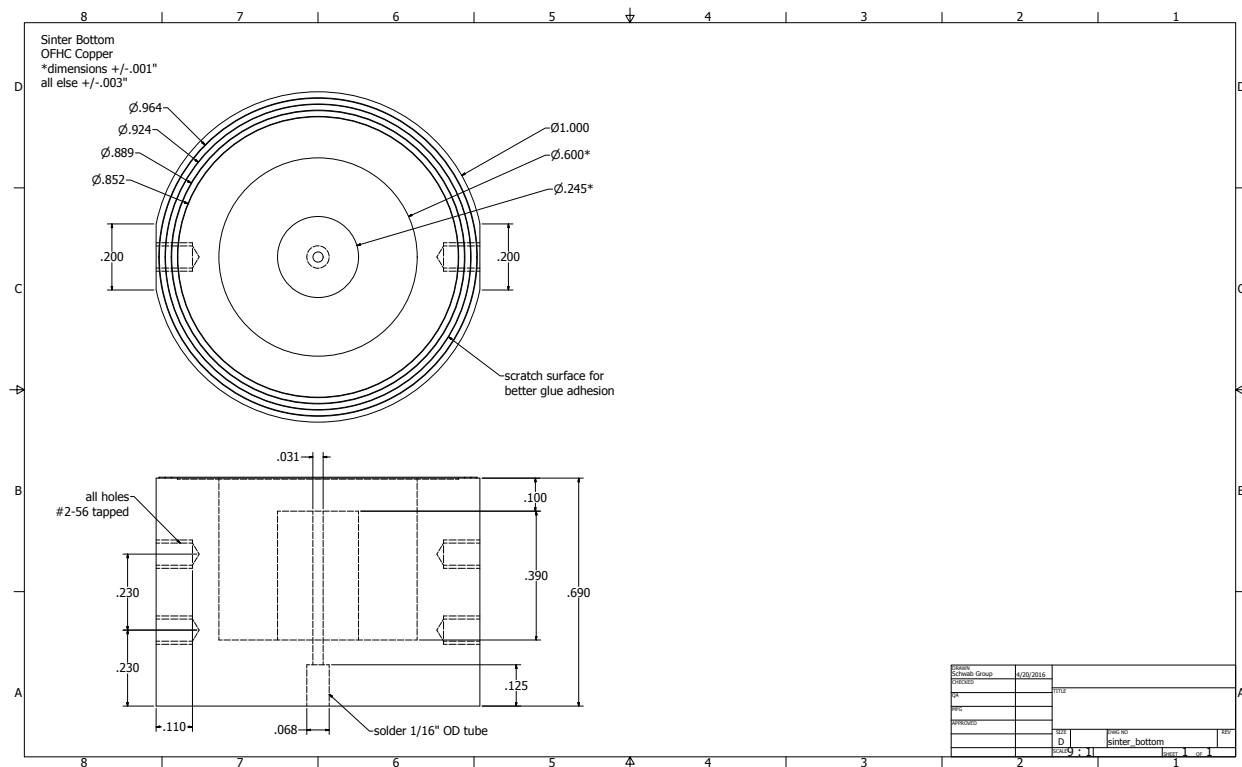


Figure E.2: Drawing of the bottom for the sintered-silver heat exchangers.

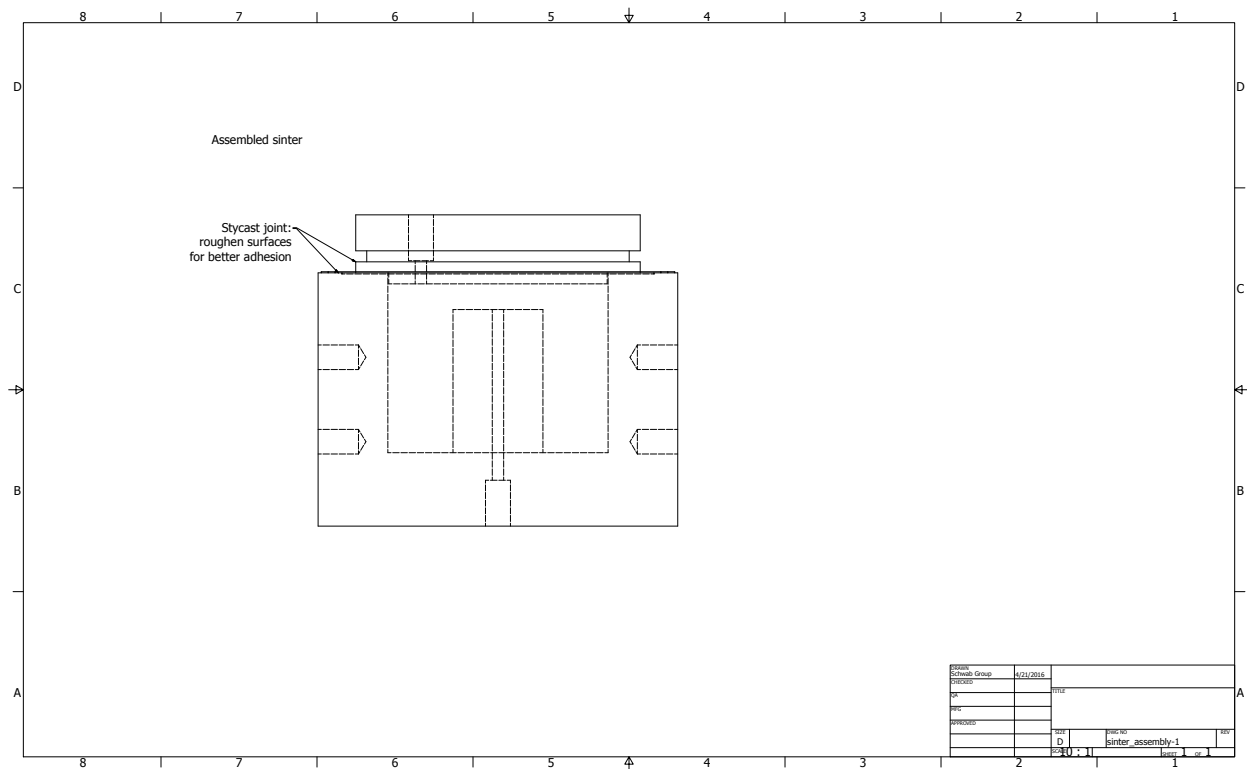


Figure E.3: Drawing of the sintered-silver heat exchangers assembly.

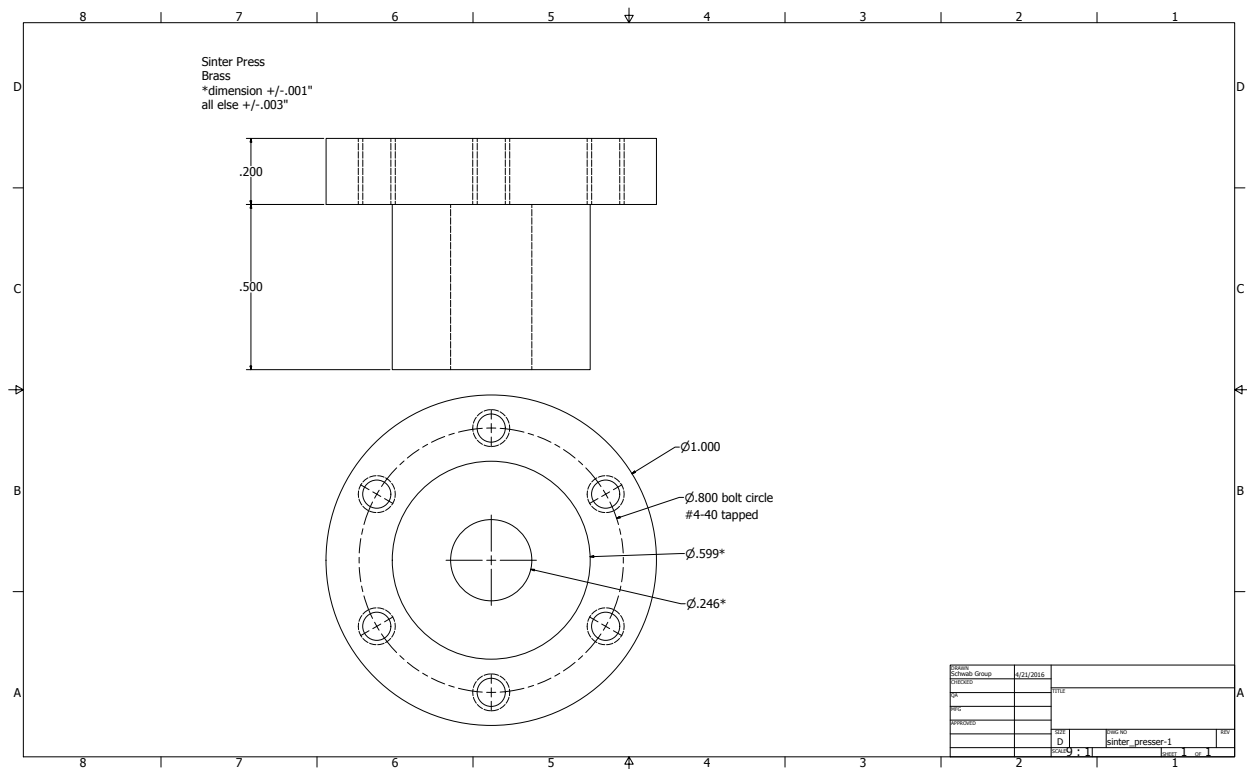


Figure E.4: Drawing of the pressing piece for the sintered-silver heat exchangers.

# Appendix F

## Suspension Drawings

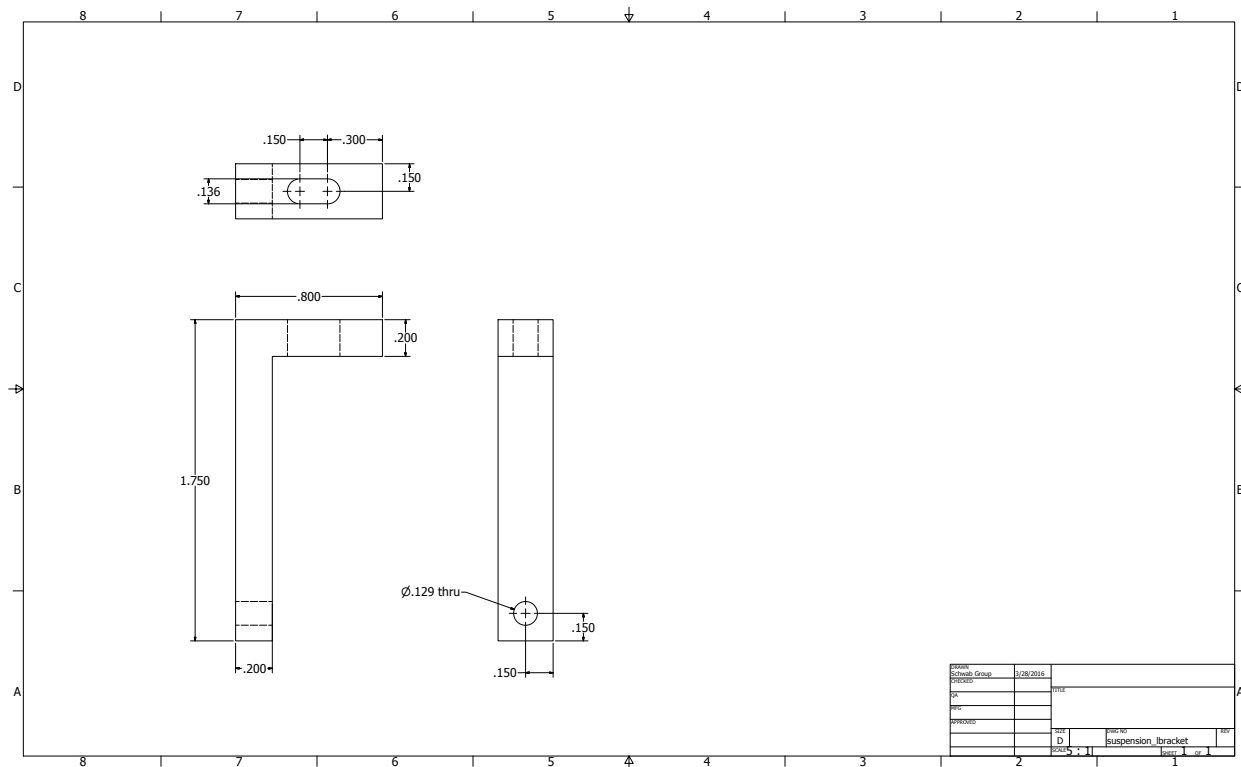


Figure F.1: Drawing of the copper L brackets used to mount the cell to the mixing chamber in Run 1.

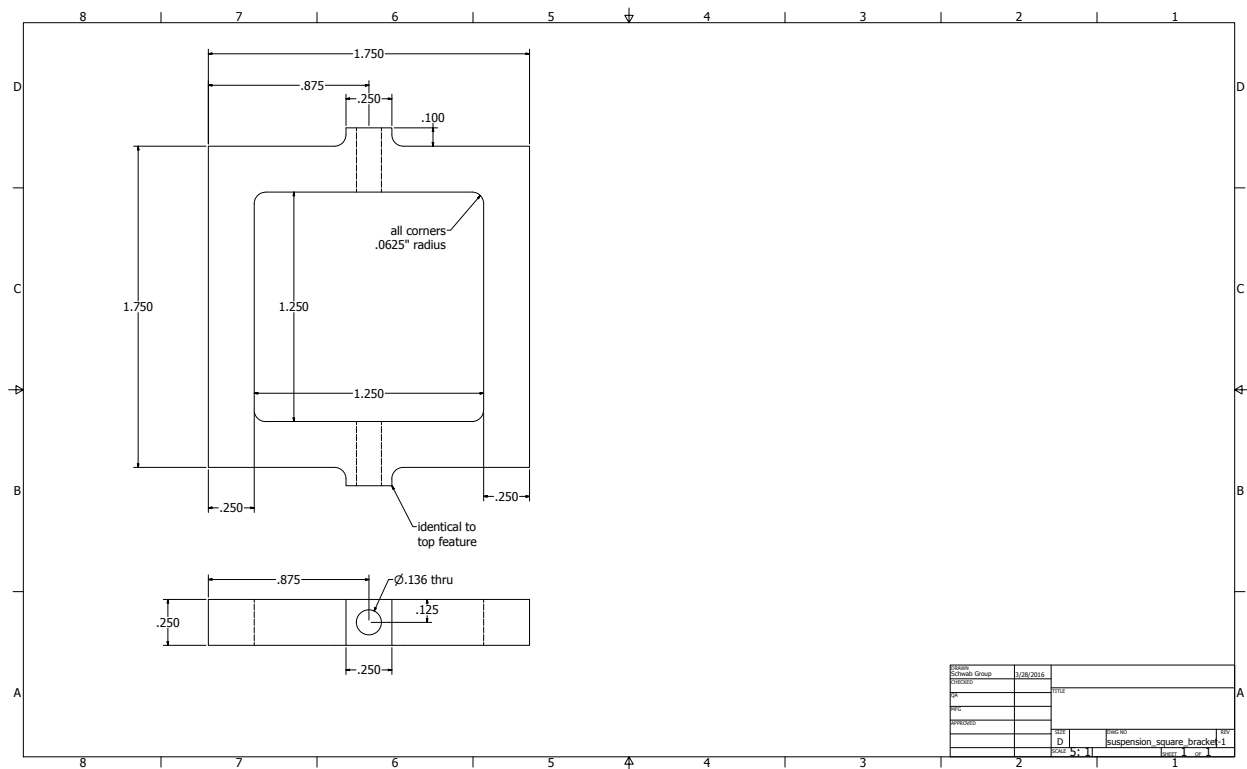


Figure F.2: Drawing of the square copper bracket used to mount the cell to the mixing chamber in Run 2.

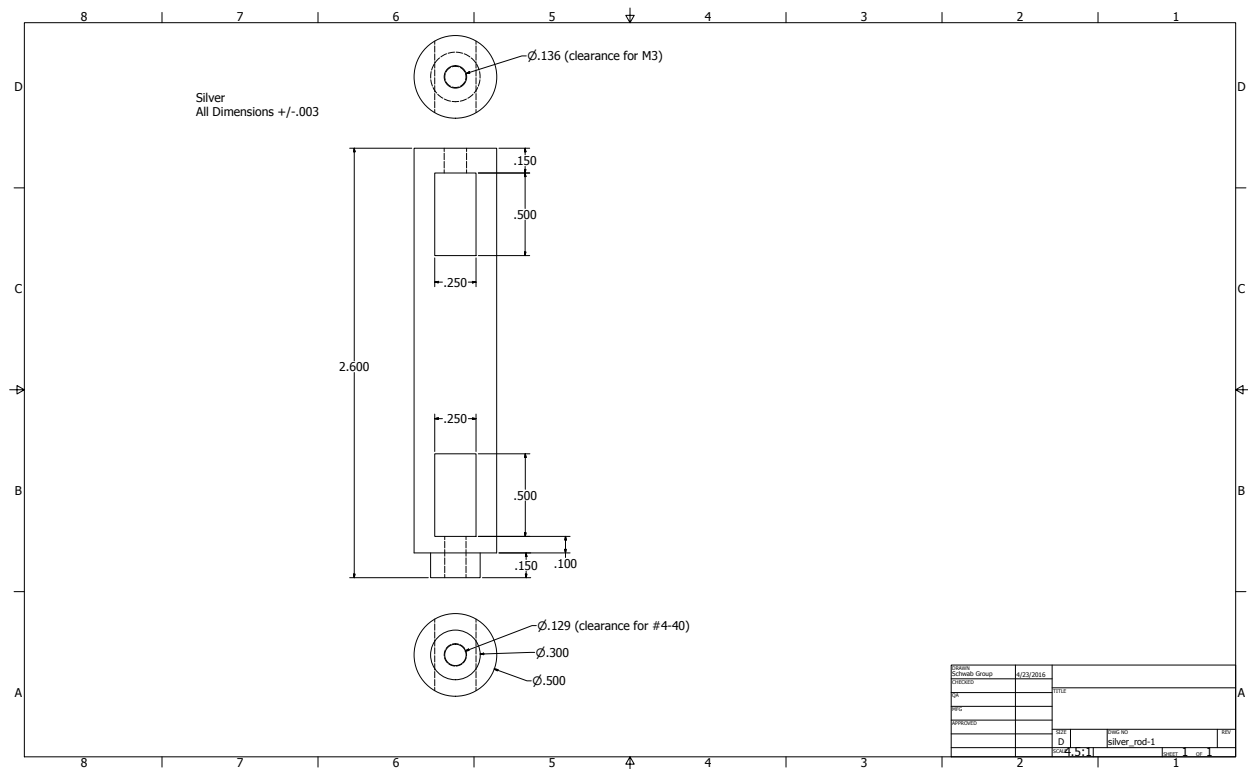


Figure F.3: Drawing of the silver rod used to mount the cell to the mixing chamber in Run 5.

# Appendix G

## Sapphire Drawings

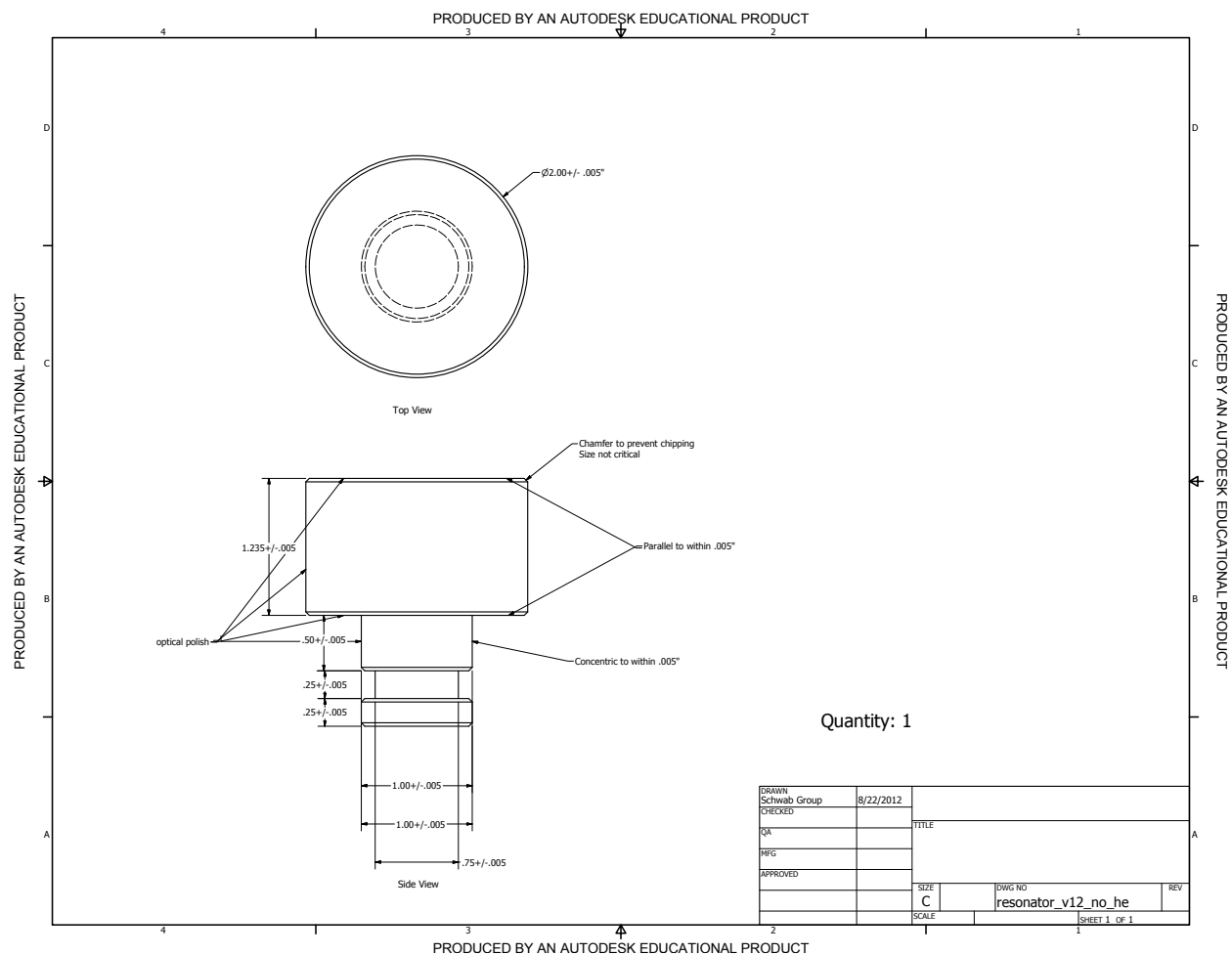


Figure G.1: Drawing of the sapphire test resonator.

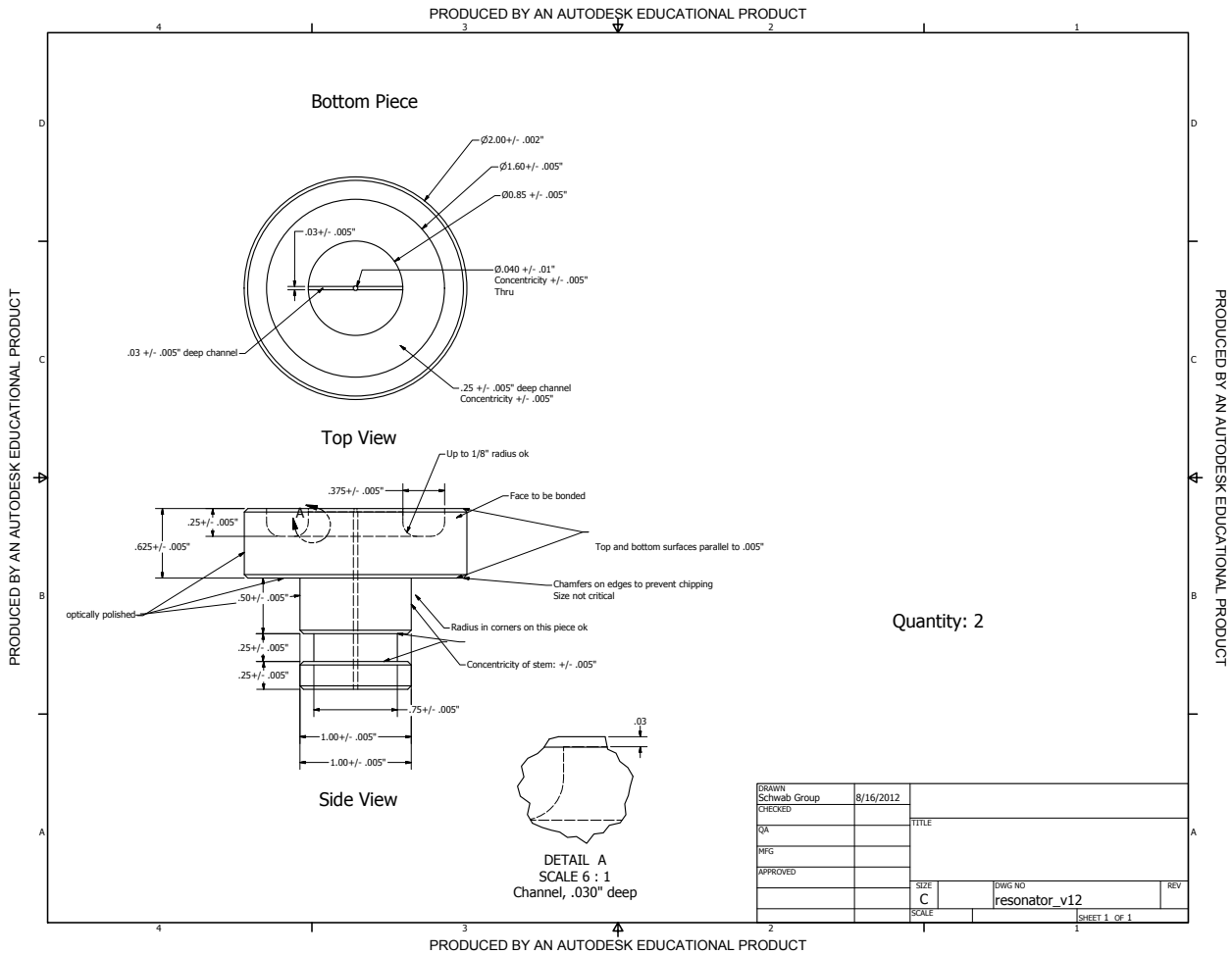


Figure G.2: Drawing of the bottom sapphire piece for the two piece helium filled sapphire cavity.

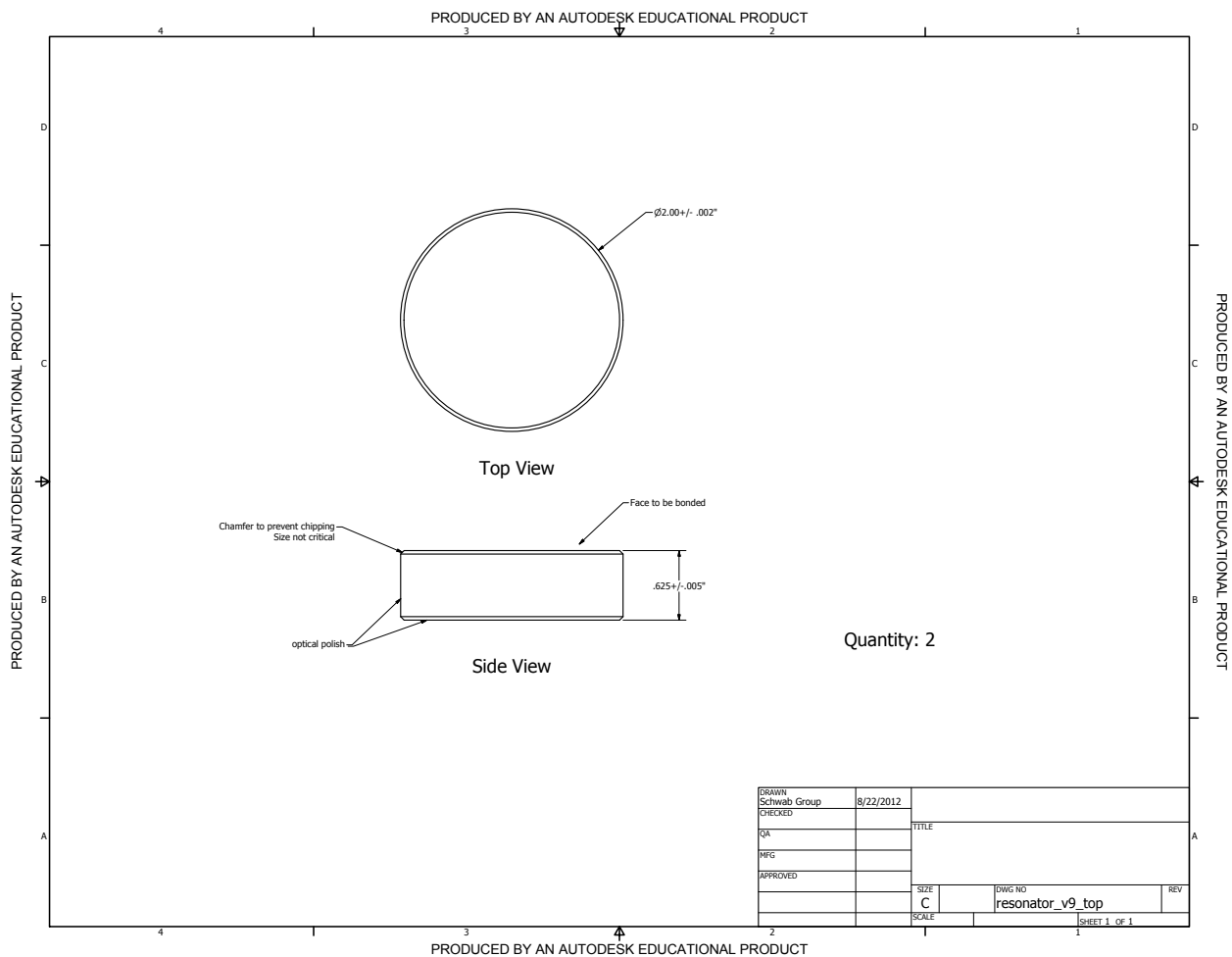


Figure G.3: Drawing of the top sapphire piece for the two piece helium filled sapphire cavity.

# Bibliography

- [1] LA De Lorenzo and KC Schwab, “Superfluid optomechanics: coupling of a superfluid to a superconducting condensate,” *New Journal of Physics*, vol. 16, no. 11, pp. 113020, 2014.
- [2] S. Singh, L. A. De Lorenzo, I. Pikovski, and K.C. Schwab, “Detecting continuous gravitational waves with a jug of superfluid,” 2016, to be published.
- [3] I. Pikovski, M. R. Vanner, M. Aspelmeyer, M. S. Kim, and C. Brukner, “Probing Planck-scale physics with quantum optics,” *Nature Physics*, vol. 8, no. 5, pp. 393–397, 2012.
- [4] J. Emsley, *Nature’s Building Blocks: An A-Z Guide to the Elements*, Oxford University Press, New York, second edition, 2011.
- [5] F. Pobell, *Matter and Methods at Low Temperatures*, Springer, 3rd edition, 2007.
- [6] H. Kragh, “The solar element: A reconsideration of heliums early history,” *Annals of Science*, vol. 66, no. 2, pp. 157–182, 2009.
- [7] American Chemical Society National Historic Chemical Landmarks, “Discovery of helium in natural gas,” April 2000.
- [8] W. M. Haynes, Ed., *CRC Handbook of Chemistry and Physics*, chapter 11, p. 3, CRC Press/Taylor and Francis, 92nd edition, 2012.
- [9] D.R. Tilley and J. Tilley, *Superfluidity and superconductivity*, Graduate Student Series in Physics Series. Adam Hilger, 1990.

- [10] L. Tisza, “On the thermal supraconductibility of liquid helium II and the bose-einstein statistics,” *C. R. Acad. Sci.*, vol. 207, pp. 1035–1037, 1938.
- [11] J. Wilks, *The Properties of Liquid and Solid Helium*, Clarendon Press, 1967.
- [12] E. M. Lifshitz and E. L. Andronikashvili, *A Supplement to Helium*, Consultants Bureau, Inc., 1959.
- [13] J. F. Allen and H. Jones, “New phenomena connected with heat flow in He II,” *Nature*, vol. 141, no. 3562, pp. 243–244, 1938.
- [14] L. D. Landau, “The theory of superfluidity of helium II,” *J. Phys. USSR*, vol. 5, pp. 71, 1941.
- [15] J. L. Yarnell, G. P. Arnold, P. J. Bendt, and E. C. Kerr, “Excitations in liquid helium: Neutron scattering measurements,” *Physical Review*, vol. 113, no. 6, pp. 1379–1386, 1959.
- [16] *Superfluid  $^3\text{He}$  in the zero-temperature limit*, vol. 329, Hiroshima, Japan, 2003.
- [17] A. E. Leanhardt, T. A. Pasquini, M. Saba, A. Schirotzek, Y. Shin, D. Kielpinski, D. E. Pritchard, and W. Ketterle, “Cooling bose-einstein condensates below 500 picokelvin,” *Science*, vol. 301, no. 5639, pp. 1513–1515, 2003.
- [18] F. London, *Superfluids*, Wiley, 1954.
- [19] M. Aspelmeyer, T. J. Kippenberg, and F. Marquardt, “Cavity optomechanics,” *Reviews of Modern Physics*, vol. 86, pp. 1391–1452, 2014.
- [20] Florian Marquardt, Joe P. Chen, A. A. Clerk, and S. M. Girvin, “Quantum theory of cavity-assisted sideband cooling of mechanical motion,” *Physical Review Letters*, vol. 99, no. 9, pp. 093902, 2007.
- [21] M. Aspelmeyer, P. Meystre, and K. Schwab, “Quantum optomechanics,” *Physics Today*, vol. 65, pp. 29, 2012.

[22] A. D. OConnell, M. Hofheinz, M. Ansmann, Radoslaw C. Bialczak, M. Lenander, Erik Lucero, M. Neeley, D. Sank, H. Wang, M. Weides, J. Wenner, John M. Martinis, and A. N. Cleland, “Quantum ground state and single-phonon control of a mechanical resonator,” *Nature*, vol. 464, pp. 697–703, 2010.

[23] J.D. Teufel, T. Donner, Dale Li, J.W. Harlow, M.S. Allman, A.J. Cicak, K. Sirois, J.D. Whittaker, K.W. Lehnert, and R.W. Simmonds, “Sideband cooling of micromechanical motion to the quantum ground state,” *Nature*, vol. 475, pp. 359–363, 2011.

[24] Jasper Chan, T.P. Mayer Alegre, Amir H. Safavi-Naeini, Jeff T. Hill, Alex Krause, Simon Groblacher, Markus Aspelmeyer, and Oskar Painter, “Laser cooling of a nanomechanical oscillator into its quantum ground state,” *Nature*, vol. 478, pp. 89–92, 2011.

[25] T. A. Palomaki, J. D. Teufel, R. W. Simmonds, and K. W. Lehnert, “Entangling mechanical motion with microwave fields,” *Science*, vol. 342, no. 6159, pp. 710–713, 2013.

[26] A. J. Weinstein, C. U. Lei, E. E. Wollman, J. Suh, A. Metelmann, A. A. Clerk, and K. C. Schwab, “Observation and interpretation of motional sideband asymmetry in a quantum electromechanical device,” *Physical Review X*, vol. 4, pp. 041003, 2014.

[27] S. M. Meenehan, J. D. Cohen, G. S. MacCabe, F. Marsili, M. D. Shaw, and O. Painter, “Pulsed excitation dynamics of an optomechanical crystal resonator near its quantum ground state of motion,” *Physical Review X*, vol. 5, pp. 041002, 2015.

[28] E. E.\* Wollman, C. U.\* Lei, A. J.\* Weinstein, J. Suh, A. Kronwald, F. Marquardt, A. A. Clerk, and K. C. Schwab, “Quantum squeezing of motion in a mechanical resonator,” *Science*, vol. 349, no. 6251, pp. 952–955, 2015.

[29] J.-M. Pirkkalainen, E. Damskogg, M. Brandt, F. Massel, and M. A. Sillanp, “Squeezing of quantum noise of motion in a micromechanical resonator,” *Physical Review Letters*, vol. 115, pp. 243601, 2015.

[30] F. Lecocq, J. B. Clark, R. W. Simmonds, J. Aumentado, and J. D. Teufel, “Quantum nondemolition measurement of a nonclassical state of a massive object,” *Physical Review X*, vol. 5, pp. 041037, 2015.

[31] R. Riedinger\*, S. Hong\*, R. A. Norte, J. A. Slater, J. Shang, A. G. Krause, V. Anant, M. Aspelmeyer, and S. Groblacher, “Non-classical correlations between single photons and phonons from a mechanical oscillator,” *Nature*, vol. 530, pp. 313–316, 2016.

[32] R. W. Andrews, R. W. Peterson, T. P. Purdy, K. Cicak, R. W. Simmonds, C. A. Regal, and K. W. Lehnert, “Bidirectional and efficient conversion between microwave and optical light,” *Nature Physics*, vol. 10, no. 4, pp. 321–326, 2014.

[33] Wojciech H. Zurek, Salmon Habib, and Juan Pablo Paz, “Coherent states via decoherence,” *Physical Review Letters*, vol. 70, no. 9, pp. 1187–1190, 1992.

[34] T. Roucheleau, T. Ndukum, C. Macklin, J.B. Hertzberg, A.A. Clerk, and K.C. Schwab, “Preparation and detection of a mechanical resonator near the ground state of motion,” *Nature*, vol. 463, pp. 72–75, 2010.

[35] A. D. Kashkanova, A. B. Shkarin, C. D. Brown, N. E. Flowers-Jacobs, L. Childress, S. W. Hoch, L. Hohmann, K. Ott, J. Reichel, and J. G. E. Harris, “Superfluid Brillouin optomechanics,” *arXiv:1602.05640*, 2016.

[36] G. I. Harris, D. L. McAuslan, E. Sheridan, Y. Sachkou, C. Baker, and W. P. Bowen, “Laser cooling and control of excitations in superfluid helium,” *arXiv:1506.04542*, 2015.

[37] D. M. Pozar, *Microwave Engineering*, John Wiley and Sons, Inc., 2005.

[38] C. G. Montgomery, *Techniques of Microwave Measurements*, McGraw-Hill Book Company, New York, first edition, 1947.

[39] R. G. Rogers, *Low Phase Noise Microwave Oscillator Design*, Artech House, 1991.

[40] F. Biquard and A. Septier, “Amelioration de la conductivite superficielle du cuivre et de l’aluminium en hyperfrequencies par abaissement de temperature,” *Nuclear Instruments and Methods*, vol. 44, no. 1, pp. 18–28, 1966.

[41] M. Reagor, H. Paik, G. Catelani, L. Sun, C. Axline, E. Holland, I. M. Pop, N. A. Masluk, T. Brecht, L. Frunzio, M. H. Devoret, L. Glazman, M. Schoelkopf, R. J. Reagor, H. Paik, G. Catelani, L. Sun, C. Axline, E. Holland, I. M. Pop, N. A. Masluk, T. Brecht, L. Frunzio, M. H. Devoret, L. Glazman, and R. J. Schoelkopf, “Reaching 10 ms single photon lifetimes for superconducting aluminum cavities,” *Applied Physics Letters*, vol. 102, pp. 192604, 2013.

[42] J. M. Pierce, “Residual microwave surface resistance of superconducting lead,” *Journal of Applied Physics*, vol. 44, no. 3, pp. 1342–1347, 1973.

[43] M. A. Allen, Z. D. Farkas, H. A. Hogg, E. W. Hoyt, and P. B. Wilson, “Superconducting niobium cavity measurements at SLAC,” *IEEE Transactions on Nuclear Science*, vol. NS18, no. 3, pp. 168–172, 1971.

[44] R. Eichhorn, D. Gonnella, G. Hoffstaetter, M. Liepe, and W. Weingarten, “On superconducting niobium accelerating cavities fired under  $n^2$ -gas exposure,” 2014.

[45] J. Bardeen, L. N. Cooper, and J. R. Schrieffer, “Theory of superconductivity,” *Physical Review*, vol. 108, no. 5, pp. 1175–1204, 1957.

[46] H. Padamsee, H. Knobloch, and T. Hays, *RF Superconductivity for Accelerators*, John Wiley and Sons, Inc., 2008.

[47] T. P. Sheahan, “Effective interaction strength in superconductors,” *Physical Review*, vol. 149, no. 1, pp. 370–377, 1966.

[48] H. Padamsee, *RF Superconductivity: Science, Technology, and Applications*, John Wiley and Sons, Inc., 2009.

[49] Alexander S. Romanenko, *Surface Characterization of Nb Cavity Sections - Understanding the High Field Q-Slope*, Ph.D. thesis, Cornell University, January 2009.

[50] V. B. Braginsky, V. P. Mitrofanov, and V. I. Panov, *Systems with small dissipation*, The University of Chicago Press, 1985.

[51] S. Rowan, G. Cagnoli, P. Sneddon, J. Hough, R. Route, E. K. Gustafson, M. M. Fejer, and V. Mitrofanov, “Investigation of mechanical loss factors of some candidate materials for the test masses of gravitational wave detectors,” *Physics Letters A*, vol. 265, no. 1-2, pp. 5–11, 2000.

[52] J. Krupka, K. Derzakowski, M. Tobar, J. Hartnett, and R. G. Geyer, “Complex permittivity of some ultralow loss dielectric crystals at cryogenic temperatures,” *Measurement Science and Technology*, vol. 10, no. 5, pp. 387–392, 1999.

[53] C. R. Locke, E. N. Ivanov, J. G. Hartnett, P. L. Stanwix, and M. E. Tobar, “Invited article: Design techniques and noise properties of ultrastable cryogenically cooled sapphire-dielectric resonator oscillators,” *Review of Scientific Instruments*, vol. 79, no. 5, pp. 051301, 2008.

[54] C. McNeilage, J. H. Searls, E. N. Ivanov, Stockwell P. R., D. M. Green, and M. Mossammaparast, “A review of sapphire whispering gallery-mode oscillators including technical progress and future potential of the technology,” *Proceedings of the 2004 IEEE International Frequency Control Symposium and Exposition*, pp. 210–218, 2005.

[55] A. N. Luiten, A. G. Mann, and D. G. Blair, “Ultrahigh Q-factor cryogenic sapphire resonator,” *Electronics Letters*, vol. 29, no. 10, pp. 879–881, 1993.

[56] D. L. Creedon, Y. Reshitnyk, W. Farr, J. M. Martinis, T. L. Duty, and M. E. Tobar, “High q-factor sapphire whispering gallery mode microwave resonator at single photon energies and millikelvin temperatures,” *Applied Physics Letters*, vol. 98, no. 22, pp. 222903, 2011.

[57] M. E. Tobar and A. G. Mann, “Resonant frequencies of higher order modes in cylindrical anisotropic dielectric resonators,” *IEEE Transactions On Microwave Theory And Techniques*, vol. 39, no. 12, pp. 2077–2082, 1991.

[58] H. Peng, “Study of whispering gallery modes in double disk sapphire resonators,” *IEEE Transactions On Microwave Theory And Techniques*, vol. 44, no. 6, pp. 848–853, 1996.

[59] D. Kajfez and P. Guillon, *Dielectric Resonators*, Noble, second edition, 1998.

[60] D. G. Blair and S. K. Jones, “High-Q sapphire loaded superconducting cavities and application to ultrastable clocks,” *IEEE Transactions on Magnetics*, vol. 21, no. 2, pp. 142–145, 1985.

[61] GTAT Corporation, 243 Daniel Webster Highway, Merrimack, NH 03054 (USA).

[62] A. N. Luiten, A. G. Mann, and D. G. Blair, “High-resolution measurement of the temperature-dependence of the  $Q$  , coupling and resonant frequency of a microwave resonator,” *Measurement science and technology*, vol. 7, no. 6, pp. 949–953, 1996.

[63] L. E. Kinsler, A. R. Frey, A. B. Coppens, and J. V. Sanders, *Fundamentals of Acoustics*, John Wiley and Sons, Inc., fourth edition, 2000.

[64] R. T. Muehleisen and A. A. Atchley, “Fundamental azimuthal modes of a constricted annular resonator: Theory and measurement,” *Acoustical Society of America*, vol. 109, no. 2, pp. 480–487, 2001.

[65] L. W. Bruch and F. Weinhold, “Diamagnetism of helium,” *Journal of Chemical Physics*, vol. 113, no. 19, pp. 8667–8670, 2000.

[66] J. J. Niemela and R. J. Donnelly, “Density and thermal expansion coefficient of liquid helium-4 from measurements of the dielectric constant,” *Journal of Low Temperature Physics*, vol. 98, no. 1/2, pp. 709–732, 1995.

[67] R. F. Harris-Lowe and K. A. Smee, “Thermal expansion of liquid Helium II,” *Physical Review A*, vol. 2, no. 1, pp. 158–159, 1970.

[68] M. Oxborrow, “Traceable 2-D finite-element simulation of the whispering-gallery modes of axisymmetric electromagnetic resonators,” *IEEE Transactions on Microwave Theory and Techniques*, vol. 55, no. 6, pp. 1209–1218, 2007.

[69] K. Gloos, C. Mitschka, F. Pobell, and P. Smeibidl, “Thermal-conductivity of normal and superconducting metals,” *Cryogenics*, vol. 30, no. 1, pp. 14–18, 1990.

[70] C. Kittel, *Introduction to Solid State Physics*, John Wiley and Sons, Inc., eighth edition, 2005.

[71] A. T. Hirshfeld, H. A. Leupold, and H. A. Boorse, “Superconducting and normal specific heats of niobium,” *Physical Review*, vol. 127, no. 5, pp. 1501–1507, 1962.

[72] R. J. Donnelly and C. F. Barenghi, “The observed properties of liquid helium at the saturated vapor pressure 2004.

[73] *RF Performance of a superconducting s-band cavity filled with liquid helium*, 2006.

[74] B. M. Abraham, Y. Eckstein, J. B. Ketterson, M. Kuchnir, and P. R. Roach, “Velocity of sound, density, and Grüneisen constant in liquid  $^4\text{He}$ ,” *Phys. Rev. A*, vol. 1, pp. 250–257, Feb 1970.

[75] J. Jäckle and K. W. Kehr, “High-frequency ultrasonic attenuation in superfluid helium under pressure,” *Physical Review Letters*, vol. 27, no. 10, pp. 654–657, 1971.

[76] D. Rugar and J. S. Foster, “Accurate measurement of low energy phonon dispersion in liquid  $^4\text{He}$ ,” *Physical Review B*, vol. 30, no. 5, pp. 2595–2602, 1984.

[77] Humphrey J. Maris, “Phonon-phonon interactions in liquid helium,” *Reviews of Modern Physics*, vol. 49, no. 2, pp. 341–359, 1977.

[78] J.B. Hertzberg, T. Rocheleau, T. Ndukum, M. Savva, A.A. Clerk, and K.C. Schwab, “Back-action evading measurements of nanomechanical motion,” *Nature Physics*, vol. 6, pp. 72–75, 2009.

[79] R. E. Thomas and A. J. Rosa, *The Analysis and Design of Linear Circuits*, John Wiley and Sons, Inc., third edition, 2001.

[80] C. E. Chase and Melvin A. Herlin, “Ultrasonic propagation in magnetically cooled helium,” *Physical Review*, vol. 97, no. 6, pp. 1447–1452, 1955.

[81] G. W. Waters, D. J. Watmough, and J. Wilks, “Absorption of sound in helium II below 0.6°K,” *Physics Letters*, vol. 26A, no. 1, pp. 12–13, 1967.

[82] B. M. Abraham, Y. Eckstein, J. B. Ketterson, M. Kuchnir, and J. Vignos, “Sound propagation in liquid  $^4\text{He}$ ,” *Physical Review*, vol. 181, no. 1, pp. 347–373, 1968.

[83] Humphrey J. Maris and Walter E. Massey, “Phonon dispersion and the propagation of sound in liquid helium-4 below 0.6°K,” *Physical Review Letters*, vol. 25, no. 4, pp. 220–222, 1970.

[84] N. E. Phillips, C. G. Waterfield, and J. K. Hoffer, “Calorimetric evidence for positive phonon dispersion in liquid helium-4,” *Physical Review Letters*, vol. 25, no. 18, pp. 1260–1262, 1970.

[85] C. H. Anderson and E. S. Sabisky, “Positive linear dispersion in the velocity of sound in He II,” *Physical Review Letters*, vol. 28, no. 2, pp. 80–82, 1972.

[86] B. M. Abraham, Y. Eckstein, J. B. Ketterson, and J. H. Vignos, “Fermion-phonon interaction: The attenuation of sound in a liquid  $\text{He}^3$ - $\text{He}^4$  solution,” *Physical Review Letters*, vol. 17, no. 25, pp. 1254–1256, 1966.

[87] L. Landau and G. Rumer, “Absorption of sound in solids,” *Physikalische Zeitschrift der Sowjetunion*, vol. 11, pp. 18–25, 1937.

[88] J. Ferreira, “Internal friction in high  $q$  materials,” in *The Detection of Gravitational Waves*, D. G. Blair, Ed. Cambridge University Press, Cambridge, 1991.

[89] Pat R. Roach, J. B. Ketterson, and M. Kuchnir, “New relaxation effect in the sound attenuation in liquid  $^4\text{He}$  under pressure,” *Physical Review Letters*, vol. 12, no. 15, pp. 1002–1005, 1970.

[90] A. Akhieser, “On the absorption of sound in solids,” *Journal of Physics-USSR*, vol. 1, pp. 277–287, 1939.

[91] K. Schwab, J. Steinhauer, J. C. Davis, and R. E. Packard, “Fabrication of a silicon-based superfluid oscillator,” *Journal of Microelectromechanical Systems*, vol. 5, no. 3, pp. 180–186, 1996.

[92] I. Wilson-Rae, R. A. Barton, S. S. Verbridge, D. R. Southworth, B. Ilic, H. G. Craighead, and J. M. Parpia, “High-q nanomechanics via destructive interference of elastic waves,” *Physical Review Letters*, vol. 106, no. 4, pp. 047205, 2011.

[93] Pat R. Roach, J. B. Ketterson, and M. Kuchnir, “Ultrasonic attenuation in liquid  $^4\text{He}$  under pressure,” *Physical Review A*, vol. 5, no. 5, pp. 2205–2214, 1972.

[94] L. T. Aldrich and A. O. Nier, “The occurrence of  $\text{He}^3$  in natural sources of helium,” *Physical Review*, vol. 74, no. 11, pp. 1590–1594, 1948.

[95] B. M. Abraham, Y. Eckstein, J. B. Ketterson, and M. Kuchnir, “Sound propagation through a dilute solution of  $^3\text{He}$ - $^4\text{He}$ ,” *Physical Review Letters*, vol. 20, no. 6, pp. 251–254, 1967.

[96] G. Baym, “Theory of first sound in dilute solutions of  $\text{He}^3$  in  $\text{He}^4$  at very low temperatures,” *Physical Review Letters*, vol. 18, no. 3, pp. 71–74, 1967.

[97] G. Baym and C. Ebner, “Phonon-quasiparticle interactions in dilute solutions of  $\text{He}^3$  in superfluid  $\text{He}^4$ : I. Phonon thermal conductivity and ultrasonic attenuation,” *Physical Review*, vol. 164, no. 1, pp. 235–244, 1967.

[98] G. Baym and W. F. Saam, “Phonon-quasiparticle interactions in dilute solutions of  $\text{He}^3$  in superfluid  $\text{He}^4$ : II. Phonon Boltzmann equation and first viscosity,” *Physical Review*, vol. 171, no. 1, pp. 172–178, 1968.

[99] G. Baym and C. Saam, W. F. Ebner, “Phonon-quasiparticle interactions in dilute solutions of  $\text{He}^3$  in superfluid  $\text{He}^4$ : III. Attenuation of first sound above  $0.2^\circ\text{K}$ ,” *Physical Review*, vol. 173, no. 1, pp. 306–313, 1968.

[100] E. Østgaard, “Properties of dilute solutions of  ${}^3\text{He}$  in liquid  ${}^4\text{He}$  at low temperatures,” *Physical Review A*, vol. 1, no. 4, pp. 1048–1062, 1970.

[101] K. A. Kuenhold, D. B. Crum, and R. E. Sarwinski, “The viscosity of dilute solutions of  ${}^3\text{He}$  in  ${}^4\text{He}$  at low temperatures,” *Physics Letters*, vol. 41A, no. 1, pp. 13–14, 1972.

[102] R. König and F. Pobell, “Temperature, pressure, and concentration dependence of the viscosity of liquid  ${}^3\text{He}$ - ${}^4\text{He}$  mixtures at low temperatures,” *Physical Review Letters*, vol. 71, no. 17, pp. 2761–2764, 1993.

[103] R. L. Rosenbaum, J. B. Landau, and Y. Eckstein, “Temperature, pressure, and concentration dependence of the thermal conductivity of very dilute solutions of  ${}^3\text{He}$  in superfluid  ${}^4\text{He}$ ,” *Journal of Low Temperature Physics*, vol. 16, no. 1/2, pp. 131–143, 1974.

[104] J. Bardeen, G. Baym, and D. Pines, “Interactions between  $\text{He}^3$  atoms in dilute solutions of  $\text{He}^3$  in superfluid  $\text{He}^4$ ,” *Physical Review Letters*, vol. 17, no. 7, pp. 372–375, 1966.

[105] Fu H. H. and C. J. Pethick, “Concentration dependence of the  ${}^3\text{He}$  quasiparticle interaction in dilute solutions of  ${}^3\text{He}$  in superfluid  ${}^4\text{He}$ ,” *Physical Review B*, vol. 14, no. 9, pp. 3837–3847, 1976.

[106] Philip M. Morse and K. Uno Ingard, *Theoretical Acoustics*, McGraw-Hill Book Company, 1968.

[107] E. H. Kennard, *Kinetic Theory of Gases*, McGraw-Hill Book Company, New York, 1938.

[108] S. M. Tholen and J. M. Parpia, “Effect of  $^4\text{He}$  on the surface scattering of  $^3\text{He}$ ,” *Physical Review B*, vol. 47, no. 1, pp. 319–329, 1993.

[109] H. Kerscher, M. Niemetz, and W. Schoepe, “Viscosity and mean free path of very diluted solutions of  $^3\text{He}$  in  $^4\text{He}$ ,” *Journal of Low Temperature Physics*, vol. 124, no. 1/2, pp. 163–168, 2001.

[110] P. C. Hendry and P. V. E. McClintock, “Continuous flow apparatus for preparing isotopically pure  $^4\text{He}$ ,” *Cryogenics*, vol. 27, no. 3, pp. 131–1, 1987.

[111] F. E. Moss, A. F. G. Wyatt, and M. J. Baird, “A simple apparatus for preparing modest quantities of isotopically pure  $^4\text{He}$ ,” *Cryogenics*, vol. 21, no. 2, pp. 114–116, 1981.

[112] P. C. Tully, “Isotopic purification of helium by differential distillation below the lambda-point,” Tech. Rep. BM-RI-8054, US Bureau of Mines, Washington, 1975.

[113] O. Avenel and E Varoquaux, “Observation of singly quantized dissipation events obeying the josephson frequency relation in the critical flow of superfluid he4 through an aperture,” *Physical Review Letters*, vol. 55, pp. 2704–2707, 1985.

[114] W. H. Zurek, “Cosmological experiments in superfluid-helium,” *Nature*, vol. 317, no. 6037, pp. 505–508, 1985.

[115] M. A. Weilert, D. L. Whitaker, H. J. Maris, and G. M. Seidel, “Magnetic levitation of liquid helium,” *Journal of Low Temperature Physics*, vol. 106, no. 1/2, pp. 101–131, 1997.

[116] J. Harris, private communication, 2012.

[117] J. J. Niemela, “Electrostatic charging and levitation of helium II drops,” *Journal of Low Temperature Physics*, vol. 109, no. 5/6, pp. 1–16, 1997.

[118] M. A. Weilert, D. L. Whitaker, H. J. Maris, and G. M. Seidel, “Laser levitation of superfluid helium,” *Journal of Low Temperature Physics*, vol. 98, no. 1/2, pp. 17–35, 1995.

[119] P. Falferi, M. Cerdonio, L. Franceschini, R. Macchietto, S. Vitale, and J. P. Zendri, “A high inductance khz resonator with a quality factor larger than  $10^6$ ,” *Review of Scientific Instruments*, vol. 65, no. 9, pp. 2916–2919, 1994.

[120] P. A. Truitt, J. B. Hertzberg, C. C. Huang, K. L. Ekinci, and K. C. Schwab, “Efficient and sensitive capacitive readout of nanomechanical resonator arrays,” *Nano Letters*, vol. 7, no. 1, pp. 120–126, 2007.

[121] M. Hartmann, R. E. Miller, J. P. Toennies, and A. Vilesov, “Rotationally resolved spectroscopy of  $\text{SF}_6$  in liquid helium clusters: A molecular probe of cluster temperature,” *Physical Review Letters*, vol. 75, no. 8, pp. 1566–1569, 1995.

[122] D. M. Brink and S. Stringari, “Density of states and evaporation rate of helium clusters,” *Zeitschrift für Physik D: Atoms, Molecules and Clusters*, vol. 15, no. 3, pp. 257–263, 1990.

[123] F. C. Brown, *The Physics of Solids*, W. A. Benjamin, Inc., New York, 1967.

[124] H. M. Ledbetter, “Elastic constants of polycrystalline copper at low temperatures: Relationship to single crystal elastic constants,” *Physica Status Solidi A*, vol. 66, no. 2, pp. 477–484, 1981.

[125] W. F. Gale and T. C. Totemeir, Eds., *Smithells Metals Reference Book*, chapter 15, p. 3, Elsevier Butterworth-Heinemann, 8th edition, 2004.

[126] W. Pabst, G. tichà, and E. GREGOROVÀ, “Effective elastic properties of alumina-zirconia composite ceramics - part 3. calculation of elastic moduli of polycrystalline alumina and zirconia from monocrystal data,” *Ceramics*, vol. 48, no. 2, pp. 41–48, 2004.

[127] J. R. Gladden, H. S. Jin, J. D. Maynard, P. W. Saxe, and Y. L. Page, “Reconciliation of *ab initio* theory and experimental elastic properties of  $\text{Al}_2\text{O}_3$ ,” *Applied Physics Letters*, vol. 85, no. 3, pp. 392–394, 2004.

[128] Kh. S. Bagdasarov, V. B. Braginsky, V. P. Mitrofanov, and V. S. Shiyan, “High-quality mechanic resonator from sapphire single-crystal,” *Vestnik Moskovskogo Universiteta Seriya Fizika Astronomiya*, vol. 18, no. 1, pp. 98–100, 1977.

[129] D. F. McGuigan, C. C. Lam, R. Q. Gram, A. W. Hoffman, D. H. Douglass, and H. W. Gutche, “Measurements of the mechanical Q of single-crystal silicon at low temperatures,” *Journal of Low Temperature Physics*, vol. 30, no. 5-6, pp. 621–629, 1978.

[130] M. Goryachev, D. L. Creedon, E. N. Ivanov, S. Galliou, R. Bourquin, and Tobar M. E., “Extremely low-loss acoustic phonons in a quartz bulk acoustic wave resonator at millikelvin temperature,” *Applied Physics Letters*, vol. 100, no. 24, pp. 243504, 2012.

[131] P.J. Veitch, J. Ferreira, D. G. Blair, and N. Linthorne, “Low temperature acoustic loss of pure and alloyed niobium and titanium with application to gravitational radiation detectors,” *Cryogenics*, vol. 27, pp. 586–588, 1987.

[132] M. Y. Yuan, M. A. Cohen, and G. A. Steele, “Silicon nitride membrane resonators at millikelvin temperatures with quality factors exceeding  $10^8$ ,” *Applied Physics Letters*, vol. 107, no. 6, pp. 263501, 2015.

[133] Jr Duffy, W., “Acoustic quality factor of aluminum alloys from 50 mk to 300 k,” *Journal of Applied Physics*, vol. 68, no. 11, pp. 5601–5609, 1990.

[134] Jr Duffy, W. and Umstattd, “Acoustic quality factor of niobium and vanadium at low temperatures,” *Journal of Applied Physics*, vol. 75, no. 9, pp. 4489–4495, 1994.

[135] Jr Duffy, W., “Acoustic quality factor of copper, brass and beryllium copper from 50 mk to 300 k,” *Cryogenics*, vol. 32, no. 12, pp. 1121–1124, 1992.

[136] Jr Duffy, W., "Acoustic quality factor of aluminum and selected aluminum alloys from 50 mk to 300 k," *Cryogenics*, vol. 42, no. 3-4, pp. 245–251, 2002.

[137] A. D. Fefferman, R. O. Pohl, A. T. Zehnder, and J. M. Parpia, "Acoustic properties of amorphous silica between 1 and 500 mk," *Physical Review Letters*, vol. 100, no. 19, pp. 195501, 2008.

[138] M. S. Kushwaha, P. Halevi, L. Dobrzynski, and B. Djafari-Rouhani, "Acoustic band structure of periodic elastic composites," *Phys. Rev. Lett.*, vol. 71, pp. 2022–2025, Sep 1993.

[139] M. M. Sigalas and E. N. Economou, "Elastic and acoustic-wave band-structure," *Journal of Sound and Vibration*, vol. 158, no. 2, pp. 377–382, 1992.

[140] Pat R. Roach, J. B. Ketterson, and M. Kuchnir, "Hydraulically actuated valve for very low temperatures," *Review of Scientific Instruments*, vol. 43, no. 6, pp. 898–899, 1972.

[141] R. B. Hallock, "A bellows seal superfluid valve," *The Review of Scientific Instruments*, vol. 43, no. 11, pp. 1713–1714, 1972.

[142] V. Dotsenko and N. Mulders, "A really simple cryogenic valve," *Journal of Low Temperature Physics*, vol. 134, no. 1/2, pp. 443–446, 2004.

[143] E. N. Ivanov, M. E. Tobar, P. J. Turner, and Blair D. G., "Noncontacting microwave coupling to a cryogenic gravitational radiation antenna," *Reviews of Scientific Instruments*, vol. 64, no. 7, pp. 1905–1909, 1993.

[144] ATI Wah Chang, 1600 NE Old Salem Road, P.O. Box 460, Albany, Oregon 97321.

[145] Fine Metals Corporation, 15117 Washington Hwy, Ashland, VA 23005.

[146] Southwest Microwave, 9055 S McKemy St. Tempe, AZ 85284-2946.

[147] Matheson Tri Gas Incorporated, 150 Allen Road, Basking Ridge, NJ 07920.

[148] P. V. E. McClintock, “An apparatus for preparing isotopically pure  $\text{He}^4$ ,” *Cryogenics*, vol. 18, no. 4, pp. 201–208, 1978.

[149] E. T. Swartz, “Cooling the sample,” in *Experimental Techniques in Condensed Matter Physics at Low Temperatures*, R. C. Richardson and E. N. Smith, Eds., chapter 3.5. Addison-Wesley, Ithaca, New York, 1998.

[150] P. A. Busch, S. P. Cheston, and D. S. Greywall, “Properties of sintered-silver heat exchangers,” *Cryogenics*, vol. 24, no. 8, pp. 445–447, 1984.

[151] V. Keith and M. G. Ward, “A recipe for sintering submicron silver powders,” *Cryogenics*, vol. 24, no. 5, pp. 249–250, 1984.

[152] Inframat Advanced Materials LLC, 151 Progress Drive, Manchester, CT 06042.

[153] S. Brunauer, P. H. Emmett, and E. Teller, “Adsorption of gases in multimolecular layers,” *Journal of the American Chemical Society*, vol. 60, no. 2, pp. 309–319, 1938.

[154] Coax Co., Ltd., 2-31 Misuzugaoka, Aoba-ku, Yokohama-shi, Kanagawa, 225-0016 Japan.

[155] ESPI Metals, 1050 Benson Way, Ashland, Oregon 97520.

[156] Servometer, 501 Little Falls Road, Cedar Grove, NJ 07009.

[157] Onyx Optics, Inc., 6551 Sierra Lane, Dublin, CA 94568.

[158] Agilent Technologies, 5301 Stevens Creek Blvd, Santa Clara, CA 95051, United States.

[159] G. Santarelli, C. Audoin, A. Makdissi, P. Laurent, G. J. Dick, and A. Clairon, “Frequency stability degradation of an oscillator slaved to a periodically interrogated atomic resonator,” *IEEE Transactions on Ultrasonics, Ferroelectrics, and Frequency Control*, vol. 45, no. 4, pp. 887–894, July 1998.

[160] T. M. Fortier, N. Ashby, J. C. Bergquist, M. J. Delaney, S. A. Diddams, T. P. Heavner, L. Hollberg, W. M. Itano, S. R. Jefferts, K. Kim, F. Levi, L. Lorini, W. H. Oskay, T. E. Parker, J. Shirley, and J. E. Stalnaker, “Precision atomic spectroscopy for improved limits on variation of the fine structure constant and local position invariance,” *Phys. Rev. Lett.*, vol. 98, pp. 070801, Feb 2007.

[161] P.-Y. Bourgeois, Y. Kersalé, N. Bazin, M. Chaubet, and V. Giordano, “A cryogenic open-cavity sapphire reference oscillator with low spurious mode density,” *IEEE Transactions on Ultrasonics, Ferroelectrics, and Frequency Control*, vol. 51, no. 10, pp. 1232–1239, 2004.

[162] E. N. Ivanov and M. E. Tobar, “Low phase-noise sapphire crystal microwave oscillators: current status,” *IEEE Transactions on Ultrasonics, Ferroelectrics, and Frequency Control*, vol. 56, pp. 263–269, 2009.

[163] J. G. Hartnett, N. R. Nand, and C. Lu, “Ultra-low-phase-noise cryocooled microwave dielectric-sapphire-resonator oscillators,” *Applied Physics Letters*, vol. 100, pp. 183501, 2012.

[164] J. Li, X. Yi, H. Lee, S. A. Diddams, and K. J. Vahala, “Electro-optical frequency division and stable microwave synthesis,” *Science*, vol. 345, pp. 309–313, 2014.

[165] Z. Chen, J. Bohnet, J. Weiner, and J. Thompson, “A low phase noise microwave source for atomic spin squeezing experiments in  $^{87}\text{rb}$ ,” *Reviews of Scientific Instruments*, vol. 83, pp. 044701, 2012.

[166] B. Abbott and et al., “Observation of gravitational waves from a binary black hole merger,” *Physical Review Letters*, vol. 116, pp. 061102, 2016.

[167] J. Weber, “Detection and generation of gravitational waves,” *Physical Review*, vol. 117, pp. 306–313, 1960.

[168] Andrew Lyne and Francis Graham-Smith, *Pulsar Astronomy*, Cambridge University Press, 2006.

[169] J. Aasi and et al., “Gravitational waves from known pulsars: Results from the initial detector era,” *Astrophysical Journal*, vol. 785, pp. 119, 2014.

[170] S .M. Carroll, *Spacetime and geometry. An introduction to general relativity.*, Addison Wesley, 2005.

[171] Hiromasa Hirakawa, Kazumichi Narihara, and Masa-Katsu Fujimoto, “Theory of antennas for gravitational radiation,” *Journal of the Physical Society of Japan*, vol. 41, no. 4, pp. 1093–1101, 1976.

[172] Kimio Tsubono, “Detection of continuous waves,” in *The Detection of Gravitational Waves*, D. G. Blair, Ed. Cambridge University Press, Cambridge, 1991.

[173] Nelson Christensen, “Measuring the stochastic gravitational-radiation background with laser-interferometric antennas,” *Phys. Rev. D*, vol. 46, pp. 5250–5266, 1992.

[174] K.C.B. New, G. Chanmugam, W.W. Johnson, and J.E. Tohline, “Millisecond Pulsars: Detectable Sources of Continuous Gravitational Waves?,” *The Astrophysical Journal*, vol. 450, pp. 757, Sept. 1995.

[175] K.R. Atkins and R.A. Stasior, “First sound in liquid helium at high pressures,” *Can. J. Phys.*, vol. 41, pp. 596, 1953.

[176] L. G. Garay, “Quantum gravity and minimum length,” *International Journal of Modern Physics A*, vol. 10, pp. 145–165, 1995.

[177] D. Amati, M. Ciafaloni, and G. Veneziano, “Superstring collisions at Planckian energies,” *Physics Letters B*, vol. 197, pp. 81–88, 1987.

[178] F. Marin, F. Marino, M. Bonaldi, M. Cerdonio, L. Conti, P. Falferi, R. Mezzena, A. Ortolan, G. A. Prodi, L. Taffarello, G. Vedovato, A. Vinante, and J.-P. Zendri, “Gravitational bar detectors set limits to Planck-scale physics on macroscopic variables,” *Nature Physics*, vol. 9, pp. 71–73, 2013.

- [179] B. Abbott and et al., “LIGO: the Laser Interferometer Gravitational-Wave Observatory,” *Reports on Progress in Physics*, vol. 72, pp. 076901, 2009.
- [180] S. Das and E. C. Vagenas, “Universality of quantum gravity corrections,” *Physical Review Letters*, vol. 101, pp. 221301, 2008.
- [181] C. Quesne and V. M. Tkachuk, “Composite system in deformed space with minimal length,” *Physical Review A*, vol. 81, pp. 012106, 2010.